Epitaxial CoxNi1-x nanowires in SrTiO3 matrix : growth, structure and control of magnetic anisotropy

Xiaorong Weng

THESE DE DOCTORAT DE SORBONNE UNIVERSITÉ

Spécialité Physique

Ecole Doctorale 397
Physique et Chimie de Matériaux

Institut des NanoSciences de Paris

Sujet de la thèse :

Epitaxial Co_xNi_{1-x} nanowires in $SrTiO_3$ matrix: growth, structure and control of magnetic anisotropy

Par WENG Xiaorong

Dirigée par Franck VIDAL et Yunlin ZHENG

Composition du jury :

Mme ANDREAZZA Caroline, ICMN-Université d'Orléans, rapportrice

M. HAUET Thomas, IJL-Université de Lorraine, rapporteur

Mme DUPUIS Véronique, ILM-CNRS, examinatrice

M. MENGUY Nicolas, IMPMC-Sorbonne Université, examinateur

M. ZHENG Yunlin, INSP-CNRS, co-directeur de thèse

M. VIDAL Franck, INSP-Sorbonne Université, directeur de thèse

Acknowledgments

Il me sera très difficile de remercier tout le monde, car c'est grâce à l'aide de nombreuses personnes que j'ai pu mener à bien cette thèse.

Mme Caroline ANDREAZZA et M. Thomas HAUET m'ont fait l'honneur d'être rapporteurs de ma thèse. Leurs remarques et suggestions m'ont permis d'améliorer mon manuscrit. Je les remercie. Je suis reconnaissante à Mme Véronique DUPUIS et M. Nicolas MENGUY pour avoir accepté de participer à mon jury de thèse et pour leurs questions et critiques constructives.

Je voudrais remercier grandement mes directeurs de thèse, Franck VIDAL et Yunlin ZHENG, pour toute leur aide durant ces trois ans. Je suis ravie d'avoir travaillé dans le groupe «Croissance et propriétés de systèmes hybrides en couches minces». Outre l'appui scientifique, les membres du groupe ont toujours été là pour me soutenir et me conseiller au cours de cette thèse.

J'adresse mes remerciements à Marcel HENNES, avec qui j'ai travaillé, pour ses conseils au cours de cette thèse. J'exprime ma totale gratitude à Dominique DEMAILLE pour le travail en croissance et en microscopie électronique. Je souhaite remercier les personnes de l'INSP qui ont toujours été agréables et disponibles.

Je voudrais remercier spécialement Sara HIDKI et Nicolas CASARETTO pour leur travail en diffraction et David HRABOVSKY et Yanling LI en magnétomètrie.

Il m'est impossible d'oublier toutes les personnes sur les lignes SIXS et DEIMOS du synchrotron SOLEIL et de l'IMPMC pour leur aide précieuse en diffraction et spectroscopie. Je voudrais spécialement remercier Alessandro COATI, Yves GARREAU, Michèle SAUVAGE-SIMKIN, Benoît GOBAUT, Philippe SAINCTAVIT et Amélie JUHIN qui ont toujours fait tout leur possible pour m'aider.

Je garderai toujours le bon souvenir des moments heureux partagés avec mes amies, Red, Yuzi et Fei.

A ma famille,

ma mère, mon père, ma sœur, mon frère et même les neveux juste nés,

je dédie ce travail.

Xiaorong WENG

Epitaxial Co_xNi_{1-x} nanowires in $SrTiO_3$ matrix: growth, structure and control of magnetic anisotropy

Abstract

This thesis describes the study of self-assembled epitaxial ferromagnetic Co_xNi_{1-x} nanowires in $SrTiO_3$ matrix deposited on $SrTiO_3(001)$ substrate. This system is grown by pulsed laser deposition. Taking advantage of the sequential deposition of wires and matrix, the diameter of nanowires is controlled in the 1.7-5.3 nm range. Due to the lattice mismatch between wires and matrix, nanowires are in tensile axial strain. The tensile strain decreases with increasing diameter and is in the 2-4% range. Large strain is thus achieved in this vertically aligned nanocomposite structure.

The total magnetic anisotropy of the nanowires is shown to result from the competition of the magnetostatic and magnetoelastic anisotropies. The magnetostatic effect favors an easy magnetization axis along the wire axis. The magnetoelastic contribution introduced by the tensile strain depends on the magnetostriction constant and the strain. It is uniaxial, negative for Ni and positive for Co concentration of about 20% and above. Under a strain larger than 0.8% (determined by the compensation of the magnetostatic and magnetoelastic anisotropies), the magnetoelastic anisotropy dominates in magnitude the magnetostatic one, leading the wire axis to be a hard magnetization axis for Ni. For Co_xNi_{1-x} alloy nanowires, the large strain reinforces the easy character of the wire axis. This results in the enhancement of the blocking temperature over room temperature, indicating the increased thermal stability of magnetization in this system. A spectroscopic study of the spin and orbital magnetic moments evidences the fact that the anisotropy of the orbital moment can be correlated with the magnetoelastic anisotropy. The control of the magnetic anisotropy by the strain or the diameter is a good starting point for the construction of 3D nanomagnetic structures.

Nanofils de Co_xNi_{1-x} epitaxiés dans une matrice de $SrTiO_3$: croissance, structure et contrôle de l'anisotropie magnetique

Résumé

Cette thèse décrit l'étude de l'auto-assemblage de nanofils ferromagnétiques de Co_xNi_{1-x} épitaxiés dans une matrice de $SrTiO_3$ sur un substrat de $SrTiO_3(001)$. Ce système est elaboré par ablation laser pulsé. Profitant du dépôt séquentiel des fils et de la matrice, le diamètre des nanofils est contrôlé dans la gamme de 1,7 à 5,3 nm. En raison du désaccord de paramètre de maille entre les fils et la matrice, les nanofils sont dilatés axialement. Cette déformation décroît lorsque le diamètre des fils augmente, elle se situe dans la gamme de 2-4%. Une déformation importante est donc obtenue dans ces structures nanocomposites alignées verticalement.

L'anisotropie magnétique des nanofils résulte de la compétition des anisotropies magnétostatique et magnétoélastique. L'effet magnétostatique favorise un axe d'aimantation facile le long de l'axe des fils. La contribution magnétoélastique introduite par la déformation dépend de la constante de magnétostriction et de la déformation. Elle est uniaxiale, négative pour Ni et positive pour une concentration de Co d'environ 20% et plus. Sous une déformation supérieure à 0,8% (déterminée par la compensation des anisotropies magnétostatique et magnétoélastique), l'anisotropie magnétoélastique prédomine, faisant de l'axe des fils un axe d'aimantation dur dans le cas du Ni. Pour les nanofils d'alliage Co_xNi_{1-x}, la grande déformation renforce le caractère facile de l'axe des fils. Il en résulte une augmentation de la température de blocage par rapport à la température ambiante, indiquant une augmentation de la stabilité thermique de l'aimantation dans ce système. Une étude spectroscopique des moments magnétiques de spin et d'orbite met en évidence le fait que l'anisotropie du moment orbital peut être corrélée à l'anisotropie magnétoélastique. Le contrôle de l'anisotropie magnétique par la déformation ou le diamètre est un bon point de départ pour la construction de structures nanomagnétiques 3D.

Résumé étendu

Les hétérostructures en épitaxie planaire ont été largement étudiées depuis de nombreuses années pour leur intérêt fondamental et leurs applications potentielles. En optoélectronique, l'empilement de couches de semi-conducteurs de même paramètre de maille dans des hétérostructures permet de modeler le potentiel électronique dans la direction de croissance avec une précision atomique. Cela permet d'élaborer des jonctions tunnel, des gaz d'électrons (et de trous) à deux dimensions, des puits quantiques, diverses structures pouvant être utilisées pour étudier de nouveaux effets physiques ainsi que pour concevoir des dispositifs ayant des applications d'intérêt technologique.

La déformation introduite par l'épitaxie, résultant du désaccord de paramètres de maille des réseaux cristallins au niveau des interfaces hétérogènes, est un puissant levier pour modifier et éventuellement contrôler les propriétés des films minces épitaxiés. Par exemple, l'ingénierie de la déformation peut être utilisée pour augmenter la température de Curie de films ferroélectriques de $BaTiO_3$ ultra-minces. Dans le domaine du nanomagnétisme, les contraintes épitaxiales ont été exploitées afin de contrôler l'anisotropie magnétique de films minces magnétiques épitaxiés en exploitant les effets magnétoélastiques.

Cependant, dans les hétérostructures en épitaxie planaire, les couches doivent être suffisamment minces pour éviter la relaxation des contraintes latérales via la formation de dislocations de *misfit*. Un très haute qualité cristalline, c'est à dire une faible densité de défauts structuraux, est donc difficile à obtenir dans le cas où le désaccord paramétrique est grand. Afin de surmonter cette limitation et de développer des hétérostructures supportant une déformation importante le long de la direction de croissance sur des épaisseurs élevées, la synthèse de nanocomposites alignés verticalement (VANs, *Vertically Assembled Nanocomposites*) a été proposée comme une nouvelle stratégie au cours de la dernière décennie. Une structure VAN étant composée d'une matrice dans laquelle sont épitaxiés des nanopilliers d'un autre matériau que celui de la matrice, ces nanopilliers ont leur grand axe le long de la direction de croissance. Le désaccord au niveau de l'hétérointerface verticale entre les deux matériaux (matrice et/ou nanopilliers) peut alors introduire une déformation verticale. Ceci peut alors être mis à profit pour ajuster une propriété physique dépendant de la déformation du nanocomposite. De plus, en raison de la géométrie, le couplage interfacial des propriétés physiques de deux matériaux peut offrir la possibilité de coupler des propriétés de la matrice et des pilliers. C'est par exemple le cas dans des systèmes alliant un composé ferroélectrique et un composé ferromagnétique qui peuvent se comporter comme des systèmes multiferroïques artificiels. Ainsi, les VANs ont été intensément étudiés ces dernières années en raison de leur intérêt dans les domaines du nanomagnétisme, de la plasmonique, de la catalyse, de la conductivité ionique, de la ferroelectricité, de la multiferroïcité, de la spintronique et du stockage de données à haute densité.

Récemment, des structures plus complexes ont pu être élaborées en intercalant des couches minces dans une structure VAN. Ceci ouvre la voie à l'élaboration de structures 3D. Parallèlement, un nouveau champ de recherche émerge en nanomagnétisme sur les structures complexes 3D. L'extension des nanostructures 2D en structures 3D permet aux configurations de spin et aux fonctionnalités de s'étendre non seulement dans le plan mais également dans la direction verticale, ce qui conduit à de nouveaux effets. Parmi les différentes géométries de systèmes nanomagnétiques 3D, les nanofils cylindriques à diamètre modulé, aux propriétés magnétiques différentes en fonction du diamètre, pourraient être réalisés à base de VANs. Avant d'atteindre cet objectif à moyen terme, être capable de contrôler le diamètre et les propriétés magnétiques des nanofils dans des nanocomposites de type VAN est le but de mon travail de thèse.

Les études précédentes sur des VANs composés de nanofils de Co_xNi_{1-x} en matrice de CeO_2 (thèse de F. J. Bonilla) et de Co_xNi_{1-x} en matrice de $Sr(Ba)TiO_3$ (thèse de V. Schuler) ont montré qu'il était en principe possible de contrôler l'anisotropie magnétique via la déformation dans ce type de systèmes hybrides métal/oxyde. Dans le cas de nanofils de Ni, il a été démontré que l'anisotropie magnéto-élastique, liée à la déformation axiale et à la constante de magnétostriction négative, est en compétition avec l'anisotropie de forme. Avec une matrice de CeO_2, un comportement magnétique isotrope a été observé pour des fils de Ni ayant une dilatation verticale d'environ 1%. Dans le cas des systèmes où la matrice est $(Sr,Ba)TiO_3$, l'anisotropie peut être inversée: l'axe des fils de Ni devient un axe d'aimantation difficile. Dans les alliages de Co_xNi_{1-x}, la constante de magnétostriction devient positive pour $x \geq 0{,}2$. Il est alors envisageable que les anisotropies de forme et magnétoélastique s'ajoutent, donnant lieu à une exaltation de l'anisotropie uniaxiale du système. Cet effet n'a pas pu être observé clairement dans les VANs à base de CeO_2 et de $(Sr,Ba)TiO_3$. Dans cette thèse, je m'intéresse au système Co_xNi_{1-x}: $SrTiO_3$ dans le but de déterminer si ce système permet de contrôler l'anisotropie magnétique via la déformation et via la composition des alliages Co_xNi_{1-x}.

Dans le **premier chapitre**, les éléments de magnétisme nécessaires à la compréhension et à l'analyse des propriétés magnétiques d'assemblées de nanofils ferromagnétiques sont introduits. Les différentes contributions à l'énergie magnétique d'un système ferromagnétique sont décrites: énergie d'échange, énergies d'anisotropie (magnétocristalline et magnétoélastique), énergie magnétostatique et énergie Zeeman (reliée au champ magnétique externe). Les longueurs caractéristiques (longueur d'échange, largeur de paroi de domaine) qui émergent de la comparaison de ces termes sont introduites. Les mécanismes de renversement de l'aimantation pertinents dans le cadre de cette étude sont ensuite évoqués (renversement uniforme et non-uniforme). Le modèle de Stoner-Wohlfarth, décrivant le renversement cohérent d'une particule mono-domaine, est détaillé. Je décris ensuite l'impact de la température sur le comportement magnétique et la transition vers le régime superparamagnétique. La loi d'évolution du champ coercitif avec la température, qui permet de remonter à l'énergie de bar-

rière pour le renversement, est donnée. Le modèle d'anisotropie magnétique aléatoire (RMA, *random magnetic anisotropy*) a été introduit. Il s'agit du cas où les domaines structuraux, dans un polycristal, par exemple, sont de taille inférieure à la largeur d'une paroi de domaine magnétique et l'axe d'anisotropie locale orienté aléatoirement. La conséquence d'une telle nanostructuration est une réduction de l'anisotropie magnétique locale. Enfin, l'effet de l'interaction dipolaire entre nanofils dans une assemblée est décrit en précisant son impact sur les champs caractéristiques et sur l'anisotropie effective du système, dans le cadre d'un modèle de champ moyen.

Le **2ème chapitre** présente les techniques expérimentales utilisées durant l'étude. La croissance des nanofils épitaxiés en matrice d'oxyde est faite par ablation laser pulsé (PLD, *pulsed laser deposition*). Le principe de la PLD est décrit: un laser pulsé ultraviolet est utilisé pour tirer sur une cible d'un matériau à déposer. Cette cible est en regard d'un substrat maintenu à la température de croissance via un four, l'ensemble étant sous vide. Lors de l'impact d'une impulsion laser sur la cible, un plasma est généré et se propage vers le substrat situé en face de la cible. Ceci permet de déposer le matériau constituant la cible sur le substrat. J'ai élaboré les couches minces de VANs à l'Institut des NanoSciences de Paris, sous la supervision de Yunlin Zheng et de Franck Vidal, et avec l'assistance de Dominique Demaille. L'exploration des propriétés structurales est effectuée en utilisant la microscopie électronique en transmission et la diffraction des rayons X (XRD, *x-ray diffraction*). Les caractérisations par microscopie ont été réalisées par Dominique Demaille à l'Institut de Minéralogie et de Physique des Milieux Condensés (IMPMC-Paris, France). Les mesures de diffraction sont réalisées sur un diffractomètre à cinq cercles à l'INSP avec l'assistance de Sarah Hidki et Nicolas Casaretto. Les différentes géomètries de mesure utilisées au cours de cette thèse sont décrites. De plus, des cartographies détaillées de l'espace réciproque ont été réalisées par diffraction des rayons X à haute-résolution sur la ligne SixS du synchrotron SOLEIL (St Aubin, France), en collaboration avec Alessandro Coati, Yves Garreau et Michèle Sauvage-Simkin. L'étude des propriétés magnétiques est réalisée par magnétométrie à échantillon vibrant (VSM, *vibrating sample magnetometry*). Les mesures d'aimantation sont faites à la plate-forme MPBT (mesures physiques à basse température) de Sorbonne Université, avec l'assistance de David Hravovsky. Enfin, la spectroscopie de dichroïsme circulaire magnétique des rayons X (XMCD, *x-ray magnetic circular dichroism*) a été utilisée pour obtenir des informations spécifiques des éléments composant les nanofils et pour déterminer les moments magnétiques de spin et d'orbite. Les principes de base de cette technique spectroscopique sont décrits. Les mesures ont été effectuées sur la ligne DEIMOS du synchrotron SOLEIL, sous la supervision de Benoît Gobaut et de Philippe Sainctavit et Amélie Juhin (IMPMC-Paris, France).

Le **3ème chapitre** décrit l'élaboration des assemblées de nanofils de Co_xNi_{1-x} dans une matrice de $SrTiO_3$ par ablation laser pulsé. La température de croissance est de 650°C et sous une pression dans

la gamme 10^{-6}-10^{-7} mbar. Une technique de dépôt séquentiel est utilisée. En tirant alternativement sur les cibles contenant les éléments magnétiques et la cible de $SrTiO_3$, il est possible d'obtenir des nanofils de Co_xNi_{1-x} de composition réglable via la séquence de dépôt utilisée. Le diamètre et la densité, et donc la porosité de l'assemblée de nanofils, sont déterminés par analyse d'images TEM en vue plane. Le caractère séquentiel de la croissance implique un temps sans dépôt pendant le changement de cible. Pendant cet intervalle de temps, les atomes diffusent et peuvent coalescer pour former des clusters métalliques à la surface de $SrTiO_3$. La croissance séquentielle conduit ensuite à la formation de nanofils dont l'axe est paralllèle à la direction de croissance. Le diamètre des nanofils peut être contrôlé via la séquence de tirs. Quand le nombre de tirs sur la cible de la matrice est constant, l'augmentation du nombre de tirs sur la cible contenant les éléments magnétiques va agrandir le diamètre du fil avec une densité similaire. Par contre, quand le nombre de tir sur la cible les éléments magnétiques n_1 est fixé, en augmentant le nombre de tirs sur la cible de la matrice n_2, le diamètre des fils va diminuer. Cette diminution du diamètre implique une mobilité verticale des atomes pendant la croissance. Expérimentalement, on montre que la section des fils (proportionnelle au diamètre au carré) augemente linéairement avec le rapport n_1/n_2 utilisé pour une séquence élémentaire de dépôt. Dans notre étude, le diamètre des nanofils de Ni/Co_xNi_{1-x} est dans la gamme de 1,7 à 5,3 nm, avec la porosité d'environ 10%.

Après l'élaboration des nanofils dans la matrice, l'étude de la structure cristallographique des nanofils par microscopie électronique et par diffraction des rayons X est présentée dans le **4ème chapitre**. L'analyse des images de microscopie électronique à haute résolution et des diffractogrammes obtenus au laboratoire montre que les nanofils Ni/Co_xNi_{1-x} ont une structure cubique à faces centrées qui est en épitaxie cube sur cube dans la matrice de $SrTiO_3$. Le caractère métallique des nanofils est confirmé par spectroscopie d'absorption au seuil K. Par ailleurs, l'analyse des données spectroscopiques obtenues en microscopie électronique montre que la composition des nanofils de Co_xNi_{1-x} est en accord avec celle qui est programmée lors de la séquentielle déposition. La composition des alliages de Co_xNi_{1-x} peut donc être contrôlée via la séquence de dépôt en ajustant le nombre de tirs sur les cibles.

Comme la déformation est une caractéristique clé dans l'étude de l'épitaxie des nanostructures alignées verticalement, nous nous concentrons ensuite sur l'étude de l'état de la déformation dans ce chapitre. La déformation est déterminée par XRD. Pour les assemblées de nanofils de Ni pur, les balayages θ-2θ hors plan donnent une grand dilatation axiale ϵ_{zz}, de 2 à 4%. Le balayage dans le plan donne une compression radiale inférieure à 0,5%, qui peut être négligée en première approximation devant la dilatation axiale. En variant le diamètre des fils, on constate le fait que quand le diamètre des fils diminue, la dilatation axiale augmente. Cela peut s'expliquer par l'équilibre entre l'énergie élastique ($\propto d^2$) et l'interaction à l'interface entre les fils et la matrice ($\propto d$), d représentant le diamètre.

Pour les alliages de Co_xNi_{1-x}, en augmentant la concentration de Co, la dilatation axiale augmente à diamètre constant. Ainsi, comparé à la déformation verticale des fils dans la matrice de CeO_2 ou (Sr,Ba)TiO_3, ϵ_{zz} est forcement augmentée dans les systèmes élaborés à base de matrice de $SrTiO_3$. On arrive à augmenter la déformation en contrôlant le diamètre du fil ou la composition de l'alliage de Co_xNi_{1-x}.

La largeur importante de la réflexion 002 du Ni dans les balayages θ-2θ indique l'inhomogénéité de la dilatation axiale. L'inhomogénéité de la structure cristallographique du Ni est aussi observée sur les images de microscopie électronique en section transverse. Si globalement on observe que les directions [001] du Ni et de $SrTiO_3$ sont alignées, une analyse plus locale révèle l'existence de franges de Moiré qui varient le long de l'axe. Ceci est lié à l'existence de domaines dans les fils, domaines dont l'orientation varie légèrement le long de l'axe. Certains domaines sont orientés avec un angle d'environ 4° entre les directions [001] du Ni et de $SrTiO_3$. Pour étudier plus en profondeur l'inhomogénéité de la déformation, des cartographies détaillées de l'espace réciproque ont été réalisées par diffraction des rayons X à haute-résolution sur la ligne SixS du synchrotron SOLEIL. Pour un échantillon typique de nanofils de Ni, à partir des cartographies d'espace réciproque autour de la réflexion 002, quatre taches supplémentaires ont été observées autour d'une tache centrale. Ces quatre taches correspondent à des domaines désorientés et moins dilatés que ceux liés à la tache centrale qui est alignée avec la matrice. Les désorientations sont vers les directions [100] et [010]. Autour de 202, ces quatre taches supplémentaires ont été retrouvées dans les cartographies d'espace réciproque. L'analyse des résultats montre que la relaxation de la déformation combinée avec une désorientation permet aux plane (101) de Ni de s'accorder avec ceux de la matrice de $SrTiO_3$. Ce mécanisme a été confirmé par des simulations des cartographies d'espace réciproque que j'ai effectuées dans le cadre de la théorie cinématique de la diffraction des rayons X. La longueur de cohérence des domaines orientés est d'environ 13 nm et celle des domaines alignés de 6 nm. Par la comparaison des cartographies de l'espace réciproque d'autres échantillons de Ni, on constate le fait que le mécanisme de relaxation avec désorientation dans des directions privilégiées existe dans les nanofils de Ni très déformés. Cependant, avec l'augmentation de la déformation, la désorientation dans des directions privilégiées est affaiblie, indiquant le renforcement du désordre cristallographique.

En parallèle, ce phénomène de désorientation a été étudié sur le diffractomètre du laboratire par figure de pôles dans le cas des nanofils de Co_xNi_{1-x}. L'analyse combinée des figures de pôles des nanofils de Ni et des cartographies de l'espace réciproque de Ni montre que les figures des pôle sont utiles pour explorer la texture des fils et permettent de mettre en évidence la désorientation par rapport à la direction [001] de $SrTiO_3$. Dans le cas des nanofils de Co_xNi_{1-x} des taches supplémentaires liées à la désorientation ont été observées aussi dans les figures de pôle. Cependant, en augmentant la concentration de Co, le signal lié à la désorientation selon les directions privilégiées [100] et [010]

devient de plus en plus faible puis disparais. Cela indique la disparation de la désorientation dans des directions privilégiées. L'augmentation de la concentration de Co renforce aussi le désordre dans les fils.

Dans le **5ème chapitre**, les propriétés magnétiques des assemblées de nanofils de Ni ont été étudiées par magnétométrie VSM. Des mesures de cycle d'hystérésis sont montrées pour des nanofils de Ni de diamètres différents. La saturation de l'aimantation est plus facile en appliquant le champ magnétique externe perpendiculaire à l'axe des fils que le long de l'axe des fils. Ce système favorise donc un axe de difficile aimantation le long de l'axe des fils. Ceci est le reflet de l'équilibre entre l'anisotropie de forme, l'anisotropie magnéto-cristalline et l'anisotropie magnéto-élastique. Il n'y a pas de différence entre les cycles d'hystérésis en appliquant le champ dans le plan selon les directions [100] et [110]. Cela indique le fait que l'effet de l'anisotropie magnéto-cristalline (cubique) n'est pas observé. Cette anisotropie est beaucoup plus faible que les deux autres termes contribuant à l'anisotropie magnétique globale. La constante de magnétostriction est négative pour Ni. Comme la déformation axiale est positive (dilatation) et beaucoup plus grande que la compression radiale, il en résulte que l'anisotropie magnéto-élastique favorise un axe de difficile aimantation le long de l'axe des fils. La compensation des anisotropies uniaxiales magnéto-élastique et de forme a lieu pour une dilatation d'environ 0.8%. Avec une grande dilatation axiale, dans la gamme 2-4%, la contribution d'anisotropie magnéto-élastique prédomine donc dans les assemblées de nanofils de Ni dans $SrTiO_3$. Ceci permet d'expliquer le fait que le système a un axe de difficile aimantation parallèle à l'axe des nanofils.

En outre, l'ouverture du cycle est similaire dans les directions d'aimantation facile et difficile. Le champ coercitif non-nul indique l'existence d'une barrière locale d'énergie. Le comportement magnétique ne peut pas être expliqué par le modèle simple de Stoner-Wohlfarth. Le modèle d'anisotropie magnétique aléatoire (RMA) a été introduit, en considérant des inhomogénéités de déformation comme source de barrières locales d'énergie. Ainsi pour le plan facile, l'axe facile d'aimantation local est considéré comme orienté aléatoirement dans le plan. La réponse magnétique globale a été alors modélisée en sommant tous les cycles d'hystérésis dans le plan facile. De plus, une distribution de constantes d'anisotropie a été prise en compte, ce qui a permis de reproduire parfaitement la réponse magnétique dans le plan à basse température.

Cependant, avec la même distribution de constantes d'anisotropie, la simulation ne permet pas de reproduire la réponse magnétique en fonction de la température. Il faut souligner que la dépendance du champ coercitif H_c en température est inhabituelle: H_c décroit exponentiellement en température. Cette évolution n'est pas en accord avec la formule de Sharrock sur la réduction thermique du champ coercitif qui est une loi de puissance en température. Nous supposons alors que les constantes

d'anisotropie, donc les barrières d'énergie, diminuent en température. Afin de vérifier ce dernier point, des mesures de courbes de renversement du premier ordre (FORCs, *first-order reversal curves*) ont été effectuées pour extraire les distributions de champs coercitifs à plusieurs températures. Les distributions de champs coercitifs extraites ont été comparées avec la simulation et permis de valider l'affaiblissement de l'anisotropie en température dans notre système. Ainsi, l'évolution thermique du champ coercitif est due d'une part à l'habituelle réduction thermique de la coercivité selon Sharrock et d'autre part à un processus thermiquement activée entrainant ue réduction de l'anisotropie elle-même.

Enfin, des mesures spectroscopiques aux seuils Ni $L_{2,3}$ ont été effectuées sur la ligne DEIMOS du synchrotron SOLEIL afin de mesurer le moment orbital et le moment de spin de Ni. Le moment total à rémanence augmente quand l'angle θ entre le champ magnétique appliqué et l'axe du fil augmente. Cela confirme l'axe d'aimantation difficile parallèle à l'axe des nanofils. Grâce aux règles de somme pour le XMCD, les valeurs du moment orbital et du moment de spin sont obtenues. Le moment du spin est indépendant de l'angle θ. Cependant, le moment orbital de Ni augmente en fonction de θ. A partir de l'évolution angulaire du moment orbital de Ni, l'énergie d'anisotropie magnétique (MAE) est évaluée à environ 31 ± 5 μeV/atome. En comparant avec la MAE déduite par les cycles d'hystérésis dans les directions facile et difficile, on trouve que la MAE déduite par XMCD est plus grande que celle liée à l'anisotropie magnéto-élastique. Des expériences complémentaires par résonance ferromagnétique pourraient être menées à l'avenir afin de déterminer plus précisément la MAE dans ces systèmes.

Le **6ème chapitre** est consacré à l'étude des propriétés magnétiques de nanofils d'alliage Co_xNi_{1-x} dans $SrTiO_3$. L'étude des cycles d'hystérésis pour différentes concentrations de Co dans la gamme 20%-80% montre que l'axe de facile aimantation est parallèle à l'axe des nanofils. Ceci est dû à la variation de la constante de magnéto-striction qui augmente avec la concentration de Co et devient positive à $\sim$20% Co. L'ansiotropie magnéto-élastique renforce donc l'effet d'anisotropie de forme. En augmentant la concentration de Co, la dilatation axiale est augmentée, ce qui renforce l'effet de l'anisotropie magnéto-élastique. Cela est reflété par l'augmentation du champ coercitif le long de l'axe de facile aimantation et de la température de blocage T_b lorsque la concentration de Co augmente. T_b est supérieure à la température ambiante pour des concentrations de Co supérieures à $\sim$60%. La stabilité thermique du système de Co_xNi_{1-x} dans $SrTiO_3$ est donc améliorée. L'analyse des variations avec la température du champ coercitif H_c montre que, contrairement aux résultats obtenus dans le cas des nanofils de Ni, H_c évolue bien en suivant une loi de Sharrock. L'estimation de l'anisotropie uniaxiale du système à partir du champ de saturation dans la direction de difficile aimantation confirme qu'une contribution additionnelle à l'anisotropie de forme doit être prise en compte.

Enfin, une étude par spectroscopie XMCD est présentée. Aux seuils L_3 de Co et Ni, les cycles

d'hystérésis sont superposés avec ceux obtenus par VSM. Ceci indique que Co et Ni forment bien un alliage et que les données XMCD reflètent bien le comportement de l'ensemble des nanofils. Le moment total à rémanence diminue quand l'angle entre le champ magnétique et l'axe des fils augmente. Cela confirme que l'axe de facile aimantation est le long de l'axe des nanofils de Co_xNi_{1-x} avec $x > 20\%$. En utilisant les règles de somme pour le XMCD, les moments orbitaux et les moments de spin de Co et Ni sont déduits. Premièrement, les moments de Ni sont beaucoup plus élevés que les valeurs du Ni massif. Les moments de Co sont proches des valeurs de Co massif. Ensuite, les moments de Co sont indépendants de l'angle θ entre le champ et l'axe des fils. Le moment de spin de Ni reste constant aussi. Cependant, l'évolution angulaire du moment orbital du Ni dépend de la composition de l'alliage Co_xNi_{1-x}. Elle est constante pour ∼20% Co et diminue avec θ pour ∼80% Co. Cela peut être expliqué par la contribution de l'anisotropie magnéto-élastique. La constante de magnéto-striction tombe à zéro à ∼20% Co, résultant en une contribution faible de l'anisotropie magnéto-élastique. Par contre, en augmentant la concentration de Co, la constante de magnéto-striction et la déformation sont renforcées, conduisant à une augmentation de l'anisotropie magnéto-élastique. L'énergie d'anisotropie magnétique déduite par l'évolution angulaire du moment orbital de Ni est du même ordre de grandeur que celle liée à l'anisotropie magnéto-élastique.

Le **dernier chapitre** présente les conclusions de cette thèse. Pour des assemblées de nanofils de Ni/Co_xNi_{1-x} épitaxiés dans la matrice de $SrTiO_3$, une déformation axiale des nanofils très élevée est obtenue, dans la gamme 2-4% avec un diamètre dans la gramme 1,7-5,3 nm. La déformation axiale dépend du diamètre et de la composition de l'alliage: elle augmente quand le diamètre diminue ou la concentration de Co augmente. Cette déformation ajustable permet de contrôler l'anisotropie magnétique via la contribution de l'anisotropie magnéto-élastique.

Quelques perspectives basées sur ces travaux sont décrites par la suite. Des nanofils bi-métalliques de Au-Co en matrice de $SrTiO_3$ ont pu être élaborés par dépôt séquentiel par ablation laser pulsé. De tels systèmes hybrides offrent la possibilité de coupler les propriétés ferromagnétiques de Co et les propriétés plasmoniques de Au. Enfin, il est possible d'envisager l'élaboration d'hétéostructures 3D à partir de nanofils ayant une anisotropie magnétique modulable le long de l'axe. L'anisotropie est contrôlée par la déformation, qui peut être modulée par une modulation du diamètre ou par une modulation de la composition de la matrice.

Contents

Introduction

The planar epitaxial heterostructures have been widely studied for their fundamental interest and their potential applications for a long time. In optoelectronics, the stacking of lattice-matched semiconductor layers in heterostructures allows to shape the electronic potential along the growth direction with atomic precision. This provides the opportunity to elaborate tunnel junctions, two-dimensional electron (and holes) gases, quantum wells, a variety of structures that can be used to study novel physics [1] and to design devices with applications. In spintronics, large tunneling magnetoresistance values can be achieved in epitaxial Fe/MgO/Fe tunnel junctions [2, 3].

Epitaxial strain, arising from the lattice mismatch at heterointerfaces, is a powerful lever to engineer the properties of epitaxial thin films. For example, strain engineering could be used successfully to increase the Curie temperature of ultrathin ferroelectric $BaTiO_3$ films [4]. In the field of nanomagnetism, epitaxial strain has been exploited in order to control the magnetic anisotropy of strained epitaxial magnetic thin films through magnetoelasticity [5].

However, in the traditional planar epitaxial heterostructures, the layers should be thin enough to avoid lateral strain relaxation via formation of misfit dislocations and the high quality of the epitaxy of two materials with large mismatch is hard to achieve, as illustrated in Fig.1(a). In order to overcome this limitation and to grow structure with large vertical strain and thickness, the synthesis of vertically aligned nanocomposites (VANs) has been proposed as a new strategy in the last decade [6]. The mismatch at the vertical heterointerface between matrix and nanopillars can introduce a vertical strain, as illustrated in Fig.1(b), that can enhance or tune a strain-driven property of the nanocomposite. Also, due to the geometry, interfacial coupling of the physical properties of two materials constituting the nanocomposite system may provide a possibility to achieve novel multifunctionality, such as artificial multiferroicity for example. VANs have thus been intensively studied in the fields of nanomagnetism [7], plasmonics [8, 9, 10], catalysis [11], ion conductivity [12], ferroelectricity [13], multiferroics [14, 15, 16, 17, 18], spintronics [19, 20, 21] and high density data storage [22, 23].

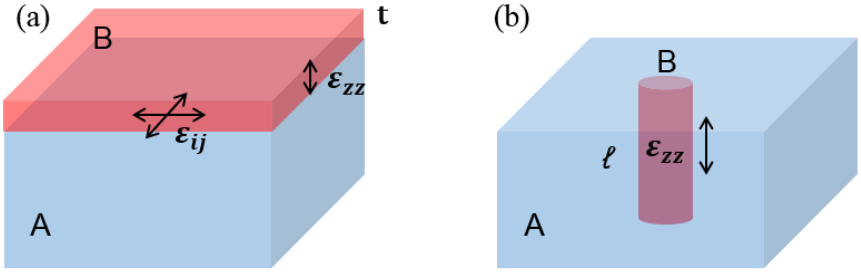

Figure 1: (a) Schematics of a planar heteroepitaxial structure. Due to the epitaxy with the substrate, the over-layer is strained in-plane ϵ_{ij} with $i, j = x$ or y and out-of-plane ϵ_{zz}. The thickness t cannot be increased indefinitely while conserving a strained state: beyond a critical thickness relaxation occurs. (b) Vertical epitaxy of material B in material A (matrix). The vertical strain ϵ_{zz} can be sustained over length much larger than the critical thickness in planar epitaxy.

Recently, 3D frameworks have been successfully established by interlayering thin films in a VAN structure. For example, 3D framed structure interlayering pure $La_{0.7}Sr_{0.3}MnO_3$ (LSMO) or CeO_2 based on the epitaxial VANs of LSMO/CeO_2 as shown in Fig.2 could be synthesized [24]. As CeO_2 is insulating and LSMO is a ferromagnetic compounds, the complex 3D structures obtained exhibit a peculiar magnetoresistive behavior that is intimately related to their architecture.

In parallel with the emerging field of 3D VAN architectures, the field of 3D nanomagnetism is burgeoning. The extension of 2D nanostructures into 3D ones allows spin configurations and capabilities to extend not only in the plane but also into the vertical direction, leading to new effects, as illustrated

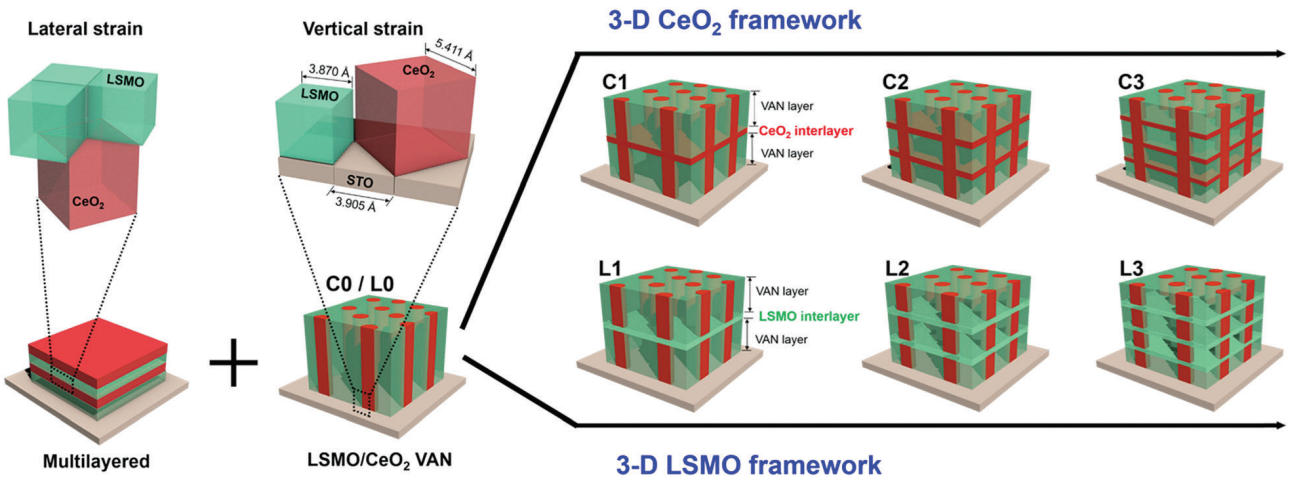

Figure 2: Schematic illustration of 2-phase heterogeneous microstructure evolution of the thin films: from VAN C0/L0 to 3D CeO_2 framed thin films C1–C3 and 3D LSMO framed thin films L1–L3. The 3D framed microstructure is achieved by alternative growth of the single phase and the VANs in multilayered fashion. This design combines the lateral strain introduced from multilayered thin film and the vertical strain from interfacial coupling in VANs, creates 3D interconnected CeO_2 or LSMO framework microstructures within the thin films, and provides a versatile tool to achieve 3D strain tuning. The unit cells and phase of LSMO are in green, and the unit cells and phase of CeO_2 are in red. Figure from [24].

in [25]. Fig.3(a) shows some examples of 3D nanomagnets extended from 2D nanomagnets (Fig.3(b)): magnetic sphere with vortex magnetization, magnetic thin film with a skyrmion, Möbius strip with perpendicular magnetization, cylindrical nanowire (NW) with modulated diameter where the magnetic configuration depends on the diameter and anitiferromagnetic superlattice with a wide soliton in the middle. Complex magnetic configurations in 3D nanostructures may lead to the emergence of new physical effects, which may have potential for applications. Among these different geometries of 3D nanomagnetic systems, cylindrical NWs with modulated diameter, with different magnetic properties depending on the diameter, may be grown using the VAN approach. Before reaching this midterm goal, a prerequisite is to be able to tune the diameter and magnetic properties of the NWs in a VAN. This is the purpose of the work presented in this thesis.

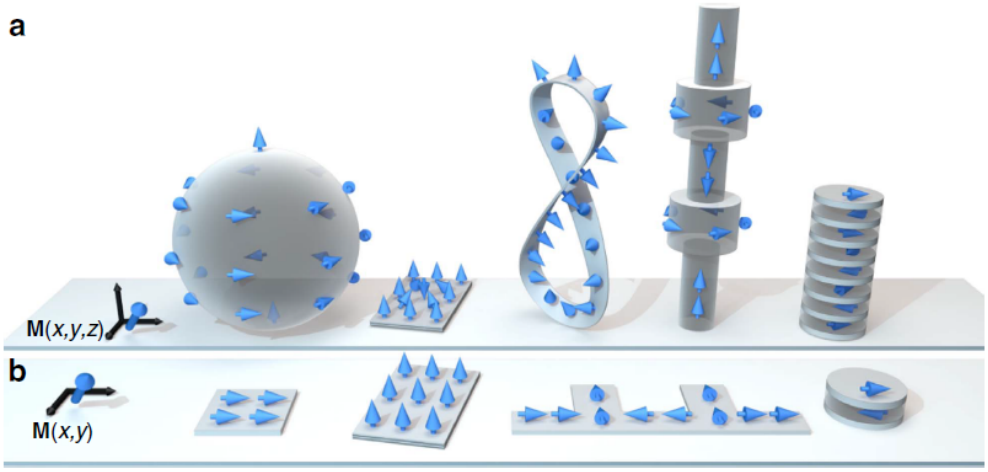

Figure 3: Schematic view of the comparison of geometries and magnetic configurations (remarked by blue arrow) for (a) 3D and (b) 2D magnetism. Adapted from [25].

Before the introduction of my work, I recall the previous works on the exploration of magnetic and structural properties of epitaxial self-assembled ferromagnetic NWs grown in an oxide matrix

carried out at INSP in the last years. The vertical strain introduced by the mismatch at the heterointerface between NWs and matrix can give rise to a magnetoelastic anisotropy contribution to the total magnetic anisotropy. This provides a possibility to tailor the anisotropy of the system by controlling the strain. The Co_xNi_{1-x}:CeO_2 system was the first metal/oxide VAN studied at INSP [26]. With $3a_{CoNi} \approx 2a_{CeO_2}$, the cube-on-cube epitaxy of NWs and matrix is achieved and it gives a vertical strain of $\sim 1\%$. Due to the negative magnetostriction constant λ_{001} of Ni, this strain allows the magnetoelastic anisotropy effect to compensate the magnetostatic anisotropy, leading Ni NWs to be almost magnetically isotropic in CeO_2 matrix. By increasing the Co concentration in Co_xNi_{1-x} alloys, the magnetoelastic anisotropy contribution, with λ_{001} becoming positive, should enhance the uniaxial anisotropy. However, such effect was not clearly evidenced. A following study of Co_xNi_{1-x} NWs in Sr(Ba)TiO_3 matrix was carried out [27]. Although the mismatch reaches more than 10%, the structural study of NWs only shows a vertical strain less than 2%. Structural disorder was evidenced in these systems and no clear effect of anisotropy reinforcement was observed. Therefore, finding an approach to enhance the vertical strain of NWs and the epitaxy quality as well is desirable. In my work, I focus on the structural and magnetic properties on epitaxial Co_xNi_{1-x} NWs in $SrTiO_3$ matrix.

In order to figure out the possibility to tune the magnetic anisotropy of the ferromagnetic Co_xNi_{1-x} NWs, studies on the growth, structure and magnetic response have been performed. The manuscript is organized in 7 chapters:

- Chap.1 introduces the elements of magnetism necessary to describe the behavior of ferromagnetic NWs.
- In Chap.2, the experimental techniques are introduced: pulsed laser deposition (PLD) for the growth of NWs in an oxide matrix; transmission electron microscopy (TEM) and x-ray diffraction (XRD) for the structural study of NWs; vibrating sample magnetometer and x-ray magnetic circular dichroism spectroscopy for the determination of magnetic properties.
- Chap.3 describes the sequential growth technique used to elaborate Co_xNi_{1-x} NWs in $SrTiO_3$ matrix and present results on the tunalibity of the diameter of NWs.
- The structural properties are explored in Chap.4 with special emphasis on the epitaxy between NWs and matrix and on the strain state of NWs.
- The magnetic responses of Ni and Co_xNi_{1-x} alloy NWs are presented in Chap.5 and Chap.6, respectively. Each term of the magnetic anisotropy contribution is discussed, together with a spectroscopic measurement of the orbital and spin magnetic moments.
- Finally, Chap.7 gives the general conclusions of this work and I sketch some perspectives for the future.

Chapter 1

Elements of magnetism

Magnetism is one of the most complex domains in Physics. It involves in particular the strong exchange interaction at atomic scale, determining local magnetic orders in materials, and the weak and long-range dipolar interaction, giving rise to magnetic domains at mesoscopic scale. In this chapter, I will briefly review elements of magnetism necessary to our study of ferromagnetic nanowires.

1.1 Magnetic energy

The total magnetic energy, E_{tot} can be described as:

$$E_{tot} = E_{ex} + E_a + E_{ms} + E_{ext} \tag{1.1}$$

Thus, the magnetization state of a magnet depends on a balance of different terms of energy: the exchange one E_{ex}, the anisotropy one E_a, the magnetostatic self-interaction one E_{ms} and the interaction with the external magnetic field E_{ext}, called Zeeman energy. The Zeeman energy term expresses the fact that the magnetization M tends to align with the external field H: $E_{ext} = -\mu_0 \vec{M} \cdot \vec{H}$.

The different energy contributions establish a complicated nonlinear and non-local problem, leading to a history dependence known as hysteresis. For simple cases, magnetization hysteresis loops of a magnet could be calculated by solving meta-stable states and in taking into account the history of the magnet. Fig.1.1 displays a typical magnetic hysteresis cycle, called the major cycle, obtained by measuring the magnetization as a function of the magnetic field. Some significant characteristics are derived from the curve: the saturation magnetization M_s reached with the applied field above the saturation field H_s; the remanence M_R, the remaining magnetization when the field is removed from the saturation one; the coercive field H_c, the absolute value of the reversal field leading to the global null magnetization. Detailed magnetic behavior should be understood by examining effects of each contribution in the magnetic energy. Next, I will describe the exchange energy and the magnetic anisotropy.

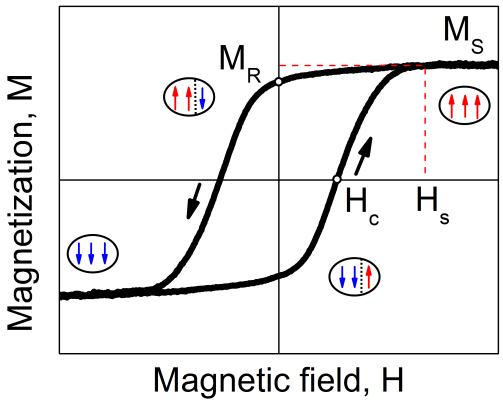

Figure 1.1: Schematic representation of the major hysteresis cycle: the saturation magnetization M_s, the saturation field H_s, the remanence M_R and the coercive field H_c.

1.2 Exchange energy

The exchange energy E_{ex} arises from a quantum effect involving indistinguishable electrons of two neighboring atoms. It is described by the Heisenberg hamiltonian for two contiguous moments $\vec{\mathfrak{m}}_i$ and $\vec{\mathfrak{m}}_j$:

$$E_{ex} = -2J\vec{\mathfrak{m}}_i \cdot \vec{\mathfrak{m}}_j \tag{1.2}$$

where J is the exchange constant and its sign depends on the material ($J > 0$ for ferromagnet and $J < 0$ for antiferromagnet). The angle between the two moments i and j is written as θ_{ij}. For small θ_{ij}, $\cos\theta_{ij} \approx 1 - \theta_{ij}^2/2$ and the expression 1.2 becomes:

$$E_{ex} \approx \text{constant} + J\mathfrak{m}^2\theta_{ij}^2 \equiv J\mathfrak{m}^2\theta_{ij}^2 \tag{1.3}$$

In a continuous description, the angular deviation density of the moments is proportional to $(\nabla\mathbf{m})^2$, with $\mathbf{m}$ the reduced magnetization. The exchange energy density is thus written as:

$$\frac{E_{ex}}{V} = \frac{J\mathfrak{m}^2 n}{a}(\nabla\mathbf{m})^2 = A(\nabla\mathbf{m})^2 \tag{1.4}$$

The exchange stiffness constant A is given by $A = J\mathfrak{m}^2 n/a$ in unit of J m^{-1}. It is related to the exchange constant J, the cubic lattice parameter a and the number of atoms in the unit cell n: n equals to 1 for the simple cubic lattice, 2 for the bcc lattice and 4 for the fcc lattice. One notices that E_{ex} depends on $(\nabla\mathbf{m})^2$ and is minimal in the case of a uniform magnetization.

Magnetic order

The magnetic local order is determined by the exchange interaction in materials. Three types of orders are generally observed: ferromagnetism, antiferromagnetism and ferrimagnetism.

(A) Ferromagnetism:
In ferromagnetic materials, the exchange constant J is positive and the magnetic moments are aligned to each other as depicted in Fig.1.2(a). This leads to the fact that the materials can be spontaneously magnetized even in the absence of the external field.

(B) Antiferromagnetism:
Contrary to the ferromagnetic case, if the exchange constant J is negative, the magnetic moments align antiparallel to each other as shown in Fig.1.2(b). This type of order is called antiferromagnetism, which occurs commonly in transition metal compounds, in particularly oxides. Due to the compensation of up and down magnetic moments, the antiferromagnets do not have a spontaneous macroscopic magnetization.

(C) Ferrimagnetism:
In ferrimagnetic materials, the exchange constant is also negative, resulting in antiparallel alignment of neighboring moments. However, these moments do not have the same magnitude. They do not compensate and a spontaneous magnetization exists as illustrated in Fig.1.2(c).

Moreover, the thermal agitation has a great influence on the magnetic order. It acts against the exchange interaction and tends to destroy the magnetic order by randomly flipping the moments. A critical point is given by the compensation of the thermal agitation and the exchange interaction, called Curie temperature or Curie point T_C for ferromagnets and ferrimagnets and Néel temperature T_N for antiferromagnets. Below T_C or T_N, the magnetic configurations, depending on J, are stable. Above T_C or T_N, the material behavior turns to paramagnetism as illustrated in Fig.1.2(d). The moment has no coupling with its neighbors.

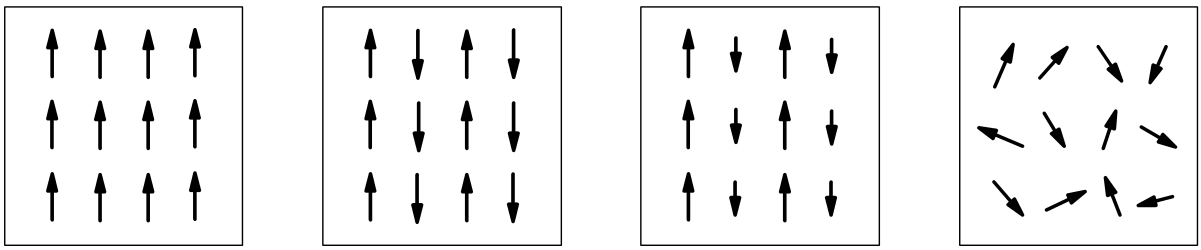

(a) (b) (c) (d)

Figure 1.2: Representations of magnetic order: (a) ferromagnetism, (b) antiferromagnetism and (c) ferrimagnetism, together with non interaction case: (d) paramagnetism. Each arrow corresponds to a magnetic moment and its length is related to the intensity of each moment.

1.3 Magnetic anisotropy

The magnetic anisotropy is an important property of magnetic materials. It determines the easy directions of magnetization along which the alignment of the magnetic moments is favored. Sources of anisotropy are the shape and the crystalline structure of the materials. In some cases, a magneto-elastic anisotropy occurs when the material is strained. In the following, I will describe each magnetic anisotropy contributions.

1.3.1 Self-demagnetization field energy: shape anisotropy

The magnetostatic energy or the self-demagnetization field energy is related to the magnetic field generated by the magnet itself. This field is called the demagnetization field H_d. Using the Maxwell's equation $div\mathbf{B} = div\mu_0(\mathbf{H} + \mathbf{M}) = 0$, the demagnetization field is given by:

$$div\mathbf{H}_d = -div\mathbf{M} \tag{1.5}$$

where μ_0 is the magnetic permeability of vacuum. The magnetostatic energy E_{ms} given by $\mathbf{H}_d$ is thus:

$$E_{ms} = \frac{1}{2}\mu_0 \int_V \mathbf{H}_d \cdot \mathbf{M}\, dV \tag{1.6}$$

where the integral is over the magnet volume, V. According to the expression 1.5, the demagnetization field $\mathbf{H}_d$ is opposite to the magnetization density $\mathbf{M}$.

In the case of a magnet with uniform magnetization and an ellipsoid shape, the demagnetization $\mathbf{H}_d$ can be expressed by:

$$\mathbf{H}_d = -N_d\mathbf{M} \tag{1.7}$$

here N_d is the demagnetization factor which is diagonal in the principal axes of the ellipsoid, x, y and z. The expression of the magnetostatic energy E_{ms} is thus transformed from the Eq.1.6 as:

$$E_{ms} = \frac{\mu_0 M_s^2 V}{2}(N_a m_x^2 + N_b m_y^2 + N_c m_z^2) \tag{1.8}$$

Here, M_s is the saturation magnetization density and $\mathbf{m} = \mathbf{M}/M_s$ the direction vector of the magnetization. E_{ms} is also named the shape anisotropy. From the expression 1.8, the demagnetization factor is separated into three factors N_a, N_b and N_c, which should satisfy $N_a + N_b + N_c = 1$.

A wire can be modelled as an ellipsoid with a=b and a large aspect ratio $\alpha = c/a \gg 1$, as illustrated in Fig.1.3. We have thus $N_a = N_b$. We can define the parallel demagnetization factor $N_{\parallel} = N_c$, the perpendicular one $N_{\perp} = N_a = N_b$, and the expression of E_{ms} becomes:

$$E_{ms} = \frac{\mu_0 M_s^2 V}{2}(N_\perp \sin^2\theta + N_\parallel \cos^2\theta) \tag{1.9}$$

with $N_\parallel = 1 - 2N_\perp$ and θ the angle between the magnetization and the long axis. This expression is equivalent to:

$$E_{ms} = \frac{1}{2}\mu_0 N_\parallel M_s^2 V + \frac{1}{4}\mu_0 M_s^2 V(1 - 3N_\parallel)\sin^2\theta \tag{1.10}$$

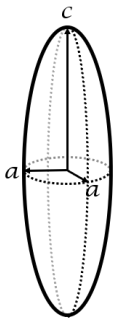

Figure 1.3: Illustration of a prolate ellipsoid: $c \gg a$.

The first term of the Eq.1.10 is independent of the magnetization direction, thus it can be removed. The shape anisotropy contribution is finally expressed as:

$$E_{ms} = \frac{1}{4}\mu_0 M_s^2 V(1 - 3N_\parallel)\sin^2\theta \tag{1.11}$$

where the demagnetization factors are simplified to one factor $N_\parallel$. For an elongated ellipsoid, $\alpha = c/a > 1$, $N_\parallel$ factor parallel to the long axis is given by [28]:

$$N_\parallel = \frac{1}{\alpha^2 - 1}\left[\frac{\alpha}{2(\alpha^2-1)^{1/2}}\ln\left(\frac{\alpha + (\alpha^2-1)^{1/2}}{\alpha - (\alpha^2-1)^{1/2}}\right) - 1\right] \tag{1.12}$$

In our case, the aspect ratio $\alpha \gg 10$ for a thin nanowire, $N_\parallel$ drops to zero. K_{ms}, the magnetostatic anisotropy or the shape anisotropy constant, is expressed as:

$$\frac{E_{ms}}{V} = \frac{1}{4}\mu_0 M_s^2 \sin^2\theta = K_{ms}\sin^2\theta \tag{1.13}$$

As a consequence, the shape anisotropy is proportional to M_s^2. The shape anisotropy is an uniaxial anisotropy. The minimum of E_{ms} appears at $\theta = 0$. Thus, in absence of other sources of magnetic anisotropy, a nanowire presents an easy axis of magnetization along the wire axis.

1.3.2 Magnetocrystalline anisotropy

The magnetocrystalline anisotropy describes the fact that the magnetization prefers to orientate along certain crystallographic directions, named easy axes. As shown in Fig.1.4, for a bulk single-crystal ferromagnetic material, the easy and hard axes of magnetization are oriented along particular crystallographic directions.

The magnetocrystalline anisotropy originates from the interplay of spin-orbit coupling and crystal field effects. The spin-orbit coupling tends to align the spin moment with the orbital moment for $3d$ transition metals. This is more difficult to achieve along crystallographic directions for which the electrostatic cost related to the crystal field is larger. Depending on the crystal structure, the magnetocrystalline anisotropy can be uniaxial or cubic.

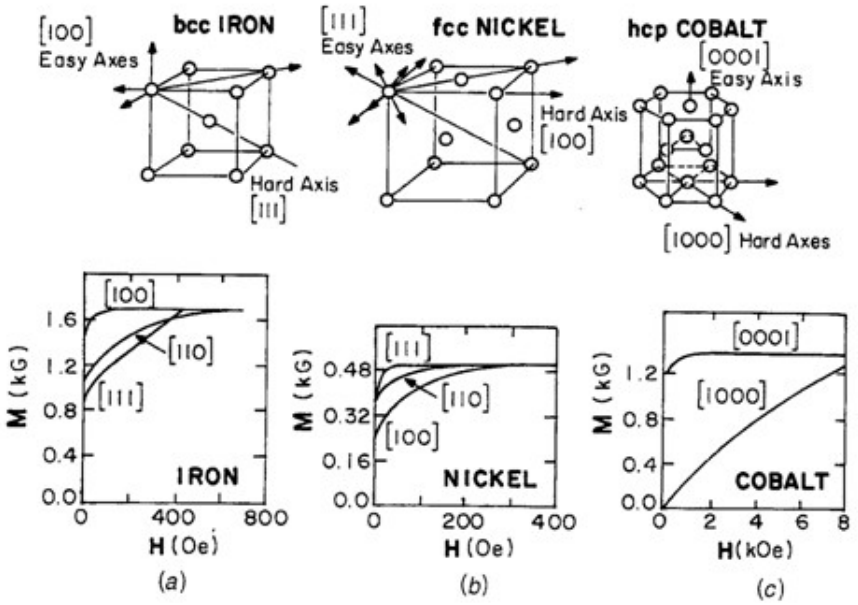

Figure 1.4: Crystalline structure and magnetization of some single-crystal ferromagnetic materials for applied magnetic fields in different directions. (a) body-centered cubic Fe; (b) face-centered cubic Ni; (c) hexagonal close-packed Co. The easy and hard axes are indicated. The intermediary direction is between the easy and hard directions, for example, [110] direction for bcc Fe and fcc Ni (Magnetic responses measured by Honda and Kaya, 1926 [29]; Kaya, 1928 [30, 31]).

Uniaxial anisotropy

The simplest anisotropy is uniaxial anisotropy which only depends on the angle θ between the reduced magnetization $\mathbf{m}$ and a given axis z (Fig.1.5(a)). It is expressed by a series expansion of even powers of $\sin\theta$:

$$\frac{E_{uniaxial}}{V} = K_0 + K_1 \sin^2\theta + K_2 \sin^4\theta \tag{1.14}$$

where V is the volume of the magnet, K_0, K_1 and K_2 are the uniaxial anisotropy constants. K_0, the constant term, is not concerned with the anisotropy. This kind of anisotropy typically applies to tetragonal and hexagonal systems, for example, hcp Co, where the z axis is the [0001] axis perpendicular to the hexagonal close-packed planes as shown in Fig.1.4(c). The first and second order uniaxial anisotropy constants K_1 and K_2 of hcp Co are of the order of 10^5 J/m^3 and 10^4 J/m^3 [32], respectively, as shown in Fig.1.7(a). With K_2 neglected before K_1, the expression of the uniaxial anisotropy can thus be simplified as:

$$\frac{E_{uniaxial}}{V} = K_1 \sin^2\theta \tag{1.15}$$

With this simplified expression, Fig.1.5(b)(c) presents the energy density plots of uniaxial anisotropy for K_1 positive and negative, where the easy direction for the magnetization is indicated. For $K_1 > 0$, the minimum of energy is at $\theta = 0$ and $\theta = \pi$. The easy axis is therefore parallel to the z direction. On the contrary, for $K_1 < 0$, the minimum of energy is at $\theta = \pi/2$. The basal plane thus becomes an easy plane where the magnetization is free and the z direction becomes a hard magnetization direction.

Cubic anisotropy

For a cubic crystal, for example, bcc Fe and fcc Ni, the magnetocrystalline anisotropy is expressed as:

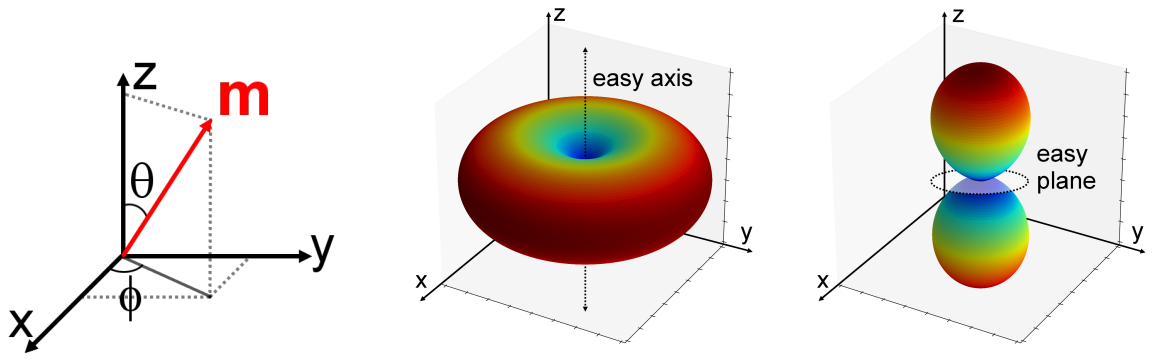

(a) (b) (c)

Figure 1.5: (a) Definition of **m** and the spherical angles θ and ϕ. (b) and (c) Energy density plots of uniaxial anisotropy for $K_1 > 0$ and $K_1 < 0$, respectively. The energy minimum is in blue and the maximum in red.

$$\frac{E_{cubic}}{V} = K_0^c + K_1^c(\alpha_1^2\alpha_2^2 + \alpha_2^2\alpha_3^2 + \alpha_3^2\alpha_1^2) + K_2^c(\alpha_1\alpha_2\alpha_3)^2 + \dots \tag{1.16}$$

here α_i denotes the direction cosines with respect to the crystallographic directions. As shown in Fig.1.6(a), $\alpha_1 = \sin\theta\cos\phi$, $\alpha_2 = \sin\theta\sin\phi$ and $\alpha_3 = \cos\theta$. The expression can thus be described in spherical coordinates by:

$$\frac{E_{cubic}}{V} = K_1^c(\frac{1}{4}\sin^2\theta\sin^2 2\phi + \cos^2\theta)\sin^2\theta + \frac{K_2^c}{16}\sin^2 2\phi\sin^2 2\theta\sin^2\theta \tag{1.17}$$

K_0^c can be removed due to its independence with the magnetization direction **m**. The energy surfaces of cubic anisotropy for the first order constant K_1^c positive and negative are shown in Fig.1.6(a) and (b). For $K_1^c > 0$, the energy minimum is at $\theta = 0$ ($\phi = 0$) and at $\theta = \pi/2$ while $\phi = 0,\ \pi/2$. The easy magnetization directions are along $< 100 >$ axes. This is the case for bcc Fe. For $K_1^c < 0$, the energy minimum and the preferential magnetization directions are the cube diagonals, corresponding to $< 111 >$ axes. It is adapted to the case of fcc Ni.

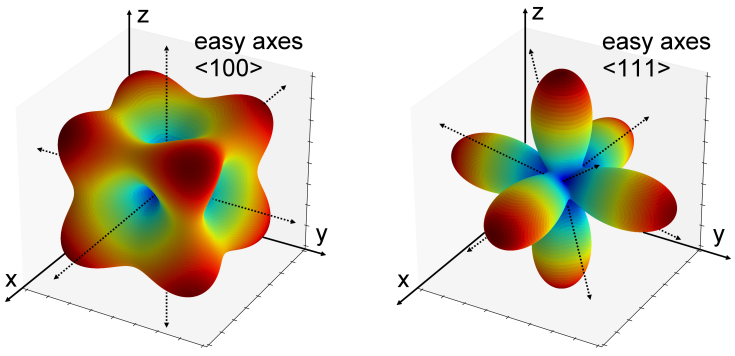

(a) (b)

Figure 1.6: Energy density plot of cubic anisotropy for (a) $K_1^c > 0$ and (b) $K_1^c < 0$. The energy minimum is in blue and the maximum in red.

In general, the second cubic anisotropy constant K_2^c is much smaller than the first order constant K_1^c at low temperature as illustrated in Fig.1.7(b). However, at room temperature for fcc Ni, K_2^c is almost equal to K_1^c and both constants are weak. The second term in Eq.1.17 is usually neglected in order to simplify the calculation at low temperature.

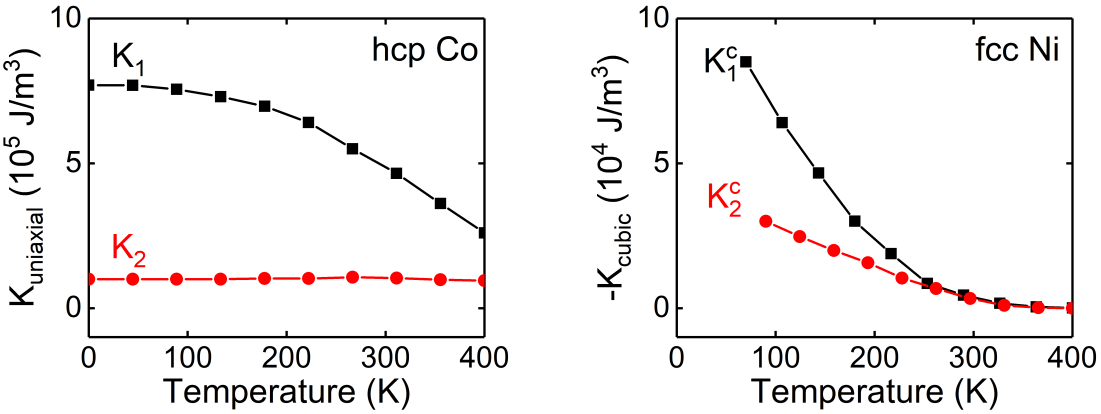

Figure 1.7: Temperature dependence of magnetocrystalline anisotropy constants of (a) hcp Co and (b) fcc Ni. Adapted from [32, 33].

1.3.3 Magnetoelastic anisotropy

Another contribution caused by the spin-orbit coupling and related to the magnetocrystalline anisotropy is the magnetoelastic anisotropy. The magnetoelastic energy arises from the interaction between the magnetization and the mechanical strain of a crystal. With the crystal strain tensor ϵ_{ij} (where i, j=x, y, z), the elastic energy in a cubic crystal is given by (Love, 1906, p.157):

$$e_{el} = \frac{E_{el}}{V} = \frac{1}{2}c_{11}(\epsilon_{xx}^2 + \epsilon_{yy}^2 + \epsilon_{zz}^2) + c_{12}(\epsilon_{yy}\epsilon_{zz} + \epsilon_{zz}\epsilon_{xx} + \epsilon_{xx}\epsilon_{yy}) + \frac{1}{2}c_{44}(\epsilon_{xy}^2 + \epsilon_{yz}^2 + \epsilon_{zx}^2) \tag{1.18}$$

where c_{ij} are elastic stiffness constants.

Moreover, the magnetoelastic energy is defined to be zero for unstrained crystal, and the anisotropy energy is only left with the magnetocrystalline anisotropy [34]. The anisotropy energy is therefore given by Eq.1.16 in neglecting the second order:

$$(e_K)_0 = \frac{E_{cubic}}{V} = K_1^c(\alpha_1^2\alpha_2^2 + \alpha_2^2\alpha_3^2 + \alpha_3^2\alpha_1^2) \tag{1.19}$$

On the contrary, for the strained crystal, the anisotropy energy expression can be expanded in Taylor's series in the strain ϵ_{ij}:

$$e_K = (e_K)_0 + B_1(\alpha_1^2\epsilon_{xx} + \alpha_2^2\epsilon_{yy} + \alpha_3^2\epsilon_{zz}) + 2B_2(\alpha_1\alpha_2\epsilon_{xy} + \alpha_2\alpha_3\epsilon_{yz} + \alpha_3\alpha_1\epsilon_{zx}) \tag{1.20}$$

Here B_1 and B_2 are the magnetoelastic coupling constants. These constants can be related to λ_{001} and λ_{111}, the saturation values of the longitudinal magnetostriction in the [001] and [111] directions, through the expressions by [34]:

$$\begin{aligned} \lambda_{001} &= -\frac{2}{3}\frac{B_1}{c_{11} - c_{12}} \\ \lambda_{111} &= -\frac{1}{3}\frac{B_2}{c_{44}} \end{aligned} \tag{1.21}$$

With the magnetostriction constants, by giving a strain along a specific crystallographic direction, the magnetoelastic anisotropy energy in Eq.1.20 can be simplified. In the case where NWs are expanded along the [001] direction of the cubic crystal and slightly homogeneously compressed in the (001) plane (ϵ_{xx}=ϵ_{yy}=ϵ_{rr}, ϵ_{rr} in-plane strain), with shear strains considered to be zero, the magnetoelastic energy is expressed as:

$$\frac{E_{me}}{V} = \frac{3}{2}\lambda_{001}(c_{11} - c_{12})(\epsilon_{zz} - \epsilon_{rr})\sin^2\theta = K_{me}\sin^2\theta \tag{1.22}$$

In this case, the magnetoelastic anisotropy is an uniaxial anisotropy. The fact that it turns to an easy axis or an easy plane is depending on the signs of the magnetostriction λ and of the strain. For the same sign of λ and $(\epsilon_{zz} - \epsilon_{rr})$, the system prefers an easy magnetization axis. On the contrary, for the opposite sign of λ and $(\epsilon_{zz} - \epsilon_{rr})$, it turns to an easy plane.

1.4 Micromagnetic scales

In summary of all magnetization contributions: the exchange, the anisotropies, the magnetostatic term and the external field effect, the total energy over a volume V can be written as:

$$\begin{aligned} E_{tot} &= E_{ex} + E_a + E_{ms} + E_{ext} \\ &= \int_V \left[A\left(\nabla\left(\frac{\mathbf{M}}{M_s}\right)\right)^2 + e_a(\mathbf{m}) - \frac{\mu_0}{2}\mathbf{M}\mathbf{H}_d - \mu_0\mathbf{M}\mathbf{H}_{ext}\right] dV \end{aligned} \tag{1.23}$$

$\mathbf{m} = \mathbf{M}/M_s$ is the direction vector of the magnetization. In the uniaxial case, e_a is represented by the anisotropy constant K and its axis $\mathbf{n}$. In replacing $\mathbf{M}$ by $M_s\mathbf{m}$, Eq.1.23 is then:

$$E_{tot} = \int_V \left[A(\nabla\mathbf{m})^2 + K(\mathbf{m}\cdot\mathbf{n})^2 - \frac{\mu_0}{2}M_s\mathbf{m}\mathbf{H}_d - \mu_0 M_s\mathbf{m}\mathbf{H}_{ext}\right] dV \tag{1.24}$$

Some micromagnetic scales can be deduced by Eq.1.24 by dividing and multiplying all the terms by $2/(\mu_0 M_s^2)$:

$$E_{tot} = \frac{\mu_0 M_s^2}{2}\int_V \left[\frac{2A}{\mu_0 M_s^2}(\nabla\mathbf{m})^2 + \frac{2K}{\mu_0 M_s^2}(\mathbf{m}\cdot\mathbf{n})^2 - \frac{1}{M_s}\mathbf{m}\mathbf{H}_d - \frac{2}{M_s}\mathbf{m}\mathbf{H}_{ext}\right] dV \tag{1.25}$$

The coefficient of the exchange contribution equals to ℓ_{ex}^2. The exchange length ℓ_{ex} is a length characteristic of the magnetic material, below which the exchange contribution dominates over the magnetization effects. ℓ_{ex} is given by:

$$\ell_{ex} = \sqrt{\frac{2A}{\mu_0 M_s^2}} \tag{1.26}$$

The coefficient of the second term, the anisotropy contribution, is defined as the quality parameter, Q. This indicates the importance of the anisotropy (K) compared to the magnetostatic contribution ($\mu_0 M_s^2/2$, Eq.1.8). It allows to classify the magnets as hard or soft materials: for the hard materials, the anisotropy dominates and $Q > 1$; on the other hand, for the soft ones, the magnetostatic terms dominate over the anisotropy, where $Q \ll 1$.

$$Q = \frac{2K}{\mu_0 M_s^2} \tag{1.27}$$

ℓ_{ex} and Q are related to another length, the domain wall-width, δ_0. It arises from the comparison of the exchange and the anisotropy contributions, and determine the separation distance of two magnetic domains with different magnetization directions. It is given by:

$$\delta_0 = \pi\frac{\ell_{ex}}{\sqrt{Q}} = \pi\sqrt{\frac{A}{K}} \tag{1.28}$$

According to this expression, the exchange effect tends to extend the domain wall-width and the anisotropy prefer narrow transition regions.

Another characteristic length related to ℓ_{ex} and Q is the critical single-domain diameter, D_{cr}. This is a length above which the multidomain configuration is energetically more favorable for a particle. It is given by:

$$D_{cr} = \frac{72\sqrt{AK}}{\mu_0 M_s^2} \tag{1.29}$$

The micromagnetic scales are shown in Tab.1.1 [35]. It indicates that hcp Co has a strong anisotropy and on the contrary, fcc Ni has a weak one.

Table 1.1: Micromagnetic scales for hcp Co and fcc Ni.

Material	ℓ_{ex} (nm)	Q	δ_0 (nm)	D_{cr} (nm)
hcp Co	4.7	0.324	25.9	96.4
fcc Ni	7.6	0.038	123	53.6

1.5 Reversal magnetization mechanism

1.5.1 Uniform reversal mode: the Stoner-Wohlfarth model

The first model for the magnetization reversal was proposed and developed by Stoner and Wohlfarth in 1948 and is still used today. This magnetization reversal mechanism applies on homogeneous single-domain particles with a constant magnetization assumed. In the beginning of this chapter, the total energy of such system is mentioned as a balance of different energy contributions as described by Eq.1.1. The first contribution corresponding to the exchange energy becomes zeros under a homogeneous magnetization. The magnetic energy of the particle thus equals to the anisotropy and the magnetostatic energies. In a magnetic field H, the total magnetic energy for the Stoner-Wolhfarth (SW) particle is thus given by:

$$E_m = \iiint (e_a(\mathbf{m}) - \frac{\mu_0}{2}\mathbf{MH}_d - \mu_0\mathbf{MH})dV \tag{1.30}$$

Without exchange, the reversal of the ensemble of individual magnetic moments is considered as that of a single moment, the SW model is therefore regarded as the simplest model. The shape of SW particle is chosen as an elongated ellipsoid as shown in Fig.1.8. The easy axis of magnetization (e.a.) parallel to the z direction corresponding to the longest axis. For a particle with a high aspect ratio, the magnetostatic contribution is expressed by Eq.1.13. The anisotropy energy is related to the magnetocrystalline energy. The total energy density can be developed as:

$$e_m = \frac{E_m}{V} = e_a(\theta) + \frac{\mu_0}{4}M_s^2 \sin^2\theta - \mu_0 M_s H \times (\cos\theta\cos\psi + \sin\theta\sin\psi\cos\varphi) \tag{1.31}$$

In absence of the external field H, the magnetization is along the anisotropy axis; with $H \neq 0$, the magnetization direction results from the balance between the external field effect and the anisotropy contribution. Here, we simplify the problem to a planar configuration (φ=0) and the energy density becomes:

$$e_m = \frac{E_m}{V} = e_a(\theta) + \frac{\mu_0}{4}M_s^2 \sin^2\theta - \mu_0 M_s H \cos(\theta - \psi) \tag{1.32}$$

In the simplest case, the magnetic field H is applied along the easy axis, thus $\psi = 0$. In order to obtain the magnetization direction, the minimization of energy $\partial e_m(\theta)/\partial\theta$ should be done. Here, the anisotropy contribution is simplified to an uniaxial anisotropy, $e_a(\theta) = K\sin^2\theta$. In this case, the anisotropy and magnetostatic contributions can be combined into an effective anisotropy constant: $K_{eff} = K + K_{ms}$. Therefore, $\partial e_m(\theta)/\partial\theta = 0$ gives:

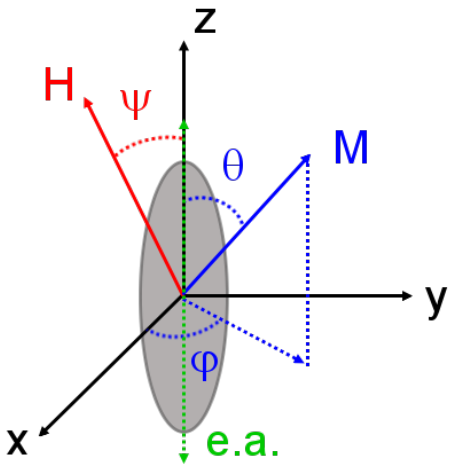

Figure 1.8: Single-domain ellipsoidal particle in a magnetic field H, showing the revelant angles ψ between this field and the anisotropy axis z, θ between the magnetization M and the anisotropy axis. φ is the angle between the projection of M in xy plane and the x axis.

$$2K_{eff}\sin\theta\cos\theta + \mu_0 M_s H\sin\theta = 0 \tag{1.33}$$

The condition of the magnetization reversal, $\cos\theta = \pm 1$, gives the coercive field H_c:

$$H_c = \frac{2K_{eff}}{\mu_0 M_s} \tag{1.34}$$

In addition, by resolving the expression 1.32, the angular dependence of the hysteresis cycles can be obtained as shown in Fig.1.9(a). The shape of hysteresis cycles depends on the direction of the applied magnetic field, ψ. For H applied along the anisotropy axis, $\psi = 0$, the cycle is square with a magnetization reversal at $H = H_a = H_c = 2K_{eff}/\mu_0 M_s$. This corresponds to the easy magnetization direction. With the increase of ψ from 0 to 90°, the cycle narrows accompanying the systematical lost of the squareness, and the coercivity is reduced. For $\psi = 90°$, where H is applied perpendicular to the easy axis, the cycle is completely closed and the slope indicates that it is a hard magnetization direction.

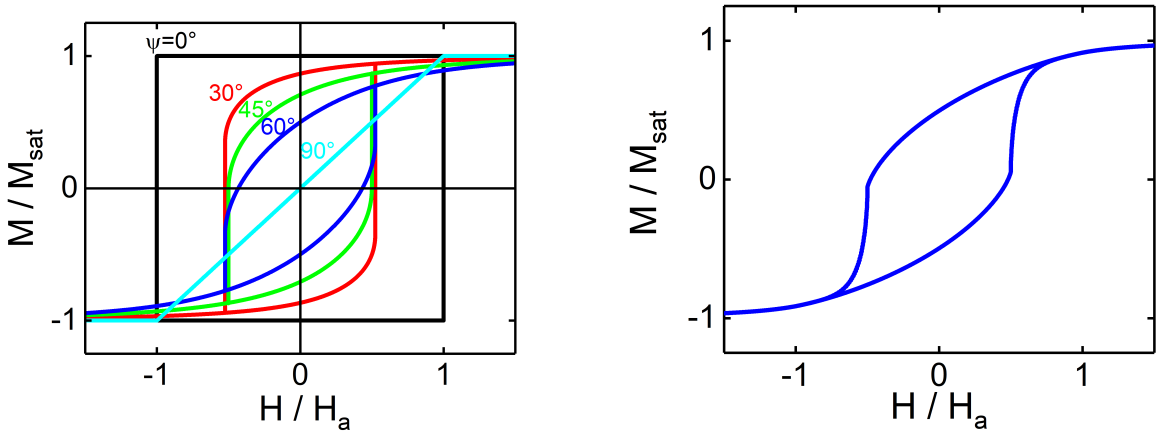

Figure 1.9: (a) Angular dependence of hysteresis cycles for SW model. (b) SW hysteresis cycle for an assembly of particles with every possible orientation of the anisotropy axis.

For a given magnetic field H, the magnetic hysteresis cycle for an assembly of SW particles with

every possible orientation of the anisotropy axis is shown in Fig.1.9(b), where θ is from 0 to 90° and φ from 0 to 180°. The remanence is reduced to 1/2 and the coercivity is reduced to $0.48H_a$. The SW model presented here with a homogeneous magnetization reversal is generally too idealized with respect to real systems. However, Jamet *et al.* measured single 3 nm Co and Fe nanoclusters and demonstrated the relevance and the perfect adequacy of the SW model for small particles [36, 37].

1.5.2 Inhomogeneous magnetization reversal

In real magnets, the magnetization reversal is an inhomogeneous or incoherent process. The local magnetic moments do not remain parallel to each other during the magnetization reversal. An example of such reversal mode is the curling process [38]. As illustrated in Fig.1.10(b), in the curling mode, the magnetization is tangential to cylindrical surfaces which have a common longitudinal axis. The demagnetization effect is reduced but the exchange energy increased. Another reversal mode between the coherent and the curling modes is also illustrated in Fig.1.10(c), the buckling mode. Differently in this mode, the deviation of the local magnetization is a periodic function of the position along a longitudinal axis.

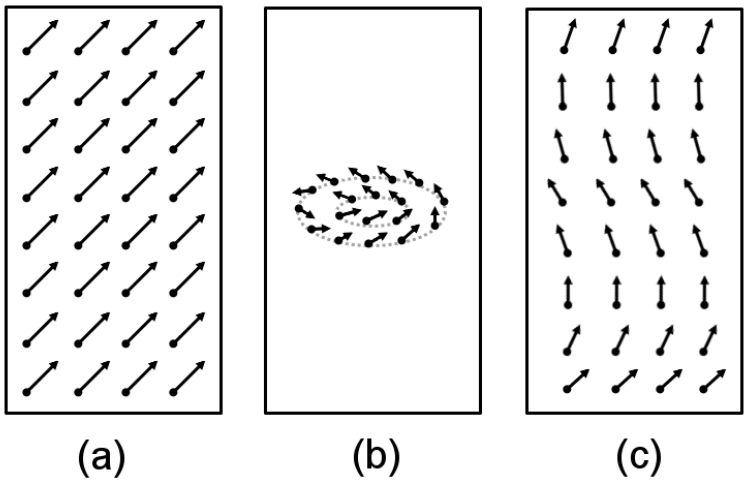

Figure 1.10: Magnetization reversal modes for the infinite cylinder: (a) uniform (coherent), (b) curling, (c) buckling.

Besides, it was demonstrated by Hertel *et al.* by micromagnetic simulations of Ni NWs that the magnetization reversal mode depends on the wire diameter. For thin wires, a domain wall nucleates and propagates along the wire axis; while for thick wires, the reversal prefers the curling mode [39].

1.6 Temperature effects

1.6.1 Blocking temperature

Here we consider magnetic particles with anisotropy K and volume V. The stability of the magnetic moment alignment in a direction depends on the competition of anisotropy energy KV and thermal activation k_BT, where k_B is the Boltzmann constant. The thermal activation can overcome the anisotropy energy barrier for the reversal of the magnetic moment even when $k_BT < KV$. The typical time between two reversals is given by the Néel-Brown law [40]:

$$\tau = \tau_0 \exp \frac{KV}{k_BT} \tag{1.35}$$

where the typical time τ is called Néel relaxation time for the moment reversal as a result of thermal fluctuation; and τ_0 is a characteristic timescale of the material, called attempt time or attempt period. Its typical value is in the range of $10^{-12} - 10^{-9}$ second. KV corresponds to the energy barrier E_b associated to the anisotropy energy. The magnetic state observed depends on the measurement time,

t_m. When the relaxation time τ is larger than t_m, the particles are in the static state, called the blocked regime. The magnetization is non zero at the observation. On the contrary, when τ is shorter than t_m, a zero magnetization is observed. The particles turn to the so-called superparamagnetic regime.

The measurement time, t_m, is in scale of 100 seconds for laboratory experiments. At a given T, using Eq.1.35, it is possible to determine the critical volume of the particles for which τ is comparable to t_m. With $t_m = 100$ s and $\tau_0 = 10^{-9}$ s, the critical volume at the edge of the superparamagnetic regime can be deduced:

$$V_{cr}^{spm} = \frac{\ln(\tau/\tau_0)k_BT}{K} \approx \frac{25k_BT}{K} \tag{1.36}$$

The critical volume for a given temperature is the maximum volume below which, the particles are observed in the superparamagnetic regime.

Likewise, for given values of K and V, a critical temperature, named the blocking temperature, T_b, can be defined:

$$T_b \approx \frac{KV}{25k_B} \tag{1.37}$$

Below T_b, ferromagnetic behavior is observed. At $T > T_b$, the particles are in the superparamagnetic regime, where the magnetization can randomly flip. Without an external magnetic field, the magnetization is zero and with an external field, the magnetic moments tend to align to the the external field.

1.6.2 Superparamagnetic regime

Here we are interested in the temperature dependence of the magnetization of an assembly of particles in the superparamagnetic regime. Under an external field, it is described by the Langevin function:

$$M(H) = NmL(x) \tag{1.38}$$

where x is the ratio of the Zeeman energy to the thermal energy, $x = \dfrac{\mu_0 Hm}{k_BT}$, N is the number of nanoparticles, m is the magnetic moment of a nanoparticle, and $L(x)$ is the Langevin function, expressed as:

$$L(x) = \coth x - \frac{1}{x} \tag{1.39}$$

The Langevin function $L(x)$ is the classical analogue of the Brillouin function, which describes the paramagnetic behavior. This indicates the similarity between the paramagnetism and superparamagnetism. In increasing the temperature beyond the Curie temperature T_C, the exchange between the atomic moments is broken and the paramagnetism regime is reached. According to the Langevin function, the magnetization curve depends only on the ratio of H/T in the superparamagnetic regime.

Il should be pointed out that the Langevin superparamagnetic regime described deals only with the Zeeman energy with respect to the thermal energy. Tournus *et al.* demonstrated that the anisotropy in particles has a great influence on the superparamagnetic regime and a detailed balance should be made between the Zeeman energy and the anisotropy one with respect to the thermal one [41, 42, 43].

1.6.3 Temperature dependence of the coercivity

For a single-domain ellipsoidal particle in a magnetic field H along the easy axis, the total magnetic energy E_m can be simplified by Eq.1.31. With $\psi = 0$, K is the constant of the uniaxial anisotropy including the magnetocrystalline and magnetostatic contributions, E_m becomes:

$$E_m = KV \sin^2\theta - \mu_0 M_s HV \cos\theta \tag{1.40}$$

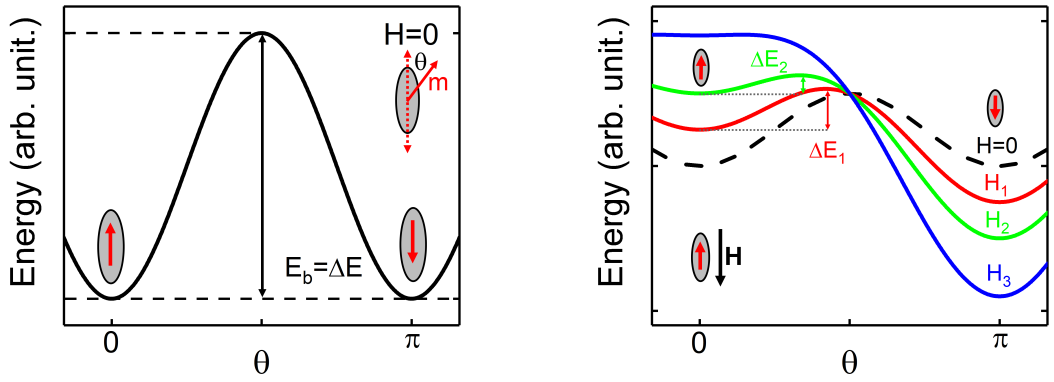

(a) (b)

Figure 1.11: Illustration of the total energy in a function of θ, where θ is the angle between the easy axis of an ellipsoidal particle and the magnetization. (a) In the case of $H = 0$, bistable states at $\theta = 0$ and π. (b) For H applied along the easy axis with different values, E_m can be normalized as $\sin^2\theta + h\cos\theta$ with $h = 2H/H_a$. $h = 0.5$, 1, 2 for $H = H_1, H_2, H_3$. With the increasing of h, the energy barrier E_b related to the energy difference ΔE decreases.

As shown in Fig.1.11, E_m is a sinusoidal funtion of θ for $H = 0$ according to the energy expression. The energy barrier E_b corresponding to the energy difference equals to KV and the energy minima occur at $\theta = 0$ and π. In the case of $H \neq 0$, E_b can be deduced by solving $\partial E_m(\theta)/\partial\theta = 0$. The minima are obtained at $\theta = 0$ and π and the maximum at $\theta = \arccos(H/H_a)$, where the anisotropy field is given by: $H_a = 2K/\mu_0 M_s$. Therefore, E_b can be described as:

$$E_b = KV\left(1 - \frac{H}{H_a}\right)^2 \tag{1.41}$$

For a given temperature, thermal energy $k_B T$ can overcome the energy barrier E_b when $E_b \simeq 25k_B T$ according to the Néel-Brown law. Introducing $E_b = 25k_B T$ into Eq.1.41, we have:

$$H_c = H_{c,0}\left(1 - \left(\frac{25k_B T}{KV}\right)^{\frac{1}{2}}\right) \tag{1.42}$$

here $H_{c,0}$ is the coercivity at $T = 0$ K, and equals to H_a, which is the first term of the expression of H_c. For the phenomenological case, the expression is modified as:

$$H_c = H_{c,0}\left(1 - \left(\frac{25k_B T}{KV}\right)^{\frac{1}{m}}\right) \tag{1.43}$$

where $m = 2$ is for SW particles. For most magnetic systems with a real structure, $m = 3/2$ [44, 45]. This expression evidences the decrease of the coercivity by a power function of T, which is called the Sharrock's formula in magnetism [46].

1.7 Random magnetic anisotropy model

The random magnetic anisotropy (RMA) model was very early suggested by Alben *et al.* [47] and Chudnovsky *et al.* [48] and has been developed by Herzer [49]. Magnetic properties of a ferromagnetic material are intimately related to its local structure. For a polycrystalline film for instance, the

actual microstructure leads to a distribution of magnetic easy axis orientation varying over the scale of the structural unit size or the structural correlation length δ_s. When the structural variations occur on a large scale, the magnetization will follow the individual easy magnetic directions of the structural units. The magnetization process, thus, is determined by the intrinsic anisotropy constant K, assumed to be uniaxial here for the sake of simplicity. For small structural correlation lengths, however, ferromagnetic exchange interaction forces the magnetic moments more and more to align parallel, thus impeding the magnetization to follow the easy axis of each individual structural unit. In other terms, the local magnetization correlation length cannot be shorter than the local exchange length. As a consequence, the effective anisotropy $\langle K \rangle$ will be an average over several structural units N and, thus, be reduced in magnitude (Fig.1.12).

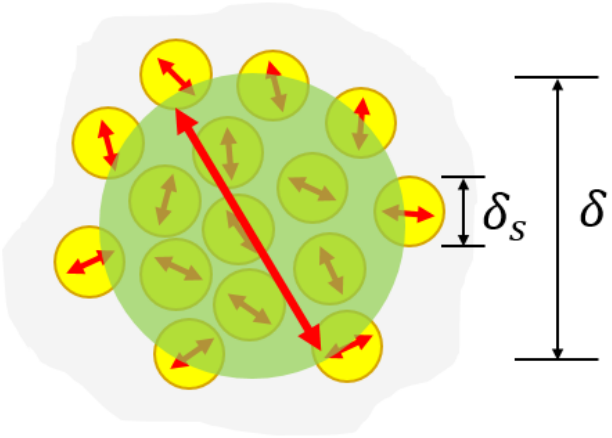

Figure 1.12: Sketch of a magnetic domain of length δ including N structural domains of size δ_s with the intrinsic anisotropy constant K and randomly oriented local anisotropy axes. Red double-headed arrows stand for anisotropy axes and the big arrow symbolizes the averaged anisotropy axis.

Here, the intrinsic magnetic length δ_0 is defined as $\sqrt{A/K}$ and the effective magnetic length δ as $\sqrt{A/\langle K \rangle}$. The anisotropy reduction is solved by $\langle K \rangle = K/\sqrt{N}$, where the number N of structural domains inside one magnetic domain scales as: $N \sim (\delta/\delta_s)^3$. 3D RMA characteristics in terms of the ratio δ_0/δ_s are listed in Table 1.2. This leads to the scaling rule between the effective magnetic length δ, the intrinsic magnetic length δ_0 and the structural length δ_s:

$$\delta/\delta_0 = (\delta_0/\delta_s)^3 \tag{1.44}$$

One notices that the number N of structural domains involved in a magnetic domain increases quickly with the decreasing structural domain size: $N \propto 1/\delta_s^{12}$. The corresponding anisotropy constant $\langle K \rangle$ is reduced with the reduction of the structural length δ_s as the power of 6. This allowed to successfully explain the coercivity reduction in soft magnetic nanocrystalline films [49, 50], as displayed in Fig.1.13.

Table 1.2: The RMA characteristics in 1D and 3D in terms of δ_0/δ_s, ratio between the intrinsic length δ_0 corresponding to the anisotropy K and the domain size δ_s: N, number of structural domains within a magnetic volume; δ, magnetic length related to the mean value of RMA anisotropy $\langle K \rangle$ over the magnetic volume.

	Anisotropy axis	N	δ/δ_0	$\langle K \rangle/K$
3D assembly	3D random	$(\delta_0/\delta_s)^{12}$	$(\delta_0/\delta_s)^3$	$(\delta_0/\delta_s)^{-6}$
1D chain	2D random	$(\delta_0/\delta_s)^{4/3}$	$(\delta_0/\delta_s)^{1/3}$	$(\delta_0/\delta_s)^{-2/3}$

In our case, the NWs are epitaxial. As it will be shown, the random anisotropy comes from the strain and the anisotropy axis is 2D randomly oriented in a plane for Ni NWs. Thus, the NWs can be structurally considered as 1D chains with 2D randomly oriented anisotropy axes. By revising the number N of structural domains in a magnetic domain for the present case, $N \sim \delta/\delta_s$, a similar treatment as previously leads to 1D RMA characteristics (Tab.1.2). As a consequence of the dimensionality, the number N increases only slowly with the reduction of the structural length δ_s. The reduction of the anisotropy $\langle K \rangle$ follows a quickly varying law of δ_s^6 for 3D and a slowly varying law of $\delta_s^{2/3}$ for 1D. It is interesting to notice that the blocking temperature is proportional to $\langle K \rangle \delta S \propto \delta_s^{1/3}$ for a 1D chain, where S is the section area of the chain. It means that fragmentation of the NWs into structural domains smaller than the magnetic length lowers the blocking temperature and leads to the thermal instability of magnetization.

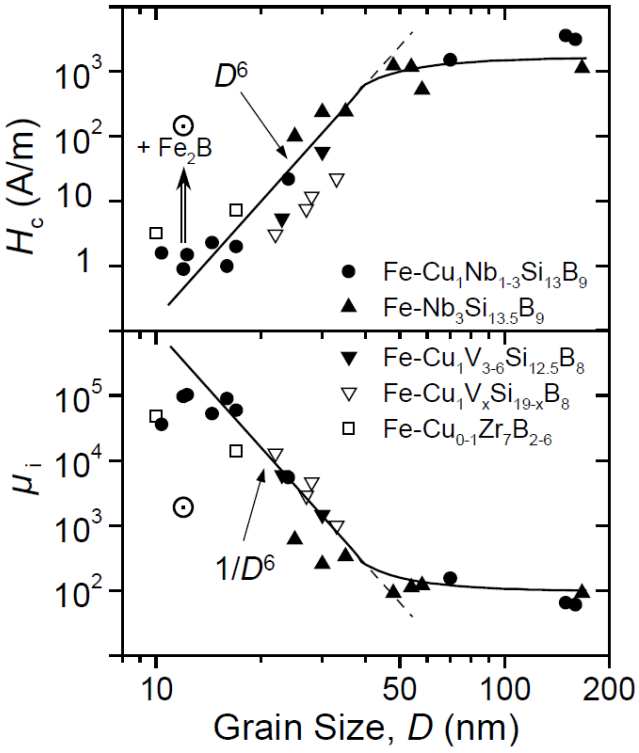

Figure 1.13: Coercivity H_c and initial permeability μ_i of Fe-based nanocrystalline alloys as a function of the average grain size D (graphs from [49]).

1.8 Dipolar interaction: inter-wire dipolar coupling

We have discussed the shape anisotropy for a single NW. For an assembly of magnets, the magnetostatic interaction between the magnets, also called the dipolar interaction, has a great influence on the magnetic behavior, in particular on the magnetization reversal. Hauet *et al.* analysed namely an ordered array of ferromagnetic Co/Pt nanobumps, evidencing the complexity and the importance of the dipolar interaction involved in the coercivity and the magnetization reversal [51].

The exact calculation of the dipolar interaction of the assembly on a NW is tedious, but it can be approximated within the mean-field framework [52]. This is sketched in Figure 1.14, leading to three terms:

$$\mathbf{H}_d - \mathbf{H}_{dip}^{NW} + \mathbf{H}_{dip}^{film} = -\mathrm{N}_d^{NW}\mathbf{M} + \mathrm{N}_d^{NW} P\mathbf{M} - \mathrm{N}_d^{film} P\mathbf{M} \tag{1.45}$$

P is the porosity (volume fraction occupied by the wires). The first term $\mathbf{H}_d$, the self-demagnetization field of a NW, determines the shape anisotropy of the NW, as shown in Section 1.3.1. The dipolar

field $\mathbf{H}_{dip}$ acting on the NW can be understood as the demagnetization field of a uniform film of $P\mathbf{M}$ magnetization density, provided that the demagnetization field of a virtual NW of $P\mathbf{M}$ magnetization density is also removed:

$$\mathbf{H}_{dip} = -\mathbf{H}_{dip}^{NW} + \mathbf{H}_{dip}^{film} = \begin{pmatrix} 1/2 & 0 & 0 \\ 0 & 1/2 & 0 \\ 0 & 0 & -1 \end{pmatrix} P\mathbf{M} \qquad \text{or} \qquad \left\{ \begin{array}{l} H_{dip,\parallel} = \frac{1}{2}\, PM_{\parallel} \\ \\ H_{dip,\perp} = -PM_{\perp} \end{array} \right\} \tag{1.46}$$

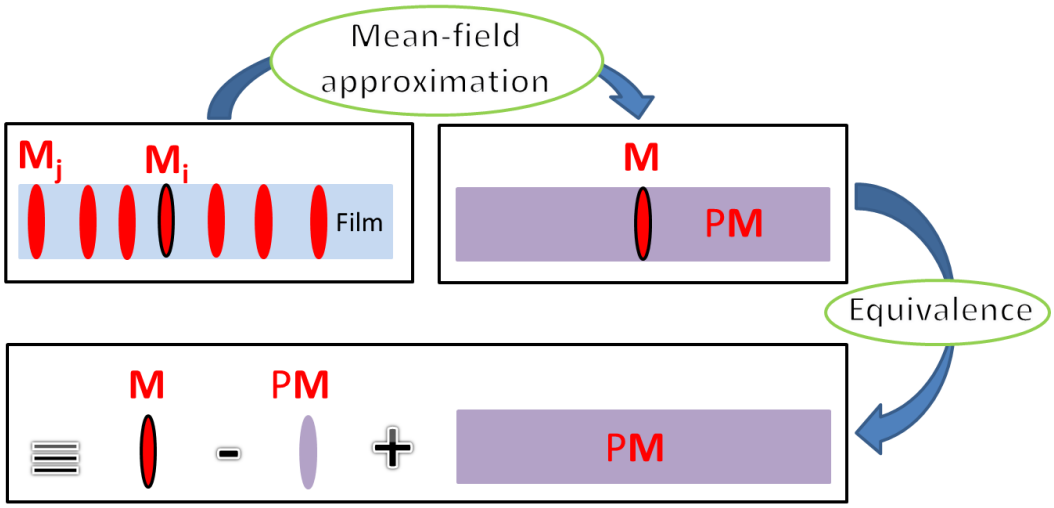

Figure 1.14: Sketch of the dipolar interaction in a film containing vertical NWs with a porosity P. On the top, NW i of magnetization density $\mathbf{M}_i$ in the film is approximated to a NW of the mean magnetization density $\mathbf{M}$ in a film of the mean magnetization density $P\mathbf{M}$ outside of the NW. On the bottom, the equivalence is made with the case of a NW of $\mathbf{M}$ immersed in the demagnetization field of a uniform film of $P\mathbf{M}$, provided that the demagnetization field of a virtual NW of $P\mathbf{M}$ is also removed.

The dipolar field induces a bias of hysteresis loops and affects their slopes. In function of the porosity P, the effect on the loop slopes can be clearly visualized, in setting H_c^{NW} to zero for clarity (Fig.1.15). While the coercive field is often extrinsic in real cases, the anisotropy field remains to be determined by the shape anisotropy: $H_a^{NW} = M_s/2$. The vertical slope along the easy-axis ($\perp$) of a single NW ($P = 0$) is inclined by the increasing dipolar field, until becoming the hard axis of the film ($P = 1$). The reverse happens along the NW hard axis ($\parallel$). The slope evolution can be followed by the saturation fields: $H_{s,\perp} = 2PH_a^{NW}$ and $H_{s,\parallel} = (1\text{-}P)H_a^{NW}$. The crossover of the $\perp$ and $\parallel$ slope evolution occurs at $P = 1/3$.

The effect was demonstrated in Ni NW arrays electrodeposited in polycarbonate porous membrane (Fig.1.16) [53]. While a diluted NW array ($P = 0.04$) exhibits the loops expected from a single NW (Fig.1.16(a)), an array with the porosity P around 1/3 displays an isotropic behavior with identical $\perp$ and $\parallel$ loops (Fig.1.16(b)). Some experiments are sensitive to the difference between the $\perp$ and $\parallel$ saturation fields, such as for example ferromagnetic resonance measurements [52, 53]. For the last case, an effective magnetostatic anisotropy constant is defined as: $K_{ms}^{eff} = K_{ms}^{NW}(1 - 3P)$. For our static measurements along one specific direction ($\perp$ or $\parallel$) in this thesis, we should pay attention on the effect of the dipolar field along the concerned direction, $H_{dip,\perp}$ or $H_{dip,\parallel}$.

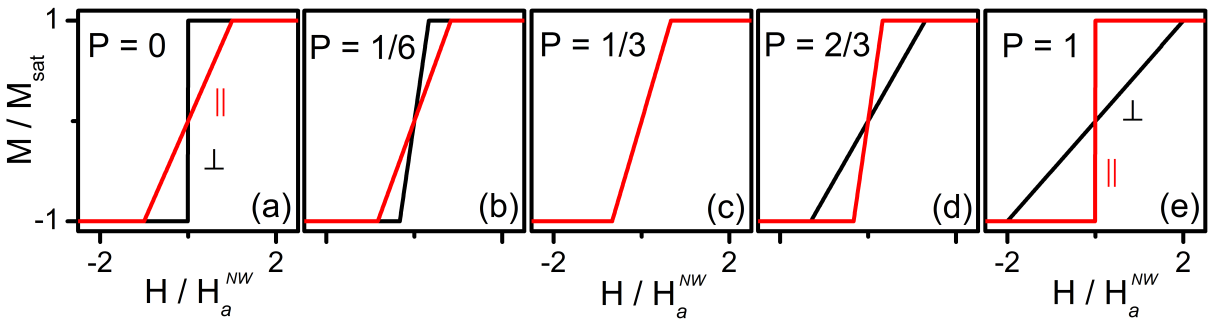

Figure 1.15: Slope evolution of hysteresis loops in function of the porosity P in a film containing vertical NWs, with the field perpendicular ($\perp$) and parallel ($\|$) to the film. (a-e) $P = 0$, 1/6, 1/3, 2/3 and 1, respectively.

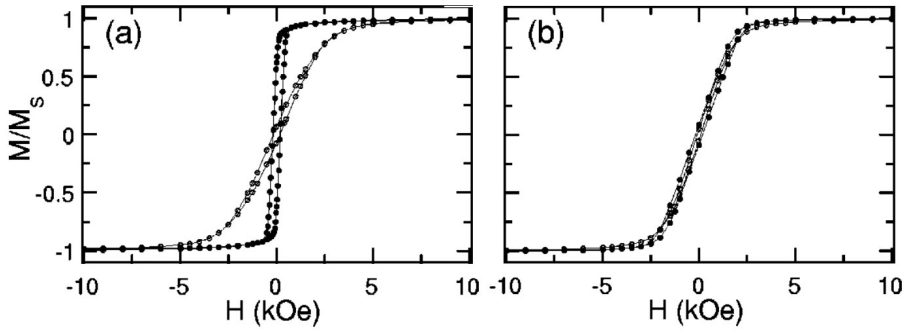

Figure 1.16: Hysteresis loops measured with the field perpendicular (filled circles) and parallel (open circles) to the films of Ni NW arrays. (a) NW diameter of 56 nm and porosity of 4%. (b) NW diameter of 250 nm and porosity of 35-38%. Graphs adapted from Fig.5 of [53].

Chapter 2

Experimental techniques

2.1 Elaboration technique: Pulsed Laser Deposition

The growth technique of pulsed laser deposition (PLD) was widely developed in the early 90's with copper oxide based high temperature superconductors. Compared to molecular beam epitaxy or sputtering adapted for semiconductors and metals, PLD is particularly suitable for oxides. Moreover, the pulsed therefore discontinuous growth with PLD can be profitably exploited, as in this work.

A typical PLD setup is composed of a pulsed UV laser and a growth chamber in which targets and substrate are kept under specific conditions of temperature and pressure (Fig.2.1). Despite the moderate average power (∼1 W) used in the technique, huge instantaneous power (between MW and GW) can be achieved due to the short duration of laser pulses (from 100 fs to a few ns). This high power causes evaporation and partial ionization of the target's material [54]. The resulting plasma is called the plume and contains atoms, molecules, electrons, ions and even potentially agglomerated solid particles, depending on the laser energy and the target surface state. The agglomerates should be avoided, since they cause loss in the crystalline quality of the deposited thin films. The plume is dense and strongly directed, expanding in a direction perpendicular to the target surface due to electric repulsion effects.

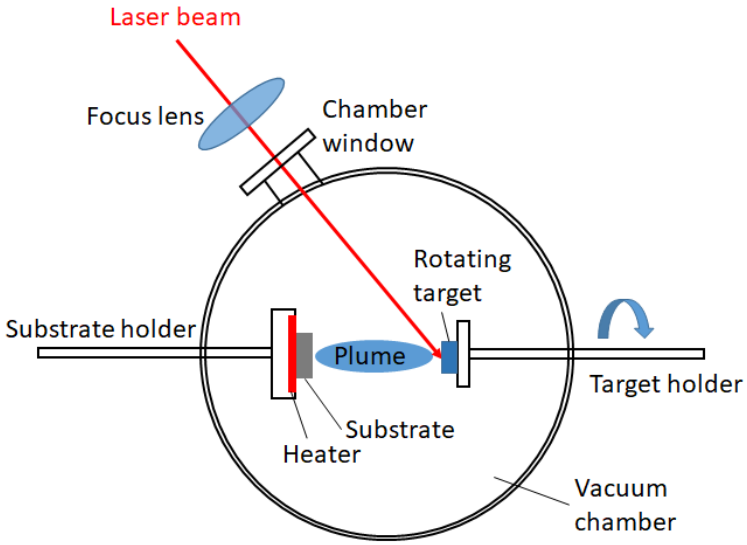

Figure 2.1: Schematics of a pulsed laser deposition setup.

The substrate is at a distance of around 5 cm in front of the target and receives the matter of the plume generated by the laser. The substrate temperature influences the diffusion length of atoms on the surface and thus plays an important role in the crystalline quality of the thin film [55]. Generally, a higher temperature enables a better crystalline quality. Besides the temperature, the pressure in the chamber is also an important control parameter of the growth. The atmosphere interacts physically with the plume, controlling the rate of matter arriving at the substrate. Furthermore, the atmosphere can also interact chemically with ions, changing their valence, or even reacting with ions and producing other materials. For oxides, the growth is generally assisted by an oxygen atmosphere of high pressure (up to 10^{-1} mbar), in order to keep the desired stoichiometry [56]. In our case, we want to

get a matrix under reduction condition in order to preserve the metallic character of embedded NWs. Thus, our growth was made under secondary or ultrahigh vacuum condition and the oxide matrix is non-stoichiometric, notably in oxygen.

2.2 Structural characterization techniques

2.2.1 Transmission electron microscopy

Transmission electron microscopy (TEM) is a powerful tool for morphological, structural and chemical characterizations of nano-objects [57, 58]. In this work, TEM was performed in a 200 kV JEOL JEM 2100F microscope with a field-emission gun (IMPMC, Sorbonne Université). The point resolution of the microscope is 1.9Å. Furthermore, the microscope is equipped with a Gatan GIF 2001 spectrometer permitting studies by electron energy loss spectroscopy (EELS) or by a chemical imaging via energy filtered TEM (EFTEM) with a spatial resolution of 1-2 nm. Energy dispersive x-ray spectroscopy (EDX) with a Si(Li) detector is available in the microscope and allows to measure the sample chemical composition. Advanced studies were made in a FEI Titan Themis 200 microscope at the Centre de Nanosciences et de Nanotechnologies (C2N, CNRS/Université Paris-Sud-Université Paris-Saclay). Scanning TEM (STEM) in combination with a high angle annular dark field (HAADF) detector or a high resolution EDX detector (EDX SuperX) offers a chemical analysis at atomic scale.

Sample preparation

In TEM, it is necessary to prepare samples thinner than 50 nm for high resolution observation or electron spectroscopy. Two types of preparation were made to observe the film from the top, plan view, or from the side, cross section view. In the case of a plan view, only the substrate side is thinned, firstly mechanically down to about 40 μm and then by argon ion milling in a Gatan Precision Ion Polishing System (PIPS) II. Two beams of 4 kV Ar ions are directed to the rotating sample in a low angle ($\sim 7°$), until producing a small hole in the sample center. Finally, low energy Ar ions ($\sim$300 V) are used to remove amorphous layer caused by the high energy ion milling. Then, edges of the hole are enough thinned to be observed by TEM. For a cross-section view, two pieces of the sample are tightly glued as a "sandwich" and then thinned similarly as previously. Both faces of the sample are now milled simultaneously by the two Ar ion beams until producing a hole including the film/substrate interfaces located on either side of the middle of the "sandwich".

Images and diffraction patterns

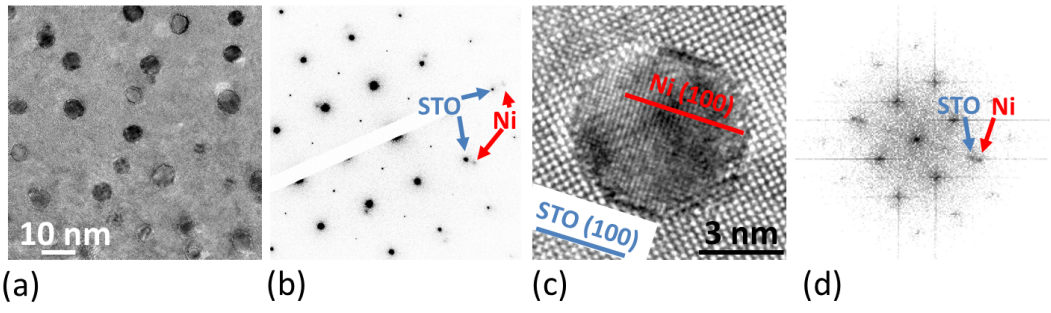

Figure 2.2: Images and diffraction of Ni NWs epitaxied in $SrTiO_3$ matrix. (a) Plan view of NWs of $\sim$5 nm diameter. (b) Electron diffraction pattern from a large area where two weak spots of Ni are indicated by red arrows and spots of the matrix by blue arrows. (c) Enlarged view of one NW. (d) Corresponding Fourier transform of the image (c).

With high resolution plan views, we can determine the epitaxy relationship between NWs and the matrix (Fig.2.2(a,c)). During the observation, electron diffraction patterns obtained in the microscope provide the global orientation of NWs with respect to the marix in a large area of several hundreds nm (delimited by a diaphragm) (Fig.2.2(b)). Local diffractograms can be obtained by Fourier transform of a selected area of an image (Fig.2.2(c,d)). The last procedure was widely used in this work to analyze locally NWs. In a cross-section view, NWs are visualized through moiré patterns resulting from the double diffraction process between a NW and the matrix, since the NW and the matrix overlap along the electron path in cross-section geometry.

Chemical analysis and maps

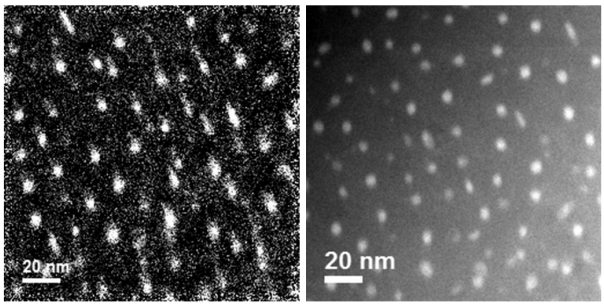

Figure 2.3: EFTEM at Ni L-edge (a) and image filtered at 100 eV (b) of Ni NWs of ∼2 nm diameter epitaxied in $SrTiO_3$ matrix.

The mean chemical composition of a film is determined by EDX and local chemical information at nanoscale obtained by EFTEM, in the JEOL JEM 2100F microscope. The EFTEM proceeds with three images: for Ni (or Co), one image of post L-edge is acquired together with two other ones just below the L-edge permitting to evaluate the background. The final EFTEM image after the background soustraction provides a map of Ni (Fig.2.3(a)). Such analysis is repeated over a large area, in order to retrieve key parameters of an assembly of NWs with good statistics: distribution of NW diameters and density of NWs (porosity of the film). However, the EFTEM mode induces high damage and pollution on the sample during the observation, especially for insulating materials such as oxides. We noticed that an image formed by electrons with the energy loss of 100-200 eV makes enough difference between the metallic Ni and the oxide matrix (Fig.2.3(b)). In other terms, the efficiency of multiple scattering process leading to the energy loss of ∼100 eV should be much higher in metal than in oxide in our case, to distinguish clearly the metal from the oxide. It allows us to acquire quickly images at ∼100 eV instead of ∼855 eV for Ni L-edge and then reduces the damage and pollution of the sample. During this work, both images filtered at 100-200 eV and EFTEM at L-edge were exploited. Furthermore, advanced mappings and line profiles sensitive to chemical elements were also performed by STEM-HAADF and STEM-EDX, in particular in the FEI Titan Themis 200 microscope at the C2N.

2.2.2 X-ray diffraction

For my work, x-ray diffraction (XRD) constituted a main technique to analyse the structure and the strain of NWs. All samples were characterized by laboratory XRD, providing information on the vertical epitaxy and mean values of the axial strain of NWs. Selected samples were analyzed in detail by synchrotron XRD, in scrutinizing 3D shapes of diffraction spots in reciprocal space. Below, I present main XRD methods used at laboratory and on SixS beamline at synchrotron SOLEIL.

Out-of-plane and in-plane diffraction

Rigaku SmartLab 5-circle diffractometer is operating with a Cu rotating anode. A Ge(220) two reflexion channel-cut monochromator can be used to select Cu $K_{\alpha 1}$ radiation (1.5406Å). The 5 circles concern the three Euler angles (ω, φ and χ) for the sample stage and the two detector angles (2θ and $2\theta_\chi$). Usual scans used in my work are illustrated in Fig.2.4. The horizontal lattice planes of an epilayer are analyzed with a $\theta/2\theta$ scan: the incidence angle ω, between the incident beam and the sample surface, is synchronized to be the half of the detector angle 2θ. When the detector is fixed at a value of 2θ, a rocking curve (ω-scan) explores an arc of the reciprocal space then the mosaicity of the planes. A reciprocal space mapping is obtained by a set of rocking curves around a reflection of interest. The $\theta/2\theta$ geometry is also called specular, since it concerns equally the mirror reflection, *i.e.* the reflectivity of an epilayer on a substrate. The samples were characterized by reflectivity allowing to determine the epilayer thickness, roughness and density.

For analyzing lattice planes inclined of an angle α with respect to the surface, a $\omega/2\theta$ scan is made: ω is always synchronized with 2θ, but with an offset of α. In this case, the incidence angle ω is equal to $\theta - \alpha$ and the emergence one to $\theta + \alpha$, or *vice versa*. It turns out that highly inclined lattice planes including vertical ones cannot be probed in this geometry ($\theta_B < \alpha$). With respect to a classic 4-circle diffractometer, the adding of the angle $2\theta_\chi$ allows the detector to quit the incidence plane defined by the incident beam and the sample normal. At a grazing incidence (0.1-0.7°), a $\varphi/2\theta_\chi$ scan allows to probe vertical planes of an epilayer, similarly to a $\theta/2\theta$ scan for the horizontal planes.

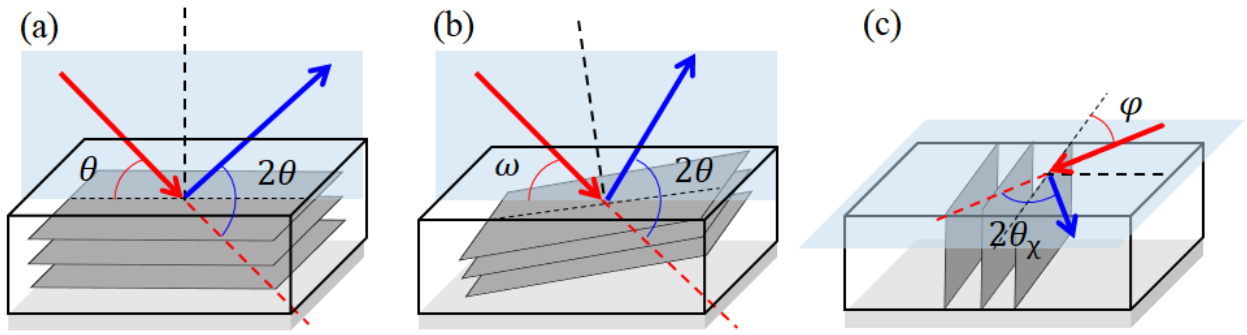

Figure 2.4: Schematics of XRD on the horizontal lattice planes ($\theta/2\theta$ scan), on inclined planes ($\omega/2\theta$ scan) and on vertical planes (in-plane $\varphi/2\theta_\chi$ scan)). The red arrow stands for incident x-rays and the blue for diffracted ones.

In addition to the restriction for inclined planes, the main limitations of a laboratory diffractometer concern a low intensity of x-ray source and the instrumental resolution. The resolution is limited by the spectral width of Cu $K_{\alpha 1}$ line ($\Delta\lambda/\lambda \approx 10^{-4}$) and a high angular divergence of the beam. The angular divergence can be reduced by the use of a parabolic multilayer mirror, slits and/or collimators. For out-of-plane, the ultimate resolution of $\Delta d/d \approx 10^{-4}$ on lattice distances d can be reached in high-angle scans. On the other hand, the resolution is at least one order of magnitude less for in-plane than for out-of-plane. Another limitation comes from the large wavelength value, hence a reduced Ewald sphere. This gives access to a small portion of the reciprocal space. For Ni and Co with a compact structure, therefore a reciprocal lattice with large unit cell, only three spots, 002, 004 and 113, are accessible out-of-plane in our epitaxial NW system.

Pole figure

Polar figures (PFs) are useful to study orientation textures in samples. The classic PFs are acquired with the source and the detector fixed (2θ fixed) as shown in Fig.2.5(a). The normal of the sample is tilted by an angle of χ out of the plane defined by the incident and diffracted beams. Then, a scan along the azimuthal angle ϕ around the normal z is performed. All the sets of χ- and ϕ- scans constitute PFs. The PFs can be visualized on the unitary sphere in the sample coordinates (x, y, z) as illustrated in Fig.2.5(b) or by the projection on the equatorial plane in Fig.2.5(c). In in-plane PF

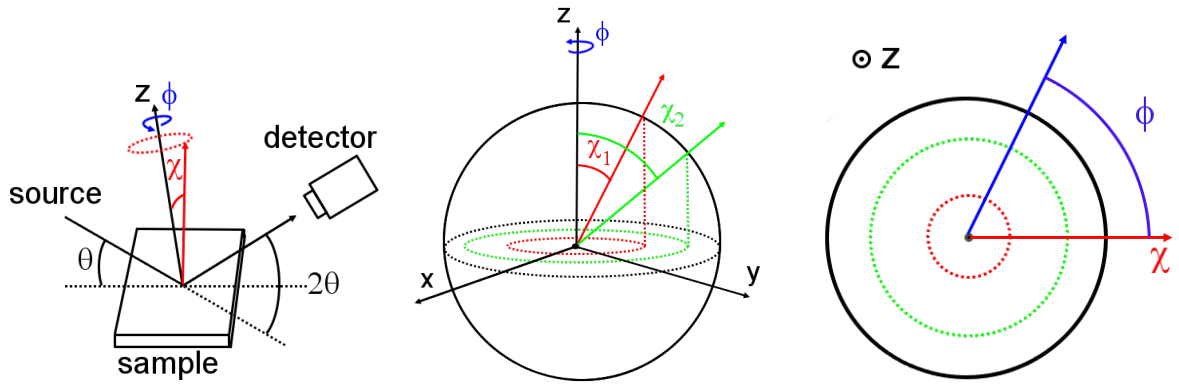

(a) (b) (c)

Figure 2.5: Schematics of XRD PFs : z-axis, normal to the sample surface ; χ, sample tilt angle ; ϕ, sample azimuthal angle. (b) 3D representation of a PF. (c) 2D projection of a PF.

geometry in practice, the sample only rotates around the normal (ϕ-scan) and remains horizontal on the stage. The source moves to an incident angle of ω and the detector lifts in the incidence plane (2θ) and quits the incidence plane ($2\theta_\chi$) to intercept the diffracted beam, in keeping the total detector angle constant at $2\theta_B$ of the lattice planes analyzed.

Synchrotron x-ray diffraction

The use of synchrotron radiation overcomes the limitations of a laboratory diffractometer indicated above and offers new possibilities with the high intensity of the radiation and the high instrumental resolution. To make XRD sensitive to the surface, the penetration of x-ray in the sample is limited by a grazing incidence from 0.1 to 0.3° and close to the critical angle of the material. On SixS beamline, the Z-axis geometry used keeps constant the grazing incidence (angle labelled α in Fig.2.6), while the sample rotates around its normal (angle ω). The detector has two degrees of freedom (angles δ and γ) to move on the half-sphere above the sample and intercepts an outgoing diffracted beam in any direction [59]. The Z-axis geometry is made for vertical and inclined planes and gives access to a large portion of the reciprocal space from the in-plane to part of the out-of-plane. In addition, we can leave the Z-axis geometry and adopt the Euler geometry to probe the rest of the out-of-plane reciprocal space near the specular zone as in the laboratory.

On SixS beamline, x-ray energy can be tuned from 5 to 22 keV. For our measurements, we used the energy of 18.4 keV (0.67Å), more than twice of Cu $K_{\alpha 1}$ line. In other terms, the Ewald sphere is more than the twice as large and the accessible reciprocal space portion eight times larger than in the laboratory. The important contribution of synchrotron radiation is the high instrumental resolution, thanks to the weak divergence of the beam (<120 μrad). The beam arriving on the sample therefore has a large intrinsic coherence length (> 800 nm). Compared to diameters of a few nm and a height of about 100 nm of NWs, we can neglect the instrumental effect.

Synchrotron reciprocal space volume acquisition

I participated to the runs on NWs carried out on SixS beamline and benefited from a measurement protocol newly settled by the SixS beamline staff. The XPAD (X-ray Pixel chips with Adaptive Dynamics) detector used is of the new generation of 2D detectors with huge gain in dynamic range and allows to record more than 1000 frames per second. Each frame represents a small cut of the reciprocal space, since each pixel of the XPAD is equivalent to a high resolution classic point detector. The performances of XPAD allow to envisage new types of measurements, in particular acquisition in a continuous mode or Flyscan mode. I contributed to establish strategies on the scan trajectories in the reciprocal space, in order to collect efficiently a 3D volume data around a diffraction spot. Data are further processed by a dedicated software *Binocular* [60] and projected on a 3D grid in reciprocal lattice coordinates to be analyzed. Thanks to the new data acquisition mode, we surprisingly discovered and

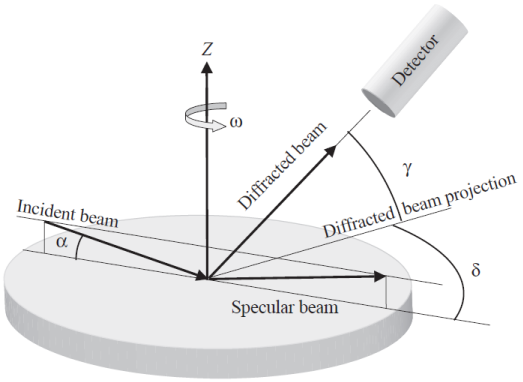

Figure 2.6: Diffraction in Z-axis geometry used on SixS beamline at SOLEIL. The incidence (angle α) is kept to be grazing ($< 1°$). The sample is rotated around its normal (angle ω) to set inclined or vertical planes at the Bragg position. The detector rotates with two degrees of freedom (angles δ and γ) to intercept the diffracted beam. Figure from [59].

then resolved a 3D structure around Ni Bragg reflections in our samples, as it will be shown in Chap.4. It should be underlined that this work would not be possible with a classic point detector performing line scans.

2.3 Magnetic characterization techniques

2.3.1 Magnetic measurements

Magnetometers

A vibrating sample magnetometer (VSM) in a Physical Property Measurement System (Quantum Design PPMS 9T) was used for this work. The magnetometer operates in a large range of temperature (1.8-350K) and of magnetic field (up to 9 T), in configuration parallel or perpendicular to the film. Strong magnetic fields are produced by a superconducting magnet immersed in liquid helium. The measurement is based on the detection of the magnetic flux induced in a coil by the oscillation of the sample. More precisely, a sample is vertically vibrating in the center of the measuring coil at a frequency of 40 Hz with a constant amplitude. The voltage induced in the sensor coil is proportional to the magnetization of the sample. Parasitic signals and drifts being rather pseudo-continuous are eliminated by a synchronous detection. The main interests of this method are its speed and high sensitivity with a RMS (root mean square) of $10^{-5}/10^{-6}$ EMU/sec. For samples of very weak magnetization, a superconducting quantum interference device (SQUID) magnetometer (Quantum Design MPMS XL 5T) was also used. The SQUID detector consists in a superconducting loop containing Josephson junctions that enable the measurement with a very high sensitivity (RMS $< 10^{-6}$ EMU/sec). As the SQUID sensor operates at low temperature, a second order gradiometer collects the flux generated by the sample and transfer it to the SQUID sensor immersed in liquid helium. The signal as a function of the sample position is read out and interpreted to the magnetization.

Hysteresis cycles and thermal curves

Two types of measurements were usually made: hysteresis cycles $M(H)$ at different temperatures and magnetization as a function of temperature $M(T)$ according to the ZFC (Zero-Field Cooling) and FC (Field-Cooling) protocols. The ZFC procedure consists in heating the sample beyond its blocking temperature to a magnetic disorder of mean null magnetization and in cooling it under zero-field until a low temperature (5 K, typically). Then, the application of a small field (0.01 T, for instance) and the gradual temperature raise (2 K/min) allow to analyze the magnetization reversal induced by the thermal activation against internal energy barriers. Comparison with the behavior under a field-cooling (FC) provides information on the blocking temperature T_b, so the energy barriers in the

system.

First-order reversal curve (FORC) method

For magnetic nanostructures and assemblies, the problem of extracting the intrinsic magnetic properties and quantifying the interaction is central. The FORC method, developed for the last two decades, consists in the measurement of a set of switching fields of an assembly and allows to extract intrinsic coercive fields (H_c) and to describe the interaction *via* bias fields (H_b). The method is based on the idea, early suggested in 1935 by Preisach [61], that a nonlinear phenomenon with hysteresis should be divisible into elementary and coupled binary processes, often called "hysterons". This fertile idea has been thoroughly developed since then, with the aim of its integration into the analysis of magnetic hysteresis [62, 63].

The protocol of measuring one FORC, $M(H_r, H)$ from a reversal field H_r, is given in Fig.2.7. A FORC contains information on the reversal switchings until H_r and the restoration switchings all along the applied field H. The FORC map, the mixed second-order derivatives of $M(H_r, H)$, brings out all double switchings, the one in restoration preceded by the one in reversal:

$$\rho(H_r, H) = -\frac{1}{2}\frac{\partial^2 M(H_r, H)}{\partial H_r \, \partial H} \tag{2.1}$$

Furthermore, the map can be transformed to $\rho(H_c, H_b)$, in comparing the restoration field with the reversal one: $H_c = (H - H_r)/2$ and $H_b = (H + H_r)/2$. In such a way, the H_c coordinates represent the apparent coercive fields of subjacent hysteresis loops and the H_b coordinates their bias.

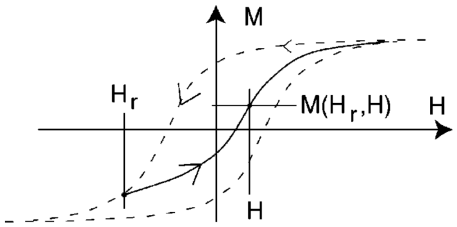

Figure 2.7: FORC protocol according to Pike [64]: after saturating the sample in a positive field, the field is lowered to a reversal field H_r and a reversal curve $M(H_r, H)$ is acquired with the increasing field H until saturation (graph from [64]).

To illustrate the main FORC features, I will use a toy model of three idealized uniaxial magnets with increasing H_c and saturation moments M (Fig.2.8). In absence of interaction between the magnets, the FORCs reproduce branches of the two expected minor loops and that of the major one, in addition to the constant curve without any reversal (Fig.2.9(a)). The only discontinuities appearing simultaneously in H_r and H occur at: $(H_r, H) = (-H_{ci}, H_{ci})$ with $i = 1$, 2 or 3 (Fig.2.9(b)). In other terms, the non-null elements of the FORC map are of the value M_i at the H_{ci} along the H_c axis without any bias. The zone is marked as the region of interest (ROI).

If we add a simple dipolar interaction represented by a unique coefficient α (arbitrarily set at 0.3), the dipolar field felt by magnet i is: $\vec{H}_{dip,i} = -\alpha\vec{M}_j - \alpha\vec{M}_k$ $(i \neq j \neq k)$. Now, all the switchings are biased by the dipolar fields (Fig.2.9(c)) and the ROI is lifted above the H_c axis (Fig.2.9(d)). For the soft magnet 1, the first reversal and restoration happen with the other magnets unchanged and at $(H_r, H) = (-H_{c1} + H_{b11}, H_{c1} + H_{b11})$, where $H_{b11} = \alpha M_2 + \alpha M_3$. It means that the lowest H_c part of the ROI is biased only. The switchings of the hard magnet 3 occur always after that of the others and at $(H_r, H) = (-H_{c3} - H_{b33}, H_{c3} + H_{b33})$, where $H_{b33} = \alpha M_1 + \alpha M_2$. In other terms, the highest H_c part of the ROI is unbiased with an apparent H_c of the hard magnet enlarged by the interaction. The case of the medium magnet is intermediary with both bias and extension of H_c. These are the main characteristics of a FORC map for an interacting particle assembly. It is obvious that if the dipolar

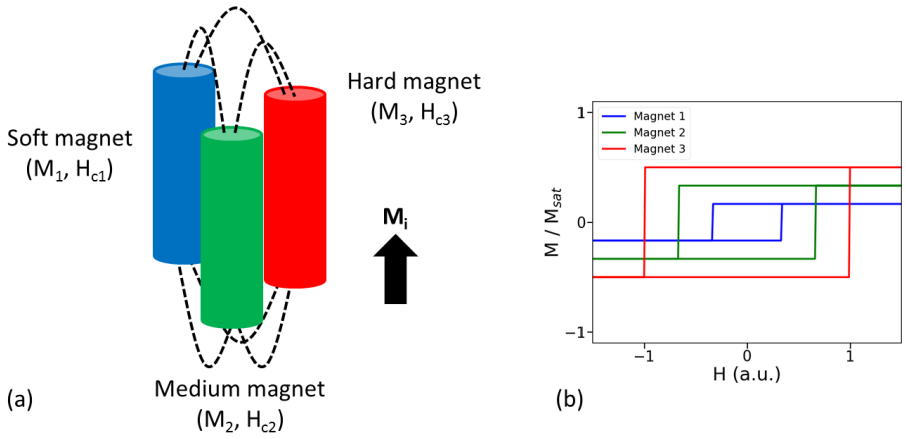

Figure 2.8: Toy model of three uniaxial magnets with the binary up and down magnetization states. (a) Schematics of the magnets where dashed lines symbolize the dipolar interaction. $H_{c1} : H_{c2} : H_{c3} = 1/3 : 2/3 : 3/3$ and $M_1 : M_2 : M_3 = 1/6 : 2/6 : 3/6$. (b) Idealized hysteresis loops.

interaction between the magnets is replaced by an exchange one, the ROI will be shifted on the other side of the H_c axis.

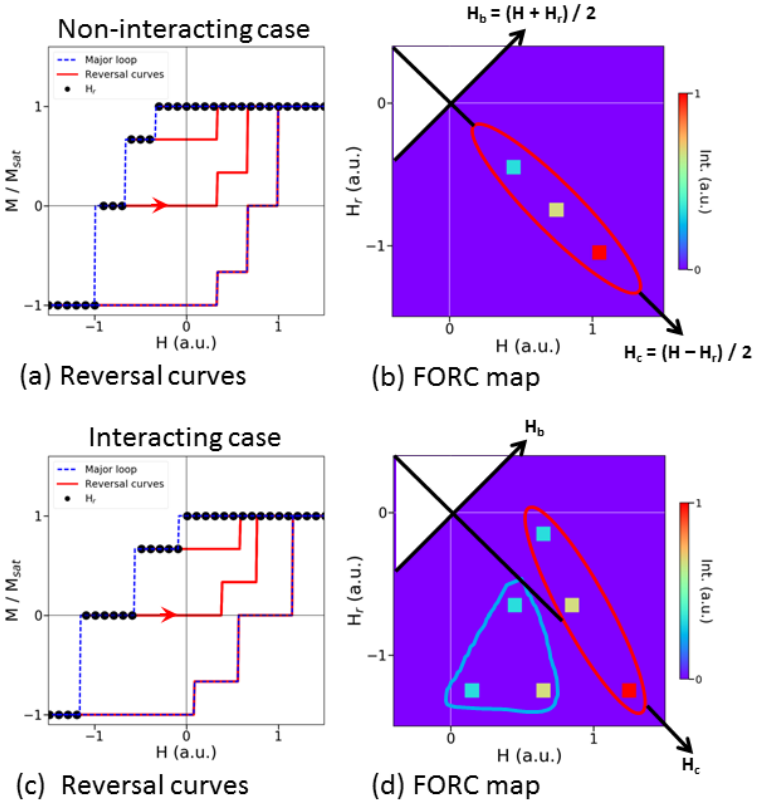

Figure 2.9: FORC method applied to the toy model without (a-b) and with (c-d) the dipolar interaction. (a) and (c), major loops (blue dashed lines) and reversal curves (red lines) starting from the reversal fields H_r (black dots). (b) and (d), FORC maps: the H_c and H_b axes are indicated; the red contours mark the main regions of interest (ROIs); the blue triangular contour in (d) symbolizes the "shadow" induced by the dipolar interaction.

The interaction induces also discontinuities in the FORC map with mixed switchings: the reversal of magnet i modifies the restoration field of magnet j ($i > j$). This is marked as the "shadow" in Fig.2.9(d), because its intensity is often weaker than that of the ROI in real cases. Surprisingly, even three negative values exist in the "shadow" (undisplayed in Fig.2.9(d)). Negative values are

not possible with a basic Preisach model. In the inaugural paper of Pike *et al.* [63], the authors pointed out that a basic Preisach model cannot explain the lifting of the ROI and negative values in the "shadow", because the model does not take into account a non-local interaction. In other terms, a bias field is not intrinsic to a magnet, such as required in a basic Preisach model. Their work established the physical basis of the FORC method, in integratig a non-local interaction in the so-called moving Preisach model within the framework of the mean-field theory. This opened the way to the extraction of intrinsic coercive fields from the FORCs and has stimulated studies of interacting assemblies, notably of nanowires [65, 66, 67, 68].

2.3.2 X-ray magnetic circular dichroism

When the absorption in a material depends on the polarization states of light, the material is dichroic. Dichroism is related to the dependence of the optical response on the relative orientation of light polarization and symmetry axes of the system. Magnetic circular dichroism is related to the difference in absorption of left circularly polarized (LCP) light and right circularly polarized (RCP) light in ferromagnetic materials. The spectroscopic study of circular dichroic effects in the absorption of a magnetic material can be used to probe magnetism. When the photons are in the x-ray range, the technique is referred as X-ray Magnetic Circular Dichroism (XMCD). XMCD is a synchrotron-based technique that has been developed in the 1990s [69, 70, 71, 72, 73] and that allow to measure the orbital and spin moments of specific elements in a magnetic material. The elemental specificity is ensured by the possibility to probe spectroscopically specific edges.

In the framework of the dipolar approximation, the probability of transition from an occupied initial state to an unoccupied final state through the absorption of a photon with energy $\hbar\omega$, calculated using Fermi golden rule, is given by:

$$W_{if}^{q} \propto |\langle \Phi_f | \mathbf{e}_q . \mathbf{r} | \Phi_i \rangle|^2 \delta(E_f - E_i - \hbar\omega)$$

In this equation, $|\Phi_i\rangle$ and $|\Phi_f\rangle$ are the initial and final state of the absorbing atom, $\delta(E_f - E_i - \hbar\omega)$ ensures the conservation of energy in the absorption process, and $\mathbf{e}_q$ is the polarization vector of light. The index q is equal to -1 for RCP light and +1 for LCP light. Circular dichroism occurs when $W_{if}^{+1} \neq W_{if}^{-1}$.

In what follows, we will concentrate on XMCD measured at the $L_{2,3}$ edges of $3d$ transition metals. The absorption is then related to transitions between $2p$ states, lying several hundreds of eV below the Fermi level E_F, and unoccupied $3d$ states above E_F. $\hbar\omega$ lies in the soft x-ray range ($\sim$850 eV for Ni). These $p \rightarrow d$ transitions are allowed under the dipolar approximation. Because of the spin-orbit coupling, the $2p$ level is split in two sub-levels: $2p_{1/2}$ and $2p_{3/2}$. $2p_{1/2} \rightarrow 3d$ transitions correspond to the L_2 edge and $2p_{3/2} \rightarrow 3d$ transitions correspond to the L_3 edge. The principle of XMCD in transition metals can be understood in the framework of the two-steps model proposed by Stöhr and Wu [74] and illustrated in Figure 2.10. The two steps involved are: (i) spin-polarized electrons are emitted by the spin-orbit split $2p$ band and (ii) the exchange split $3d$-band acts as a spin detector. In the first step, selection rules, with transition matrix elements that depend on the polarization of light, can be used to show that:

- at the L_2-edge, LCP (RCP) light excites 75% (25%) spin down and 25% (75%) spin up electrons,
- at the L_3-edge, LCP (RCP) light excites 37.5% (62.5%) spin down and 62.5% (37.5%) spin up electrons.

The exchange split d-band then acts as a spin detector. Thus, if there is an unbalance in the spin up and spin down populations, there will be circular dichroism. This can be understood most simply by considering two extreme cases: a material with a $3d$ band that is not exchange-split will exhibit no dichroism. In contrast, if we consider an exchange splitting large enough to have a spin-up $3d$ band totally occupied, transitions from the $2p$ levels towards the spin-up $3d$ band cannot occur and, based on the probabilities of transition, a strong dichroism will occur.

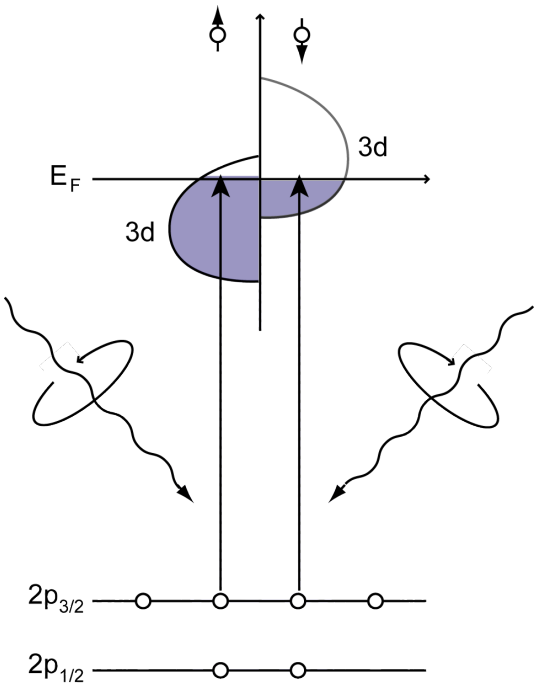

Figure 2.10: Schematic illustration of XMCD in the framework of the two-steps model. Figure adapted from M. Sacchi and J. Vogel, *Dichroism in X-ray Absorption* in Reference [75].

From the analysis of XMCD spectra at the $L_{2,3}$ edges of Fe, Co and Ni, applying sum rules [76, 77] that will be detailed in Chap.5, one can in principle access to the expectation value of the spin and orbital moments. Furthermore, these values are the projections of the moments along the propagation direction of light. Thus, by varying the incidence angle of light, it is possible to monitor the anisotropy of the moments.

In the framework of this thesis, x-ray absorption spectroscopy and x-ray magnetic circular dichroism experiments were carried out on the DEIMOS beamline of SOLEIL synchrotron [78, 79, 80]. Data were acquired in total electron yield mode. The samples were kept under ultrahigh vacuum at 4.2 K during measurements. The applied magnetic field was collinear to the x-ray propagation vector. The incidence on the sample was set through a rotation of the sample by an angle θ. θ=0 refers to normal incidence. XAS and XMCD spectra were acquired at the Ni and Co $L_{2,3}$ edges by scanning the photon energy in the 760-880 eV range. Element-specific hysteresis loops were acquired by scanning the magnetic field at constant x-ray energy, set to the maximum of the XMCD signal, for left and right circular polarization. For the acquisition of XMCD spectra at remanence, the following scheme was used: the sample is submitted to a magnetic field exceeding the saturation field in the positive direction, the field is then set to zero and absorption spectra are recorded with left and right circular polarizations. The same procedure is then applied with the saturating field in the opposite direction. The XMCD spectra at remanence are then obtained by properly averaging data recorded for both directions of application of the field.

Chapter 3

Elaboration of vertically self-assembled nanowires

In this chapter, I will precise the growth conditions of vertically self-assembled ferromagnetic nanowires embedded in an oxide matrix and discuss the possibility of controlling the diameter of the nanowires.

3.1 Growth of nanowires embedded in $SrTiO_3$ matrix

The growth of Ni/CoNi nanowires embedded in $SrTiO_3$ matrix is achieved by sequential deposition of Ni (or/and Co) and $SrTiO_3$ on a $SrTiO_3$ (001) substrate using pulsed laser deposition (PLD). As shown in Fig.3.1, a pulsed laser beam is focused into a vacuum chamber to strike a rotating target. The targets of materials to be deposited are held on a target carousel, which can accommodate up to 6 different targets. With a rotating axis of the target holder, a sequential shooting on the targets can be allowed during the growth. A plasma plume expands towards a substrate in front of the target. The substrate is fixed by a substrate holder, with a heater behind the substrate to control the substrate temperature.

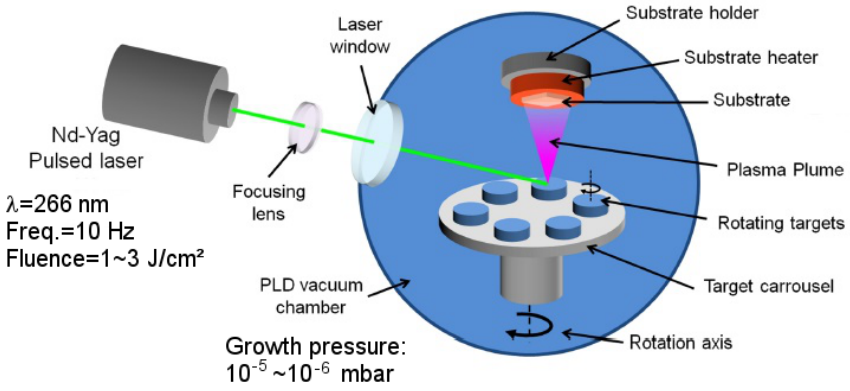

Figure 3.1: Sketch of the pulsed laser depostion set-up used to grow ferromagnetic nanowires embedded in $SrTiO_3$ epitaxial films.

The radiation source used was a quadrupled Nd-YAG laser with a wavelength of 266 nm, an operating rate of 10 Hz and a fluence in the 1-3 J.cm^{-2} range. Two PLD set-ups were used to obtain series of sample: (i) one set-up is under ultrahigh vacuum with a pressure of about 10^{-8} mbar during the growth (base pressure 2.10^{-10} mbar) and the samples were labelled as U-series; (ii) the second set-up is under secondary vacuum with a pressure of about 10^{-6} mbar during the growth, and the samples were labelled as S-series.

Before the growth, the surface of the targets is cleaned by a laser pre-ablation. Then, the $SrTiO_3$ substrate is introduced into the growth chamber to be heated up to around 650°C at the rate of 10°C/min and kept at 650°C during one hour for thermalization before the deposition.

Prior to the growth of self-assembled nanowires, a 4 nm thick pure $SrTiO_3$ layer was deposited on a $SrTiO_3$(001) substrate. Then the thin film containing vertically aligned nanowires of Ni or CoNi alloy in $SrTiO_3$ matrix was grown by shooting sequentially on NiO, CoO and $SrTiO_3$ targets, as shown in

Fig.3.2(a). The growth mechanism of nanowires and matrix is illustrated simply in Fig.3.2(b): after a deposition of 4 nm $SrTiO_3$, Ni atoms diffuse, nucleate and grow into clusters on the surface of $SrTiO_3$; further deposition of $SrTiO_3$ leads to partial burial of the clusters; re-deposition of Ni will lead to growth on the top of the clusters. In repetition of the sequential depositions, the nanowires are grown vertically embedded in the matrix as presented in Fig.3.2(c). The growth process can be understood as a combination of 2D growth of the oxide matrix and 3D growth of the metal as a consequence of the distinct surface energies of the materials.

The single sequence of shots to grow Ni nanowires in $SrTiO_3$ matrix can be written as $(n_1 \times \text{NiO} + n_2 \times \text{SrTiO}_3) \times \text{N}$, where n_1 is the number of shots on the NiO targets, n_2 the number of shots on the $SrTiO_3$ target and N the number of elementary sequences. For the growth of CoNi alloy nanowires, the shot ratio on the matrix target and metallic materials targets was kept constant. The sequence can be written as $((n_1 \times \text{CoO} + n_2 \times \text{SrTiO}_3) \times n_3 + (n_1 \times \text{NiO} + n_2 \times \text{SrTiO}_3) \times n_4) \times N$. In this case, the compositions of CoNi alloy nanowires can be adjusted by simply tuning the ratio of n_3/n_4. For a typical growth, the total shot number on $SrTiO_3$ target is about 20000 and a $SrTiO_3$ film of about 100 nm is obtained. This gives a growth rate of 0.005 nm of $SrTiO_3$ per shot. The amount of Co or Ni deposited per shot is around one third of that of $SrTiO_3$.

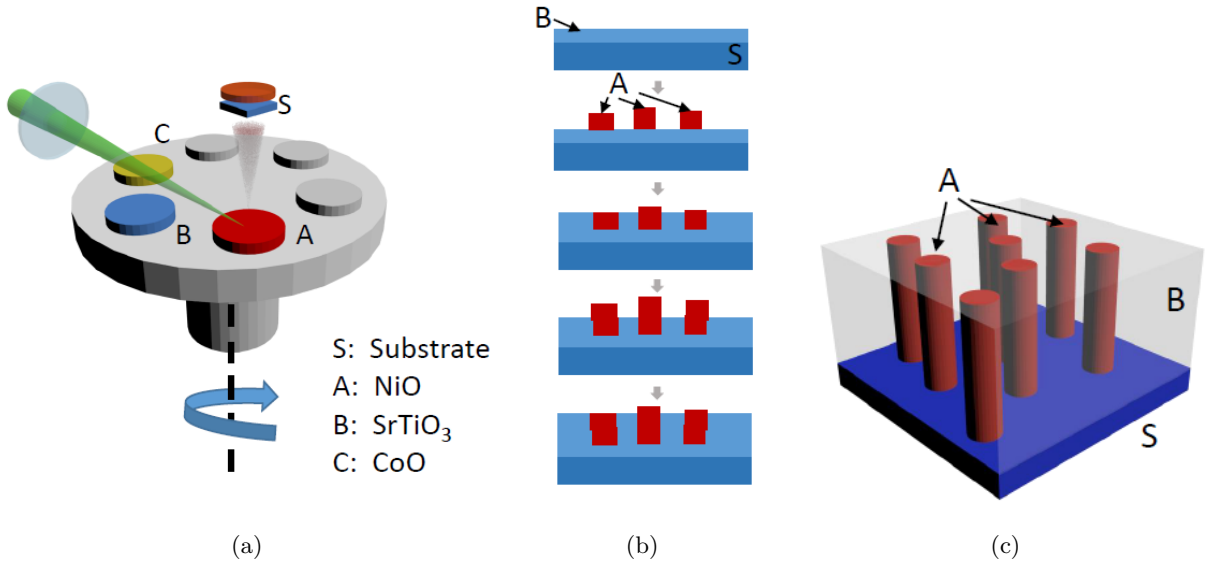

Figure 3.2: Sequential pulsed laser deposition. (a) Sketch of the target holder with A, B, C materials targets. (b) Illustration of the sequential growth of self-assembled wires of A in B matrix. (c) Final sample: vertically aligned nanowires of material A embedded in a matrix of material B.

In general, a 2-4 nm thick pure layer of $SrTiO_3$ or AlO_x was been deposited on the top of the film to avoid the oxidation of metallic nanowires. After the growth, the samples were cooled down to room temperature at a rate of 10 °C/min.

3.2 Control of the diameter of the nanowires

Many factors during the sequential deposition can have an influence on the nanowires features, particularly on the diameter and density. It should be paid attention to the fact that the substrate temperature, the vacuum and even the laser fluence have influences on the structural properties of nanowires. For example, a high substrate temperature increases the mobility of the diffusing adatoms. This results in the increase of the diameter and thus the reduction of the density. In our case, in order to explore the effect of the growth sequence, we keep the same conditions on the growth temperature T_g, the pressure P_g and the laser fluence F. In what follows, I show that varying the growth sequence gives a possibility to tune the diameter of the nanowires. This is examplified in the case of Ni nanowires in $SrTiO_3$, and the effect of the sequence on the diameter and density is assessed

by analyzing TEM plan views of the samples. The sequences used are defined as Ni(n_1):$SrTiO_3$(n_2), where n_1 is the shot number on NiO target and n_2 on $SrTiO_3$ target in one sequence.

Before presenting results showing that the diameter of the nanowires can be controlled by playing with the growth parameters, I give here some considerations on the growth mechanism of the embedded nanowires. One peculiar feature of the process used to obtain our samples is its sequential nature. During pulsed laser deposition, shooting on a target leads to a high supersaturation on the surface, with a high density of nucleus that will grow and coalesce. In our case, alternating the deposition of materials is achieved by rotating the target carousel. During this rotation, deposition is interrupted for several seconds. During this interval where no deposition occurs, the atoms can rearrange on the surface, until the next deposition step. The impact of this sequential character of the growth has been studied previously, using kinetic Monte-Carlo simulations, in the case of nanowires embedded in CeO_2 and in (Sr,Ba)TiO_3 by V. Schuler [81]. Simulations have also been performed in the case of $SrTiO_3$ matrix and compared to experimental results [82]. The simulations have highlighted the impact of the non-deposition time between two deposition events during the sequence, illustrated in 3.3. Because the time between shots is 0.1 second and the target alternating time is about 10 seconds, $2n$ shots instead of n shots only increases very slightly the duration of one sequence. As illustrated in Fig.3.3, when the time between two sequences is much longer than the relaxation time for the nucleation saturation on the surface, the final density does not change. It means that the density is independent of the shots on nanowire target. With the density constant, the increased number of shots on nanowire targets results in the increase of the diameter.

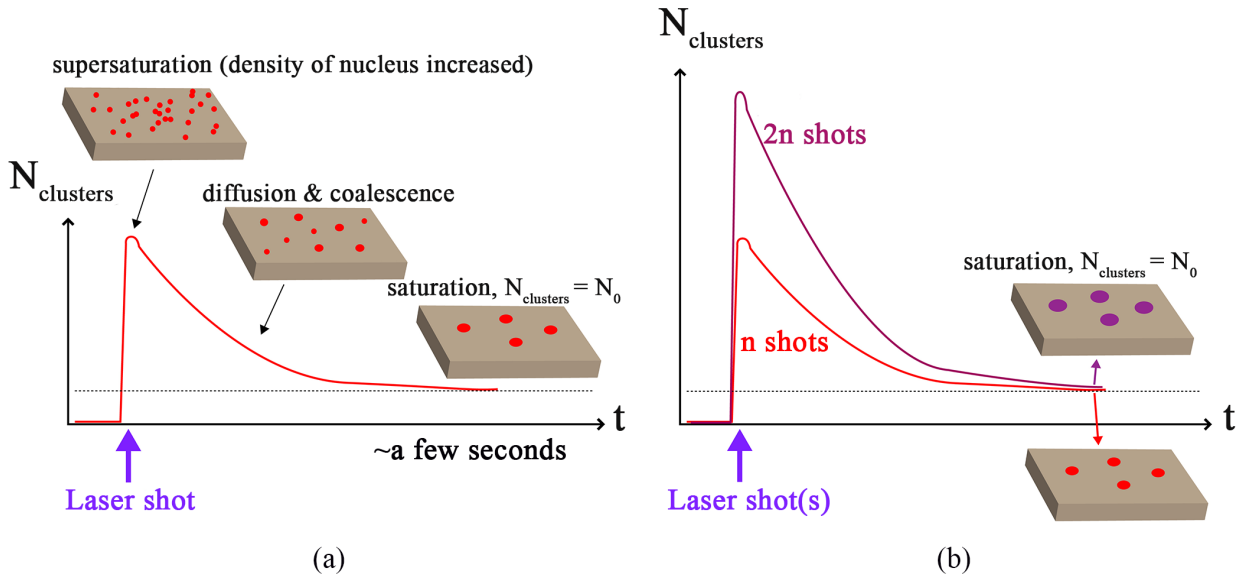

Figure 3.3: Cluster density evolution on the surface. (a) Clusters formed by the diffusion and nucleation after a laser shot. (b) Comparison of the cluster density evolution after n laser shots and $2n$ laser shots.

This increase of the diameter with constant density, illustrated in Fig. 3.3(b), is confirmed by TEM images in Fig.3.4 showing plan views of samples grown with the following sequences: Ni(2):$SrTiO_3$(12) and Ni(4):$SrTiO_3$(12). The surface density of nanowires is found to be nearly the same in these two samples. In contrast, it is obvious that the mean diameter is larger in the sample grown with the Ni(4):$SrTiO_3$(12) sequence. Thus, when the number of shots on nanowire target n_1 increases with that on matrix target n_2 kept constant, n_1/n_2 increases and the diameter is increased with an almost constant density.

Another way to control the diameter of the wires at fixed density is to vary n_2 with n_1 kept constant. Indeed, by keeping the shots on nanowire target n_1 constant, the increase of the shots on the matrix target n_2 gives a decrease of the diameter. This is illustrated in Fig.3.5 that shows TEM plan views of three samples with the same number of shots on NiO n_1=2, and n_2=12, 24 and 48. The

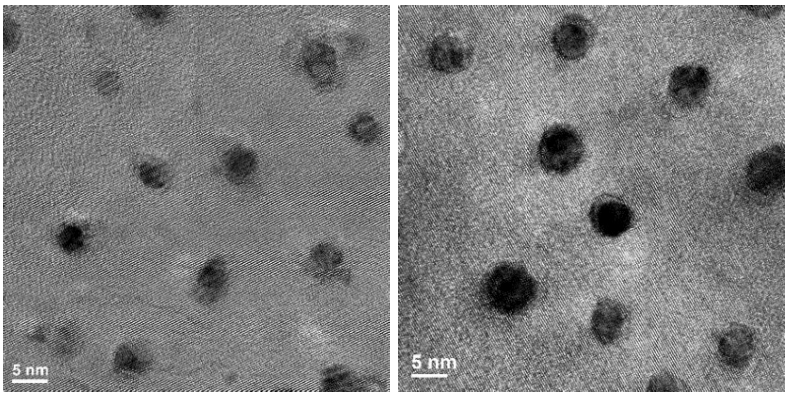

(a) Ni(2):$SrTiO_3$(12) (b) Ni(4):$SrTiO_3$(12)

Figure 3.4: TEM images of Ni nanowires in $SrTiO_3$ elaborated by different sequences: (a) Ni(2):$SrTiO_3$(12); (b) Ni(4):$SrTiO_3$(12). The shot number on matrix target n_2 is kept constant, while that on NiO target n_1 is doubled.

diameter decreases from around 5 nm to less than 2 nm. In contrast, the density of wires in these three samples is almost the same.

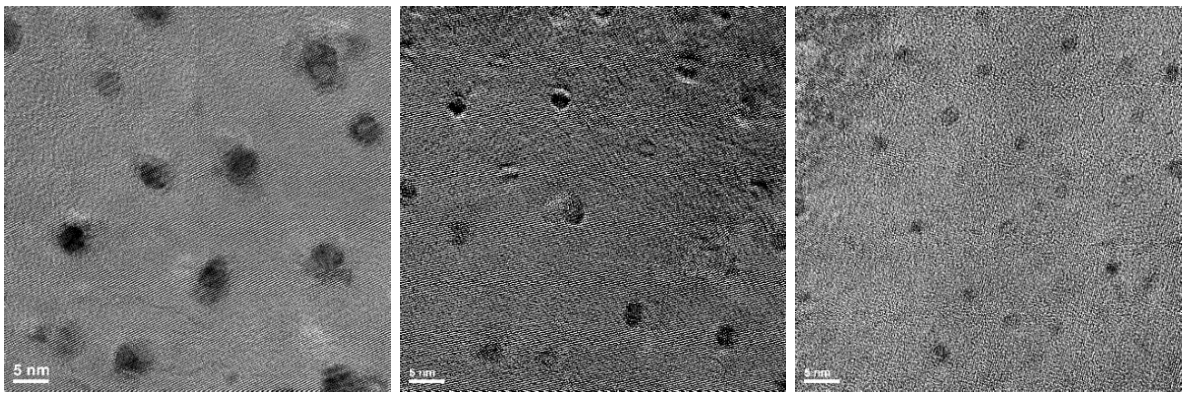

(a) Ni(2):$SrTiO_3$(12) (b) Ni(2):$SrTiO_3$(24) (c) Ni(2):$SrTiO_3$(48)

Figure 3.5: TEM images of Ni nanowires in $SrTiO_3$ elaborated by different sequences: (a) Ni(2):$SrTiO_3$(12); (b) Ni(2):$SrTiO_3$(24); (c) Ni(2):$SrTiO_3$(48). The shots on the NiO target n_1 are constant, while that on matrix target n_2 increases from 12 to 48. The shot ratio n_1/n_2 is thus reduced from 1/6 to 1/24.

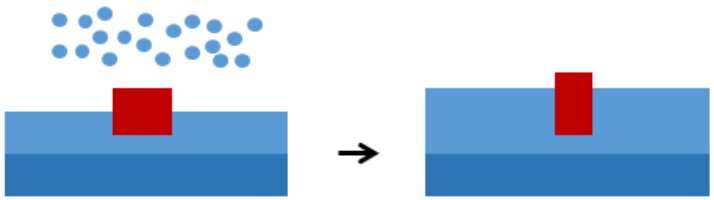

Figure 3.6: Schematic illustration of the heterointerface re-arrangement and vertical mobility leading to diameter reduction as n_2 is increased while n_1 is kept constant.

These results indicate that the supplemental deposition of matrix in a sequence (*i.e.* the increase in n_2) induces a vertical mobility of Ni atoms and a re-arrangement of the metal/oxide heterointerface. This vertical mobility, along the growth direction of the nanowires, contributes to the decrease of the diameter of the nanowires as illustrated schematically in Fig.3.6.

In considering all these observations, one suggests that when the saturation density has been

achieved, the diameter is influenced by the ratio of shots on the nanowire and matrix targets n_1/n_2. The diameter increases with the increase of n_1/n_2. The quantity of deposited material is proportional to the number of laser shots of the target. The areal density of Ni is proportional to $\pi d^2/4$ with d the diameter. Thus, $d^2 \propto n_1$: the diameter should scale as $\sqrt{n_1}$, as seen in Fig.3.4. Likewise, the mechanism (Fig.3.6) implies that the diameter should scale as $1/\sqrt{n_2}$ as demontrated in Fig.3.5. This suggests that the diameter of the wire should follow the following scaling law:

$$d \propto \sqrt{\frac{n_1}{n_2}}$$

Figure 3.7 shows that the diameter is indeed proportional to $\sqrt{n_1/n_2}$ for the series of samples considered in this chapter. By controlling the ratio n_1/n_2, the diameter of the obtained nanowires can be tuned in the 2-6 nm range.

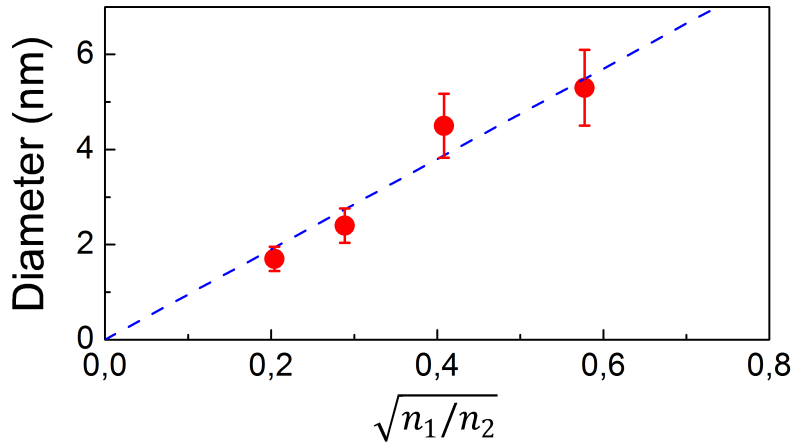

Figure 3.7: Mean diameter of the Ni nanowires in $SrTiO_3/SrTiO_3(001)$ as a function of $\sqrt{n_1/n_2}$ with n_1 (n_2) the number of laser shots on the NiO ($SrTiO_3$) target in a sequence. Sequence n_1/n_2 with increasing diameter: 2/48, 2/24, 2/12, 4/12.

3.3 Conclusions

- Ni/CoNi nanowires have been successfully embedded vertically in $SrTiO_3$ matrix by the alternating and sequential growth process.
- For the system of Ni/CoNi:$SrTiO_3$, the density of nanowires is almost constant for given T_g, P_g and F, due to the fact that the time between two sequences is much longer than the relaxation time.
- For given T_g, P_g and F, the diameter depends only on the ratio of laser shots on nanowire and matrix targets n_1/n_2: the diameter increases linearly with $\sqrt{n_1/n_2}$.

Therefore, by tuning the deposition sequence, the diameter of nanowires studied can be reduced to less than 2 nm, which is interesting for the study of the strain and then of the magnetic behavior of ultrathin nanowires.

Chapter 4

Structural properties of nanowires

In thin films, strain, which arises from the lattice mismatch at heterointerfaces, is a key parameter affecting the physical properties, such as ferroelectricity [83], magnetic anisotropy [84, 85] or superconductivity [86]. Recently, the synthesis of vertically assembled nanocomposites (VAN) has been proposed as a strategy in order to achieve a high strain in film with a good epitaxial quality. VANs are made of two phases that grow epitaxially with each other on a common substrate, resulting in nanowires (NWs) of a given material embedded in a matrix of another material. This, in principle, allows one to obtain large values of the axial strain in the embedded nanowires through epitaxial strain. In this chapter, I will discuss their structural properties of the vertical self-assembled Ni and Co_xNi_{1-x} alloy nanowires embedded in $SrTiO_3$ matrix on $SrTiO_3(001)$ substrate, using transmission electron microscopy (TEM), x-ray diffraction (XRD) and x-ray absorption spectroscopy (XAS).

4.1 General features of Ni nanowires

4.1.1 Diameter, density and chemical composition

Morphology and chemical composition of nanowires were explored by TEM, XAS and x-ray reflectivity. A selected series of eleven samples will be presented: U-1 to U-5 for the ultrahigh vacuum series and S-1 to S-6 for the secondary vacuum series. As shown previously, the diameter of the NWs can be controlled by the growth conditions. In the following, I will analyze the structural properties of samples with diameter in the 1.7-5.3 nm range.

Fig.4.1(a) shows a low resolution plan view TEM image of Ni NWs embedded in a $SrTiO_3$ matrix of sample U-4, unveiling a dense assembly of NWs. From the statistical analysis of several such TEM images, the diameter distribution of wires is extracted as shown in Fig.4.1(b). The mean value of the diameter $\langle D \rangle$ is 2.2 nm with a full width at half maximum of about 25% of the mean value. Such distribution of the diameter exists in every sample studied. The density of nanowires ρ can also be deduced by such plan view TEM images. From the self-correlation of such images, a line profile obtained can be used to extract the average distance between nearest neighbor wires as displayed in Fig.4.1(c). The first oscillation appears at 5 nm indicating the mean distance between wires for sample U-4.

Results of the measurements of $\langle D \rangle$ and ρ for the S-series and U-series are given in Tab.4.1. The thickness of the samples measured by x-ray reflectivity is from the order of 50 nm to about 200 nm, depending on the growth sequence repetition. The length of the NWs over the diameter is from 10 (sample S-6) up to above 50 (samples U-3, S-2, S-3). This ensures that the aspect of NWs is large.

From Tab.4.1, the density ρ is higher and the diameter $\langle D \rangle$ smaller for U-series samples compared to those for S-series ones. This can be explained by the different growth conditions. For example, lower substrate temperature for U-series offers less energy to the atomic diffusion, leading to an increase of the density and a decrease of the diameter.

In addition to the analysis of NW size and density, we scrutinized the chemical composition of the wires by performing STEM-HAADF imaging and EDX-mapping of Sr, Ti, O and Ni. Fig.4.1 (d-h) shows the distribution of these elements of sample S-2. Compared to Fig.4.1(d), Ni NWs can be easily identified in the Z-contrast image by Ni map as displayed in Fig.4.1(e). The location of Ni is also correlated with spots of high Ni-concentration. Fig.4.1(f-h) indicates that Ni NWs are surrounded by Sr, Ti, O. The quantitative analysis can be used to determine the matrix structure.

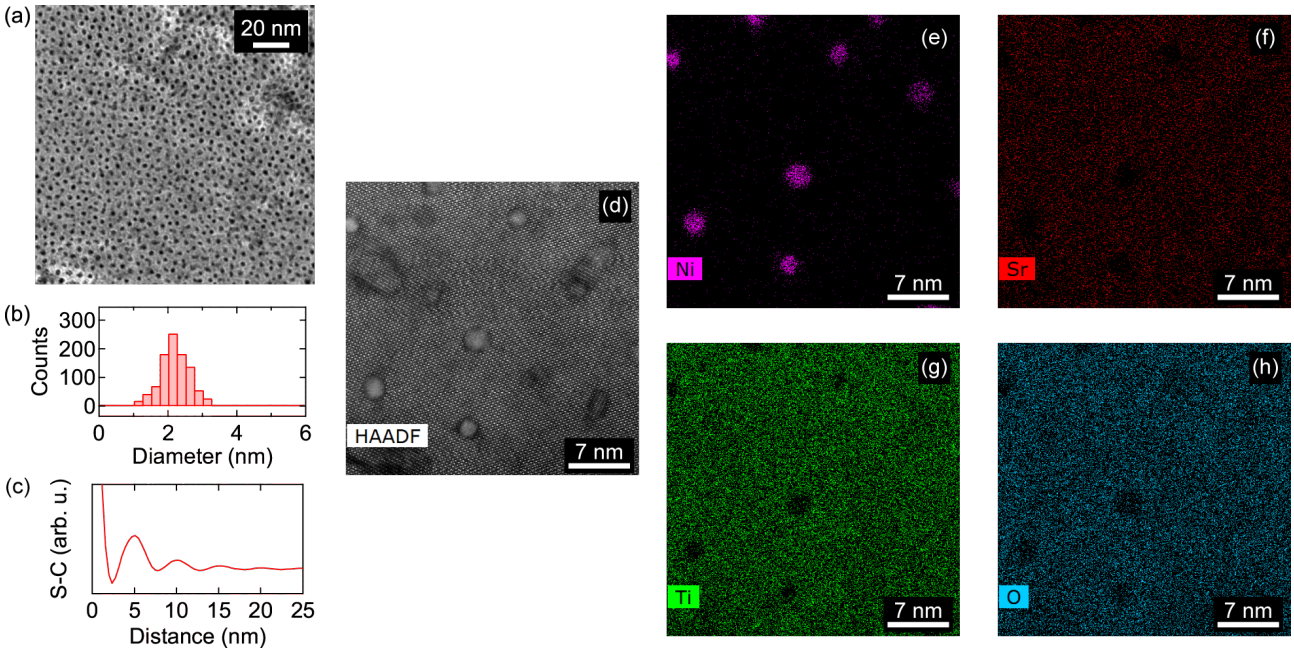

Figure 4.1: (a) Low resolution plan view TEM image of Ni nanowires embedded in a $SrTiO_3$ matrix (sample U-4). (b) Diameter distribution of Ni nanowires as extracted from TEM images such as the one displayed in (a). (c) Line profile obtained from the self-correlation of (a), with oscillations enabling to extract the mean distance between wires. (d) STEM-HAADF plan view of Ni nanowires (sample S-2). (e-h) Chemical maps obtained by EDX in the same region as the one in (d). (e) Ni map, (f) Sr map, (g) Ti map, and (h) O map.

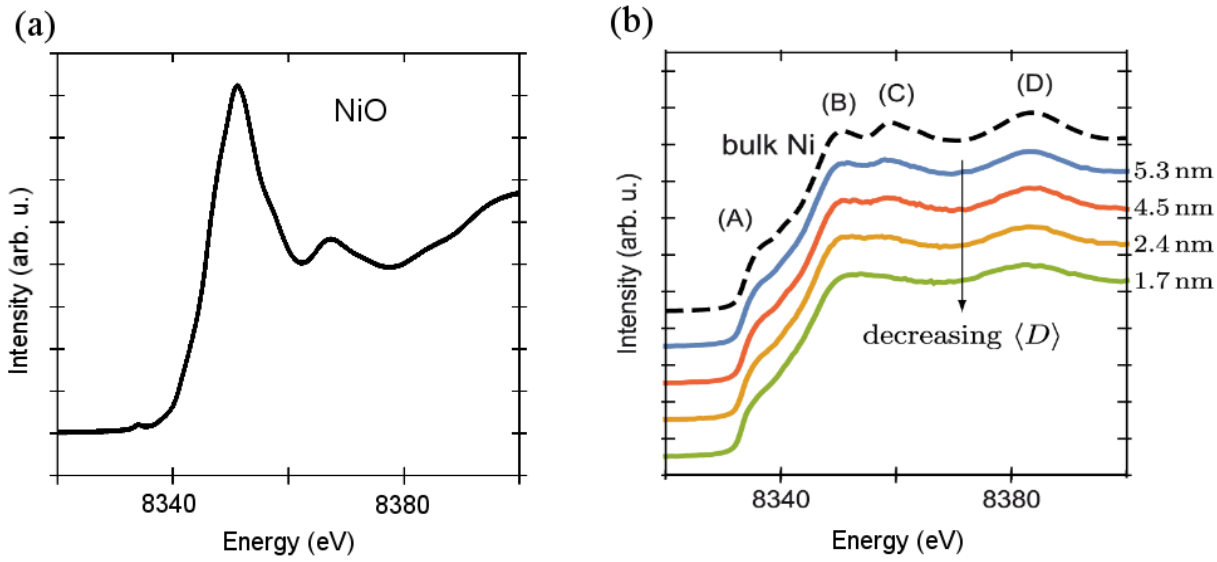

Figure 4.2: XANES spectra of (a) NiO as a reference; (b) Ni foil as a bulk Ni reference and metallic Ni nanowires with the diameter decreased from 5.3 to 1.7 nm.

Table 4.1: Structural parameters deduced from TEM and x-ray reflectivity analysis of the nanocomposites. $\langle D \rangle$: mean diameter of the NWs, ρ: in-plane density of the NWs, t: epilayer thickness.

Sample	$\langle D \rangle$ (nm)	ρ (cm^{-2})	t (nm)
U-1	1.7	3.0 10^{12}	–
U-2	1.8	4.5 10^{12}	62
U-3	1.9	5.8 10^{12}	125
U-4	2.2	4.4 10^{12}	59
U-5	2.5	3.9 10^{12}	77
S-1	1.7	7.8 10^{11}	–
S-2	2.4	5.9 10^{11}	139
S-3	4.1	1.8 10^{12}	231
S-4	4.5	4.2 10^{11}	74
S-5	5.0	5.1 10^{11}	106
S-6	5.3	4.1 10^{11}	51

For example, for the sample S-2, by analyzing the EDX signal, $c(\mathrm{Ni}) < 0.25\%$ is obtained. In contrast, we observe small, albeit non-negligible matrix component concentrations when analyzing single NWs. For example, $c(\mathrm{Ti}) = 6.7 \pm 2.7\,\mathrm{at\%}$, $c(\mathrm{Sr}) = 2.8 \pm 2.2\,\mathrm{at\%}$ and $c(\mathrm{O}) = 25.8 \pm 6.9\,\mathrm{at\%}$, is obtained when averaging over the NWs shown in Fig.4.1(d). We stress here that large relative errors result from the small volumes probed when restricting the analysis region to single ultrathin NW. Within measurement uncertainty, the aforementioned data are roughly compatible with $SrTiO_3$ stoichiometry. This is contrary to the Sr, Ti, O contributions from the EDX signal, which can be explained by the presence of the $SrTiO_3$ capping layer covering the thin film.

To complement these local spectroscopic data, x-ray absorption spectroscopy was carried out at the SAMBA beamline of SOLEIL synchrotron. Spectra were acquired in fluorescence mode at the Ni K-edge, probing the whole Ni content of the samples. The results, together with reference spectra for bulk Ni metal and NiO, are displayed in Fig.4.2. Comparison of the spectra obtained for Ni NWs with the reference spectra shows that Ni is metallic in the samples. Finer comparison with the spectrum of bulk Ni reveals a progressive flattening of the spectra with the decrease of the wire diameter. The characteristic peaks B, C and D become more and more blurred. The loss of XANES fine structure, resulting from a reduction of multiple scattering events, is an indication of the disorder or amorphous materials. This has been reported in various metallic systems, such as matrix-embedded Co and Ge nano-particles [87, 88] or sonochemically-prepared amorphous Fe [89].

To summarize these results, our structural and chemical analyses ensure the self-assembly of nanowires embedded in an oxide matrix with tunable $\langle D \rangle$ in the 1.7 - 5.3 nm range depending on the growth conditions, such as temperature, growth chamber pressure and laser fluence. This allows us to study the effect of diameter reduction on the epitaxy and structure of Ni nanowires embedded in $SrTiO_3$ matrix on $SrTiO_3(001)$ substrate, as it will be discussed in the following section.

4.1.2 Vertical epitaxy and mean strain

The schematics of a metal-oxide system is shown in Fig.4.3: vertically epitaxy of Ni nanowires in $SrTiO_3$ matrix, noted as Ni:$SrTiO_3$. In our case, the matrix and nanowires are grown on the surface of a $SrTiO_3$ substrate oriented [001] which has a perovskite structure of lattice parameter $a_{SrTiO_3} = 3.905$ Å at room temperature. This allows to obtain the cube-on-cube epitaxy of Ni NWs. In order to verify the quality of epitaxy and to determine the axial strain generated by the mismatch of lattice between the wires and the matrix, XRD measurements are performed on all samples.

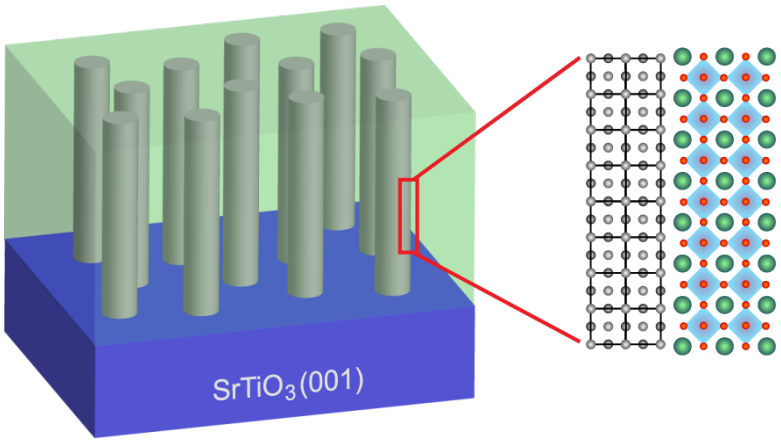

Figure 4.3: Schematics of vertically assembled epitaxial Ni nanowires embedded in a $SrTiO_3$ matrix, with crystallographic structure of Ni and $SrTiO_3$.

In this chapter, we use the reciprocal lattice units (r.l.u.) of $SrTiO_3$. For example, the 002 reflection of Ni is located at ℓ=2.216 r.l.u. ($d_{002}^{Ni} = \frac{a_{bulk}^{Ni}}{2} = \frac{a_{bulk}^{SrTiO_3}}{2.216}$, with a_{bulk}^{Ni}=3.524Å).

Before the exploration of the epitaxial properties of nanowires, firstly we are interested in the structural characters of a thin film of $SrTiO_3$ on $SrTiO_3$(001) grown under the same conditions of the nanowire growth. From the XRD θ-2θ scan in Fig.4.4, the 002 peak of $SrTiO_3$ is located at $\ell < 2$, indicating a significant vertical strain of $SrTiO_3$ film. The strain is related to the non-stoichiometry of $SrTiO_3$. This is a consequence of the growth under an oxygen free atmosphere. Quantitatively, the $SrTiO_3$ film is expanded by about 1.7% even without wires in it. It will enhance the vertical mismatch between wires and $SrTiO_3$ matrix.

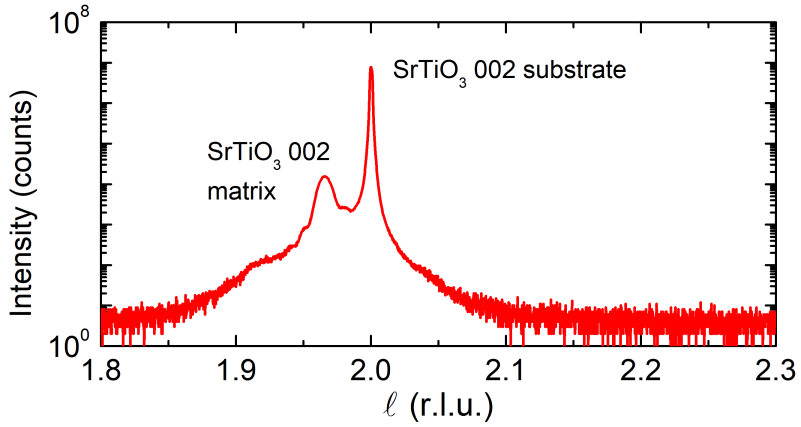

Figure 4.4: θ-2θ scan of a $SrTiO_3$ thin film grown on a $SrTiO_3$(001) substrate under ultra high vacuum.

Fig.4.5(a) shows a HRTEM image in plan view of sample U-4. By applying a Fast Fourier Transform (FFT) on such a image, the diffraction pattern obtained as displayed in Fig.4.5(b) indicates a cube-on-cube epitaxy of face-centered cubic (fcc) Ni in the $SrTiO_3$ matrix. The 200 and 020 spots of Ni, highlighted by red circles, are aligned with the 200 and 020 spots of the matrix. The cube-on-cube epitaxy is further confirmed by XRD θ-2θ scans out of plane in Figure 4.6(a), where the 002 peak of Ni is aligned with the 002 peak of matrix. The in-plane and out-of-plane alignment of cube-on-cube epitaxy are both verified. From the diffraction pattern of HRTEM plan views, it is found that the $SrTiO_3$ substrate and matrix are difficult to be distinguished, which indicates that the $SrTiO_3$ matrix is pseudomorphic with the substrate. It is also confirmed by the ϕ-$2\theta_\chi$ scan in Fig.4.6(b), where the 200 peaks of matrix and substrate are superposed.

A peculiar character of the Ni nanowires is their strain states. The average axial strain, noted

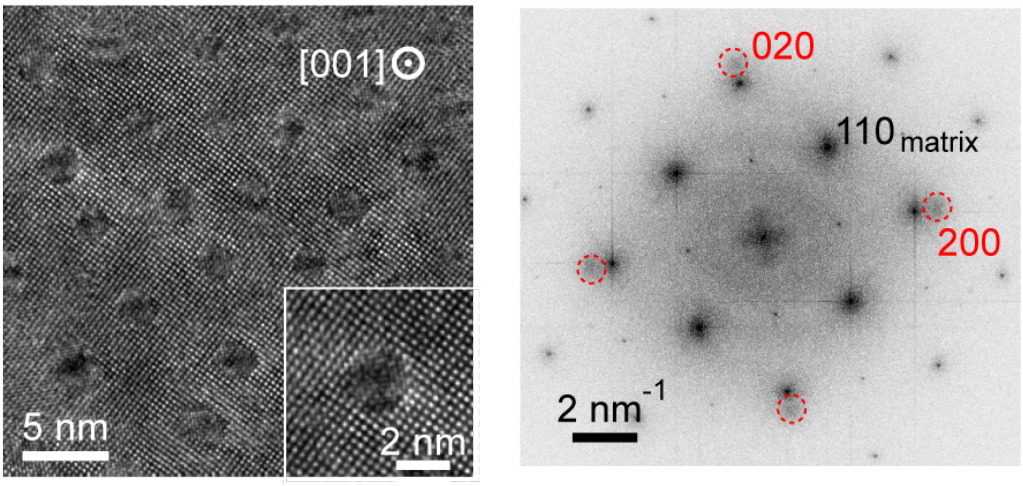

(a) (b)

Figure 4.5: (a) High resolution plan view TEM image of Ni nanowires embedded in a $SrTiO_3$ matrix (sample U-4); inset: zoom on a single nanowire. (b) FFT of image (a) indicating the epitaxy of Ni along $SrTiO_3$ matrix.

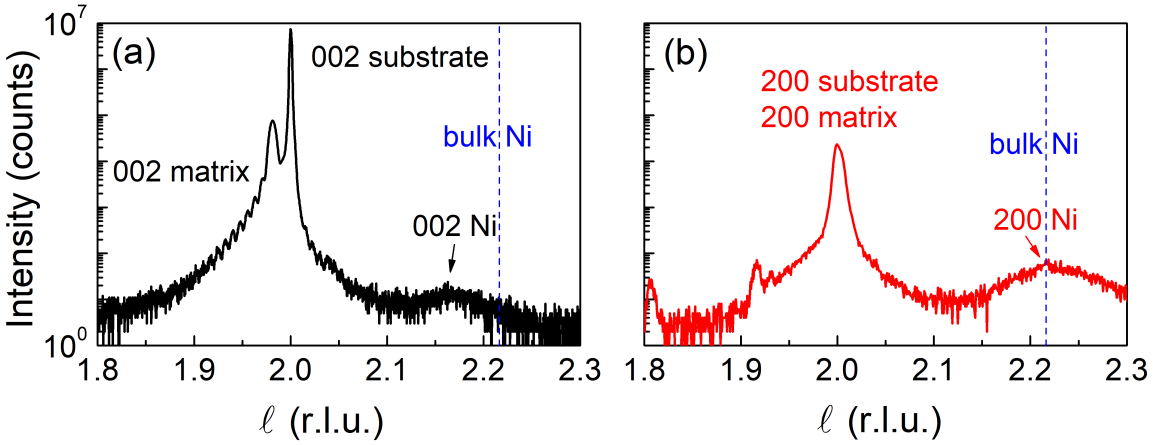

Figure 4.6: (a) Out-of-plane θ-2θ scan and (b) in-plane ϕ-$2\theta_\chi$ scan of sample S-6 by XRD. The abscissa is in $SrTiO_3$ reciprocal lattice unit (r.l.u.). The vertical dashed line indicates the position of the 002/200 peak for bulk Ni.

$\langle\epsilon_{zz}\rangle$, can be deduced by XRD θ-2θ scans. As shown in Fig.4.6(a), by comparing the value of ℓ of 002 peak position of strained Ni with the value of the relaxed bulk Ni, $\langle\epsilon_{zz}\rangle$ is determined in the order of several percents. The axial strain of all samples is listed in Tab.4.2 including the axial strain of the matrix. The strain of wires is a consequence of epitaxy due to the mismatch of lattice parameter between the wires and the matrix. For Ni and $SrTiO_3$, the mismatch ϵ_{mf} is about 11%. In order to tune the lattice planes, the wires are expended by several percents which results in an increase of the elastic energy. Furthermore, $\langle\epsilon_{zz}\rangle$ reflects the balance between the interface energy and the elastic energy. In a basic model, the interface energy depends on the area of interface between wires and matrix, which is proportional to the diameter. By removing the weak radial strain of nanowires (several parts per thousand deduced by the ϕ-$2\theta_\chi$ scan shown in Fig.4.6(b)), it can be written as:

$$E_{interface} = \gamma_s d(\epsilon_{zz} - \epsilon_{mf})^2 \tag{4.1}$$

The elastic energy is related to the volume of wires, hence proportional to the square of the diameter, which is written as:

$$E_{elastic} = \gamma_v d^2 \epsilon_{zz}^2 \tag{4.2}$$

The minimization of the total energy $E_{total} = E_{interface} + E_{elastic}$ gives an expression:

$$\epsilon_{zz} = \epsilon_{mf} \frac{1}{1 + \frac{\gamma_v}{\gamma_s} d} \tag{4.3}$$

This can explain the evolution of $\langle\epsilon_{zz}\rangle$ on the diameter as shown in Fig.4.7: $\langle\epsilon_{zz}\rangle$ decreases when the diameter increases. For our samples, the axial strain is increased from 2.3% up to 3.9% when the diameter decreases from 5.3 nm down to 1.9 nm (Tab.4.2). This provides a possibility to tailor the magnetic properties through the magneto-elastic anisotropy.

Table 4.2: Structural parameters deduced from TEM and XRD analysis of the nanocomposites. $\langle D\rangle$: mean diameter of the NWs, $\langle\epsilon_{zz}\rangle$: mean axial strain of the NWs, and $\langle\epsilon_{zz}^{matrix}\rangle$: mean axial strain of the matrix.

Sample	$\langle D\rangle$ (nm)	$\langle\epsilon_{zz}\rangle$ (%)	$\langle\epsilon_{zz}^{matrix}\rangle$ (%)
U-1	1.7	–	2.4
U-2	1.8	–	2.8
U-3	1.9	3.9	1.7
U-4	2.2	3.6	1.9
U-5	2.5	3.4	1.9
S-1	1.7	–	1.1
S-2	2.4	3.6	1.0
S-3	4.1	3.2	0.7
S-4	4.5	2.8	1.0
S-5	5.0	2.4	0.9
S-6	5.3	2.3	0.9

From Tab.4.2, it should be noticed that the axial strain of the matrix $\langle\epsilon_{zz}^{matrix}\rangle$ is larger for the U-series samples than that for the S-series one. This is due to the non-stoichiometry of the matrix under low oxygen pressure condition for the U-series than that for the S-series.

HRTEM plan views provide local information but do not allow to obtain statistical properties of the NW assembly. From the large width of the 002 Ni peak in XRD, one can suspect that the strain of NWs is not homogeneous along NW axis. To confirm this supposition, the HRTEM cross-sectional imaging was performed. As shown in Fig.4.8, nanowires are embedded in the matrix, but

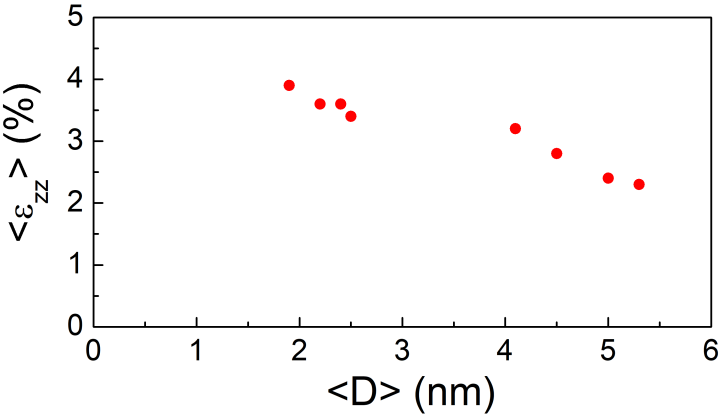

Figure 4.7: Evolution of the mean axial strains obtained by θ-2θ scans as a function of nanowire diameter.

the structure of wires is evidently not homogeneous along the growth direction. The Moiré pattern arising from multiple diffraction events in cross-sectional geometry is observed to vary when moving along the [001] direction. This reveals the existence of the inhomogeneity and the axial misorientation of the NWs. As shown in the inset of Fig.4.8, the selected area diffraction patterns, obtained by performing FFTs, evidence two different orientations of NWs. The upper one corresponds to a section of slightly misoriented wires with an angle α=4° of $[001]_{Ni}$ with respect to the [001] direction of the matrix; and the lower one shows a section of wire aligned with the [001] direction of the matrix. The length of the misoriented section is about 10-20 nm. Furthermore, the FFT of the total TEM image shows reflections of Ni nanowires highlighted by red arrows in Fig.4.8(b). As the total FFT is the superposition of the aligned and tilted sections, it evidences that the major sections are aligned with the matrix. However, the sections are not homogeneous along the wire axis. Thus, it is remarked that the epitaxial relationship is not as simple as initially deduced from symmetrical θ-2θ scans. Indeed, given the large width of the Ni 002 peak in θ-2θ scans, such an inhomogeneity is not surprising.

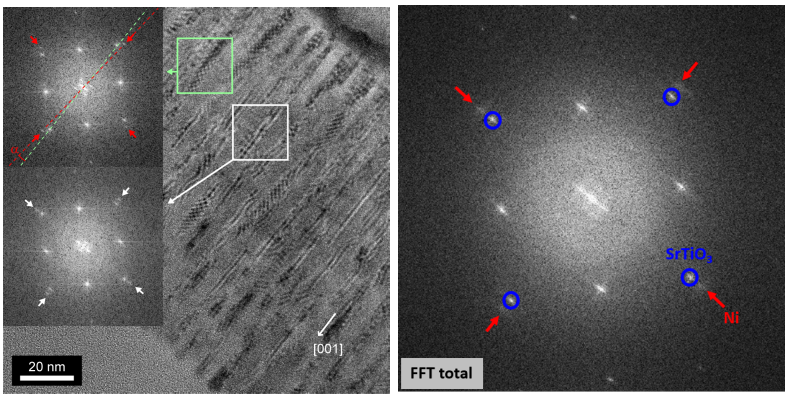

(a) (b)

Figure 4.8: (a) Cross section TEM image of Ni nanowires in $SrTiO_3$ matrix (sample S-3); insets: FFT of selected areas delimited by light squares. The inset at top evidences the local misorientation α of the Ni lattice with respect to the $SrTiO_3$ lattice. (b) FFT of the total area of TEM image of (a). The reflection of Ni wires are lighted by red arrows.

4.2 Reciprocal space mapping and simulation

As the epitaxial strain is complex, we continued the study using high resolution diffraction experiments conducted at the SixS beamline of sychrotron SOLEIL. In this section, the experimental

results will be analyzed and modelled by simulations. The strain state and the mechanism of strain relaxation will be discussed [90].

4.2.1 Characterization of the inhomogeneous structure

In order to characterize the inhomogeneous structure of the highly strained Ni nanowires, extensive reciprocal space mappings (RSMs) were performed using synchrotron x-ray diffraction. These measurements indicate the composite nature of the diffraction peaks related to Ni. For example, Fig.4.9(a) shows a sketch of Ni 002 reflection for sample S-3 deduced by the measurements: around the central peak at l=2.15 and h=k=0, 4 tilted spots at ℓ=2.18(5) and h=$\pm h_s$ with k=0 or k=$\pm h_s$ with h=0, where h_s=0.1575, are observed. This is demonstrated by slices of the reciprocal space shown in Fig.4.9(b) and (c). We stress that the 4 spots that deviated from the ℓ axis can not be detected by $\theta - 2\theta$ scans. The misorientation angle can be deduced by their position. For example, in $h\ell$ plane, misorientation angle α is deduced by $\tan\alpha = h/\ell$ and it can be simplified as $\alpha = h/\ell$ in the case of small α. Besides, the axial strain can be determined by $\epsilon_{zz} = d^{Ni}/d^{Ni}_{bulk} - 1 = \ell^{Ni}_{bulk}/\ell - 1$, where ℓ^{Ni}_{bulk}=2.216 r.l.u. These four tilted spots are thus associated to domains misoriented by about 4.15° and are observed along [100] and [010] with an axial strain of about 1.4%. Two spots along [010] are symmetric in size and intensity as displayed in Fig.4.9(d). On the contrary, along [100] direction (Fig.4.10(a)), the reciprocal space shows a difference in intensity due to the variation of the x-rays incidence angle during the data acquisition. Around 002 reflection, the inter-reticular distance d is given by $d_{002} = a_{SrTiO_3}/\ell$. For the spots located at ℓ=2.18(5), d_{002}=1.79 Å. According to the Bragg's law, $2d\sin\theta_B = \lambda$, the incidence angle θ_B is thus deduced to 10.85°. As we know, these four additional spots are associated by domains tilted by α=4.15° with respect to the matrix [001] direction. The incidence angles ω are therefore $\theta_B \pm \alpha$. With the irradiation volume proportional to $1/\sin\omega$, the intensity ratio of the spots located at $-h_s$ and at $+h_s$ can be written as:

$$\frac{I_{-h_s}}{I_{+h_s}} = \frac{\sin(\theta_B - \alpha)}{sin(\theta_B + \alpha)} \tag{4.4}$$

With θ_B=10.85° and α=4.15°, the intensity ratio due to the incidence angle was estimated ${I_{-h_s}/I_{+h_s}}^{calc}$ =0.45. The experimental results shown in Fig.4.10(b), a profile of diffraction intensity along h, indicate that ${I_{-h_s}/I_{+h_s}}^{exp}$=0.45. This evidences that the intensity difference on a certain ℓ plane is only caused by the incidence angle variation during the diffraction. Hence, by taking the incidence effect into consideration, these four tilted spots have the same intensity and the system is considered as a four-fold symmetrical system.

The width of the spots can be determined by fitting line profiles as shown in Fig.4.11. Fig.4.11(a) presents a profile along k with h=0 and ℓ=2.18(5) plane. The width of the symmetric spots at k=±0.1575 is about 0.1115. It gives a radial coherent length of 3.5 nm. This value is quite close to the mean value of the diameter of the NWs in this sample, $\langle D\rangle$=4.1 nm. The situation along ℓ is quite different. In Fig.4.11(b), a profile along ℓ of a tilted spot at k=-0.1575 with h=0, the width is 0.0311, corresponding to an axial coherent length L^{tilted}_{coh} of about 12.6 nm. This is significantly smaller than the physical length of the NWs (t=231 nm, see Tab.4.1) and should indeed be comparable to the typical length observed for the Moiré patterns axial variation in Fig.4.8, of the order of 10-20 nm. According to Fig.4.9(d), the central spot at h=k=0 is much broader both along ℓ and h or k. ℓ profile gives a coherent length $L^{aligned}_{coh}$=6 nm. By the line profiles, the intensity and the size of each spot are obtained as shown in Tab.4.3. With the intensity corrected by the incidence effect (Eq.4.4), the four tilted spots are identical in intensity and size. Each of these four spots occupies ∼10% and the central one ∼60%. This indicates that more than half of the domains are aligned with the matrix. It is consistent with the FFT pattern of cross section TEM images in Fig.4.8: majority of NWs sections are crystallographically aligned with the matrix.

Fig.4.12 shows cuts of the reciprocal space around the 202 Ni reflection. The composite structure is better seen than in 002 RSM. The non-homogeneity of central spot can be clearly observed from the $h\ell$ cut of the reciprocal space at k=0 in Fig.4.12(a). This spot is composed of an elliptical spot

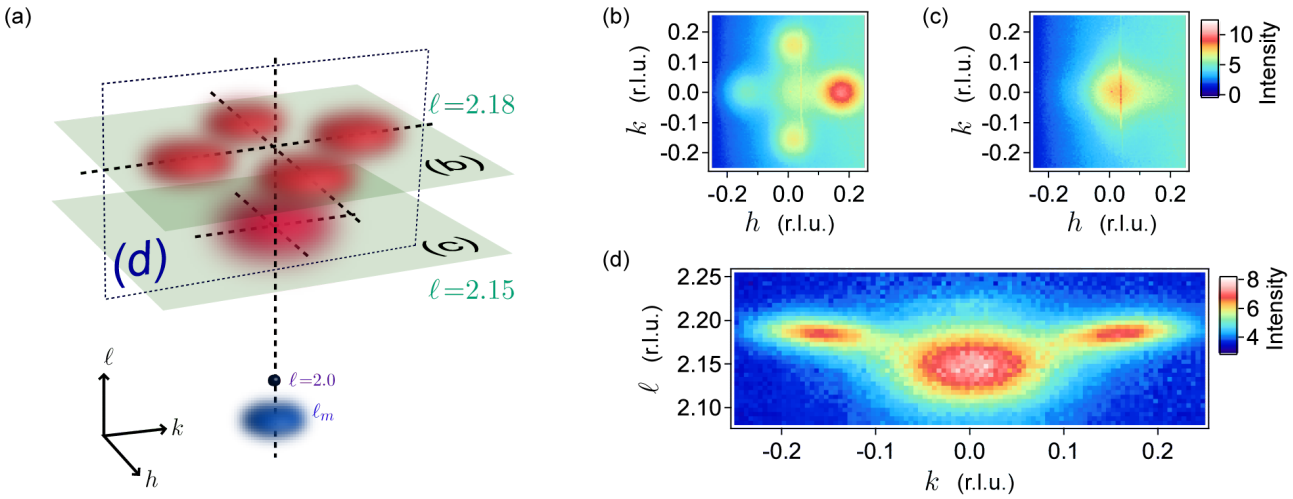

Figure 4.9: Reciprocal space mappings of sample S-3. (a) Sketch of the diffraction diagram in the reciprocal space of the 002 reflections. The reflection of $SrTiO_3$ substrate is located at ℓ=2.0. ℓ_m is the position of the $SrTiO_3$ matrix reflection. The 002 reflection of Ni is complex: a spot at h=k=0, ℓ=2.15 and four spots in the plane of ℓ=2.18(5), at h=±0.1575 and k=±0.1575. Planes labeled (b,c,d) correspond to the cuts of the reciprocal space shown in (b,c,d) figures on the right. (b) Cut of reciprocal space at ℓ=2.18(5) plane. (c) Cut of reciprocal space at ℓ=2.15 plane. (d) cut of reciprocal space of h=0 plane.

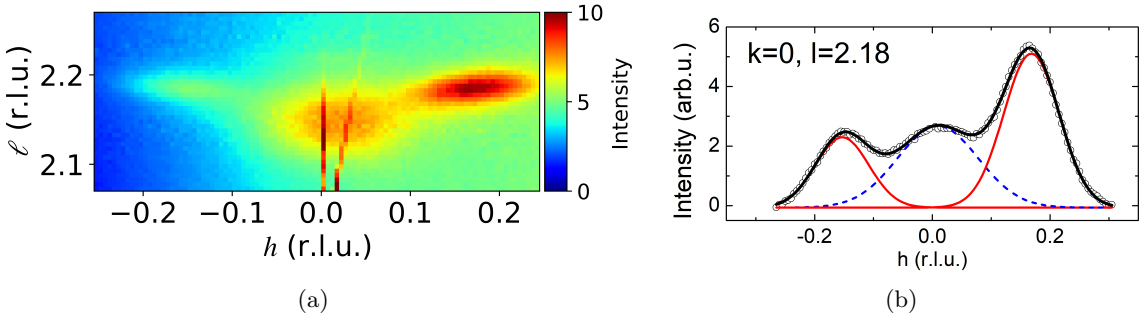

Figure 4.10: (a) Cut of reciprocal space of k=0 plane. (b) Profile of diffraction intensity along h for k=0, ℓ=2.18(5).

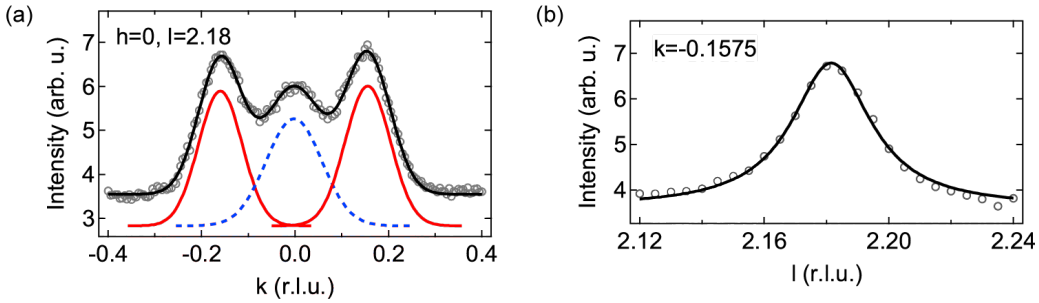

Figure 4.11: (a) Profile of diffracted intensity along k for h=0, ℓ=2.18(5), obtained from data in Fig.4.9(b). (b) Profile of diffracted intensity along ℓ for h=0 and k=-0.1575, obtained from data in Figure 4.9(d).

Table 4.3: Intensity and width of 5 spots detected around 002 Ni reflection. Δh, Δk, $\Delta \ell$ are FWHM of the spots, and proportion represents the percentage of each spot, calculated by $\text{Int}_{cor} \times \Delta h \times \Delta k \times \Delta \ell / \text{Int}_{total}$, where Int_{cor} is the corrected intensity for two spots situated at $h = \pm h_s$ with $h_s = 0.1575$ r.l.u. Int_{total} is the total integrated intensity.

Spot position (h k l)	Int (Int_{cor}) (counts)	Δh (r.l.u.)	Δk (r.l.u.)	$\Delta \ell$ (r.l.u.)	Proportion
(0 0 2.15)	3.543	0.190	0.184	0.072	62.9%
($-h_s$ 0 2.18)	2.229 (3.063)	0.106	0.113	0.035	9.0%
($+h_s$ 0 2.18)	4.955 (3.071)	0.111	0.109	0.036	9.4%
(0 $-h_s$ 2.18)	3.051	0.112	0.110	0.035	9.3%
(0 $+h_s$ 2.18)	3.097	0.114	0.114	0.033	9.4%

with a long axis oriented at 45° and of a smaller, more symmetric and less oriented spot. The four additional spots observed around 002 Ni reflection can be identified in the 202 Ni reflection. Two spots centered at h=2.05, ℓ=2.37 and h=2.39, ℓ=2.00(5) at k=0 plane correspond to the two spots along h shown in Fig.4.9(b). Two symmetrical spots centered at k=±0.1575, ℓ=2.18 at h=2.225 plane, as shown in Fig.4.12(b), correspond to the two spots symmetrically located along k in Fig.4.9(d). These four additional spots, associated to the tilted NW domains of the four orientation directions, can be found in every Ni reflection. This is schematized in Fig.4.12(c), the orientation angle α is the angle of $[001]_{Ni}$ direction with respect to the [001] direction of the $SrTiO_3$ matrix. From the position of spots in reciprocal space, the misorientation angle α and the strains ϵ_{xx}, ϵ_{zz}, ϵ_{xz} can be determined.

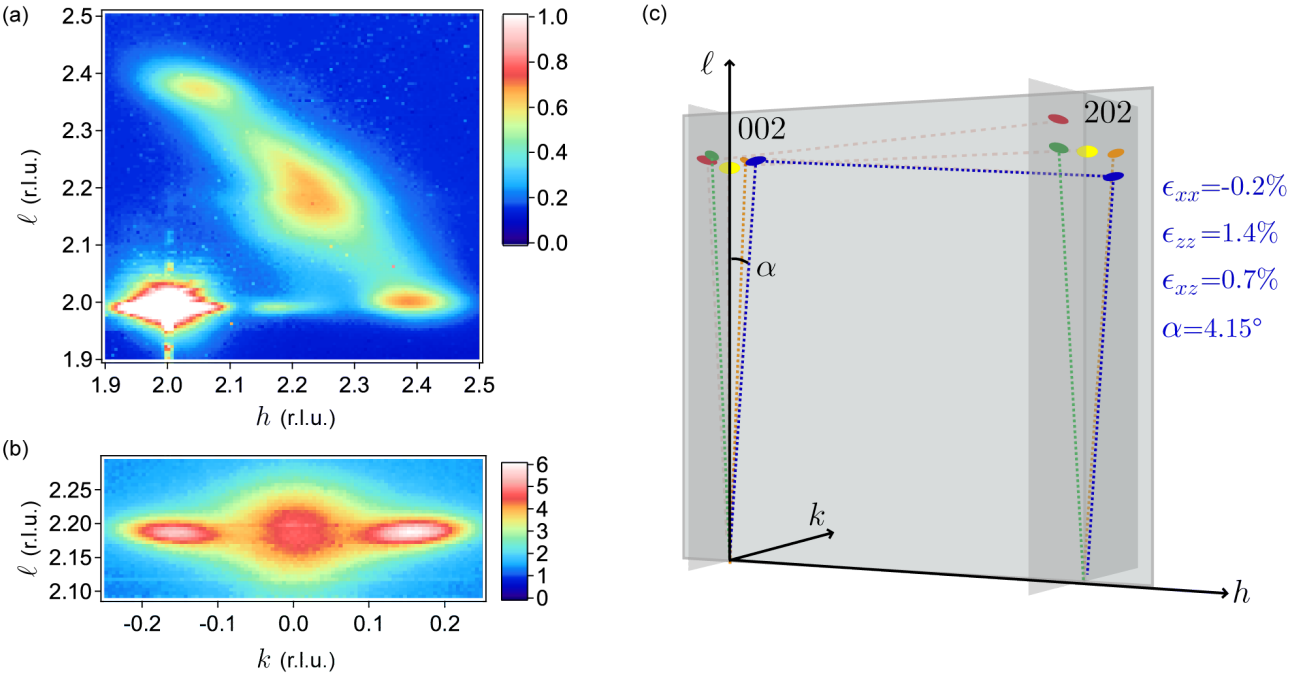

Figure 4.12: RSM of sample S-3. (a) $h\ell$ cut of the reciprocal space around the 202 Ni reflection at k=0. (b) $k\ell$ cut of the reciprocal space around the 202 Ni reflection, at h=2.225. (c) Schematic representation of the reciprocal lattice space with 002 and 202 Ni reflections associated to the different domains of Ni nanowires. The values of the orientation angle α and of ϵ_{ij} are noted in dark blue on the sketch.

The composite central spot is associated with diffraction of highly strained domains with $\langle\epsilon_{zz}\rangle$=3.2%, $\langle\epsilon_{xx}\rangle$=-0.4% and $\langle\epsilon_{xz}\rangle$=0. Among these domains, two families can be distinguished to compose the composite central spot. The first one corresponds to the well-aligned domains, with α=0, which are

highly strained. The second one is associated to the domains oriented by angle from -α to α around [100] and [010] directions, which results in these four equivalent additional spots and a part of the central spot in diffraction. From the peak position, the strain can be determined. These domains are partially relaxed compared to the aligned one and slightly sheared, with $\langle\epsilon_{zz}\rangle$=1.4%, $\langle\epsilon_{xx}\rangle$=-0.2%, $\langle\epsilon_{xz}\rangle$=-0.7% and α=4.15°.

As each domain corresponds to a flat spot in reciprocal space, the inclination directions of additional spots versus [100] or [010] directions can be considered as a composite of multi-domains with a strain related to the misorientation. The radial and axial coherent lengths will be larger than the values estimated by the line profiles before. Here I introduce at first a simple mosaic block model to interpret a distribution of misoriented domains. The shape of diffraction spot is considered to be determined by the mosaic spread of domains and their lateral coherent length as illustrated in Fig.4.13. More preciously, the shape is the result of the convolution of the mosaic spread and the lateral correlation. We notice that the mosaic effect tilts the spots only clockwise for the positive quarter of the reciprocal space ($h > 0$ and $\ell > 0$ in Fig.4.13).

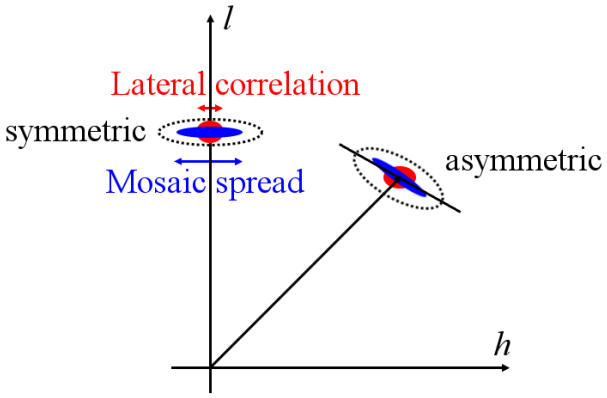

Figure 4.13: Schematic diagram of two reflections in reciprocal space in a mosaic block model.

However, in our case, at $h\ell$ cut around 002 Ni reflection, the additional spots at $h = h_s$ are rotated anticlockwise by about 4-5° (Fig.4.10(a)). Around 202 reflection, the orientation of two additional spots in the $h\ell$ plane is quite different to each one as shown in Fig.4.12(a). The upper spot associated to α_0 tilted domains is oriented clockwise by about 17° and the lower one corresponding to $-\alpha_0$ tilted domains is almost horizontal. Such big differences can not be related to a simple mosaic spread. As a consequence, the strain and orientation seem to be coupled in a complex way. I will thoroughly analyze the correlation between the strain and the orientation by the simulation in the Section 4.2.2.

In addition to the 002 and 202 Ni reflections, these four tilted spots can also be found at 111 Ni reflection as shown in Fig.4.14. The slice at ℓ=1 shows two spots below the central spot at ℓ=1.11(5). The slice at ℓ=1.18(5) shows two spots above the central one. This result corresponds well to the complex Ni structure. Two upper spots are associated to the red and green ellipses in the schematic representation of reciprocal space in Fig.4.12(c); two lower spots are linked to the dark blue and orange ones. Attention should be paid to the fact that around both 202 and 111 Ni reflection, intensity of the upper spot(s) is smaller than that of the lower spot(s). In consideration of the strain relaxation with misorientation, the distribution of the strain can be dilated at large ℓ and be compressed at small ℓ. The spot is the superposition of the diffracted spots associated to each domain. With a dilated distribution, the size of spot expands and the intensity decreases. On the contrary, with a compressive distribution, the size compresses and the intensity increases. Therefore, the upper spot is less intense than the lower one.

Fig.4.15 shows the RSMs of sample S-3 around 200, 400 and 113 Ni reflections. In-plane diffraction at grazing incidence and emergence, only one additional tilted spot is detected in the $h\ell$ cut around 200 and 400 reflection. The radial strain of the central spot ϵ_{xx} is estimated at about -0.4% (the negative sign represents a radial compression of NWs). The tilted spot indicates a misorientation by about 4°

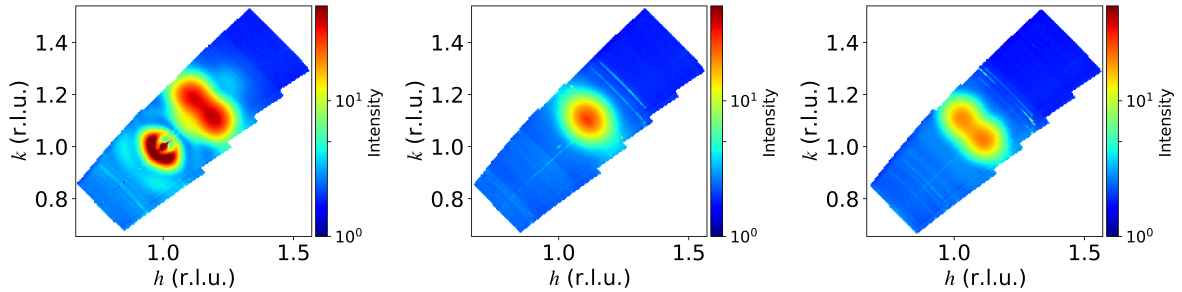

(a) ℓ=1 (b) ℓ=1.11(5) (c) ℓ=1.18(5)

Figure 4.14: RSM of sample S-3 around 111 Ni reflection: (a) slice at ℓ=1; (b) slice at ℓ=1.11(5); (c) slice at ℓ=1.18(5).

with a relaxation of -0.2%. Furthermore, around 113 Ni reflection in Fig.4.15(c), two additional tilted spots are detected from the $h\ell$ cut of reciprocal space at k=1.11 r.l.u. This evidences the existence of the tilted domains in NWs.

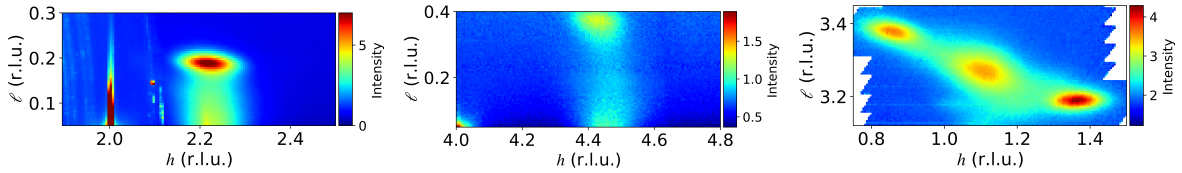

(a) RSM 200 (b) RSM 400 (c) RSM 113

Figure 4.15: RSMs of sample S-3 around (a) 200 Ni reflection, $h\ell$ cut at k=0; (b) 400 Ni reflection, $h\ell$ cut at k=0; (c) 113 Ni reflection, $h\ell$ cut at k=1.11.

The deduced structure for the NWs, with domains having distinct orientations, is consistent with cross-sectional imaging by TEM. The value of the inclination angle α matches well with the one deduced from the Moiré analysis. ϵ_{ij} values indicate that the strain state is peculiar within the Ni domains. The $|\epsilon_{xx}/\epsilon_{zz}|$ ratio falls well below the Poisson ratio of bulk Ni (ν=0.31), indicating a large expansion of the unit cell volume. This reflects a consequence of the constraints imposed by vertical epitaxy.

4.2.2 Simulation of the reciprocal space mappings

In order to deepen the analysis of the RSMs, I performed calculations in the framework of the kinematical theory of x-ray diffraction in taking into account the coherent lengths, the strain and the misorientation. To simplify the calculation, the simulations were performed in 2D instead of 3D in considering specific $h0\ell$ RSMs involving only x and z components of the atomic displacements.

According to the result analysis of the reciprocal space mapping around Ni 002 and 202 reflection, there are two families of domains formed during the growth of nanowires. As shown in Fig.4.16, these two families are highlighted by the orange ellipses and the black ellipse at 002 and 202 Ni reflection. The orange ellipses correspond to the domains oriented by an angle from -α to α, with a distribution of orientation centered at $\alpha = \pm 4.15°$ and 0°, respectively for the two tilted spots and a component of the central spot. The black ellipse corresponds to the highly strained but aligned domains, with an axial coherent length smaller than the tilted domains.

I start the simulation of the RSMs with the measured parameters. Fig.4.17 sketches the atomic structure of Ni nanowire. The black points represent the positions of bulk fcc Ni, called original state, shown in Fig.4.17(a). The domains are divided into two families, the highly strained but aligned domains and the tilted domains. The aligned ones are shown in Fig.4.17(b). The blue crosses represent the atomic positions under a large axial strain $\langle\epsilon_{zz}\rangle$ of 3.2% and a small in-plane strain

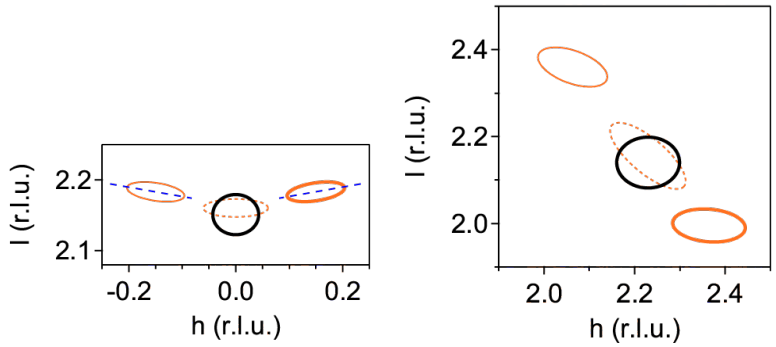

(a) RSM 002 (b) RSM 202

Figure 4.16: Schematics of $h0\ell$ map of the reciprocal space around (a) 002 and (b) 202 Ni reflections. The line thickness represents the intensity. Two families of spots are distinguished by the line color.

$\langle\epsilon_{xx}\rangle$ of -0.4%. Compared to the original state (black points), the vertical atomic distance is obviously dilated. A section of the tilted domains is shown in Fig.4.17(c), where the red squares describe the atomic positions after a misorientation of 4.15° with strains of $\langle\epsilon_{zz}\rangle$ = 1.4%, $\langle\epsilon_{xx}\rangle$ = -0.2% and $\langle\epsilon_{xz}\rangle$=-0.7%. For calculations of the RSMs, the width of domains is 4 nm. The coherent length is different for two types of domains. The L_{coh} given by ℓ profile of the tilted spots around 002 Ni reflection is at least of 12.6 nm. For the calculation, I chose 14 nm, noted L_{coh}^{tilted}. On the other side, as the schematics of $h0\ell$ maps in Fig.4.16, the central spot is the superposition of a contribution of tilted domains family at α=0 and a broad spot associated to highly strained aligned domains. Therefore, the coherent length for the aligned domains $L_{coh}^{aligned}$ is 6 nm for the calculation.

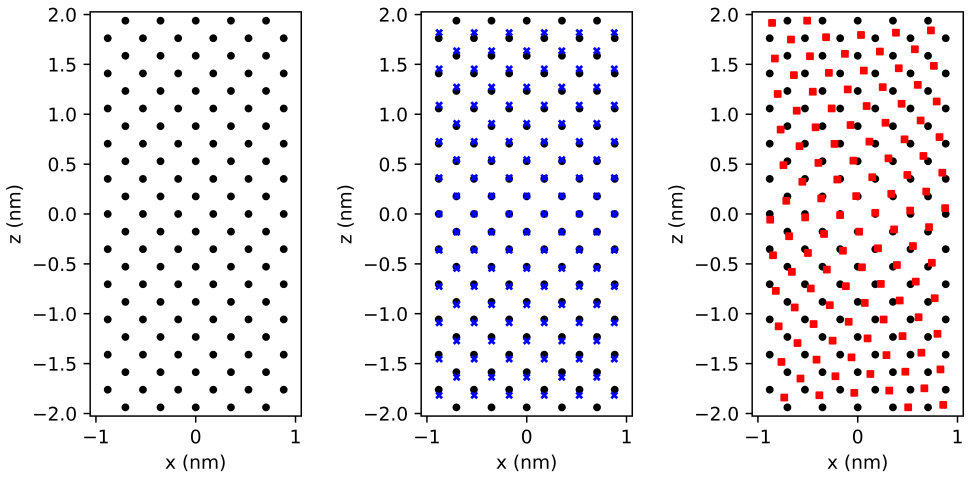

(a) (b) (c)

Figure 4.17: Sketch of Ni atomic structure. (a) Bulk fcc Ni (black point). (b) Highly strained and aligned Ni (blue cross), with $\langle\epsilon_{zz}\rangle$=3.2%, $\langle\epsilon_{xx}\rangle$=-0.4% and $\langle\epsilon_{xz}\rangle$=0. (c) Oriented and partially relaxed Ni (red square), with $\langle\epsilon_{zz}\rangle$=1.4%, $\langle\epsilon_{xx}\rangle$=-0.2%, $\langle\epsilon_{xz}\rangle$=-0.7% and α=4.15°.

By taking the square modulus of the Fourier transform of the atomic positions, the calculated RSMs at 002 and 202 Ni reflections are shown in Fig.4.18 for the three cases described in Fig.4.17. The diffraction spot of the bulk Ni is located at ℓ=2.216 in Fig.4.18(a) and (d), with $\langle D\rangle$=4 nm, L_{coh}=14 nm. The diffraction spot of aligned domain under a large strain of 3.2% is centered at ℓ=2.15 in Fig.4.18(b) and (e). It is much thicker than spot of bulk Ni domain due to the smaller L_{cor} of 6 nm. Fig.4.18(c) and (f) are associated to the tilted domains details in Fig.4.17(c), with L_{coh}=L_{coh}^{tilted}=14nm. The spots around 002 and 202 reflections are located at h=0.16, ℓ=2.185 and h=2.05, ℓ=2.37 respectively, corresponding to the experimental RSMs.

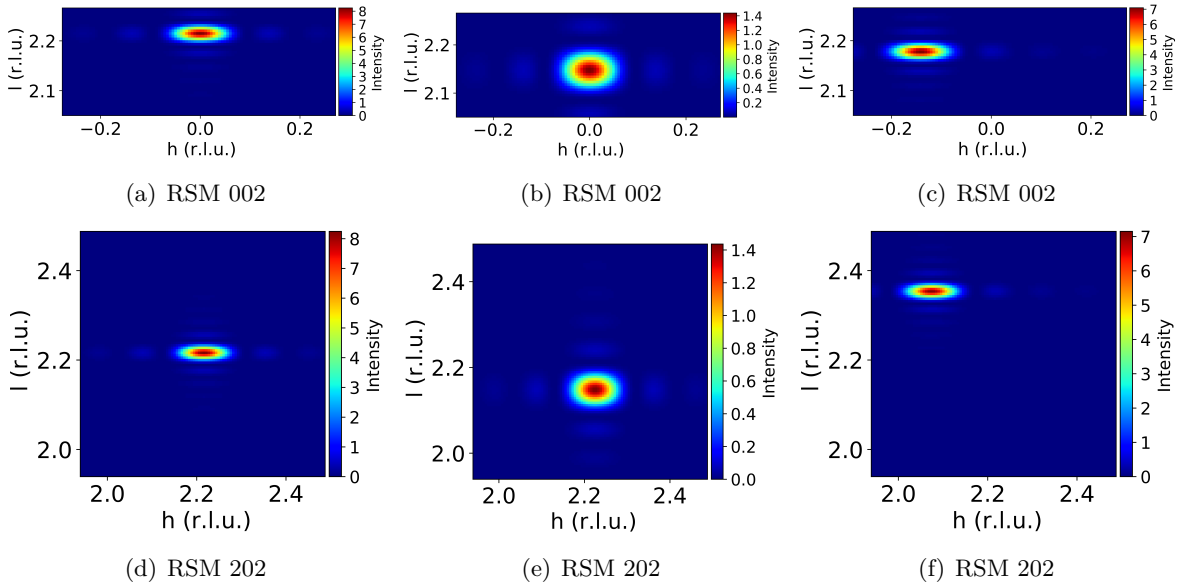

(a) RSM 002 (b) RSM 002 (c) RSM 002

(d) RSM 202 (e) RSM 202 (f) RSM 202

Figure 4.18: Calculated RSMs around 002 and 202 Ni reflections corresponding to the three cases of Fig.4.17. (a)(d) Bulk Ni domain of D=4 nm and L=14 nm; (b)(e) Highly strained Ni domain of D=4 nm and L=6 nm; (c)(f) Oriented and partially relaxed Ni domain of D=4 nm and L=14 nm.

At this point, I firstly considered the RSMs as the sum of contributions of the independent domains. Fig.4.19 shows the RSMs around 002 and 202 reflections of the combination of the aligned and tilted domains. In adjusting the proportion of aligned domains, the intensity ratio of the central spot and the tilted one is set to 6:1.

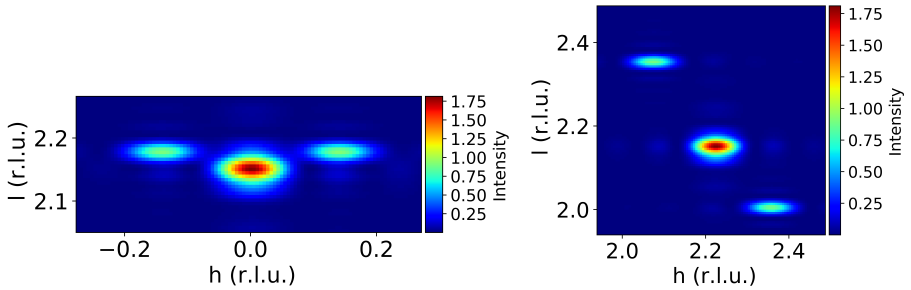

(a) RSM 002 (b) RSM 202

Figure 4.19: RSMs around 002 and 202 Ni reflections by combination of the aligned and misoriented domains.

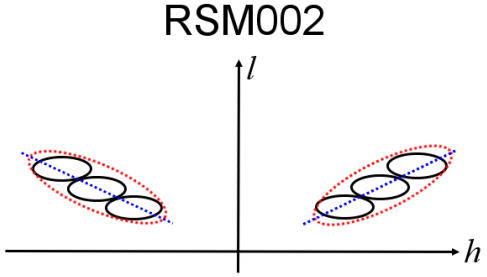

Figure 4.20: Illustration of the combination of spots with strain correlated to the misorientation of domains.

However, the diffraction spot associated to a domain is a flat ellipsoid. In order to generate the clockwise and anticlockwise rotations of additional spots, I assumed that the spots can be considered as the combination of the flat ellipsoids with the axial strain associated to the orientation, ϵ_{zz} *versus* α,

as illustrated in Fig.4.20. It corresponds to a mosaic block model more elaborated than the basic one firstly presented in Fig.4.13. The clockwise and anticlockwise rotations indicate that the more tilted a domain is, the more relaxed it is. Moreover, the left and right spots are symmetric, with respect to ℓ axis. This fact leads me to build a function of the square of α: $\epsilon_{zz} = g(\alpha^2)$, as well as for ϵ_{xx}. The shear strain ϵ_{xz} is set to zero for the aligned domains and is proportional to α for tilted ones, in considering the symmetry of the spots. Therefore, the strain in function of the orientation angle α can be modelled by:

$$\begin{aligned} \epsilon_{zz} &= \epsilon^0_{zz} + \beta_{zz}(\alpha/\alpha_0)^2 \\ \epsilon_{xx} &= \epsilon^0_{xx} + \beta_{xx}(\alpha/\alpha_0)^2 \\ \epsilon_{xz} &= \epsilon_{zx} = \beta_{xz}(\alpha/\alpha_0) \end{aligned} \tag{4.5}$$

where ϵ^0_{zz} and ϵ^0_{xx} correspond to the axial tensile and radial compressive strains for the second component of the central spot, the dashed orange ellipse in Fig.4.16. Their values can be deduced by the position of the central spot around 002 and 200 Ni reflections where α=0. Therefore, $\epsilon^0_{zz} = +3.0\%$ and ϵ^0_{xx}=-0.4%. For the domains tilted of the angle $\alpha = \alpha_0$, the expression is simplified as $\epsilon_{ii} = \epsilon^0_{ii} + \beta_{ii}$, where $i = x$ ot z. With ϵ_{zz}=1.4% and ϵ_{xx}=-0.2% for the tilted domains, the values of β_{ii} are thus deduced: β_{zz}=-0.016, β_{xx}=+0.002. The slight shear component in tilted domains is reflected by the coefficient β_{xz}. For the α_0-tilted domains, the measured shear strain is about -0.7%. The coefficient β_{xz} is thus -0.007.

As the tilted domain family is centered at $\alpha = 0$ and $\pm\alpha_0$, the mosaic block model consists on a distribution of the misorientation $f(\alpha)$. As illustrated in Fig.4.21, $f(\alpha)$ is simplified to be the sum of three Gaussian distribution centered at 0 and $\pm\alpha_0$. This resembles the h or k profiles of 002 RSMs (Fig.4.10(b) and 4.11(a)), except here the additional highly strained domains are not involved. Moreover, from the $h\ell$ and $k\ell$ cuts around 002 Ni reflection, the tilted spots spread until $\pm$0.25 in h or k. For a domain of diameter of 4 nm, the flat spot width is about 0.1. Taking the spot half width into consideration, the spot center moves from $-h_s$-0.05 to $+h_s$+0.05, leading to the misorientation from $-5.4°$ to $5.4°$.

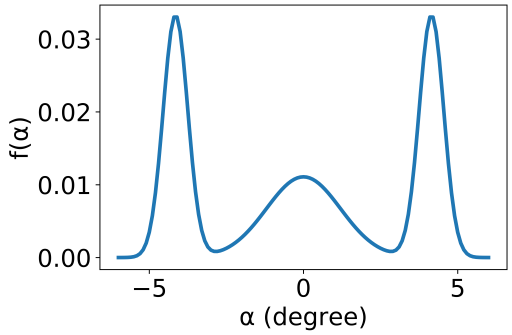

Figure 4.21: The distribution of misorientation α.

Based on the relationship between the strain and the misorientation of domains, together with the misorientation distribution, the simulated RSMs around 002 and 202 reflections related to the tilted family of domains are shown in Fig.4.22, where the incidence effect is included for 002 RSM. The spot position is well reproduced. Besides, the orientation of the spots is slightly improved compared to the flat spots simulated in Fig.4.19. The orientation of two additional spots around 002 and 202 reflections is in the right direction as expected. One composite of the central spot is oriented et about 45°.

In summary, a distribution of an uniform deformation in a domain correlated with its misorientation reproduces well RSMs, in position and intensity. However, the bending of the diffraction spots is still not correctly calculated. This evidences that the mosaic block model is too simplistic and indicates existence of internal distortion inside domains. XRD study of randomly deformed structures was early proposed by Krivoglaz [91] and has been developped [92, 93, 94, 95]. For instance, Kaganer *et al.*

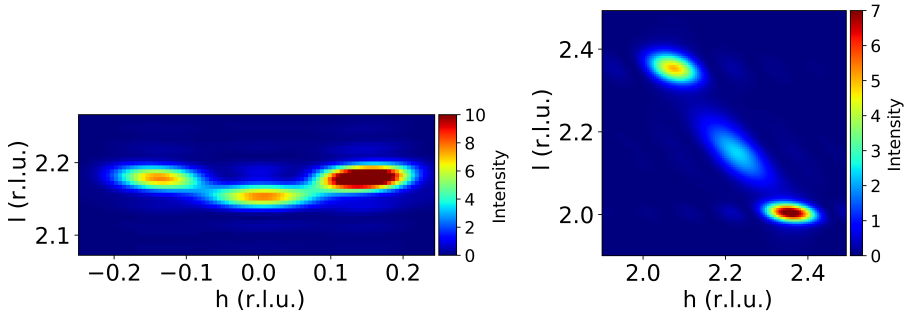

(a) 002 RSM (b) 202 RSM

Figure 4.22: RSMs at 002 and 202 Ni reflection for the tilted domain family, based on the relationship (Eq.4.5) between the strains and the misorientations, together with the orientation distribution. The incidence effect is included for 002 RSM.

[94] showed that random atomic displacements induced by randomly distributed misfit dislocations in a heteroepitaxial film can bend diffraction spots clockwise or anticlockwise, depending on the case. It results that distortion should be taken into account, in order to reflect random atomic displacements in our case.

In combining the misorientation and the strain, the displacement $\vec{u}$ can be expressed by:

$$\vec{u} = \left(\begin{bmatrix} 1 & -\alpha \\ \alpha & 1 \end{bmatrix} \begin{bmatrix} 1+\epsilon_{xx}(\alpha) & \epsilon_{xz} \\ \epsilon_{xz} & 1+\epsilon_{zz}(\alpha) \end{bmatrix} - \mathrm{I} \right) \vec{r}$$

here $\vec{r}$ is the position of each atom. The rotation matrix is simplified as the value of α is small. In neglecting the second order and ϵ_{xz} before α ($\epsilon_{xz} \ll \alpha$), the displacements are simplified as:

$$\vec{u} = \begin{bmatrix} \epsilon_{xx} & -\alpha \\ \alpha & \epsilon_{zz} \end{bmatrix} \vec{r}$$

With the expressions of ϵ_{ii} in function of α, where $i = x$ or z, $\vec{u}$ is considered as a result of the misorientation α. Therefore the displacement $\vec{u}$ on the spatial coordinates z and x is described as:

$$\begin{aligned} u_z &= \left(\epsilon^0_{zz} + \beta_{zz}(\alpha/\alpha_0)^2\right) z + \alpha x \\ u_x &= \left(\epsilon^0_{xx} + \beta_{xx}(\alpha/\alpha_0)^2\right) x - \alpha z \end{aligned} \tag{4.6}$$

In order to generate a random internal distortion, I simply introduce a random variable $\delta\alpha$ inside each coherent domain. Taking the center of a domain as reference, the random atomic displacements δu_z and δu_x are parameterized by the random variable $\delta\alpha$ as follows:

$$\begin{aligned} \delta u_z &= (x + 2z\beta_{zz}\alpha/\alpha_0^2)\delta\alpha \\ \delta u_x &= (-z + 2x\beta_{xx}\alpha/\alpha_0^2)\delta\alpha \end{aligned} \tag{4.7}$$

where the $\delta\alpha$ is a random orientation angle in the range of [-0.7°, 0.7°]. Such an ingredient makes the distortion divergent from the center of a domain and gives a coherent length of about 15 nm. It allows us to reproduce satisfactorily the bending of the diffraction spots at 002 and 202 Ni reflection. As shown in Fig.4.23, by applying this internal distortion on the tilted domains family, the bending of spots at 002 and 202 reflection was successfully reproduced in comparison of the experimental results.

Finally, in adding the highly strained domains family into the calculation, the final simulated $h0\ell$ RSMs around 002 and 202 Ni reflections are presented in Fig.4.24(b)(d). The simulation is in good

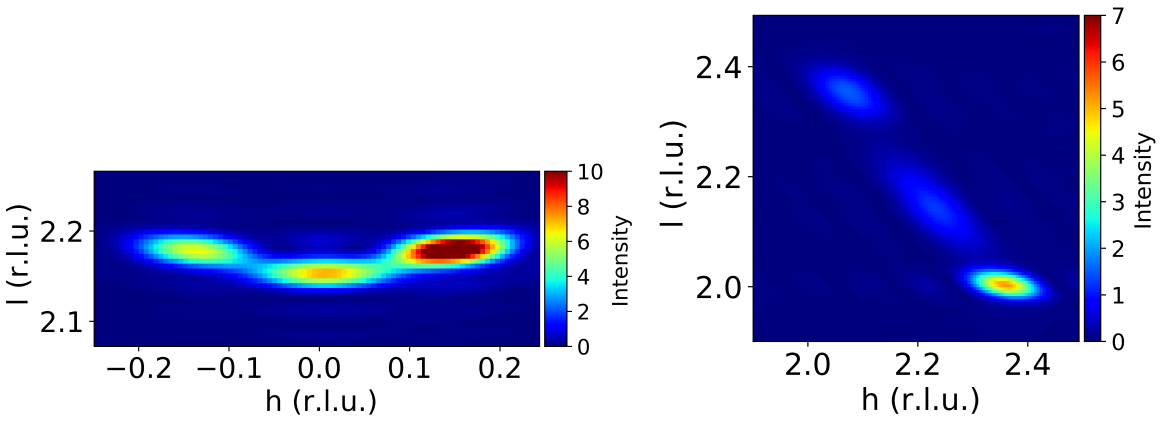

(a) RSM 002 (b) RSM 202

Figure 4.23: RSMs at 002 and 202 Ni reflections by applying an internal distortion on tilted domain family. The bending of diffraction spots is correctly reproduced.

agreement with the experimental RSMs (Fig.4.24(a)(c)), even though the intensity is not correctly reproduced in detail. This ensures that the main structural characteristics of the epitaxial Ni NWs in the $SrTiO_3$ matrix are well described.

4.2.3 Discussion: strain relaxation mechanism

The lattice mismatch between bulk Ni (a_{Ni}=3.524 Å) and bulk $SrTiO_3$ (a_{SrTiO_3}=3.905 Å) is quite large, about 11%. In the present case, the 002 reflection of the matrix is at ℓ=1.98. This indicates that the $SrTiO_3$ matrix is expanded to a parameter c=3.944 Å due to the lack of oxygen during the growth.

Considering the domains tilted by $|\alpha|$=4.15°, in $h0\ell$ map of reciprocal space around 202 Ni reflection in Fig.4.12(a), the spot falls at ℓ=2.00(5). This indicates that the rotation allows to nearly reach the lattice matching of (101) planes along the vertical heterointerface. The schematic representation is shown in Fig.4.25. We take $\vec{g}^*_{202}$ as the reciprocal vector associated with the 202 reflection. The inter-reticular distance viewed along the direction z of heterointerface, $d^{\parallel}_{202}$, is given by $1/(\vec{g}^*_{202} \cdot \vec{e}_z)$.

Since $\vec{g}^*_{202} \cdot \vec{e}_z$=2.00(5) for the domains tilted by 4.15°, we get $d^{\parallel}_{202}$=a_{SrTiO_3}/2.00(5) =1.948 Å, to be compared with d^{matrix}_{002}=1.972 Å (ℓ=1.98) for the matrix. It is thus obvious that the tilt by about 4° allows to reduce the mismatch drastically by matching (101) planes as sketched in Fig.4.25. The mismatch is indeed lowered to 1.2%. It should be noted that the aforementioned simulation of the RSMs indicates that strain relaxation and rotation of the $[100]_{Ni}$ axis occur in a correlated manner.

Considering the aligned domains with $\langle\epsilon_{zz}\rangle$=3.2%, the average lattice parameter along z is equal to 3.637 Å, this corresponds to a mismatch of 7.8% that could be accommodated by domain epitaxy with 13 unit cells of Ni matching 12 unit cells of $SrTiO_3$ matrix along z. This can give a rough estimation of the axial coherent length for the aligned domains, about 5 nm, which is not too far from the one used in the simulation of the RSM ($L^{aligned}_{coh}$=6 nm). A possible interpretation of the composite domain structure could be that both matching mechanisms compete and that the energy barrier between these two (meta)-stable states can be crossed at the growth temperature. It should be noted that the curved interface between a NW and the matrix in the (001) plane, in absence of fully developed faceting of the NWs, implies that the (101) plane matching cannot be effective on the whole perimeter of the embedded nano-objects. As a result, structural disorder will be generated at the Ni-$SrTiO_3$ interface and its relative contribution will evidently increase with decreasing NW diameter. In a similar fashion, the coexistence of [001] aligned regions with tilted ones within the NWs implies that a certain volume fraction is occupied by low-angle tilt boundaries between domains inside Ni NWs. Again, this will be linked to the creation of structurally disordered regions, and the fraction of disordered Ni, related to grain boundary (GB) regions, may increase upon diameter reduction.

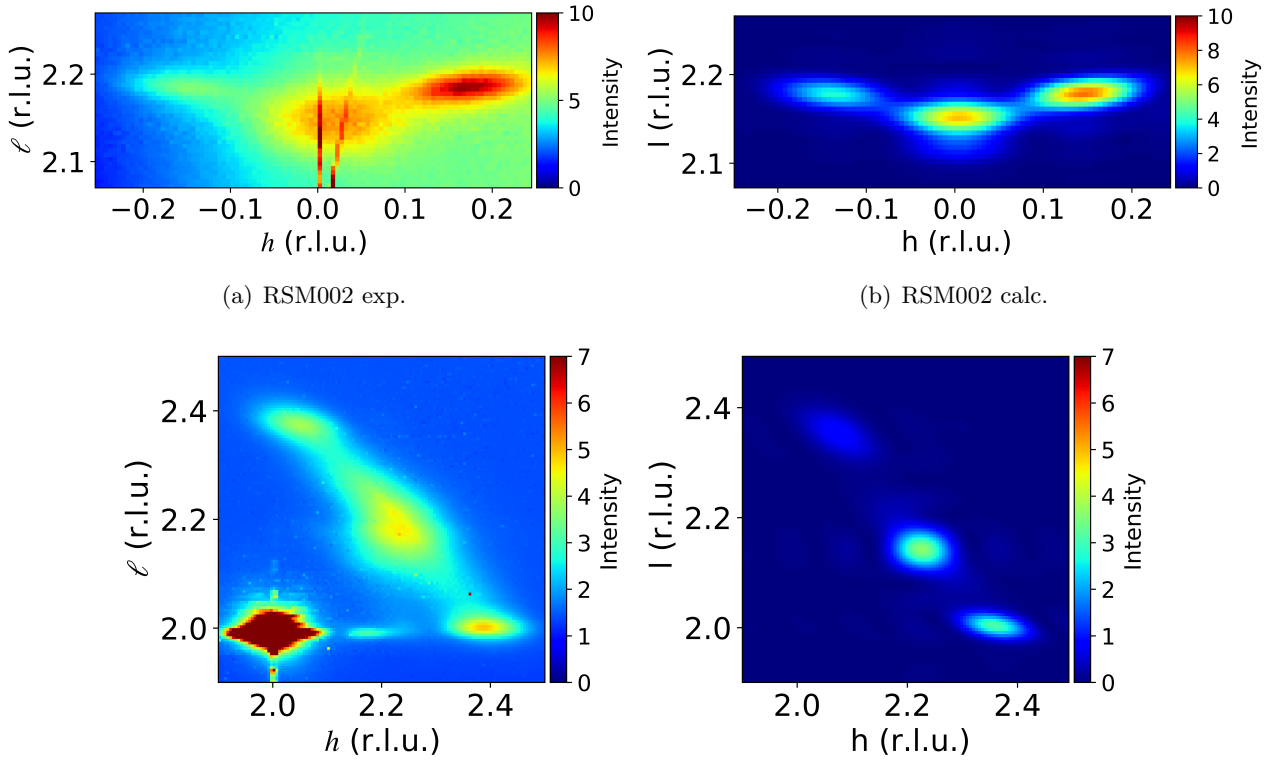

(a) RSM002 exp.

(b) RSM002 calc.

(c) RSM202 exp.

(d) RSM202 calc.

Figure 4.24: Comparison between the experimental and calculated RSM around 002 and 202 Ni reflections. (a)(c): experimental $h0\ell$ plane of reciprocal space. (b)(d): simulated $h0\ell$ plane of reciprocal space.

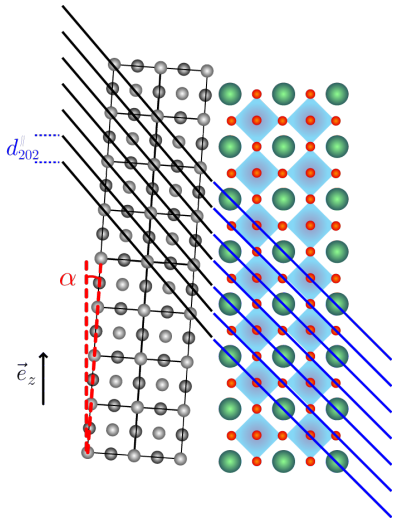

Figure 4.25: Sketch of the lattice matching for Ni domains with a 4° misorientation of the [001] direction with respect to the [001] direction of the matrix.

Indeed, we observe a significant evolution of the diffraction patterns upon reduction of $\langle D \rangle$. As shown in Fig.4.26(c), the diffracted intensity is much weaker for $\langle D \rangle$=2.2 nm. The composite nature of the diffraction spots is still present and the fact that a sizable portion of the diffracted intensity is located near ℓ=1 for the Ni 111 spot indicates that tilt and associated GBs are still present upon diameter reduction. Fig.4.26(d) gives a schematic picture of the sources of crystallographic disorder in the NWs, compatible with the measured diffraction patterns. The low angle GBs are created by the rotation of Ni crystallite. Along the axis of wires, the coherent length of aligned domains $L_{coh}^{aligned}$ is about 6 nm and that of the tilted domains L_{coh}^{tilted} is about 14 nm. The probability of misorientation towards the four directions is equivalent, with respect to the four-fold symmetry of the system.

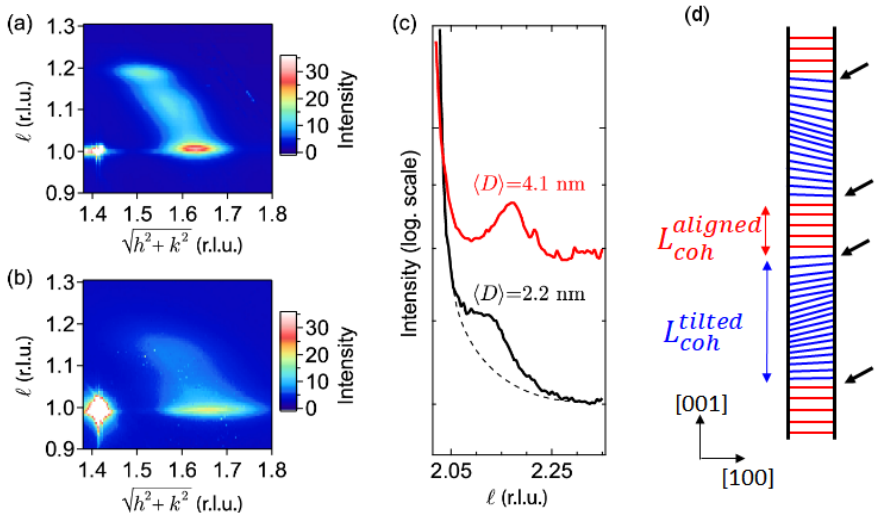

Figure 4.26: Vertical-epitaxy-induced disorder in NW composites. (a-b) (111) maps for two different samples with large difference in NW diameter [$\langle D \rangle$=4.1 nm in (a), $\langle D \rangle$=2.2 nm in (b)] reveals large intensity loss for $\langle D \rangle$=2.2 nm. (c) $\theta - 2\theta$ scans for the same two samples, evidencing the loss of crystalline order along ℓ. (d) Schematics of the Ni-$SrTiO_3$ interface with tilted Ni domain, where the arrows indicate the creation of low angle GBs.

In summary, metallic fcc Ni NWs are grown epitaxially in $SrTiO_3$ matrix with diameter from 1.7 to 5.3 nm. The axial strain increases from 2.3 to 3.9% with decreasing diameter. Under such a large strain, a novel strain relaxation with misorientation occurs to obtain the coincidence of the crystallographic (101) or (111) planes between the NWs and the matrix. This generates the GBs inside NWs and increases the disorder of Ni NWs.

4.3 Structural properties of Co_xNi_{1-x} alloy nanowires

4.3.1 General features of Co_xNi_{1-x} alloy nanowires

According to the previous works, Co and Ni can be well alloyed into Co_xNi_{1-x} nanowires and grown epitaxially in CeO_2 matrix [26]. The system of Co_xNi_{1-x} alloy nanowires embedded in CeO_2 gives an axial strain smaller than 1%. To increase the axial strain to enhance the contribution of magneto-elastic anisotropy, a series of Co_xNi_{1-x} alloy nanowires with different Co proportions was grown in $SrTiO_3$ matrix for x from 20% up to 80% by controlling the ratio of laser shots on CoO and NiO targets. The growth sequence is written as:

$$((n_1\times\mathrm{CoO}+n_2\times\mathrm{SrTiO_3})\times n_3+(n_1\times\mathrm{NiO}+n_2\times\mathrm{SrTiO_3})\times n_4)\times N$$

Here n_1, n_2 are respectively the shot number on the metal target and on the matrix target; n_3 and n_4 is the repetition times of subsequence; and N is repetition times of total sequence. Thus, the Co proportion can be expected as $n_3/(n_3+n_4)$. The final compositions of nanowires are determined by the EDX spectrum of Co_xNi_{1-x} in TEM measurement. For example, Fig.4.27 shows an EDX spectrum of Co_xNi_{1-x} with n_3=4 and n_4=1. The Co proportion is deduced to be about 78%, close to the expectation. The diameter, the density and other structural characteristics of NWs are determined by TEM and XRD. The results are presented in Tab.4.4. By capping 2-3 nm of Al_2O_3, the epilayer thickness in this series is about 110 nm.

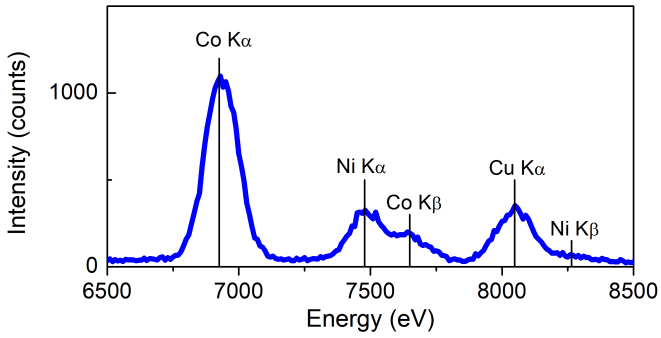

Figure 4.27: EDX spectrum in TEM measurement of $Co_{0.78}Ni_{0.22}$.

In bulk Co_xNi_{1-x} alloy, the phase transition from fcc to hcp occurs at Co content more than 65% at room temperature [96]. The lattice parameter of fcc Co_xNi_{1-x} varies linearly with the Co concentration x, and it is estimated to 3.548 Å for bulk fcc Co. For Co_xNi_{1-x} alloy NWs with diameter larger than 100 nm, this phase transition always occurs for Co-rich alloy, in agreement with bulk Co_xNi_{1-x} alloy [97]. However, in decreasing the dimension of Co_xNi_{1-x}, the hcp phase can transit to fcc in rich-Co alloy nanostructure. For example, the phase transition from hcp to fcc occurs for Co_xNi_{1-x} alloy NWs with diameter of 35 nm and Co content of 80% [98]. In our case, with diameter under 10 nm, Co_xNi_{1-x} alloy NWs show a fcc structure even at x=78%.

Furthermore, Co_xNi_{1-x} is metallic in $SrTiO_3$ matrix, as determined by Co and Ni $L_{2,3}$ edges absorption spectra described later in Chap.5.

By θ-2θ scans in laboratory XRD (Fig.4.28), it is established that the axial strain increases when Co proportion increase as listed in Tab.4.4. The axial strain increases from 2.4% up to 4.8% for Co proportion from 0 to 0.78. In addition, from the θ-2θ scan of $Co_{0.78}Ni_{0.22}$ in Fig.4.28(a), a non-negligible contribution of relaxed domains is indicated by a small peak at $\ell=\ell^{bulk}_{Co_{0.78}Ni_{0.22}}$. It happens in all Co_xNi_{1-x} samples of this series as shown in Fig.4.28(b). Compared to the complex Ni structure, we can suppose that in addition to the highly strained domains in Co_xNi_{1-x} nanowires, there exists some totally relaxed ones. Moreover, the broad width of Co_xNi_{1-x} 002 peak indicates a distribution of axial strain, similarly to Ni NWs.

Table 4.4: Structural parameters deduced from TEM and XRD analysis of the nanocomposites. n_3 and n_4: numbers of subsequences involving Co and Ni, respectively; $\langle D \rangle$: mean diameter of the NWs; ρ: in-plane density of the NWs; t: epilayer thickness; $\langle \epsilon_{zz} \rangle$: mean axial strain.

Sample	$n_3/(n_3+n_4)$	Co content	$\langle D \rangle$ (nm)	ρ (cm^{-2})	t (nm)	$\langle \epsilon_{zz} \rangle$(%)
S-5	0	0	5.0	5.1×10^{11}	106	2.4
S-7	0.2	0.18	5.3	4.5×10^{11}	110	2.8
S-8	0.6	0.57	5.0	3.9×10^{11}	113	3.1
S-9	0.8	0.78	4.8	4.3×10^{11}	106	4.2

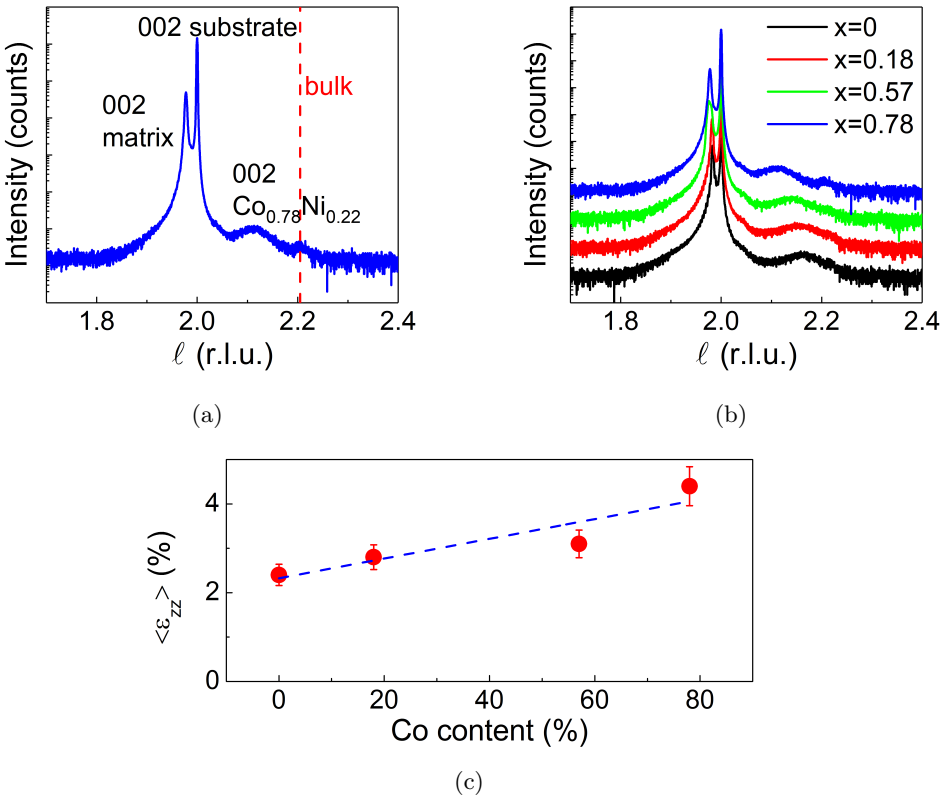

Figure 4.28: (a) XRD θ-2θ scan of sample S-9. The vertical dashed line indicates the position of 002 peak for relaxed bulk $Co_{0.78}Ni_{0.22}$. (b) XRD θ-2θ scans performed on Co_xNi_{1-x} with x =0, 0.18, 0.57 and 0.78. (c) Evolution of the mean axial strains as a function of Co proportion. The 0% Co sample S-5 is included in this series. The blue dashed line is the linear fitting curve.

4.3.2 Pole figures and analysis

The inhomogeneity and misorientation of domains in Co_xNi_{1-x} NWs have been explored by XRD pole figures (PFs) in laboratory. Here, I will compare the results obtained with RSMs at sychrotron SOLEIL and laboratory PFs for sample S-3. Then, I will analyze the PFs of Co_xNi_{1-x} in order to understand their microsturcture.

PF is a useful method to study orientation texture in NWs. The acquisition of PFs is described in section 2.2.2. With the sturctural information from RSMs, the angular configurations can be determined to acquire PFs. For sample S-3, around 002 Ni reflection, the domains axially strained by 3.2% are searched at ℓ=2.15 or 2θ=50.19° for Cu $K_{\alpha1}$ radiation. For misoriented domains, ℓ=2.18 and 2θ=50.94°. For 202 and 111 reflections, 2θ is respectively fixed at 75.87° and 44.72°. The 002, 202 and 111 PFs of sample S-3 are shown in Fig.4.29. Compared to synchrotron RSMs, 4 additional tilted spots are also detected around a central spot by PFs (Fig.4.29). PF for 002 reflection at ℓ=2.18(5)

(Fig.4.29(b)) shows that these 4 additional tilted spots are equivalent in intensity and shape, reflecting the four-fold symmetry of the system, as what the RSMs give. Furthermore, the tilt angle χ is of 4.0±0.3°, in agreement with the synchrotron results where the domains tilted by 4.15°. For 202 reflection shown in Fig.4.29(c), two spots are symmetric at χ=45.3°. This is associated to the two symmetric spots centered at k=±h_s and ℓ=2.18(5) in RSM 202 in Fig.4.12(b). The spot near the circle center (at small χ of 40.4°) is associated to the upper spot in 202 RSM in Fig.4.12(a), and the one away from the center (at large χ of 49.8°) corresponds to the lower spot in RSMs. For 111 reflection, due to the large angular divergence of the incident beam, the spots are more indistinguishable with increasing χ. Thus, two spots at $\chi = 51.8°$ can be slightly recognized and those at $\chi = 58.4°$ are mixed. The fact that the spots at large χ are more intense than the ones at small χ is in accordance with the result from synchrotron 202 and 111 RSMs. In view of the comparison between the synchrotron RSMs and the laboratory PFs, PFs constitute an efficient tool to explore the misorientation of domains in NWs.

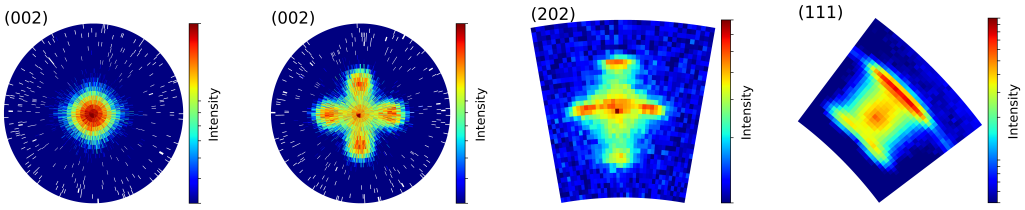

(a) (b) (c) (d)

Figure 4.29: Pole figures of sample S-3: (a) 002 Ni reflection at the sphere of 3.2% axially strained Ni NWs. χ=[0, 10°], ϕ=[0, 360°]; (b) 002 Ni reflection at the sphere of 1.4% axially strained Ni NWs. χ and ϕ are in the same range of (a); (c) 202 Ni reflection. χ=45±9°, ϕ=0±8°; (d) 111 Ni reflection, χ=54.7°+[-6.7°, 8.3°], ϕ=45±8°.

Evidence of domain misorientation is given by another Ni NW sample, S-5, with a larger diameter and smaller axial strain, with respect to sample S-3. Fig.4.30 shows the 002, 202 and 111 PFs of sample S-5. For 002 reflection, 4 additional tilted spots are observed at [100] and [001] directions. The tilt angle χ is determined at 3.5°. Compared to the PFs of sample S-3 in Fig.4.29, these 4 spots are less intense than the central spot. It indicates that the mechanism of strain relaxation with misorientation in privileged directions, [100] and [010], is weakened. This is confirmed by 202 PF, where 4 tilted spots are hard to be distinguished as shown in Fig.4.30(b). However, for 111 reflection, the mixed spots at large χ are still intense. This is a significant fact that the coincidence of Ni (111) lattice planes to the matrix (001) ones still exists, although such mechanism is weakened.

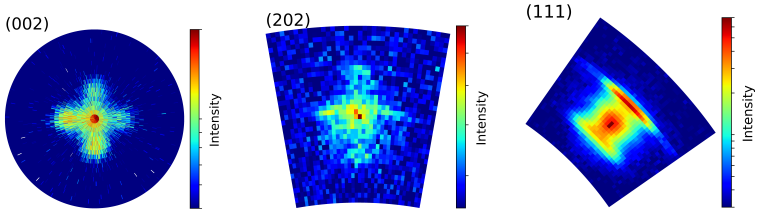

(a) (b) (c)

Figure 4.30: PFs of sample S-5. (a) 002 reflection with χ=[0, 10°] and ϕ=[0, 360°]. (b) 202 reflection with χ=45±9° and ϕ=0±10°. (c) 111 reflection with χ=54.7°+[-7.7°,8.3°] and ϕ=45±10°.

The structural study of Co_xNi_{1-x} alloy nanowires is made by the PFs. As shown in Fig.4.31, the 002, 202 and 111 PFs are performed for Co_xNi_{1-x} with x increasing from 0.18 to 0.78. Upon the increase of Co content x, a significant evolution of PFs was observed. For 002 and 202 reflections, the 4 additional spots associated to the tilted domains can be observed only at small content of Co (x=0.18). This can be clearly visualized by χ profiles along [100] and [110] directions in 002 PFs as displayed in Fig.4.32. The intensity difference between these two directions evidences the misorientation of domains along [100] direction. The tilt angles deduced are 4.0, 3.5 and 3.5° for samples S-3, S-5 and

S-7, respectively. At x =0.57 for sample S-8, the intensity difference between the [100] and [110] directions is no more measurable. This indicates the disappearance of the mechanism of the strain relaxation with misorientation along privileged directions with the increasing Co content. For 111 reflection, the spots at small χ become weak and disappear when the Co content increases. This reinforces the idea that the strain relaxation with misorientation found in Ni NWs is dramatically weakened with the increase of Co content. It should be underlined that the intense spots at large χ in 111 PF are always persistent, in spite of the increasing structural disorder with increasing Co content. This demonstrates the matching of (111) lattice planes to the matrix is always privileged.

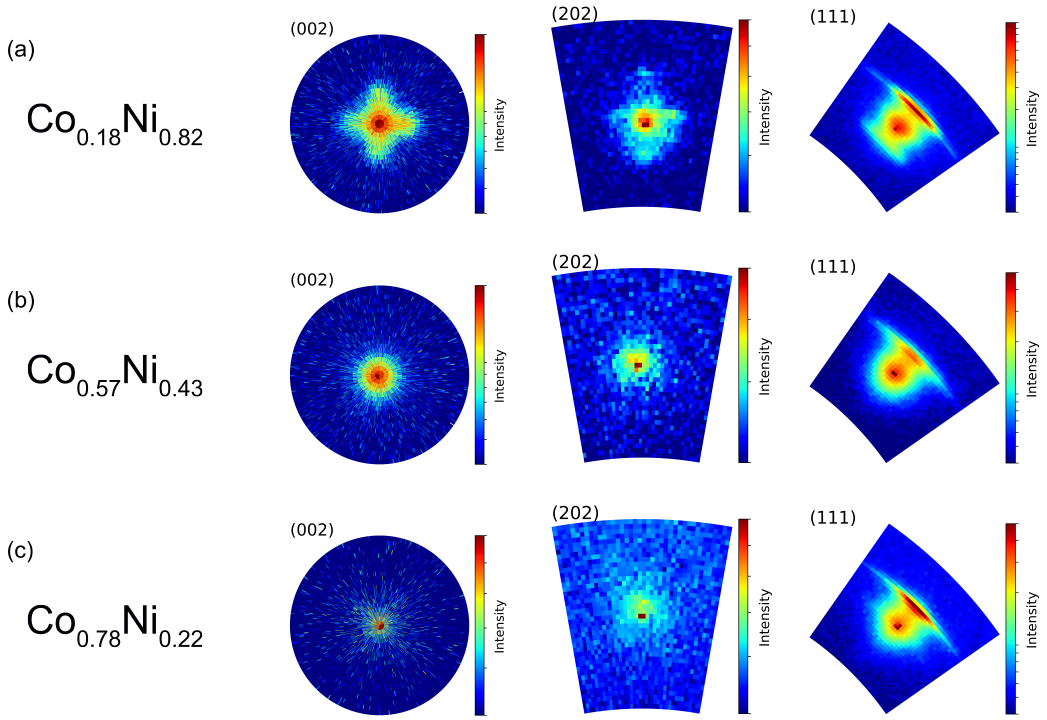

Figure 4.31: 002, 202 and 111 PFs of Co_xNi_{1-x} alloy NW samples: (a) S-7; (b) S-8; (c) S-9.

In summary, the contribution of the strain relaxation mechanism with misorientation along privileged directions decreases with the decreasing strain for Ni NWs. For Co_xNi_{1-x} NWs, with the increase of the Co content, such mechanism weakens and then disappears. In consideration of the broad width of Co_xNi_{1-x} 002 peak in the θ-2θ scan as presented in Fig.4.28, we came to a conclusion that: when the axial strain increases with increasing Co content, the strain relaxation with misorientation occurs no longer only in privileged directions to match the lattice planes of the NWs and matrix. However there is still a preferential misorientation of lattice planes, leading to the matching of NW (111) planes and the matrix, for both Ni and Co_xNi_{1-x}.

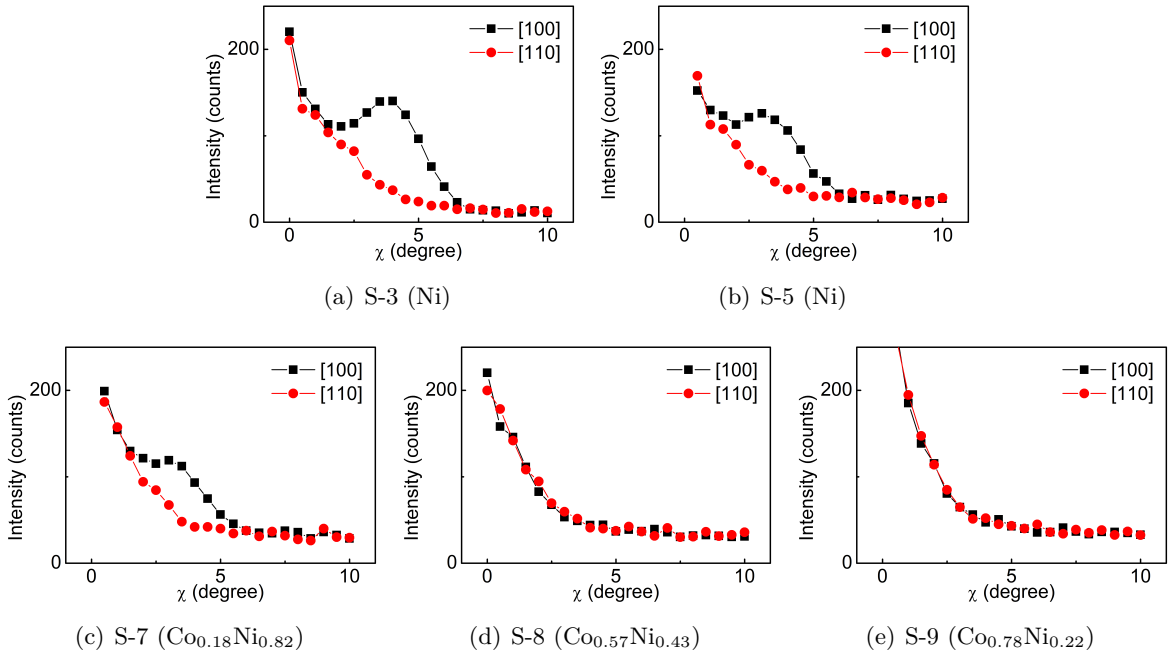

(a) S-3 (Ni) (b) S-5 (Ni)

(c) S-7 ($Co_{0.18}Ni_{0.82}$) (d) S-8 ($Co_{0.57}Ni_{0.43}$) (e) S-9 ($Co_{0.78}Ni_{0.22}$)

Figure 4.32: χ profiles along [100] and [110] directions around 002 reflection for PF performed samples (a) S-3, Ni; (b) S-5, Ni; (c) S-7, $Co_{0.18}Ni_{0.82}$; (d) S-8, $Co_{0.57}Ni_{0.43}$; (e) S-9, $Co_{0.78}Ni_{0.22}$.

4.4 Conclusion

I conclude this chapter by summarizing key results obtained on the structure of Ni and CoNi NWs.

- Ultrathin NWs with diameters ranging from 1.7 to 5.3 nm were vertically epitaxied in a $SrTiO_3$ matrix by sequential and alternating growth process.
- The metallic character of NWs was established by x-ray absorption spectroscopy.
- NWs are highly strained with an axial dilatation increasing from 2 up to 4%, when the NW diameter decreases from about 5 to 2 nm.
- A novel strain relaxation mechanism in the NW vertical epitaxy was evidenced, such as it was detailed in sample S-3 of Ni NWs by synchrotron XRD and simulation.
  - Highly strained parts in NWs ($\epsilon_{zz} \approx 3.2\%$) have a short coherent length of about 6 nm; the coherent length increases to about 13 nm with strain relaxation (ϵ_{zz} down to 1.4%).
  - Strain is relaxed in a correlated way with a rotation of lattice planes until 4° around the [100] or [010] axis, generating four equivalent variants.
  - For one set of (101) or (111) dense lattice planes, the lattice mismatch along the NW/matrix interface is drastically reduced to about 1%, as revealed by the position and the enhanced intensity of one rotated variant in 202 or 111 Ni spot.
- For CoNi alloy NWs, the axial strain increases up to 4.2% with increasing Co content until 80%, with a broad strain distribution similarly to the case of Ni NWs.
- The mechanism of strain relaxation *via* lattice rotation around one particular axis weakens and vanishes with increasing content of Co, as shown by 002 and 202 PFs.
- Surprisingly, the set of (111) lattice planes, the one mostly matched with the matrix, is always enhanced, as evidenced by 111 PFs.

The results obtained unveil an original mechanism in the NW vertical epitaxy: strain relaxation proceeds by favoring one set of inclined and dense lattice planes, among the four equivalent ones, to

achieve the lattice matching along the NW/matrix interface. As will be shown in the following, the peculiar NW structure and the broad strain distributions have an important impact on the magnetic behavior of the NWs.

Chapter 5

Magnetic behavior of Ni NWs

The strain is a key parameter affecting the magnetic anisotropy. For ultrathin Ni NWs embedded in $SrTiO_3$ matrix, a large axial strain of 2-4% has been achieved with the NW diameter from 5 down to 2 nm. Furthermore, the strain is not homogeneous along the wire axis. In this chapter, experimental results on magnetic hysteresis of Ni NWs will be firstly described. Then, I will analyze the magnetic behavior of Ni NWs in connection with their strain state, by modelling and simulation. Finally, I will show an element-specific study and focus on the orbital moment contribution to the magnetic anisotropy, by x-ray magnetic circular dichroism (XMCD) spectroscopy.

5.1 Magnetic response of Ni NWs

5.1.1 Anisotropy at low temperature

I start with magnetic hysteresis cycles obtained by vibrating sample magnetometer (VSM). Fig.5.1(a) shows hysteresis cycles $M(H)$ of sample U-5 at 10 K in applying an external magnetic field along the wire axis and perpendicular to the wire axis along [100] and [110] directions. It can be seen that the magnetization saturation is easier to reach in the [100] and [110] directions, in-plane (IP) directions, than in [001] direction, out-of-plane (OP) direction. Thus the wire axis is the magnetization hard axis and the film plane is the easy plane. Moreover, the cycles are similar along the azimuthal [100] and [110] directions. This indicates the overall isotropy in the easy plane. Besides, the opening of cycles occurs along the hard axis and in the easy plane and the coercive fields are of the same order (inset of Fig.5.1(a)).

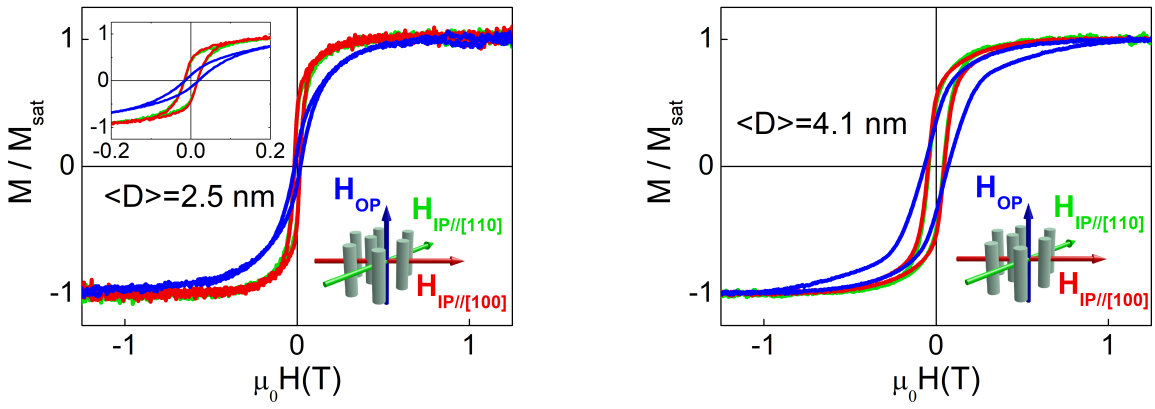

(a) (b)

Figure 5.1: Normalized hysteresis cycles $M(H)$ of (a) sample U-5 and (b) S-3 made at 10 K in applying an external magnetic field H in three directions: out-of-plane field, H_{OP} (blue), parallel to the wire axis; in-plane field along [100] and [110] directions, noted as $H_{\mathrm{IP}\|[100]}$ (red) and $H_{\mathrm{IP}\|[110]}$ (green), respectively. Inset: enlargement of $M(H)$.

The character of the hard axis along the NW axis has been confirmed in all measured samples with the wire diameter from 1.9 to 5.3 nm. Also, the cycles are almost the same along the two IP directions [100] and [110] in all samples. For a sample, a slight difference of the cycles can be distinguished in the saturation approach along the two IP directions. This can be due to the measurement imprecision.

Thus, the easy plane is globally isotropic. This is in the contrary of the expectation from the Ni magnetocrystalline anisotropy contribution at low temperature and seems to be more likely linked to the strain in NWs.

Table 5.1: IP ($\parallel$) and OP ($\perp$) magnetic hysteresis characteristics of the samples at 10 K: $\langle D \rangle$, mean NW diameter; H_c, coercive field; H_s, saturation field; m_R, remanence.

	Sample	$\langle D \rangle$ (nm)	$\mu_0 H_c$ (mT)	$\mu_0 H_s$ (T)	m_R
IP ($\parallel$)	U-3	1.9	10	0.65	0.36
	U-5	2.5	17	0.48	0.42
	S-3	4.1	47	0.83	0.54
	S-4	4.5	37	0.70	0.43
	S-5	5.0	71	0.75	0.61
	S-6	5.3	37	0.50	0.47
OP ($\perp$)	U-3	1.9	7	1.00	0.04
	U-5	2.5	17	0.83	0.13
	S-3	4.1	69	1.10	0.36
	S-4	4.5	23	1.00	0.15
	S-5	5.0	95	0.85	0.40
	S-6	5.3	29	0.67	0.25

The magnetic hysteresis characteristics of the most significant samples are listed in Tab.5.1. By comparing the samples in detail, some features appear to be sample-dependent and other ones general. The first group of samples U-3, U-5, S-4 and S-6 has a relatively small coercivity with the respect to the second group of samples S-3 and S-5. The coercive field is from 10 to 37 mT in IP direction and from 7 to 29 mT in OP direction with increasing wire diameter for the first group. The coercive field for the second group is 2-3 times larger than that for the first one with the similar wire diameter. The OP saturation approach in the second group has a shape different from that in the other samples, as illustrated in Fig.5.1(b). For the two groups of samples, the coercive field, as well as the remanence m_R, increases with increasing wire diameter. An alternative lecture is that the coercive field and the remanence increase with decreasing strain. The IP saturation field, $H_{s,\parallel}$, does not have an obvious tendency with the wire diameter. The OP saturation fields $H_{s,\perp}$, *i.e.* the global anisotropy fields, are of the same order in all samples, ranging from 0.85 to 1 T. All these characteristics reflect a complex interplay between the strain and the magnetic anisotropy that I will analyze in Section 5.2.

5.1.2 Thermal evolution of coercivity

Another significant magnetic characteristic is the blocking temperature T_b above which the NWs are in the superparamagnetic state. T_b is determined by the convergence of the zero field cooling (ZFC) and field cooling (FC) curves. As shown in Fig.5.2(a), in-plane T_b is estimated at 26±3 K for sample U-5. This is consistent with the closure of the hysteresis cycles at 30 K (Fig.5.2(b)). The thermal evolution of the coercive field in sample U-5 is illustrated in Fig.5.2(c). Surprisingly, H_c exhibits an exponential decay with increasing temperature in the easy plane. This departs from the thermal activation law after Sharrock, which is a power law in T. Moreover, the decay of H_c is always exponential in T, in the easy plane and along the hard axis for all measured samples as illustrated in Fig.5.3.

At a given temperature, the thermal energy $k_B T$ is to be considered against the anisotropy energy barrier. According to the thermal activation criterion of $25 k_B T_b = K_{eff} V^*$, T_b is proportional to the effective anisotropy constant K_{eff} if the activation volume V^* is constant. As a first estimation and taking V^* constant, the remanence can be considered as the sum of the magnetization of all parts

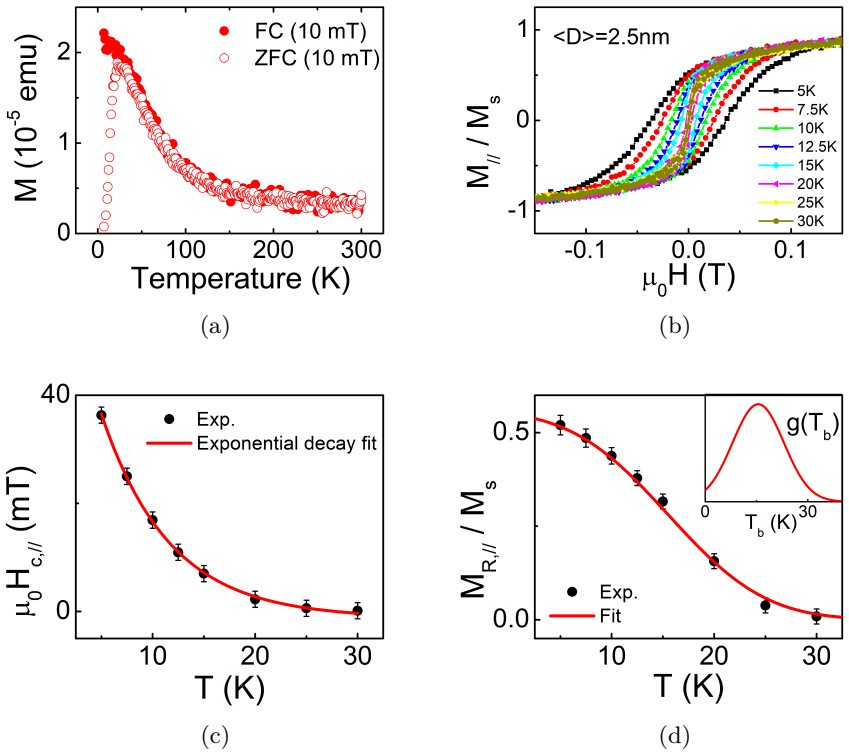

Figure 5.2: Thermal evolution of magnetic responses of sample U-5. (a) In-plane ZFC/FC measurements made with a bias field of 10 mT. (b) In-plane hysteresis cycles from 5 to 30 K. (c) Coercivity $\mu_0 H_{c,\parallel}$ extracted from the cycles and fitted by an exponential decay with increasing temperature. (d) Remanence extracted from the cycles and fitted by the partition function of a distribution of T_b: $m_R = M_{R,\parallel}/M_s \propto \int_T^{+\infty} g(T_b) dT_b$. Inset: corresponding distribution $g(T_b)$.

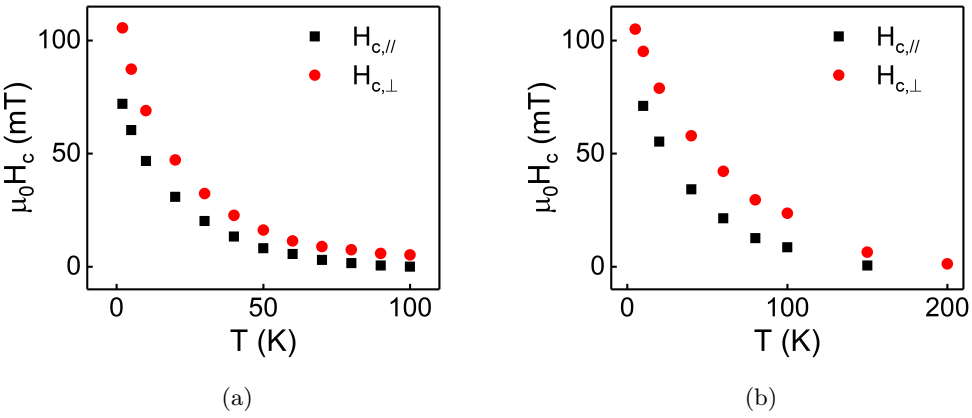

Figure 5.3: Temperature dependence of the coercivity in IP and OP directions for samples: (a) S-3; (b) S-5.

still blocked at a given temperature: $m_R \propto \int_T^{+\infty} g(T_b)dT_b$. For sample U-5, the mean value $\langle T_b \rangle$ is of 15.5 K and the variance σ_{T_b} of 7.5 K, shown in inset of Fig.5.2(d). With such a broad distribution, $m_R(T)$ is well fitted (Fig.5.2(d)). Broad distributions of T_b were similarly found in all samples along the wires and in the plane. The IP and OP blocking temperatures determined by ZFC/FC curves or the hysteresis cycles are summarized in Tab.5.2. It is confirmed that the blocking temperatures T_b increases with decreasing axial strain for the two groups of samples.

Table 5.2: Blocking temperatures of the samples in IP ($\|$) and OP ($\perp$) directions, together with the mean diameter and strain.

Sample	$\langle D \rangle$ (nm)	$\langle \epsilon_{rr} \rangle$ (%)	$T_{b,\|}$ (K)	$T_{b,\perp}$ (K)
U-3	1.9	3.9	20±3	-
U-5	2.5	3.4	26±3	23±7
S-3	4.1	3.2	80±10	97±10
S-4	4.5	2.8	100±10	-
S-5	5.0	2.4	150±30	200±30
S-6	5.3	2.3	120±20	-

Unlike the thermal reduction of the coercivity described by Sharrock's law, the exponential decrease of H_c in T observed in Ni NWs is intriguing. In literature, it was claimed that different shapes of $H_c(T)$ could be retrieved with different forms of anisotropy distribution [99]. In our case, we have not found a suitable form of anisotropy distribution leading to the exponential decrease of $H_c(T)$, in both IP and OP for all samples. However, the simulation shown in the next Section 5.2 suggests rather the existence of an additional thermally activated mechanism, in addition to the Sharrock's thermal reduction of the coercivity.

In order to identify and certify such a mechanism, the first-order reversal curve (FORC) measurements were performed at 5, 40 and 80 K for sample S-5 in IP as shown in Fig.5.4. $T_{b,\|}$ is of 150 K for this sample. The FORC measurements allow to extract the coercivity field distribution $\rho(H_c)$ at the three temperature as shown in Fig.5.5, in integrating the FORC intensities on the $\mu_0 H_c$ axis. It can be seen that $\rho(H_c)$ changes and moves towards lower value of H_c with increasing temperature. However, the Sharrock's thermal reduction narrows also the hysteresis cycles. At this stage, it can not be determined if the Sharrock's thermal reduction alone can explain the thermal evolution of $\rho(H_c)$. The last point will be detailed by simulation, in order to check whether the anisotropy distribution is static in temperature.

Besides, the FORC measurements also provide information of the bias field H_b, reflecting the interaction between NWs or parts of the NWs. This is especially visible at 5 K where the intensity is distributed with a slight slope below the $\mu_0 H_c$ axis, *i.e.* the values of H_b are negative or subjacent hysteresis cycles biased towards negative fields due to the mutual interaction. It should be pointed out that in easy-axis NW arrays, the bias fields are positive [65, 66]. As described by Pike *et al.* [63] in the mean-field framework, the interaction field H_{int} is proportional to the mean magnetization M:

$$H_{int} = k\frac{M}{V} = k\frac{M_{sat}}{V}\frac{M}{M_{sat}} = kPM_s m \tag{5.1}$$

where m is reduced magnetization and given by M/M_{sat}, P the porosity, M_s the magnetization density of Ni, M_{sat} the saturation magnetization of the sample and V the film volume. If the interaction concerns only the dipolar effect, $H_{int} = H_{dip}$. The dipolar field felt by a NW from the film mean IP magnetization leads to $k = +1/2$ for the easy-plane case, instead of $k = -1$ for the easy-axis case (see Section 1.7). We checked that the bias field H_b in the FORC map at 5 K can be removed in replacing the applied field by the effective local field: $H_{eff} = H + H_{dip}$. As the saturation magnetization density of Ni is low, this leads only to a marginal correction to $\rho(H_c)$ displayed in Fig.5.5. We will not take

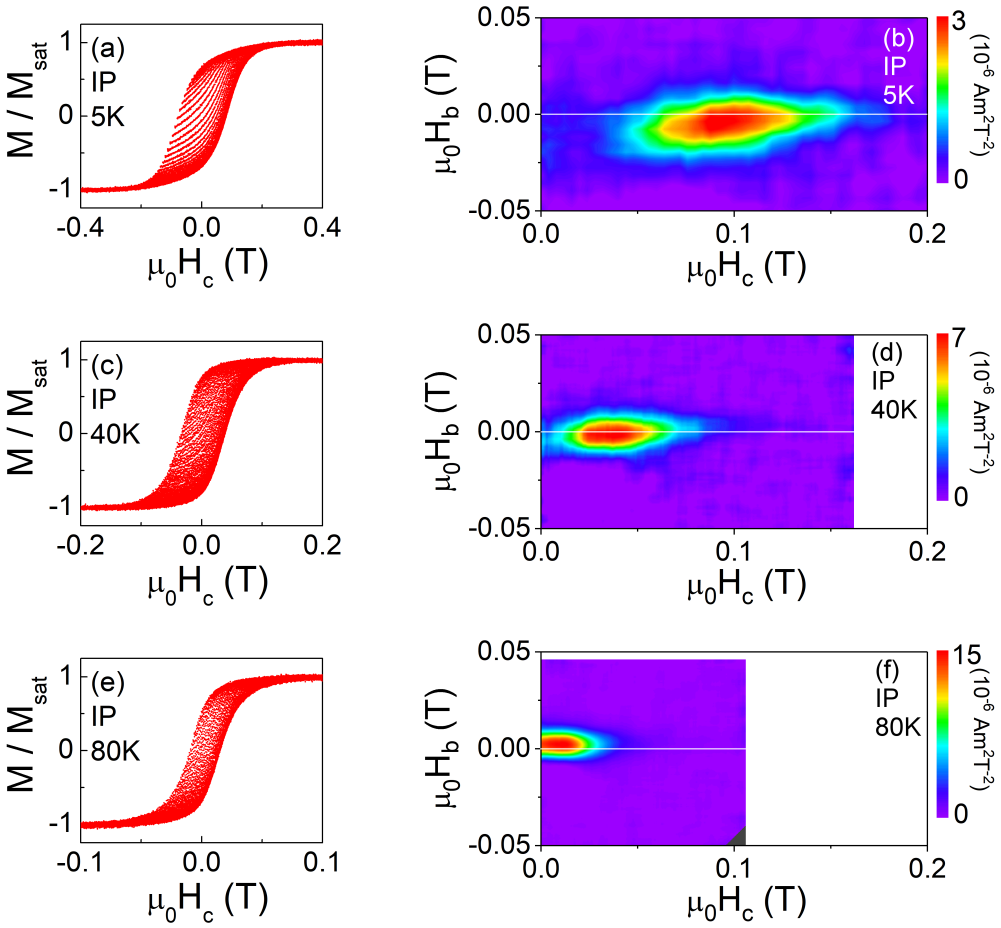

Figure 5.4: IP FORCs and corresponding FORC maps of sample S-5 at 5, 40 and 80 K. (a-b) Reversal curves made at 5 K after saturation at 0.8 T and corresponding FORC map. (c-d) Reversal curves made at 40 K after saturation at 0.5 T and corresponding FORC map. (e-f) Reversal curves made at 80 K after saturation at 0.3 T and corresponding FORC map.

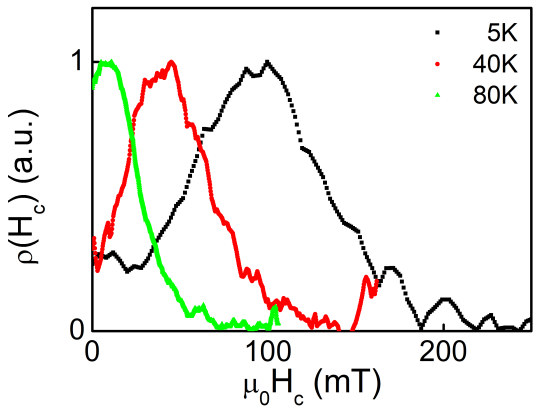

Figure 5.5: IP coercivity field distribution extracted from the FORC maps.

into account the last correction for simplification, especially since the bias effect becomes very small at 40 K and undetectable at 80 K.

5.2 Analysis of magnetic anisotropy

5.2.1 Magnetic anisotropy constants in Ni NWs

Here, I will evaluate contributions of the magnetostatic anisotropy K_{ms}, magnetocrystalline anisotropy (K_{mc}) and the magnetoelastic anisotropy K_{me} at low temperature. The cubic magnetocrystalline anisotropy constant K_{mc} is negative at -1.3×10^5 J/m^3 (Tab.5.3), with the easy axes along ⟨111⟩ directions. The aspect ratio of the present Ni NWs being high (length/diameter>20), K_{ms} is thus determined by $\frac{\mu_0 M_s^2}{4}$ and equals to 0.8×10^5 J/m^3. K_{me} is related to the axial strain, given by $K_{me} = \frac{3}{2}\lambda_{001}(c_{11} - c_{12})(\epsilon_{zz} - \epsilon_{rr})$. The coefficients λ_{001} and $(c_{11} - c_{12})$ are listed in Tab.5.3. Since the magnetostriction λ_{001} is negative for Ni, K_{me} plays against K_{ms} in the case of a tensile strain ($(\epsilon_{zz} - \epsilon_{rr}) > 0$). In neglecting ϵ_{rr}, the compensation of these two terms occurs at $\epsilon_{zz} \approx 0.8\%$. In our study, Ni NWs are highly strained with $\epsilon_{zz} > 2\%$. The magnetoelastic anisotropy should dominate the magnetostatic one.

Table 5.3: Constant of Ni: M_s, the saturation magnetization density [35]; $K_{mc} \equiv K_1^c$, the first order constant of the cubic magnetocrystalline anisotropy at 0 K [33]; λ_{001}, the magnetostriction constant [100]; $(c_{11} - c_{12})/2$, the elastic constant.

M_s (A/m)	K_1^c (J/m^3)	λ_{001}	$(c_{11} - c_{12})/2$ (N/m^2)
5.1×10^5	-1.2×10^5	-5.9×10^{-5}	5.5×10^{10}

The values of K_{me} of the samples evaluated with the mean strain are listed in Tab.5.4, together with the total anisotropy constants $K_{tot} = K_{ms} + K_{me}$. It can be seen that the absolute value of K_{me} is one order of magnetitude larger than that of K_{ms} for highly strained Ni NWs ($\langle\epsilon_{zz}\rangle$ from 2.3 to 3.9%). This indicates that the strain is at the origin of the appearance of a hard magnetization axis along the wire axis, as observed in Fig.5.1. With increasing strain, K_{tot} is increased. The ratio of the IP and OP saturation fields, $H_{s,\perp}/H_{s,\parallel}$, constitutes a criterion to appreciate the increase of the anisotropy. The ratio $H_{s,\perp}/H_{s,\parallel}$, observed increases from 1.3 to 1.7 for the group of samples U-3, U-5, S-4 and S-6 and from 1.1 to 1.3 for that of samples S-3 and S-5, with increasing strain or increasing value of magnetic anisotropy. It confirms that the strain increase reinforces the hardness of the NW axis for the magnetization, with respect to the plane perpendicular to the wire axis.

Table 5.4: Structural properties of NWs and magnetic anisotropy contributions of samples: $\langle D\rangle$ the mean diameter of wires; K_{ms} the magneto-static anisotropy constant; $\langle\epsilon_{zz}\rangle$ the mean axial strain of NWs; K_{me} the magneto-elastic anisotropy constant.

Sample	$\langle D\rangle$ (nm)	$\langle\epsilon_{zz}\rangle$	K_{me} (J/m^3)	$K_{ms} + K_{me}$ (J/m^3)
U-3	1.9	3.9%	-3.8×10^5	-3.1×10^5
U-5	2.5	3.6%	-3.3×10^5	-2.6×10^5
S-3	4.1	3.2%	-3.1×10^5	-2.4×10^5
S-4	4.5	2.8%	-2.7×10^5	-2.0×10^5
S-5	5.0	2.4%	-2.3×10^5	-1.6×10^5
S-6	5.3	2.3%	-2.2×10^5	-1.5×10^5

In summary, the establishment of the easy magnetization plane and hard axis in Ni NWs is compatible with the magnetic anisotropy constants. With a large tensile strain ($\gg 0.8\%$), the magnetoelastic anisotropy predominates over the magnetostatic effects and imposes the hard magnetization axis along the wire axis. However, many questions remain about the magnetic hysteresis of Ni NWs: (i) what is the origin of the opening of IP and OP hysteresis cycles? (ii) why is the easy plane isotropic?

5.2.2 Anisotropy with the Stoner-Wohlfarth model

I will now detail the hysteresis cycles expected from the fully coherent Stoner-Wohlfarth (SW) model. If one considers at first only the magnetostatic anisotropy K_{ms} and the magnetoelastic anisotropy K_{me}, the system is uniaxial along the wire axis and the anisotropy energy E_a density is written as:

$$\frac{E_a^{uni}}{V} = (K_{ms} + K_{me}) \sin^2\theta = \left(\frac{\mu_0}{4} M_s^2 + \frac{3}{2}\lambda_{001}(c_{11} - c_{12})(\epsilon_{zz} - \epsilon_{rr})\right) \sin^2\theta \tag{5.2}$$

The compensation between the shape effect and the elastic effect occurs at $\epsilon_{zz} - \epsilon_{rr}$=0.8%. In our case, the axial strain is of about 3% and the in-plane strain is neglected before the axial strain anisotropic behavior. This leads to the total anisotropy $K_{ms} + K_{me}$ of about -2.2×10^5 J/m^3. The resulting hysteresis cycles are shown in Fig.5.6(a). It indicates an easy magnetization plane and a hard axis without coercivity.

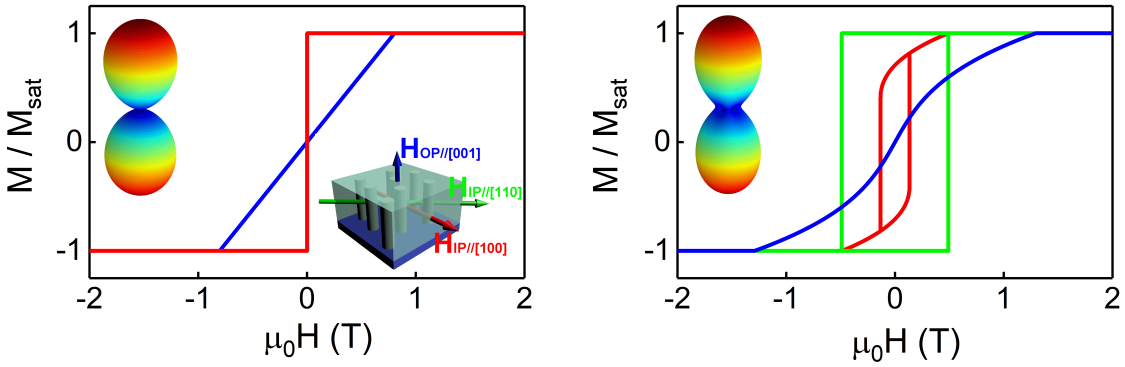

(a) (b)

Figure 5.6: Relative magnetization of Ni NWs according to the SW model for a strain $\epsilon_{zz} - \epsilon_{xx}$ of about 3%. (a) Uniaxial case with K_{ms} and K_{me}. Inset: uniaxial anisotropy energy density $E_a^{uni}/V(\theta)$ plot. (b) Tetragonal case including K_{mc}. Inset: tetragonal anisotropy energy density $E_a^{tetra}/V(\theta,\phi)$ plot. The external magnetic field is applied in three directions: H_{OP} (blue), $H_{IP\|[100]}$ (red) and $H_{IP\|[110]}$ (green)

The Ni cubic magnetocrystalline constant K_{mc} is -0.05×10^5 J/m^3 at room temperature and highly increased at 0 K, of -1.2×10^5 J/m^3, which is comparable to $(K_{ms} + K_{me})$. In taking K_{mc} into consideration, the total anisotropy is of tetragonal symmetry. The total anisotropy energy E_a can be described as the sum of these three terms:

$$\frac{E_a^{tetra}}{V} = K_1 \sin^2\theta - K_{mc} \sin^4\theta + K_q \sin^4\theta \sin^2 2\phi \tag{5.3}$$

where K_1=$K_{ms} + K_{me} + K_{mc}$, K_q=$K_{mc}/4$. θ and ϕ are the angles of the magnetization M. The K_{mc} contribution implies the existence of the IP easy axis along [110] direction ($\phi = \pi/4$) and of an IP secondary hard axis along [100] direction ($\phi = 0$). When the field H is applied along [001] direction, the magnetization evolves through the IP easy axis ($\phi = \pi/4$). The total free energy density F in including the Zeeman energy is given by:

$$F = -\mu_0 M_s H \cos\theta + K_1 \sin^2\theta - \frac{3}{4} K_{mc} sin^4\theta \tag{5.4}$$

By minimizing the free energy density, $\partial F/\partial\theta$=0, a resolution of M(H) cycle is shown in Fig.5.6(b) in blue. When H is applied in the plane (θ=$\pi/2$) along an azimuthal angle of ϕ_H with respect to [100] direction. The free energy density is written as:

$$F = -\mu_0 M_s H \cos(\phi - \phi_H) + K_q \sin^2 2\phi \tag{5.5}$$

Thus, ϕ_H is 0 for H_{IP} along [100] direction and $\pi/4$ along [110]. The minimization of the free energy density, $\partial F/\partial\phi$=0, provides the $M(H)$ cycles in [100] and [110] directions shown in Fig.5.6(b) in red and green, respectively.

For the hard axis, the magnetocrystalline effect bends the magnetization curve. K_1 contains the three anisotropy contributions along the hard axis, where the constant K_{mc} is negative as like the constant K_{me}. This increases the saturation field along the hard axis, determined by the absolute value of K_1. In the easy plane, the cycles are open. Due to the quadratic modulation of the anisotropy energy in the plane, the minimum of coercive fields is found for $H_{IP\|[100]}$: $H_{c,[100]} = 130$ mT. The maximum of coercive fields is obtained by applying $H_{IP\|[110]}$: $H_{c,[110]} = 490$ mT. It should be pointed out that this was not observed: not only the IP coercive fields measured are not in the range of $[130 - 490]$ mT, but also there is no difference between [100] and [110] direction as shown in Fig.5.1. These features indicate that the opening of cycles is not related to the magnetocrystalline anisotropy contribution. Therefore, we will neglect K_{mc} thereafter and consider K_{me} as the main effect on the magnetic behavior.

A large tensile strain even with a broad distribution does not give arise to the IP coercivity. In order to take into account local energy barriers in the easy plane, it is thus necessary to introduce a second uniaxial constant K_r reflecting a non-homogenous IP strain along the NWs. In a simple case where only the IP compressive strains, ϵ_{xx} and ϵ_{yy}, are concerned, the strain tensor $\widehat{\epsilon}$ is written as:

$$\widehat{\epsilon} = \begin{bmatrix} \epsilon_{xx} & 0 & 0 \\ 0 & \epsilon_{yy} & 0 \\ 0 & 0 & \epsilon_{zz} \end{bmatrix} \tag{5.6}$$

In considering the magneto-static and magnetoelastic contributions, the anisotropy constant $\widehat{K}$ is a tensor of second rank and expressed by: $E/V = -\mathbf{m} \cdot \widehat{K}\mathbf{m}$, where $\mathbf{m}$ is the magnetization unit vector:

$$\widehat{K} = \begin{bmatrix} K_r/2 & 0 & 0 \\ 0 & -K_r/2 & 0 \\ 0 & 0 & K_1 \end{bmatrix} \quad \text{with} \quad \left\{ \begin{array}{l} K_r = -B_1(\epsilon_{xx} - \epsilon_{yy}) \\ \\ K_1 = -B_1(\epsilon_{zz} - \epsilon_{rr}) + K_{ms} \end{array} \right\} \tag{5.7}$$

where ϵ_{rr} is defined as $(\epsilon_{xx}+\epsilon_{yy})/2$ and the magnetoelastic coupling constant B_1 equal to $-3/2\ \lambda_{001}\ (c_{11}-c_{12})$. The anisotropy energy density is thus written as:

$$E/V = -K_1 \cos^2\theta - \frac{K_r}{2} \sin^2\theta \cos(2\phi) \tag{5.8}$$

If the IP strain is homogeneous, $\epsilon_{xx} = \epsilon_{yy} = \epsilon_{rr}$, one recovers the uniaxial anisotropy defined by: $E/V = -K_1 \cos^2\theta$. When there is a difference in the IP strain along the two axes $(\epsilon_{xx} - \epsilon_{yy})$, a local anisotropy barrier appears in the easy plane and is represented by the constant K_r. This can be easily generalized in taking into account the IP shear strain ϵ_{ij} $(i \neq j = x \text{ or } y)$ with the associated magnetoelastic coupling constant B_2 $(=-3\lambda_{111}\ c_{44})$. In this case, the IP easy axis is oriented at an azimuthal angle ϕ_0. For Ni, the values of B_1 and B_2 are close [Sander 1999] and the IP principal axes of the anisotropy are almost aligned with that of the IP strain. The anisotropy energy density E/V can be expressed by:

$$E/V = -K_1 \cos^2\theta - \frac{K_r}{2} \sin^2\theta \cos(2(\phi - \phi_0)) \tag{5.9}$$

According to the XRD measurements, the IP strain ϵ_{rr} is much weaker that the axial strain ϵ_{zz}. It can be deduced that the value of K_r, associated to the variance of ϵ_{rr}, should be weaker than the absolute value of K_1, determined by $(\epsilon_{zz} - \epsilon_{rr})$. Fig.5.7 displays the anisotropy energy density of a

typical case for the present Ni NWs where $K_r/|K_1| = 1/3$.

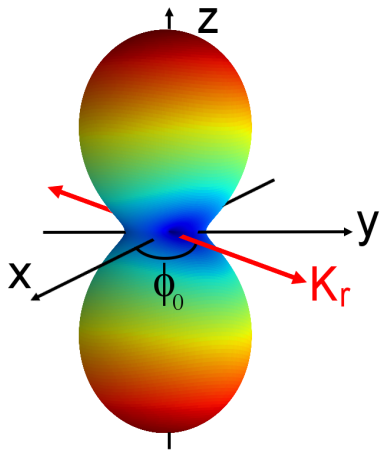

Figure 5.7: Plot of local anisotropy energy surface $E_a(\theta, \phi)/V$, with $|K_1|$ 3 times larger than K_r. The easy axis is oriented in-plane at the azimuthal angle of ϕ_0.

Furthermore, the anisotropy axes (ϕ_0) should be IP randomly oriented. In such a way, it is locally anisotropic and overall isotropic, in accordance with the experiments. This provides a general picture where the anisotropy in the easy plane is modulated along the NW axis by the IP strain inhomogeneity. I will deepen this idea by focusing first on the activation volumes possibly involved in the magnetization reversal with such anisotropy and then make the simulation in using the parameters of the analysis.

5.2.3 Activation lengths according to the RMA model

Considerations based on the SW coherent model deal with the anisotropy constants, independently of the volume concerned. However, the activation or magnetization switching volume is fundamental. For local magnetization correlation, we take as the scale the width of a Bloch wall, $\delta_0 = \pi\sqrt{A/|K|}$ where A is the exchange stiffness constant. The exchange strength prevents the length of local magnetization correlation to be shorter than the width of one domain wall. For Ni, δ_0 is equal to 29 nm for $|K|$ of 10^5 J/m^3. For our ultrathin NWs, magnetization can be considered to be coherent in a section of a NW, given the smallness of the present NW diameters before δ_0. On the other side, it was established that magnetization switching is in general localized along a NW, initiated by morphological, structural or anisotropy inhomogeneities and nucleated over a length of a domain wall [101, 102, 7]. One notices that the magnetic length δ_0 is larger than the structural domain size δ_s, from 6 to 13 nm as measured by XRD. It indicates that the magnetization reversal unit is composed by more than a structural domain with a random anisotropy direction. This unit is called macrospin. According to Herzer, the effective local anisotropy should be averaged or renormalized with an averaged anisotropy $\langle K \rangle$ over N neighboring domains [49]. It means that the anisotropy constants magnetically measured are not directly those deduced by the strain or the magnetoelastic effect, but those further softened by the local averaging.

For the 3D case, when K and the domain size δ_s are fixed and only the anisotropy axis is randomly oriented, a magnetic domain of δ^3 volume includes N structural domains of volume δ_s^3, so that the anisotropy constant $\langle K \rangle$ averaged over the magnetic volume scales is of $K/\sqrt{N}$ and results in a magnetic length δ as $\pi\sqrt{A/\langle K \rangle}$. The equilibrium is found with the scaling rule: $\delta/\delta_0 = (\delta/\delta_s)^3$ (Tab.5.5). In other terms, the magnetic correlation length δ increases with decreasing domain size δ_s with a cubic power law and the averaged anisotropy consant $\langle K \rangle$ with a law in δ_s^6. This allows to explain successfully the coercivity reduction as a law in power 6 of the average grain size in soft magnetic nanocrystalline films [49, 50].

For the 1D case, a similar consideration leads to the scaling rule of $\delta/\delta_0 = (\delta_0/\delta_s)^{1/3}$ (Tab.5.5).

If the domain size δ_s in Ni NWs is chosen at 6 nm and the magnetic length δ_0 at 29 nm, the magnetic length δ deduced is about 50 nm. In other terms, a magnetic volume of 8-9 structural domains acting as a macrospin would be concerned in the magnetization reversal. Specifities of the Ni NWs in our case should be noticed: (a) the IP anisotropy fluctuation comes from the IP strain inhomogeneity; (b) a NW is considered as a 1D chain, where the anisotropy easy axis is randomly oriented in the plane perpendicular to the NW.

Table 5.5: RMA characteristics in the 1D and 3D cases in term of δ_0/δ_s, ratio between the intrinsic magnetic length δ_0 associated to the anisotropy constant K and the domain size δ_s: N, number of domains within a magnetic volume; δ, magnetic length related to the mean anisotropy constant $\langle K \rangle$ over the magnetic volume.

	N	δ/δ_0	$\langle K \rangle / K$
3D	$(\delta_0/\delta_s)^{12}$	$(\delta_0/\delta_s)^{3}$	$(\delta_0/\delta_s)^{-6}$
1D	$(\delta_0/\delta_s)^{4/3}$	$(\delta_0/\delta_s)^{1/3}$	$(\delta_0/\delta_s)^{-2/3}$

5.3 Modelisation and simulation

5.3.1 Simulation of the IP hysteresis cycles at low temperature

Based on the above considerations, I will calculate the IP hysteresis cycles with the SW model in considering a magnetically correlated domain as a macrospin with its anisotropy constant K_r and magnetic length $\pi\sqrt{A/K_r}$. The IP anisotropy axis is randomly oriented. Furthermore, a distribution of the anisotropy constant K_r is considered, with regard to the broad distributions of blocking temperatures T_b observed in the samples as shown in Fig.5.2. In this approch, the macrospins are considered independent of each other. A difference with the experiments would provide inidcation on the lacking parameters concerning the interaction between the macroscpins, *i.e.* the dipolar interaction or the exchange coupling.

I start the calculation by integrating all SW hysteresis cycles of an assembly with a unique constant K_r and 3D or 2D randomly oriented anisotropy axes (Fig.5.8). One notices that the remanence m_R is 1/2 for the 3D random case and higher at 0.64 for the 2D random case. The coercive field H_c is equal to $0.48H_a$ for the 3D case and $0.51H_a$ for the 2D case, where $\mu_0 H_a = 2K_r/M_s$. For different values of K_r, the cycles for the 2D case keep the same shape with the coercive field H_c varying linearly with K_r (Fig.5.9(a)). Thus, a distribution of the anisotropy constant $f(K_r)$ will be taken into account by integrating all these cycles weighted by the volumes concerned.

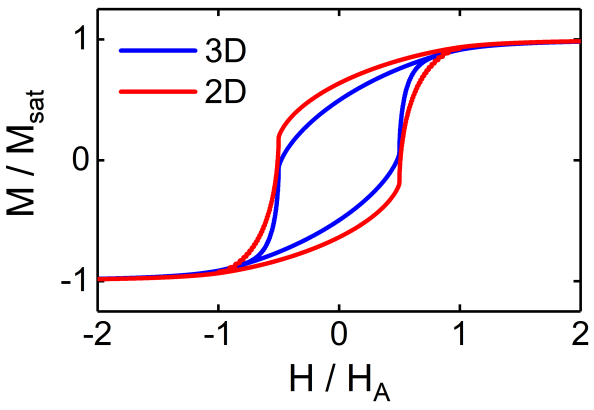

Figure 5.8: Hysteresis cycles of an assembly with 3D and 2D randomly oriented anisotropy axes.

The thermal effect is complex and concerns both activation and agitation effects. Concerning the thermal activation, the Sharrock's law applied to the 2D random case gives:

$$H_c = 0.51 \times \frac{2K_r}{\mu_0 M_s} \times \left(1 - \left(\frac{25k_BT}{K_rV}\right)^{2/3}\right) \tag{5.10}$$

for $25k_BT < K_rV$. The volume V concerned here is equal to $S \times \delta$, with S the section area of a NW and $\delta = \pi\sqrt{A/K_r}$. The cycle is narrowed with increasing temperature, until the closure of the cycles at the blocking temperature $T_b = K_rV/(25k_B)$. From the closure of the cycles, the Langevin superparamagnetic treatment is used in the calculation.

The regular shapes of the SW hysteresis cycles, rectangular form for a easy axis and a slope for a hard axis, are too idealized. Different approachs exist in the literature in order to integrate the thermal agitation effect in the calculation of the SW cycles. For a hard axis, the thermal effect on the magnetization can be easily added according to the thermal partition of $\exp[-E/(k_BT)]$ where E is the sum of the Zeeman energy and the anisotropy one. When the cycle is open, the thermal agitation should be considered, only if the thermal activation does not occur. Here, we adopt the approach of Franco and Conde [103]: magnetization remains in its local energy well and is distributed following the thermal partition of $\exp[-E/(k_BT)]$, as long as the height of the well is below $25k_BT$. This procedure improves the shape of the calculated cycles, namely around the coercive field. An example of the cycle reduction between 0 and 10 K is shown in Fig.5.9(b), in including the thermal activation and agitation effects.

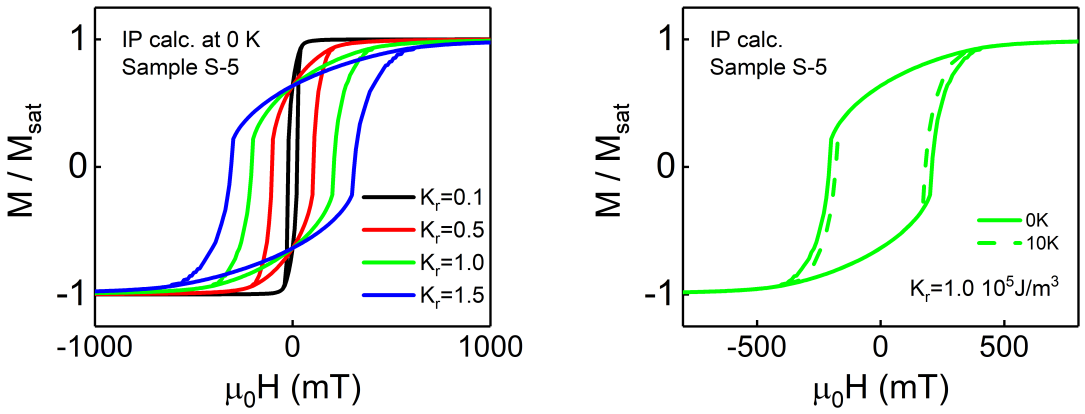

(a) (b)

Figure 5.9: (a) Calculations of hysteresis cycles at 0 K for sample S-5 for different anisotropy K_r in unit of 10^5 J/m^3. (b) Calculated hysteresis cycles at 0 K and 10 K with a constant K_r of 1.0×10^5 J/m^3.

In including all these ingredients, notably a distribution of the anisotropy constant $f(K_r)$, the calculated hysteresis cycles at 10 K for sample S-5 is shown in Fig.5.10, together with the experimental cycle. Surprisingly, such a simplified model with non-interacting macrospins fits quite well with the experiments. This suggests the interaction between macrospins should be weak, as it was also reflected in the FORC measurements. From the distribution of K_r used (Fig.5.10(b)), the mean value $\langle K_r \rangle$ is of about 0.5×10^5 J/m^3. The magnetic length δ used evolves with K_r (Fig.5.10(c)). For weak values of K_r ($< 0.1 \times 10^5$ J/m^3), δ is limited to the physical NW length of 106 nm for this sample. In increasing K_r until 10^5 J/m^3, δ decreases to about 1/3 of the physical NW length. The mean length $\langle \delta \rangle$ related to $\langle K_r \rangle$ is estimated to 41 nm.

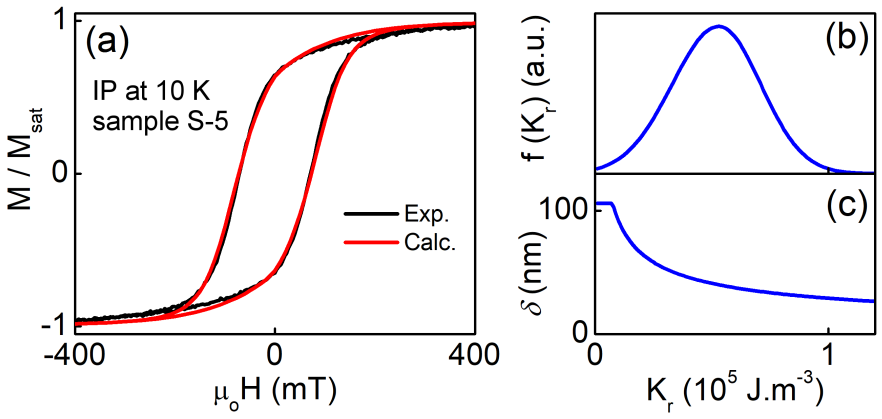

Figure 5.10: IP magnetic behavior at 10 K in sample S-5. (a) Measured and calculated IP hysteresis cycles. (b) Distribution of IP anisotropy $f(K_r)$ used in the calculation. (c) Magnetic length δ in function of K_r, with limitation of the physical NW length of 106 nm for sample S-5.

5.3.2 Simulation of the IP hysteresis thermal evolution

The previous simulation of the IP hysteresis cycles fits well only for one given temperature and cannot reproduce the thermal evolution of the cycles. It is to say that the thermal evolution, in particular the exponential decrease of $H_c(T)$, cannot be understood with a temperature-independent distribution of the anisotropy constant $f(K_r)$ and the Sharrock's thermal reduction of the coercivity. Here, I adopt an alternative strategy in considering that the distribution $f(K_r)$ is not constant in temperature. For one temperature, the cycle is fitted with a best suitable distribution $f(K_r)$ and the volume distribution of anisotropy $\rho(K_r)$ deduced as: $\rho(K_r) = f(K_r) \times \delta(K_r) \times S$ with $f(K_r)$ and $\delta(K_r)$ similarly to that shown in Fig.5.10. Then, the coercivity distribution $\rho(H_c)$ is retrieved from $\rho(K_r)$ by the Sharrock's formula (Equation 5.10).

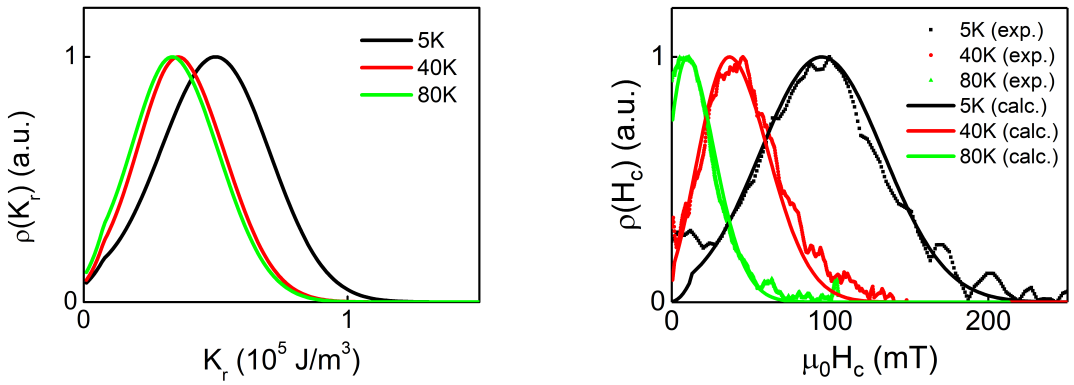

(a) (b)

Figure 5.11: Anisotropy and coercivity of sample S-5 at 5, 40 and 80 K. (a) Volume distribution of the IP anisotropy $\rho(K_r)$. (b) Coercivity distribution $\rho(H_c)$ deduced from $\rho(K_r)$ in applying the Sharrock's law and comparison with $\rho(H_c)$ extracted from the FORC measurements.

For sample S-5, the fitted volume distributions of anisotropy constant $\rho(K_r)$ at 5, 40 and 80 K are displayed in Fig.5.11(a)). The deduced coercivity distributions $\rho(H_c)$ are compared with the experimental $\rho(H_c)$ extracted from the FORC measurements (Fig.5.11(b)). The distribution $\rho(K_r)$ moves towards lower values of K_r with increasing temperatures. For sample S-5, the mean value of K_r decreases from 0.50 to 0.33×10^5 J/m^3 from 5 to 80 K. This evidences a thermal sofetning of the anisotropy in Ni NWs, in addition to the usual Sharrock thermal reduction of coercivity. With a thermal softening of anisotropy, the calculation was made for each measurement temperature up to the blocking temperature. Selected experimental and calculated cycles of sample S-5 at 5, 20, 40 and

80 K are shown in (Fig.5.12(a,b)). It can be seen that the whole shapes of the measured cycles and also the exponential decrease of $H_c(T)$ (Fig.5.12(c)) are well reproduced. It means that the exponential decrease of $H_c(T)$ is directly related to the thermal softening of anisotropy.

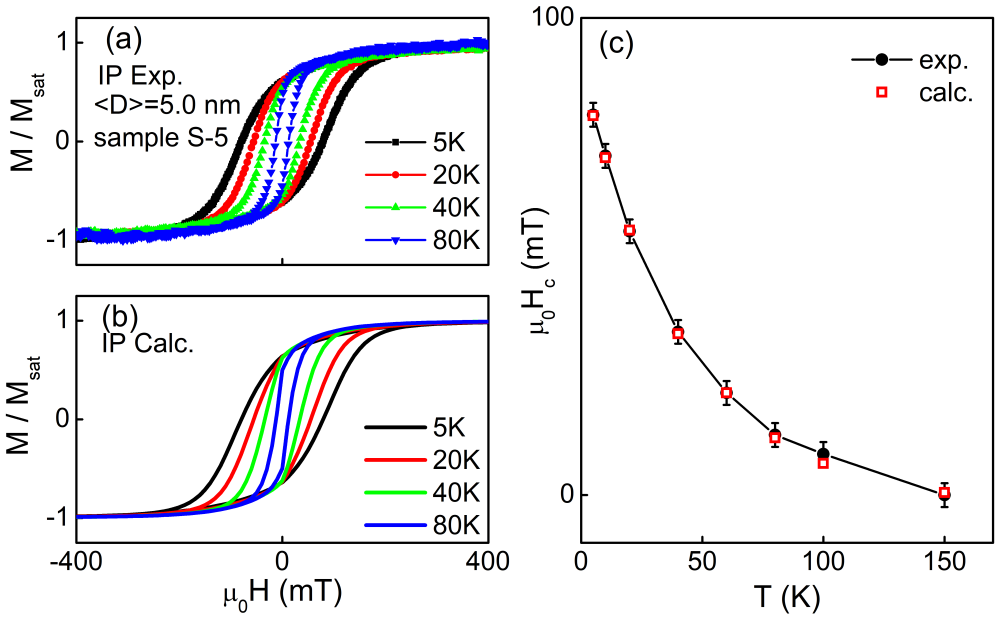

Figure 5.12: IP thermal evolution of hysteresis cycles and coercive field in sample S-5: (a) measured cycles at 5, 20, 40 and 80K; (b) calculated cycles with a thermal retraction of $\rho(K_r)$; (c) temperature dependence of the calculated and experimental coercivity $H_c(T)$.

The calculation made on the measured cycles of the samples confirmed the general tendency of the thermal softening of $\rho(K_r)$. Here, I choose the examples of samples U-5, S-3 and S-5, because the IP blocking temperatures $T_{b,\|}$ concerned are quite different: 26, 80 and 150 K, respectively for the three samples. The lecture of the results can be rationalized by tracking the mean value of K_r in temperature expressed in the reduced units of T/T_b (Fig.5.13). The mean values $\langle K_r \rangle$ extrapolated at 0 K are 0.47, 0.51 and 0.54 in 10^5 J/m^3 for samples U-5, S-3 and S-5, respectively. It indicates that the inhomogeneity in IP strain is in the 0.4-0.5% range, which is comparable to the IP strain $\langle \epsilon_{rr} \rangle$ of 0.3 to 1.0%. With increasing temperature, $\langle K_r \rangle$ decreases, leading to the acceleration of the hysteresis cycle closure in temperature. Correlatively, the magnetic lengths $\langle \delta \rangle$ increase with increasing temperature as displayed in Fig.5.13(b). The increase is about 30-40% from 0 K to T_b. One should pay attention to the fact that the mean value length $\langle \delta \rangle$ at 0 K for the three samples are of the same order, around 50 nm. This would indicate that whatever the details of the IP strain state in Ni NWs, the local averaging according to the RMA model leads to a similar magnetic correlation length.

Discussion on anisotropy thermal softening

The thermal softening of anisotropy constitutes a key feature of the magnetic properties of Ni NWs. Many works reported on variation of anisotropy in temperature and are often related to the variation of physical constants, such as magnetoelastic coupling constants or magnetocrystalline constants [104]. This possibility cannot be excluded in the present case. But, the dominating effect should not be related to a variation of constants. The samples show a similar thermal retraction of anisotropy distribution towards lower values, over different temperature ranges until 150 K. This suggests a general thermally activated process and not the thermal variation of a constant that would impact the samples differently in temperature. Intrinsic and extrinsic mechanisms should be searched in order to understand the thermal softening of anisotropy. As the magnetic correlation lengths and the anisotropy constants are fully equivalent within the RMA model, a thermally induced increase of the magnetic length implies a reduction of the anisotropy constant and *vice versa*.

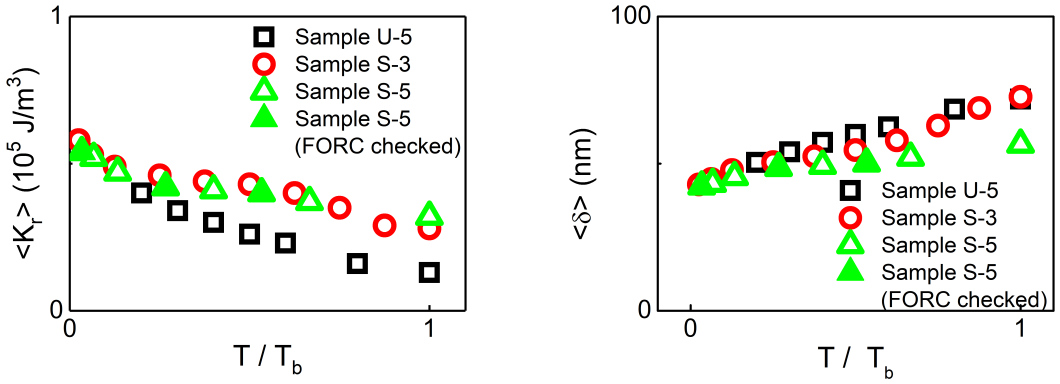

(a) (b)

Figure 5.13: IP thermal evolution of (a) the mean value of the anisotropy constant $\langle K_r \rangle$ and (b) the mean value of the magnetic activation length $\langle \delta \rangle$ for samples U-5, S-3 and S-5. The three values validated by the FORC measurements at 5, 40 and 80 K in sample S-5 are marked by green solid scatters.

The basic intrinsic mechanism involves the thermal increase of a domain wall (DW) width $\delta_0(T)$. The fact that the DW width increases linearly in temperature is important for the understanding of the DW motion in nanostructures [105, 106]. It is a general phenomenon for DWs, including ferroelectric ones [107]. The exchange energy of a DW of δ length in a NW scales as $A(\theta/\delta)^2\delta S$ and the anisotropy energy as $(K/2)\delta S$, where S is the wire section area and θ an effective angle constant. By minimizing the total energy, $E \approx (\delta_0/\delta + \delta/\delta_0)/2 \times K\delta_0 S$, one finds δ_0, the intrinsic DW width at 0 K, that fits with the usaul Bloch DW width in choosing $\theta = \pi/\sqrt{2}$. At finite temperature, the numeric resolution of the thermal partition of $\exp(-E/(k_B T))$ provides a linear increase of the intrinsic DW width: $\delta_0(T) = \delta_0(1 + \alpha T)$, where $\alpha = 1.534 k_B/(K\delta_0 S)$. For sample S-5, $S = 19.6$ nm^2 and the intrinsic DW width δ_0 is estimated to 29 nm. Thus, $\delta_0(T_b)$ increases by about 6% from 0 K to T_b of 150 K. According to the RMA model, the increase of $\delta_0(T)$ induces consequently that of the local effective $\delta(T)$. This can be estimated through the scaling relationship in Tab.5.5, which leads to $\delta(T) \approx \delta_0(T)^{4/3}$. Therefore, the total intrinsic thermal increase of $\delta(T)$ from 0 K to T_b is evaluated at around 8%. Such an intrinsic thermal increase of δ is still far from 34% observed in Fig.5.13(b). This effect does not cover the decay rate of the coercivity. Hence, other mechanisms of anisotropy softening in Ni NWs should be considered.

Few cases of exponential decreasing $H_c(T)$ reported were often related to random nanomagnets or nanocomposites [108, 109, 110]. Causes mentioned in these studies dealed with the pinning of DWs. This would suggest that the DW pinning could be inherent to nanostructured magnets and the thermal softening of anisotropy a general feature of RMA. Intrinsic DW pinning at lattice planes occurs for narrow DWs and can be ruled out for the present large DWs. Extrinsic pinning due to defects can be envisaged, but need to be detailed beyond a phenomenological description of DW pinning [111]. Kirby *et al.* proposed a mechanism of incoherent magnetization reversal in thin films with a $1/H$ field dependence of energy barriers [112]. This model predicts that the activation volume varies linearly with T at low temperature and as T^2 at high temperature. In a detailed study in an epitaxial Co/Ni-based spin-valve wire, Le Gall *et al.* analyzed the DW depinning meachanism by magnetic field and current [113].

This quick review indicates that the thermal softening of anisotropy observed in the present NWs could be qualitatively related to intrinsic and/or extrinsic thermal activated process. Further theoretical work will be needed to establish a quantitative analysis, particularly with regard to possible defects at the origin of DW pinning in the vertical NWs epitaxied in matrix.

5.3.3 Magnetic behavior along the hard axis

The IP anisotropy examined does not give rise to the OP coercivity. As the thermal evolution of the IP and OP coercivity is similar, the same magnetoelastic origin can be considered for the hard axis. Compared to the IP mechanism, the OP anisotropy is more complex to be detailed. For a NW assembly, one should take into account the distributions of the OP anisotropy constant K_1 and the IP anisotropy constant K_r and include the magnetoelastic effect related to the local axial shear strain (ϵ_{rz} and $\epsilon_{\theta z}$). This would result on a wandering of the hard axis around the OP axis, as depicted in Fig.5.14. It means that the OP hysteresis cycles evolves from a hard axis cycle towards the 3D random anisotropy case. Il should be pointed out that random ferromagnets with a wandering easy axis was very early pointed out by Chudnovsky *et al.* [48]. Analysis of a wandering hard axis or easy plane has not been reported in the literature to our knowledge.

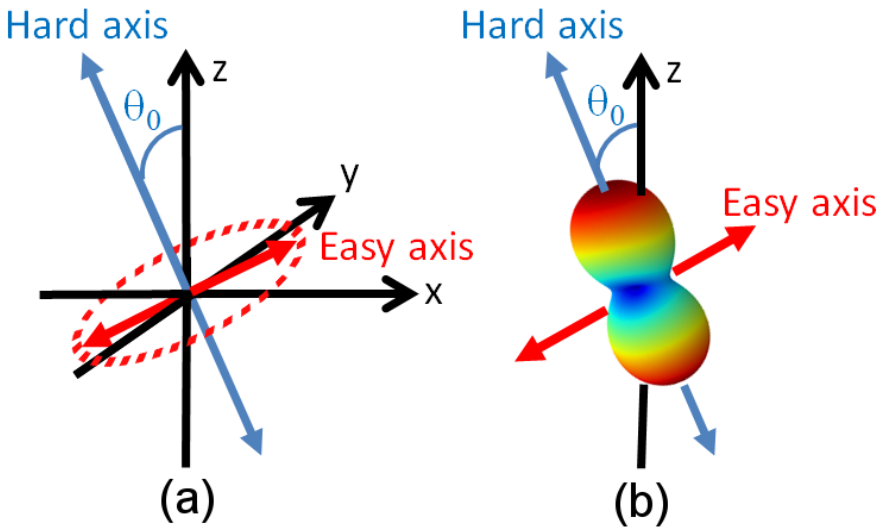

Figure 5.14: Sketch of local anisotropy energy surface $E(\theta, \phi)$ where the hard axis is apart from the z axis by an angle of θ_0. (a) Definition of the axes, where the dashed cycle represents possibe orientations of the easy axis. (b) Plot of $E(\theta, \phi)$.

Even within the SW model, the 3D evolution of the magnetization is complex in this case. With a rude approximation that the OP axis, the hard axis and the easy axis are in one plane, an estimation of the order of magnetude of the wandering angle θ_0 could be obtained. The assumption is equivalent to consider only part of the tensor $\widehat{K}$:

$$\widehat{K'} = \begin{bmatrix} K_r/2 & K_{rz} \\ K_{rz} & K_1 \end{bmatrix}$$

where K_{rz} is related to the local shear strain ϵ_{rz} through the magnetoelastic coupling constant B_2. In this case, the remanence is of the order of $\sin(\theta_0)$ and the saturation field H_s given by the anisotropy constant difference ΔK between the hard axis and easy axis: $\mu_0 H_s = 2\Delta K/M_s$ where $\Delta K = |K_1 - K_r/2|/\cos 2\theta_0$ established by diagonalizing $\widehat{K'}$. Using the measured OP remanence $m_{R,\perp}$ and the OP saturation field $H_{s,\perp}$ (in Tab.5.1), the mean value of the wandering angle θ_0 of the hard axis with respect to the z axis and that of the OP anisotropy K_1 can be approximately estimated.

The mean values of K_1 and θ_0 are listed in Tab.5.6, together with $\langle K_r \rangle$ determined by the simulation of IP hysteresis cycles. The strain effect is clearly reflected in the values of $\langle K_1 \rangle$ and $\langle \theta_0 \rangle$. With increasing axial strain, the value of $\langle K_1 \rangle$ is increased, while the wandering angle $\langle \theta_0 \rangle$ is reduced, similarly for the group of samples U-3, U-5, S-4 and S-6 and the group of S-3 and S-5. The absolute value of $\langle K_1 \rangle$ is much larger than that of $\langle K_r \rangle$, reflecting the hard axis character of the NWs. It should be noticed that the absolute values of $\langle K_1 \rangle$ are of 20-40% lower than those calculated by the shape effect and the mean strain ($K_{ms} + \langle K_{me} \rangle$). The lowering of $\langle K_1 \rangle$ should be related to the RMA local averaging.

Table 5.6: Mean IP and OP anisotropy constants $\langle K_r \rangle$ and $\langle K_1 \rangle$ and mean wandering angle $\langle \theta_0 \rangle$ of the hard axis estimated for the samples at 10 K.

Sample	$\langle K_r \rangle$ (10^5 J/m^3)	$\langle K_1 \rangle$ (10^5 J/m^3)	$\langle \theta_0 \rangle$ (°)
U-3	0.38	-2.3	2
U-5	0.27	-1.8	8
S-3	0.41	-1.8	21
S-4	0.40	-2.1	9
S-5	0.51	-1.2	24
S-6	0.32	-2.0	15

5.4 Summary and discussion

The mean anisotropy of the Ni NW assembly, *i.e.* the OP hard axis and the mean isotropic IP easy plane, is induced by the mean axial tensile strain. The IP coercivity is deduced by the IP strain inhomogeneity. Similarly, arising of the OP coercivity is interpreted by the wandering of the local hard axis caused by fluctuation of the local axial shear strains. The IP hysteresis cycles are simulated by macrospins of length scaling as the local RMA magnetic correlation length. The exponential decay of $H_c(T)$ in temperature is understood as due to the Sharrock's effect and a thermally activated process of anisotropy softening or equivalently of increasing in magnetic correlation length.

Focus has been made on the magnetoelastic effect due to the epitaxial strain of the Ni NWs in STO matrix. Other possible causes of strain and anisotropy should be examined. Firstly, it is intriguing that the magnetocrystalline effect is not observable in the measurements, while as $|K_{mc}|/4$ is of the same order of K_r at low temperature. Jorritsma and Mydosh [114] reported Ni NWs horizontally aligned and strained on patterned InP substrate where K_{mc} was also ignored for the whole range of 5-300 K. Two assumptions can be made: (a) K_{mc} is weaker than expected, especially in highly strained NWs; (b) strain distortion destroys locally the tetragonal symmetry and then masks the K_{mc} effect. For example, if local strain is considered as part of Ni fcc to bcc transformation, the Bain tetragonal path [115] is characterized by ϵ_{xx}=ϵ_{yy}=-$\epsilon_{zz}/2$ for small values of ϵ_{zz}. Even if the mean strain in our NWs respects the tetragonal symmetry, the ratio of $|\epsilon_{rr}|/\epsilon_{zz}$ is far from 1/2 of the Bain path and varies from 1/3.6 to 1/8. A second and trigonal path exists with $\langle 111 \rangle$ direction as symmetry axis [116]. Averaging over the four equivalent $\langle 111 \rangle$ variants leaves the only non-null value in the mean strain $\langle \epsilon_{zz} \rangle$ and could explain the departure of the mean strains from the Bain path. It is plausible that local strain distortion in the NWs includes large part of the trigonal deformation masking the K_{mc} effect.

Surface anisotropy [117] becomes important for objects of nanosize. The anisotropy energy density induced should scale as the inverse of the NW diameter. For the present case, no evident feature can be related to the surface anisotropy. Contrary to the case of a film, the cylindrical interface between the NWs and the matrix should make the contribution of surface anisotropy negligible to the coercivity. Indeed, a uniform radial contribution does not contribute to K_r which comes from the IP inhomogeneity. A surface contribution is at least of second order: only the IP angular fluctuation of surface anisotropy contributes to the IP coercivity.

For the thermal evolution of the coercivity, thermal variation of physical constants cannot be excluded, namely concerning the elastic ones, the magnetoelastic coupling ones and the magnetocrystalline ones. The effect is supposed to be secondary here, with respect to the common thermal anisotropy softening observed in different temperature ranges in the samples.

Thermal origin of the strain should be also questioned. The difference in the thermal expansion of the Ni NWs and matrix may constitute source of strain in NWs, as demonstrated in Ni NWs

electrodeposited on porous alumina templates [118, 119]. The thermal expansion coefficient is 13.4 for Ni and around 9.5 for $SrTiO_3$ in 10^{-6}/K units. From the growth temperature to the room one, NWs would sustain a radial dilatation from the matrix and consequently a NW axial compression, contrary to the NW axial tensile strain observed. The maximal thermal strain can be estimated as the product of the temperature difference by the difference of the thermal expansion coefficients of Ni and $SrTiO_3$. The maximal thermal strain is then $\leq$0.25%, one order of magnitude lower than the measured strain.

The magnetoelastic effect resulting from the epitaxial strain analyzed here appears to be the dominating effect. It should be pointed out that absence of any coercivity is a specificity of the mean anisotropy with a hard axis and an easy plane (Fig.5.1), contrasting with the case of an easy axis and a hard plane. Any additional contribution of cylindrical symmetry does not give rise to coercivity neither. It means that other sources of anisotropy, such as surface anisotropy or thermal strain, do not change the anisotropy, but only modifies the hardness of the hard axis, *i.e.* the value of K_1. Coercivity arises from local fluctuation of a contribution. Therefore, strain distortion established by XRD measurements constitutes the main source of the coercivity.

5.5 XMCD investigation at Ni $L_{2,3}$ edges

Spectroscopic measurements at the Ni $L_{2,3}$ edges were performed at DEIMOS beamline of synchrotron SOLEIL in order to measure the spin and orbital moment of Ni.

5.5.1 XMCD spectroscopy measurements and analysis

The Ni sample used to perform the spectroscopic measurements is sample S-5, with $\langle D \rangle$ of 5 nm and capped with a thin layer of AlO_x of thickness 1-2 nm in order to prevent sample oxidation, as shown in Fig.5.15(a). The principle is illustrated in Fig.5.15(b): under an external magnetic field H parallel or antiparallel to the direction of the x-ray propagation, the circularly polarized light can penetrate the sample to excite the electrons. The difference of the absorption spectra in taking the left and right circularly polarized x-rays provides information of the magnetic properties, such as the spin and orbital moments. In rotating the sample by angle θ, we can explore the angular evolution of magnetic characteristics in the system. $\theta = 0°$ is related to the case where the applied magnetic field is perpendicular to the sample, noted H_{OP}.

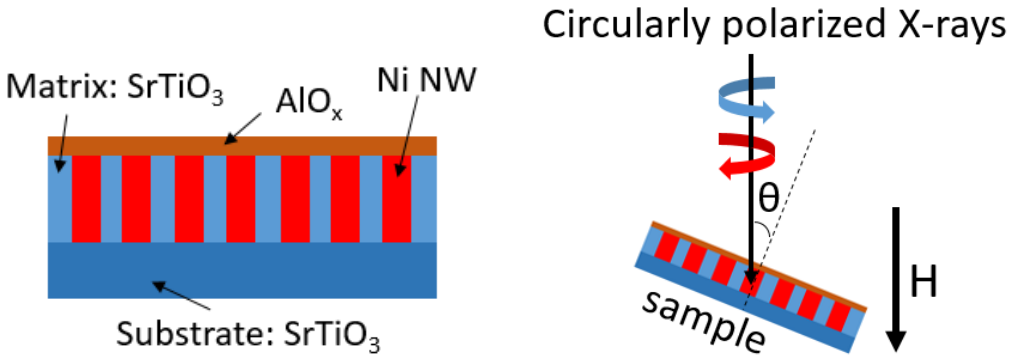

(a) (b)

Figure 5.15: (a) Schematics of a sample for the XMCD measurements. (b) Illustration of the principle of XMCD measurements. θ is the angle between the sample normal and the magnetic field.

Attention should be paid to the fact that the penetration depth of x-rays of energy in the 700-900 eV range is about 0.5 μm, which is much larger than the thickness of our samples. However, the electron escape length in Ni is only several nanometers. Therein, the detected intensity corresponds only to the absorption of parts of the wires near the surface.

Fig.5.16 depicts the Ni $L_{2,3}$ edges XMCD spectra at $\theta = 0°$. Here, μ^+ corresponds to the

following cases: the external field is parallel to the left circularly polarized x-ray propagation direction $(H+, CL)$ and is antiparallel to the right circularly polarized x-ray propagation direction $(H-, CR)$. On the contrary, μ^- corresponds to the cases where the external field is parallel to the right circularly polarized x-ray propagation direction $(H+, CR)$ or antiparallel to the left circularly polarized x-ray propagation direction $(H-, CL)$. At Ni $L_{2,3}$ edges, the absorption is different for the μ^+ and μ^- cases. The XMCD spectrum is obtained by the expression $\Delta\mu = \mu^+ - \mu^-$, as displayed in Fig.5.16(b). The surface areas below and above 0 represent separately the absorption difference at Ni L_3 and L_2 edges. The absorption spectra indicate that the Ni is metallic in the wires.

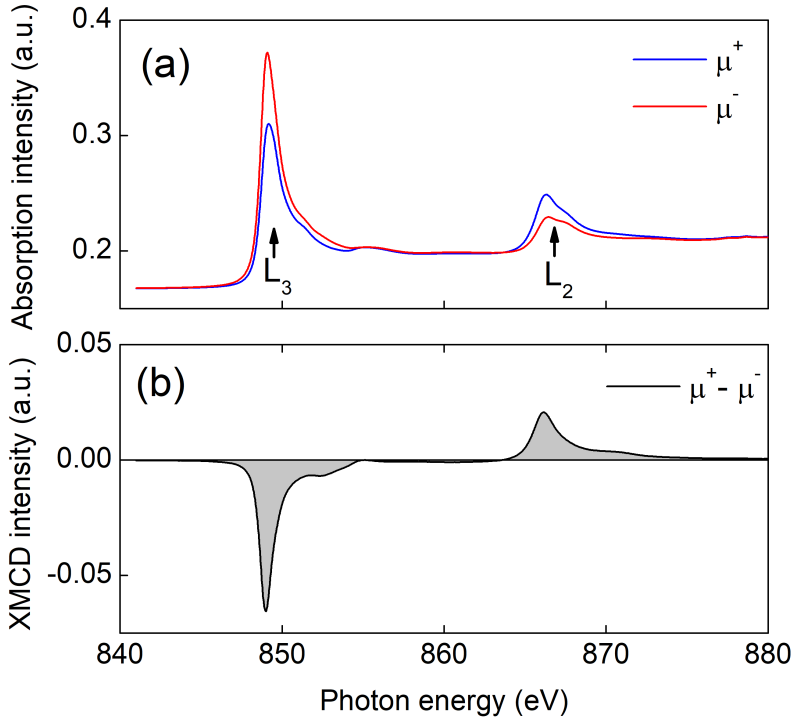

Figure 5.16: (a) Absorption spectra at the Ni $L_{2,3}$ edges, θ=0°. (b) Corresponding XMCD data.

Application of XMCD sum rules

The orbital and spin contributions m_ℓ and m_s can be obtained by using the sum rules [76, 77, 73] on the x-ray absorption spectrum and its associated circular dichroism spectrum. According to the XMCD sum rules, the orbital and spin magnetic moments can be deduced from the XAS and XMCD spectra by the following equations:

$$m_\ell = -\frac{2n_h\mu_B}{3I_{av}} \int_{L_3+L_2} \Delta\mu \; dE \tag{5.11}$$

and

$$m_s^{eff} = m_s + 7\langle T_z \rangle = \frac{n_h\mu_B}{I_{av}} \left(\int_{L_3} \Delta\mu \; dE - 2\int_{L_2} \Delta\mu \; dE \right) \tag{5.12}$$

where n_h is the d-hole number given by $10 - n_{3d}$ (n_{3d}: 3d electron occupation number); μ_B is the Bohr magneton; $\langle T_z \rangle$ is the expectation value of the spin magnetic dipole operator. $\Delta\mu = \mu^+ - \mu^-$ is the experimentally obtained XMCD spectrum given in Fig.5.17, displayed in black solid line. The integration of $\Delta\mu$ shown in Fig.5.17 by red dashed line gives two integrals p and q, equaling to $\int_{L_3} \Delta\mu \; dE$ and $\int_{L_3+L_2} \Delta\mu \; dE$, respectively. The factor I_{av} corresponds to the average absorption intensity at Ni $L_{2,3}$, which is related to $2p \rightarrow 3d$ transition intensity. It is given by:

$$I_{av} = \int_{L3+L2} \left(\frac{\mu^+ + \mu^-}{2} - \mu^{BG} \right) \, dE \tag{5.13}$$

where μ^{BG} is the background absorption spectrum expressed by the two step functions, as shown in Fig.5.17. Thus, the integration of the average XAS intensity can be replaced by an integral r displayed in Fig.5.17. In summary, with the three integrals p, q and r, the orbital and the effective spin magnetic moments m_ℓ and m_s^{eff} become:

$$\begin{aligned} m_\ell &= -\frac{2q}{3r} n_h \mu_B \\ m_s^{eff} &= -\frac{3p - 2q}{r} n_h \mu_B \end{aligned} \tag{5.14}$$

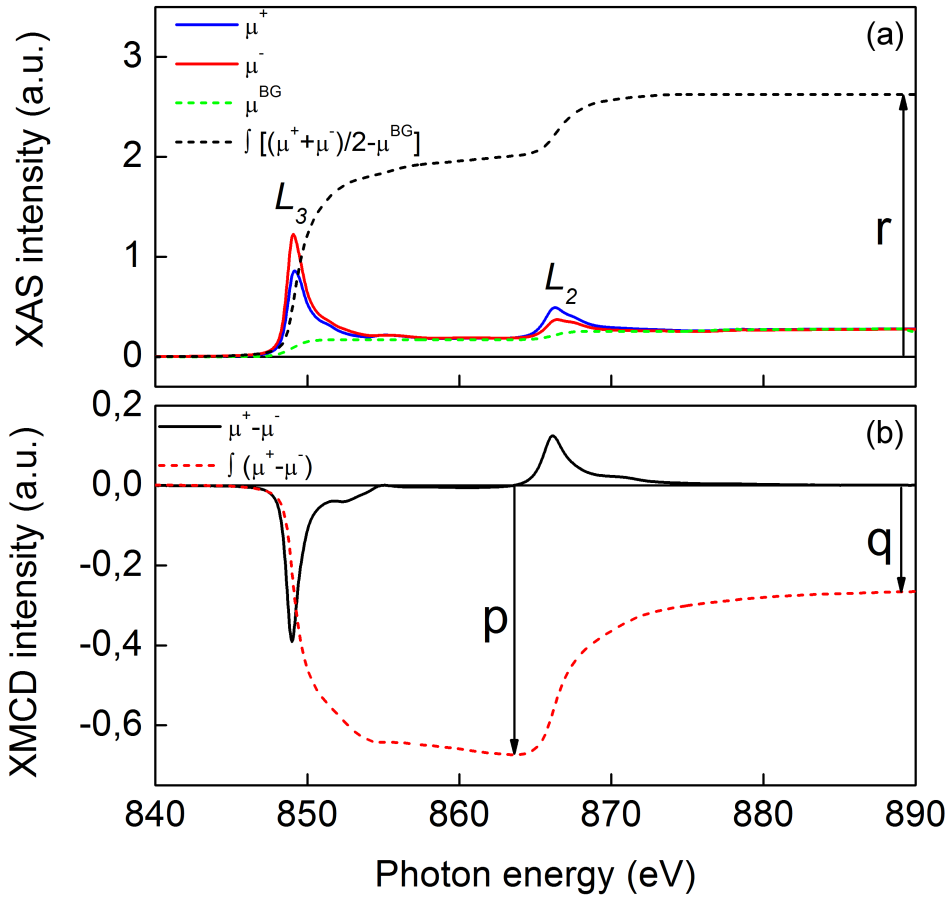

Figure 5.17: $L_{2,3}$ edges XAS and corresponding XMCD spectra of Ni: (a) the XAS spectra obtained in taking μ^+ and μ^- cases at 4.2 K under an external field H=2 T, accompanied with the background absorption μ^{BG}. The black dashed line represents the integration of the average XAS intensity in removing the background absorption contribution; (b) the associated XMCD spectrum deduced from the XAS spectra in (a). The red dashed line is the integration of the XMCD intensity, where p and q are separately the surface area of the XMCD spectrum at L_3 edge and the sum of that at L_3 and L_2 edges.

For $\langle T_z \rangle$, although the sum of T_z over the whole d band is zero, it is very large for each d state. Therefore, the $\langle T_z \rangle$ is negligible only for atoms with cubic symmetry. For a non-cubic symmetric atoms, $\langle T_z \rangle$ can be strongly enhanced over the d band. For example, $7\langle T_z \rangle$=0.027μ_B/atom for bulk-like fcc Ni and it can be enhanced to 0.082 μ_B/atom for Ni atoms on the surface [120]. Furthermore,

T_z can be related to the linear dichroism (LD) signal due to the anisotropic charge distribution around the atom. T_z is large when the LD signal is large. By expressing T_z as a function of the quadrupole moment Q_{xx} which represents the anisotropic charge distribution of $3d$ electrons around the atom, m_s^{eff} for a $3d$ metal with a uniaxial symmetry can be expressed as [121, 122]:

$$m_s^{eff} = m_s + 7\langle T_z \rangle = m_s + 14Q_{xx} - 21Q_{xx}\sin^2\theta \tag{5.15}$$

m_s^{eff} is in function of θ. Only when m_s^{eff} is independent of θ, the T_z term can be neglected, leading m_s to be equal to m_s^{eff}.

5.5.2 Magnetic hysteresis cycles by XMCD measurements

In the XMCD measurements, in maintaining the circularly polarized x-ray energy at the value of the Ni L_3 edge absorption energy, E=849.2 eV, by homogeneously varying the external field from H to -H and returning to H, the absorption is recorded as a function of the magnetic field for left and right circular polarizations. The XMCD Ni hysteresis cycles at 4.2 K and at $\theta = 0°$ is shown in Fig.5.18(a), together with the OP hysteresis cycle at 5 K measured by VSM. By neglecting the unstable signal at weak field for the XMCD measurements, its evolution with the field is very similar to that obtained by VSM measurements. In particular, the coercive field deduced from the two different methods is the same. This indicates that the ferromagnetic behavior of NWs in the vicinity of the surface can represent that of the whole sample. This allows the analysis of angle-dependent XMCD signals to be considered representative for the whole sample.

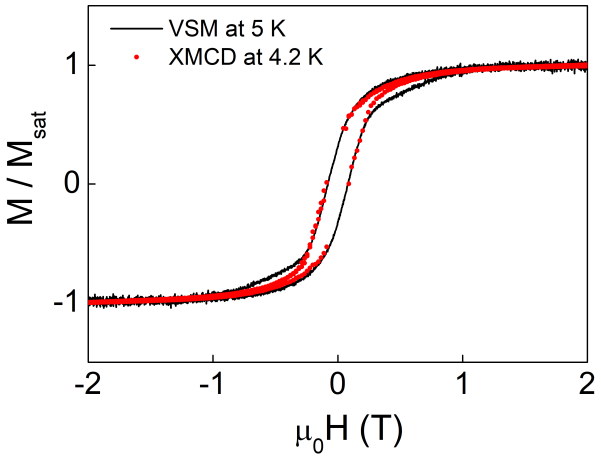

Figure 5.18: Hysteresis cycle at 4.2 K obtained by spectroscopic measurements for $\theta = 0°$ (symbols), compared with the OP hysteresis cycle obtained by VSM measurements at 5 K (line).

In order to study the angular evolution of the magnetic properties, the absorption measurements are performed at different angles θ: 0, 15, 30, 45 and 60° for sample S-5. In applying a field of 2 T, which is larger than the saturation field of the sample, the XMCD spectra at saturation are obtained and displayed in Fig.5.19(a). Compared to the dichroism signal at Ni L_3 edge, the variance is less than 5% for different θ. The dichroism is thus considered as independent of θ. Then, in removing the external field after the magnetization saturation, a series of XMCD spectra at remanence are recorded. As illustrated in Fig.5.19(b), the dichroism signal at Ni L_3 edge is enhanced with increasing θ. Using the XMCD sum rules, the orbital and spin moments are deduced to determine the total magnetic moment: $m_{tot} = m_s^{eff} + m_\ell$. Thus, the remanence $m_{tot}^{rem}/m_{tot}^{sat}$ is simplified to $(9p-4q)^{rem}/(9p-4q)^{sat}$. The angular evolution of the normalized remanence is therefore plotted in Fig.5.19(c). As $\theta = 0°$ stands for the OP field ($\perp$) case and 90° for the IP field ($\parallel$) one, the increase of the remanence in θ unveils the hard magnetization direction along the wire axis and the easy direction parallel to the sample surface.

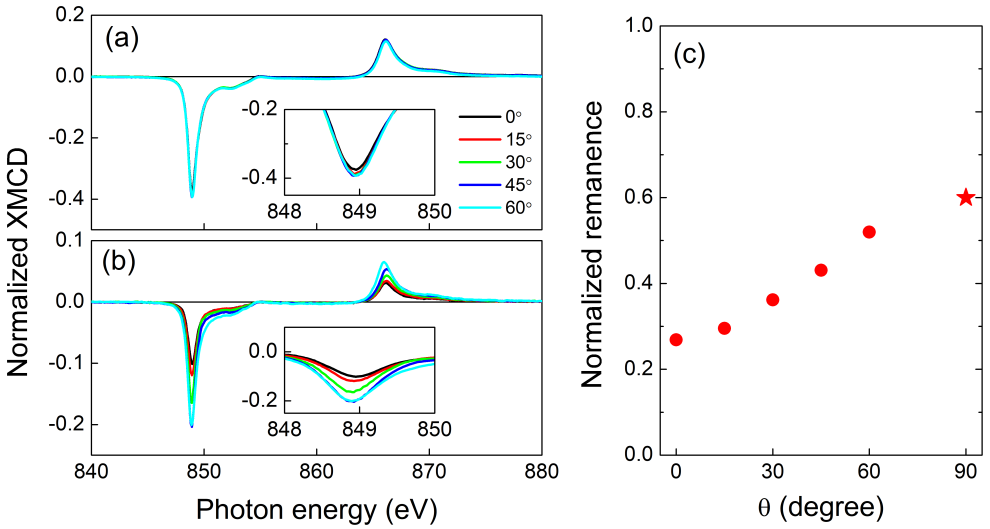

Figure 5.19: Comparison of the normalized XMCD for different θ: 0, 15, 30, 45 and 60° for sample S-5. (a) XMCD spectra at saturation field. Inset: enlargement of the spectra at Ni L_3 edge. (b) XMCD spectra at remanence. Inset: enlargement of the spectra at Ni L_3 edge. (c) Angular evolution of the remanence deduced from (a-b). The red star stands for the IP remanence obtained from IP hysteresis cycle at 5 K measured by VSM.

5.5.3 Determination of the orbital and spin moments

Before the determination of m_ℓ and m_s, I would like to discuss the T_z term in our case. X-ray linear dichroism (XLD) measurements have been performed for sample S-5. As shown in Fig.5.20, the XLD signal is given by the difference of two XAS spectra obtained in applying horizontal and vertical linearly polarized x-rays. It indicates that the cubic symmetry is destroyed and can be linked to the tetragonal structure related to the strain ($\langle\epsilon_{zz}\rangle = 2.4\%$, $\langle\epsilon_{rr}\rangle \approx -0.3\%$). The XLD signal is modest: only ~2% dichroism compared to the absorption signal (Fig.5.20). This may indicate that the expectation value of T_z is small in our system. This is indeed further substantiated by the fact that the measured m_s^{eff} of Ni is independent of the angle θ. In what follows, I will thus consider that $\langle T_z\rangle$ is small enough to be neglected and consider that $m_s = m_s^{eff}$. The ratio of the orbital and spin moment is therefore described as:

$$\frac{m_\ell}{m_s} = \frac{2q}{9p - 6q} \tag{5.16}$$

m_ℓ/m_s is thus independent of the hole number n_h. It only depends on the integration of the XMCD spectra. In the following study, I will precise m_ℓ and m_s, give a comparison of the magnetic moments deduced by XMCD and VSM measurements and then explore the possibility to relate m_ℓ to the magnetic anisotropy in Ni NWs.

Angular evolution of the orbital and spin moments

According to the expression 5.14, the hole number n_h is a significant coefficient to determine the absolute values of m_ℓ and m_s. It depends on the electronic structure. For example, n_h is 1.45 for bulk Ni and can be reduced towards 1.00 for few monolayers of Ni [123]. Supposing n_h of Ni to be 1.3±0.2, the angular evolutions of m_ℓ and m_s are displayed in Fig.5.21. The bulk values of m_ℓ and m_s of Ni, experimentally determined by Hjortstam in 1996 [124], are: $m_\ell^{bulk} = 0.058\ \mu_B$/atom and $m_s^{bulk} = 0.58\ \mu_B$/atom, marked by black dashed line in the figure. As can be seen, the absolute values of m_ℓ and m_s are larger than the bulk ones. m_s is constant and m_ℓ increases with increasing θ. This results in an increase of the ratio m_ℓ/m_s in θ. It is also a bit larger than the bulk value (0.1).

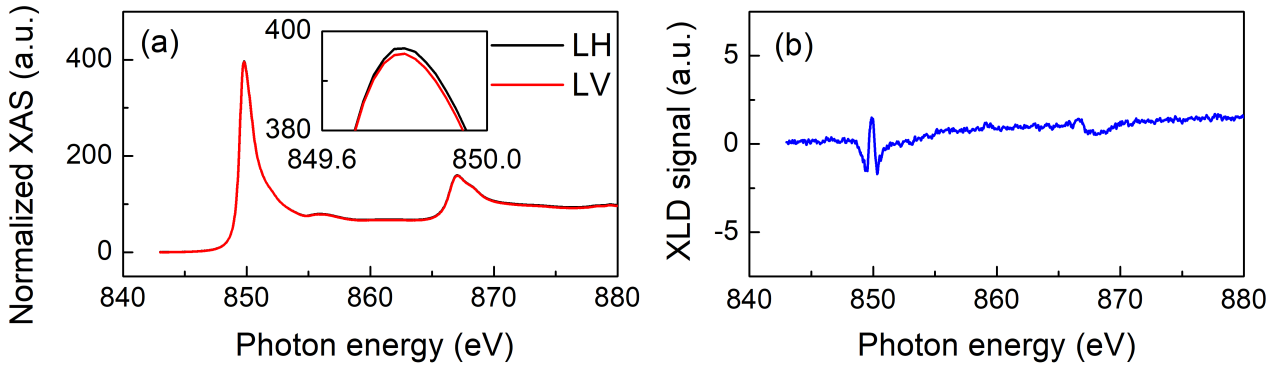

Figure 5.20: (a) XAS spectra at Ni $L_{2,3}$ edges at $\theta = 0°$ of sample S-5 by applying horizontal and vertical linearly polarized x-rays, noted LH and LV, respectively. Inset: enlargement of the peak at Ni L_3 edge. (b) Corresponding XLD signal.

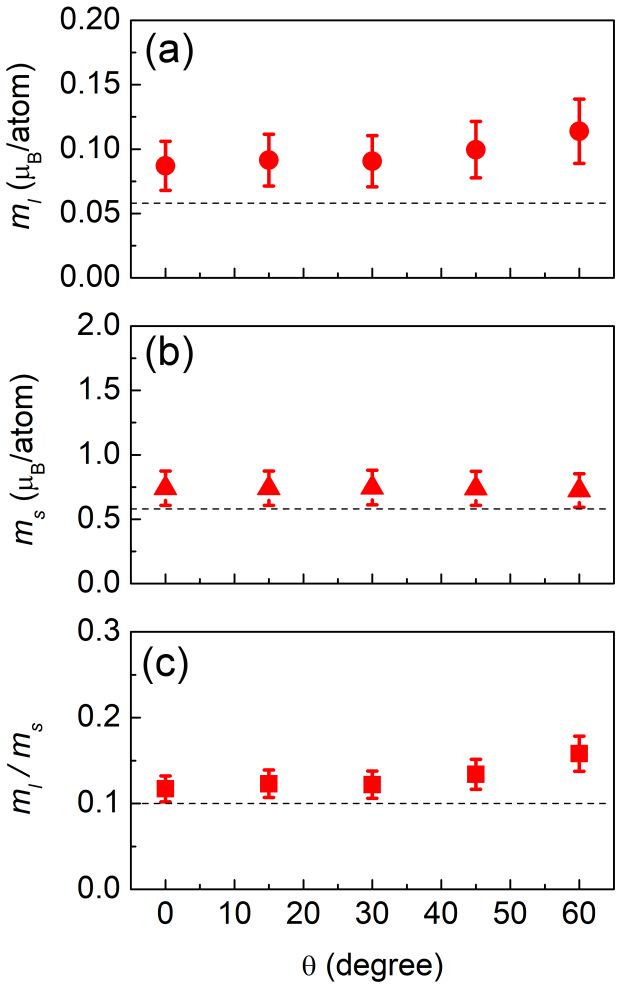

Figure 5.21: Angular evolution of magnetic moments for sample S-5 with $n_h = 1.3 \pm 0.2$: (a) the orbital moment, m_ℓ; (b) the spin moment, m_s; (c) the ratio, m_ℓ/m_s. The bulk values are represented by dashed lines.

5.5.4 Discussion

With the determination of the orbital and spin moments, the total magnetic moment is deduced by $m_\ell + m_s$ and listed in Tab.5.7. Compared to the reduced saturation moment deduced from the major hysteresis cycle in easy-magnetization direction, the values are in the same order. This is an excellent indication that the magnetic behavior corresponds well to the atomic analysis. Moreover, the total magnetic moment is larger than the saturation moment, indicating that the hole number may be less than 1.3 in our case, even lower than 1.1. As shown in Fig.5.21, m_s almost falls at the bulk value but m_s is a bit larger than the bulk one at small hole number. As the ratio m_ℓ/m_s is independent of the hole number, the enhancement of m_ℓ/m_s is due to the enhancement of m_ℓ compared to the bulk value.

Table 5.7: The determination of the total magnetic moment of Ni, together with the reduced saturation magnetization moment deduced from the major hysteresis cycle. Here the hysteresis responses are obtained along easy magnetization axis direction (θ=90°).

sample	XMCD				Hysteresis cycle
	m_ℓ^{Ni} (μ_B/atom)	m_s^{Ni} (μ_B/atom)	m_{tot}^{Ni} (μ_B/atom)	M_{sat}^{XMCD} (10^5 A/m)	$M_{sat} = m_{sat}/V^{NWs}$ (10^5 A/m)
S-5	0.11±0.02	0.72±0.11	0.83±0.13	6.9±1.1	4.5±0.7

The orbital moment m_ℓ is enhanced by about 30% when θ increases from 0 to 60°. As the spin moment has only a fluctuation below 3%, much lower than the angular enhancement of m_ℓ, m_s is considered as constant. Therefore, the increase of the ratio m_ℓ/m_s with increasing θ results from to the increase of m_ℓ. The angular enhancement of m_ℓ provides a way to determine the magnetic anisotropy energy (MAE). In first approximation, by counting the spin-orbit coupling in a second-order perturbation theory [125], the magnetic anisotropy energy can be linked to the anisotropy of the orbital magnetic moment m_ℓ, and is given by:

$$MAE = \alpha \frac{\xi}{4\mu_B} \Delta m_\ell \tag{5.17}$$

where ξ is the spin-orbit coupling constant, α is a prefactor depending on the electronic structure and Δm_ℓ represents the difference of the orbital magnetic moment between an easy magnetization axis and a hard one. It means the difference Δm_ℓ at $\theta = 0°$ ($\perp$) and 90° ($\parallel$) in our case: $\Delta m_\ell = m_\ell^\perp - m_\ell^\parallel$. The XMCD measurements performed on Ni NWs only varies θ from 0 to 60°, and the angular evolution of m_ℓ is plotted in Fig.5.21. In fitting the angular evolution of m_ℓ by the expression:

$$m_\ell(\theta) = m_\ell^\perp - \Delta m_\ell \sin^2\theta \tag{5.18}$$

The fitting of our experimental data is shown with the red dashed line of Fig.5.22(a). Hence, Δm_ℓ can be deduced to about -0.024±0.004 μ_B/atom *via* the slope of the fitting line. Δm_ℓ corresponds to about 30% of the bulk value of m_ℓ of Ni. From the first principle calculation of the magnetocrystalline anisotropy of transition metals by Daalderop [126], the spin-orbit coupling constant ξ is of 105 meV. The prefactor α is in 0.05-1 range in tetragonal and cubic Ni [117]. The MAE is deduced to -31±5 μeV/atom at minimal prefactor, α=0.05. In addition, the MAE can also be estimated by the magnetization cycles. As shown in Fig.5.22(b), the OP and IP hysteresis cycles are recorded by VSM at 5 K. The area difference between the two cycles along easy- and hard- magnetization axes, represented by the shadow, is proportional to the effective anisotropy constant K_{eff}. It is thus deduced to be -0.65×10^5 J/m^3. In removing the magnetostatic anisotropy contribution, the sum contribution of magnetocrystalline and magnetoelastic anisotropy is about -1.4×10^5 J/m^3. By unit conversion, the MAE deduced from cycles is about -10 μeV/atom. However, if we only consider the magnetoelastic anisotropy contribution, the strain of 2.4% gives a MAE of $\approx -17\mu$eV/atom, larger

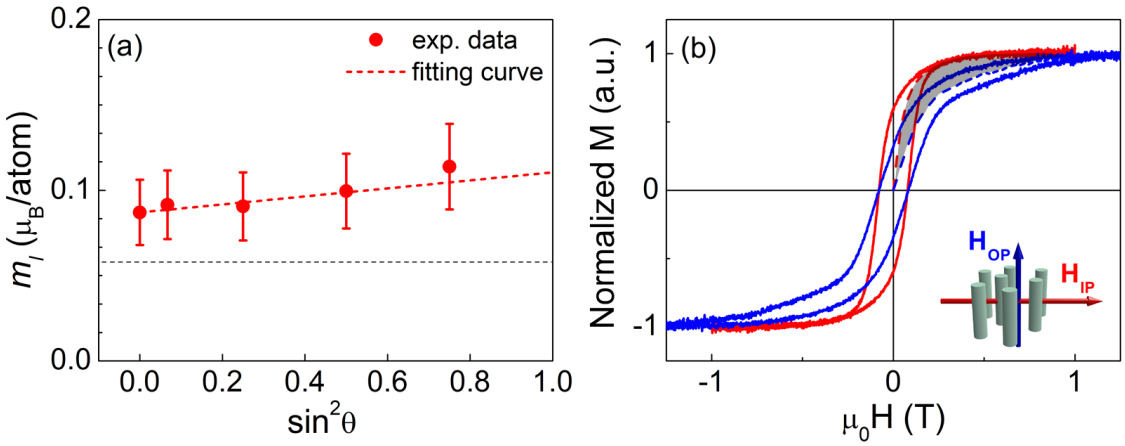

Figure 5.22: MAE determination for sample S-5. (a) Angular evolution of the orbital magnetic moment: m_ℓ *versus* $\sin^2\theta$, together with a fitting line by red dashed line according to the expression 5.18. $m_\ell^\perp$ stands for $\theta = 0°$ and $m_\ell^\parallel$ for $\theta = 90°$. (b) VSM-hysteresis cycles along easy-(red line) and hard-(blue line) magnetization axis at 5 K. MAE may be determined from the area included between the two cycles and the coordination axes, represented by the shadow.

than that estimated by the cycles (here, the magnetocrytalline anisotropy contribution is neglected). The estimated value of MAE from XMCD measurements is larger than that of theoretical K_{me} and of the experimental effective K extracted from the hysteresis cycles. In the near future, further measurements of ferromagnetic resonance (FMR) should be performed in order to determine a reliable value of the effective anisotropy constant K_{eff}.

5.6 Conclusion

- In the case of Ni NWs, an axial strain of 0.8% leads the magnetoelastic anisotropy contribution to compensate the magnetostatic effect. For highly strained NWs by about 2-4%, the magnetoelastic anisotropy dominates the other anisotropy effects. The magnetoelastic anisotropy is uniaxial with a negative constant due to the negative magnetostriction coefficient. Thus, the magnetization prefers an easy plane perpendicular to the wire axis.
- The inhomogeneities of the axial strain lead to an inhomogeneities of the anisotropy, described by a distribution of anisotropy. The IP hysteresis cycles can be simulated by a simple model where the anisotropy axis orients randomly in the easy plane. The OP cycle is related to the wandering anisotropy axis. This random anisotropy model results in the opening of the cycles both in IP and OP directions.
- The non-difference of the hysteresis cycles obtained by applying an external field in ⟨100⟩ and ⟨110⟩ directions indicates that the contribution of the magnetocrystalline anisotropy is too weak to be detected.
- Furthermore, a static distribution of the anisotropy cannot reproduce the exponential decay of the coercivity in temperature. In adding a thermal retraction of the anisotropy into the Sharrock's thermal reduction with increasing temperature, the exponential decrease of the coercivity can be successfully reproduced.
- This exponential reduction of the coercivity in temperature is due to the thermal evolution of the magnetic correlation length, of around 40-50 nm. It is can be related to intrinsic and/or extrinsic thermal softening of the local averaging of magnetic anisotropy.
- XMCD study shows that the orbital moment is enhanced in Ni NWs with respect to the bulk and the anisotropy of m_ℓ is evidenced. The Δm_ℓ value leads to a MAE estimation. In the framework

of Bruno model, it is about -31±5 μeV/atom. The estimation derived from magnetometry measurements is only about -10 μeV/atom.

Chapter 6

Magnetic behavior of Co_xNi_{1-x} NWs

Similarly to the Ni NWs, the magnetic behavior of Co_xNi_{1-x} alloy NWs has been explored in relationship with their structural properties. Magnetic hysteresis properties are mainly studied by using VSM magnetometer. Intrinsic coercive field distributions were retrieved by FORC measurements. An element-specific study by XMCD spectroscopy will be also presented.

6.1 Magnetic response of Co_xNi_{1-x} NWs

6.1.1 Anisotropy at low temperature

Figure 6.1 shows the hysteresis cycles obtained for Co_xNi_{1-x} alloy NWs at 10 K, with Co concentration of 18%, 57% and 78%. The cycles are recorded with the magnetic field applied along the wire axis (out-of-plane direction, OP) and perpendicular to NWs (in-plane, IP). Unlike the pure Ni NWs in $SrTiO_3$ system where the wire axis is the hard magnetization direction, here the Co_xNi_{1-x}:$SrTiO_3$ system reverses the wire axis to be the easy axis when $x > 18\%$. Besides, it is seen that the opening of OP hysteresis cycle increases with increasing Co concentration. The main magnetic hysteresis characteristics are listed in Tab.6.1. The OP coercive field $\mu_0 H_{c,\perp}$ increases from 0.21 to 0.63 T for Co concentration from 18 up to 78%. It is one order larger than the IP coercive field $\mu_0 H_{c,\parallel}$. The OP remanence reaches over 0.85 and the IP one is lowered to about 0.10. Besides, the IP saturation field $H_{s,\parallel}$ is also enhanced from 0.5 to 1.6 T with increasing Co concentration. Recalling that $H_{s,\parallel}$ is the maximal field to saturate the magnetization in the hard magnetisation direction, which is related to the anisotropy field, the increase of $H_{s,\parallel}$ indicates the enhancement of the magnetic anisotropy with increasing Co concentration in alloy NWs.

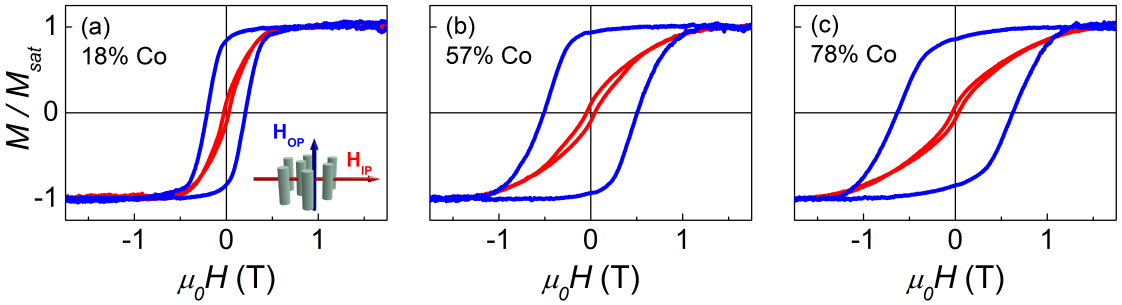

Figure 6.1: Hysteresis cycles measured at 10 K for (a) sample S-7: $Co_{0.18}Ni_{0.82}$; (b) sample S-8: $Co_{0.57}Ni_{0.43}$; (c) sample S-9: $Co_{0.78}Ni_{0.22}$.

Table 6.1: IP ($\parallel$) and OP ($\perp$) magnetic hysteresis characteristics of the Co_xNi_{1-x} samples at 10 K: coercive field H_c; saturation field H_s and remanence m_R, together with the composition and the mean diameter of wires $\langle D \rangle$.

Co%	$\langle D \rangle$ (nm)	$\mu_0 H_{c,\perp}$ (T)	$\mu_0 H_{s,\perp}$ (T)	$m_{R,\perp}$	$\mu_0 H_{c,\parallel}$ (T)	$\mu_0 H_{s,\parallel}$ (T)	$m_{R,\parallel}$
18	5.3	0.21	0.5±0.1	0.85	0.027	0.5±0.1	0.12
57	5.0	0.51	1.2±0.1	0.93	0.045	1.4±0.1	0.11
78	4.8	0.63	1.3±0.1	0.85	0.034	1.6±0.1	0.05

6.1.2 Intrinsic distribution of coercivity

As the strain in Co_xNi_{1-x} NWs increases with the Co content as mentioned in Chap.4, the strain inhomogeneity should lead to a broad distribution of anisotropy, similarly to the case of Ni NWs. The OP coercive field distribution results from the combination of the extrinsic effect of the dipolar interaction between the NWs and the intrinsic distribution of anisotropy. In what follows, I will extract the intrinsic component from the measurements in removing the dipolar interaction.

The FORC method is efficient for providing information on the switching field distribution and internal interaction in an assembly of NWs. The FORC measurements are performed for the Co_xNi_{1-x} alloy samples and the corresponding FORC maps are displayed in Fig.6.2. The verical scale concerns the bias field H_b. One notices that the intensity in the FORC maps is distributed above the $\mu_0 H_c$ axis. In other terms, the bias field H_b is positive and the mean interaction field is negatively proportional to the mean magnetization. This is consistent with the dipolar interaction [63]. Thus, the following transformation is made for both applied field H and reversal field H_r (see Section 1.7):

$$H_{eff} = H + H_{dip} \quad \text{and} \quad H_{r,eff} = H_r + H_{dip} \tag{6.1}$$

where $H_{dip} = -M_{exp}/V_{film} = -PM_s m_{exp}$ along the OP direction, with the film porosity P, the measured OP magnetization M_{exp} and the reduced magnetization m_{exp}. The dipolar interaction corrected FORC maps are displayed in Fig 6.2, together with the raw FORC maps. The FORC intensity is now distributed around the $\mu_0 H_c$ axis. It is chekced that the remaning vertical spead of the intensity along the $\mu_0 H_b$ axis is mainly intrumental, due to the field steps used for the measurements and those used in the calculation of the mixed second-order derivatives in the *FORCinel* software (the smoothing factor) [127]. The maximal bias fields removed in the treatment are from 0.077 to 0.126 T corresponding to the values of PM_s for the three samples respectively, as expected.

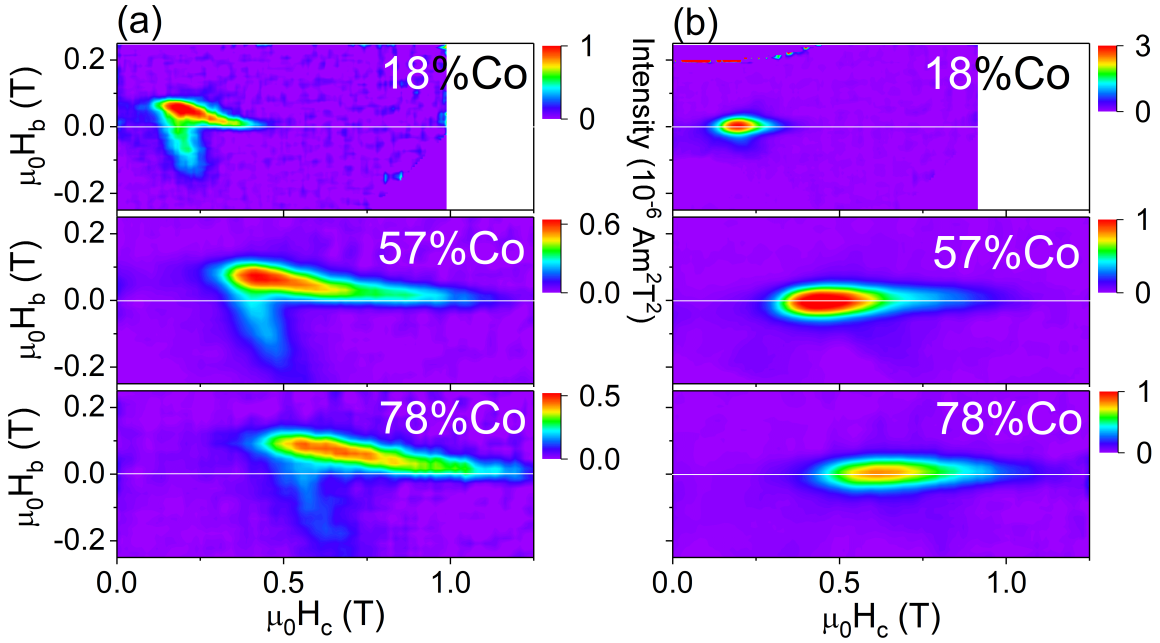

Figure 6.2: Raw and dipolar interaction corrected FORC maps at 5 K for the Co_xNi_{1-x} samples. (a) Raw FORC maps for 18, 57 and 78% Co in CoNi alloy; (b) corresponding dipolar interaction corrected maps from (a).

The intrinsic coercive field distributions obtained for the three samples are displayed in Fig.6.3, together with the raw distributions. The mean coercive field $\mu_0\langle H_c\rangle$ from the FORC maps is 0.24, 0.54 and 0.68 T for the Co concentration of 18%, 57% and 78%, respectively. One notices that the distribution becomes broader with higher Co concentration, with the FWMH in $\mu_0 H_c$ varying from 0.1 to 0.4 T (see Tab.6.2). It is in accordance with the fact that the strain and the strain inhomogeneity

in Co_xNi_{1-x} NWs increase with increasing Co content, as determined by the XRD measurements. It should be underlined that the FWMH of the coercive field is small for 18% Co. This may be explained by the fact that λ_{001} falls to 0 at this concentration of Co, implying a minimum of sensitivity to the strain inhomogeneity.

After the correction of dipolar interaction, the distribution of H_c is narrowed for different Co concentrations.

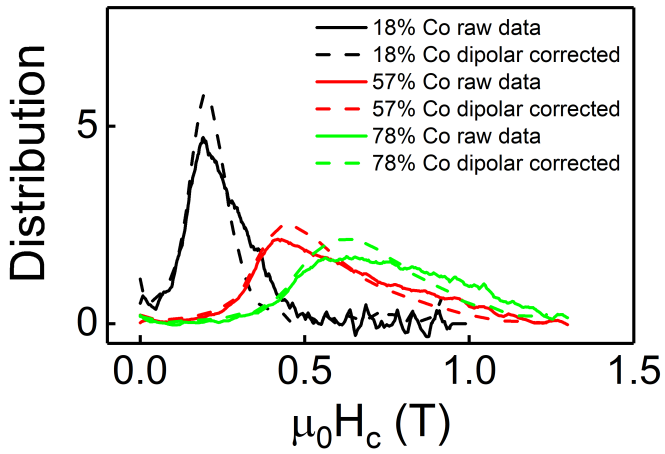

Figure 6.3: Raw and dipolar interaction corrected coercive field H_c distributions at 5 K for the samples of 18, 57 and 78% Co.

Table 6.2: Characteristics from the FORC measurements for 18, 57 and 78% Co: (a) mean coercive field, $\mu_0\langle H_c\rangle$; (b) FWHM.

Co%	$\mu_0\langle H_c\rangle$ (T)	FWHM (T)
0.18	0.24	0.1
0.57	0.54	0.3
0.78	0.68	0.4

6.1.3 Thermal evolution of the magnetic behavior

Variation with the Co content

The OP hysteresis cycles at different temperatures were measured in the samples, as in the example of S-9 displayed in (Fig.6.4(a)). The thermal decay of coercivity $H_c(T)$ was obtained for the three samples (Fig.6.4(b)). The decay is fitted by the Sharrok's law: $H_c(T) = H_{c,0}(1-(T/T_b)^{2/3})$. Thus, the coercive field at 0 K ($H_{c,0}$) and the blocking temperature ($T_{b,\perp}$) are extracted for the three samples along the easy axis. As displayed in Fig.6.4(c)(d), $T_{b,\perp}$ is linearly enhanced with increasing Co concentration, as well as the coercive field $H_{c,0}$. The OP H_c at 5 K deduced from the Sharrock's thermal evolution are listed in Tab.6.3, together with the mean values of $\langle H_c\rangle$ determined by the FORC measurements at 5 K after the dipolar interaction correction. The values obtained by the two methods are consistent with each other.

Thermal evolution of coercivity

The thermal evolution of coercivity along the easy axis was detailed by FORC measurements in sample S-9, $Co_{0.78}Ni_{0.22}$. Figure 6.5 shows the dipolar-interaction-corrected FORC maps at 5, 100 and 200 K for the sample, together with the corresponding intrinsic coercive field distributions extracted.

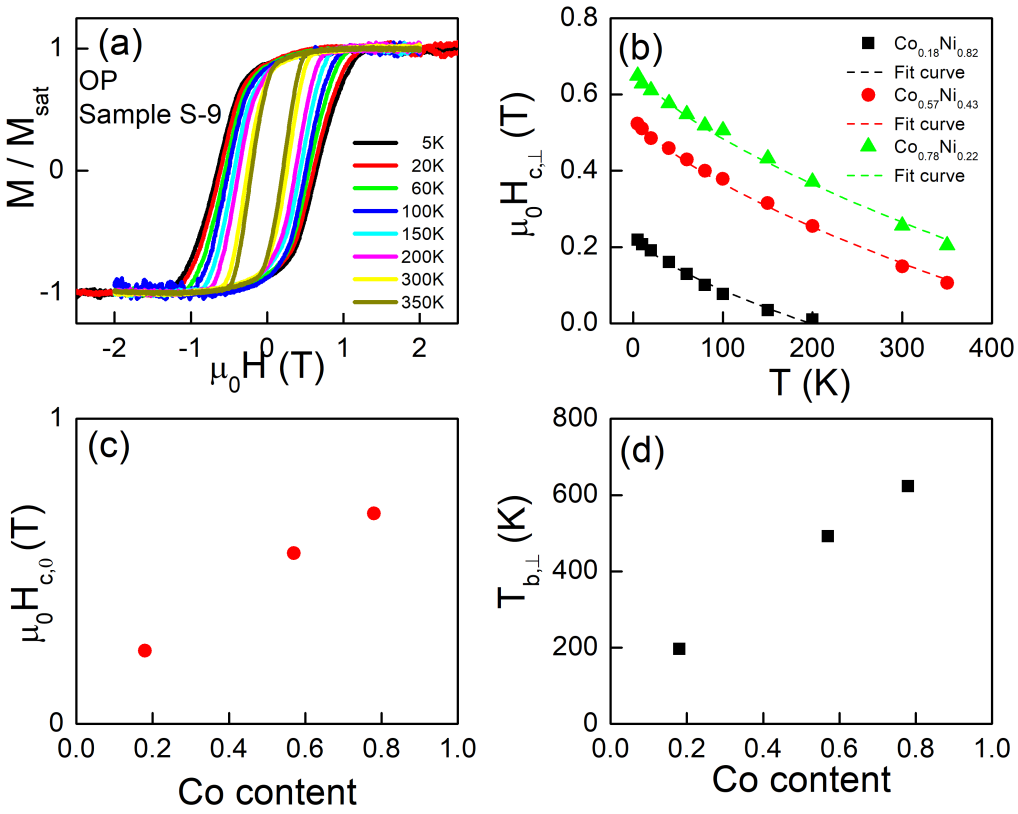

Figure 6.4: (a) Thermal evolution of the hysteresis cycles of sample S-9, $Co_{0.78}Ni_{0.22}$. (b) Temperature dependence of the coercivity for the three Co_xNi_{1-x} samples, together with the fit curves according to the Sharrock's thermal reduction law: $H_c = H_{c,0}(1-(T/T_b)^{2/3})$. Evolution of (c) the estimated coercivity at 0 K and (d) the OP blocking temperature in function of Co concentration.

Table 6.3: The OP blocking temperature $T_{b,\perp}$ and the coercivity at 0 K $H_{c,0}$ estimated by the Sharrock's thermal reduction fit curves for the three samples with different Co concentrations, together with the mean value of H_c deduced from the H_c distribution in FORC measurements at 5 K after the correction of the dipolar interaction.

	Sharrock's reduction			FORC
Co%	$T_{b,\perp}$ (K)	$\mu_0 H_{c,0}$ (T)	$\mu_0 H_c$ at 5 K (T)	$\mu_0\langle H_c\rangle$ at 5 K (T)
18	197	0.24	0.22	0.24
57	492	0.56	0.53	0.54
78	623	0.69	0.66	0.68

The mean value of the coercive field for these three temperatures are listed in Tab.6.4, in comparison with the estimated coercivity by the Sharrock's thermal reduction law with $\mu_0 H_{c,0} = 0.69$ T and T_b =623 K for sample S-9. The estimated values of the coercivity by the Sharrock's thermal reduction are very closed to that deduced from the FORC diagrams (Tab.6.4). This fact confirms that the thermal decay of coercivity is only related to the Sharrock thermal reduction. In other terms, the anisotropy barriers in the system can be considered stable in temperature.

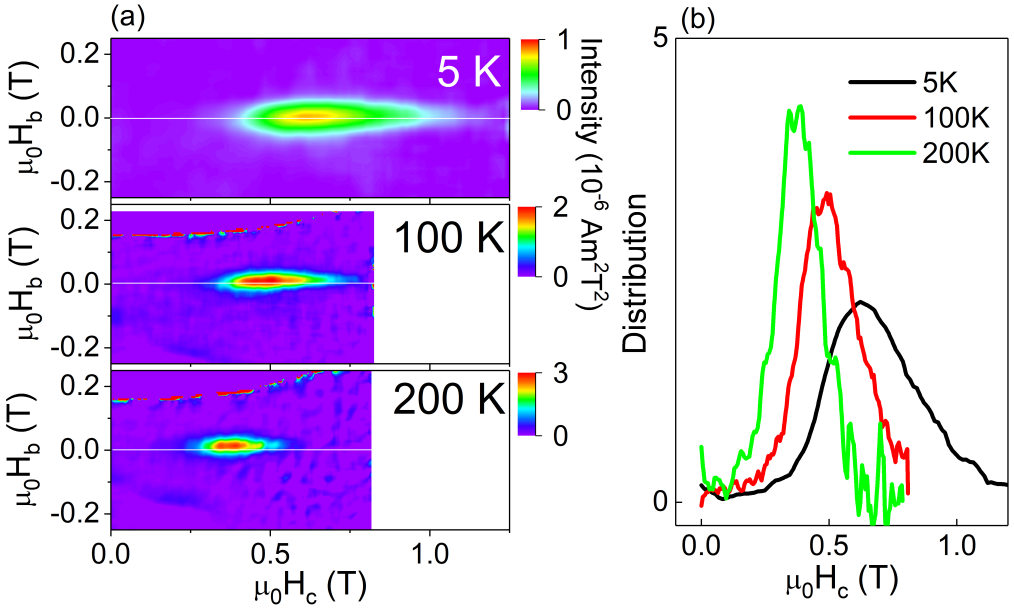

Figure 6.5: (a) Dipolar interaction corrected FORC maps for sample S-9 at 5, 100 and 200 K and (b) corresponding H_c distributions..

Table 6.4: The mean value of the coercivities deduced from the coercivity distribution obtained from the FORC diagrams for sample S-9 at 5, 100 and 200 K, in comparison with the coercivities estimated by the Sharrock's thermal reduction at these three temperatures.

Temperature (K)	$\mu_0\langle H_c\rangle$ (T) (FORC)	$\mu_0 H_c$ (T) (Sharrock's reduction)
5	0.68	0.66
100	0.50	0.49
200	0.38	0.37

6.2 Analysis of magnetic anisotropy in Co_xNi_{1-x} NWs

6.2.1 Anisotropy constants

In order to understand the total magnetic anisotropy of Co_xNi_{1-x} NWs, I will review each contribution of the magnetostatic anisotropy K_{me}, the magnetocrystalline anisotropy K_{mc} and the magnetoelastic anisotropy K_{me}. The values of K_{ms}, K_{mc} and K_{me} at 0 K are listed in Tab.6.5.

The magnetostatic anisotropy is uniaxial due to the wire shape, $K_{ms} = \mu_0 M_s^2/4$. For a Co_xNi_{1-x} alloy, the saturation magnetization M_s is related to the composition, given by $M_s = xM_s^{Co} + (1-x)M_s^{Ni}$, with $M_s^{Ni} = 5.1 \times 10^5$ A/m, $M_s^{Co} = 13.9 \times 10^5$ A/m. Hence, the magnetostatic anisotropy contribution increases with increasing Co concentration.

The fact that all the Co_xNi_{1-x} NWs in our case are epitaxied in the $SrTiO_3$ matrix and of fcc structure was verified by TEM images. Thus, the cubic magnetocrystalline anisotropy contribution is

associated to the coefficient of first order K^1_{mc}, which varies dramatically with the temperature. Kadowaki and Takahashi measured the magnetocrystalline anisotropy constants of Ni-Co alloy between 77 K and 700 K and provided an expression of K^1_{mc} at 0 K: $K^1_{mc}(x) = 14.0 - 65x - 142\exp(-36x)$, where x is the Co concentration in Co_xNi_{1-x} alloys [128]. The evolution of K^1_{mc} is illustrated in Fig.6.6(a). It should be underlined the fact that K^1_{mc} tends to be zero at ∼20% Co.

For the magnetoelastic effect, it is important to underline that the magnetostriction constant λ_{001} increases linearly with the Co concentration [100], as shown in Fig.6.6(b). For pure Ni (x=0), λ_{001} is negative. In increasing the Co concentration, it turns to positive at x=0.17. Hence, the magnetoelastic anisotropy favors an easy magnetization axis along wire axis when x >0.17: it contributes in the same direction as the shape effect. The elastic coefficient $(c_{11} - c_{12})/2$ decreases by about 20% when Co concentration increases from 0 to 80%. Here again, the in-plane strain ϵ_{rr} is negligible before the axial one ϵ_{zz}. In using the expression of the magnetoelastic anisotropy, $K_{me} = 3/2\lambda_{001}(c_{11} - c_{12})(\epsilon_{zz} - \epsilon_{rr})$, the values of K_{me} deduced with the mean axial strain ϵ_{zz} are listed in Tab.6.5.

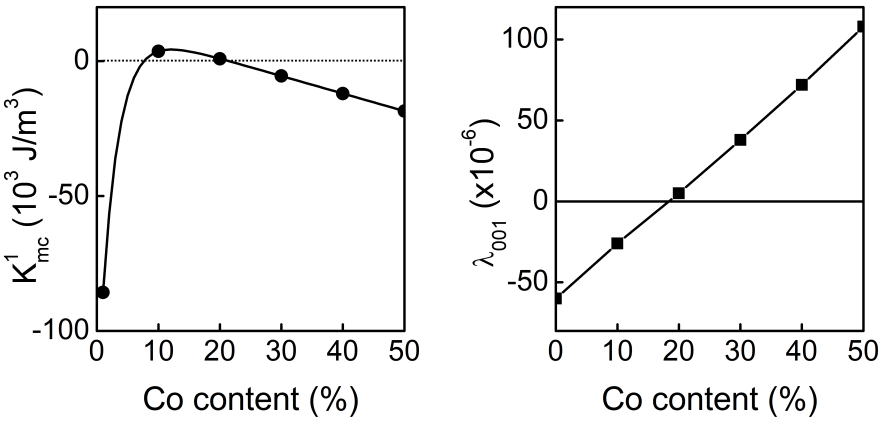

(a) (b)

Figure 6.6: (a) The magnetocrystalline anisotropy K^1_{mc} of the Co_xNi_{1-x} alloy, adapted from [128]. (b) The magnetostriction constant λ_{001} of the Co_xNi_{1-x} alloy, adapted from [100].

Table 6.5: Calculations of the magnetic anisotropy contributions for different Co concentrations: the magnetostatic anisotropy K_{ms}, the magnetocrystalline anisotropy K_{mc} and the magnetoelastic anisotropy K_{me}. M_s, the saturation magnetization, a theoritical value from [35]; λ_{001}, the magnetostriction constant; $(c_{11} - c_{12})/2$, the elastic constant and $\langle\epsilon_{zz}\rangle$, the mean value of the axial strain. Here the sample S-5 of pure Ni with similar $\langle D\rangle$ and P is added for comparison.

Co%	magnetostatic anisotropy		magnetocrystalline anisotropy	magnetoelastic anisotropy			
	M_s (10^5 A/m)	K_{ms} (10^5 J/m^3)	K^1_{mc} (10^5 J/m^3)	λ_{001} (10^{-6})	$\frac{c_{11}-c_{12}}{2}$ (GPa)	$\langle\epsilon_{zz}\rangle$	K_{me} (10^5 J/m^3)
0	5.1	0.8	-1.28	-59	55	2.4%	-2.3
18	6.7	1.4	-0.02	5	53	2.8%	0.2
57	10.1	3.2	-0.23	143	48	3.1%	6.4
78	12.0	4.5	-0.37	218	45	4.2%	12.4

One notices that the contribution of the magnetocrystalline anisotropy is over 10 times weaker than that of the sum of the magnetostatic and magnetoelastic ones for Co concentration over 18%. Thus, the magnetocrystalline anisotropy can be neglected in the following discussions. At a low Co concentration of about 18%, the magnetoelastic anisotropy falls to around zero and the magnetostatic

anisotropy becomes the dominating effect, leading the wire axis to be easy axis for the magnetisation. As the magnetostriction constant and the axial strain are both enhanced with increasing Co concentration, the magnetoelastic effect is thus highly increased. In Co rich NWs, the magnetoelastic anisotropy contribution is 2-3 times larger than the magnetostatic one and becomes the main effect. The system is considered as a uniaxial case, with the easy magnetization axis along the NW axis.

6.2.2 Characteristic fields

From the FORC measurements, the dipolar interaction is observed. It can be removed, in order to obtain the intrinsic distribution of coercive field and the effective saturation field in hysteresis cycles. The effective saturation field is determined by $H_{s,\perp}^{eff} = H_{s,\perp} - PM_s$ for OP direction and by $H_{s,\parallel}^{eff} = H_{s,\parallel} + \frac{P}{2}M_s$ for IP direction (see Chapter 1). The saturation field in hard magnetisation direction ($H_{s,\parallel}^{eff}$) is related to the total magnetic anisotropy contribution. H_{ms} is associated to the shape effect. Therefore, the effective magnetoelastic anisotropy contribution is defined by $H_{me}^{eff} = H_{s,\parallel}^{eff} - H_{ms}$. The comparison of these fields are listed in Tab.6.6. H_{me}^{eff} increases with increasing Co concentration, indicating the enhancement of the magnetoelastic anisotropy effect. At 18% Co, the magnetoelastic contribution is weak. This is in agreement with the anisotropy calculation by $\langle\epsilon_{zz}\rangle$ (see Tab.6.5). However, compared to its corresponding field H_{me}, the effective one H_{me}^{eff} is smaller at Co-rich sample. This may be due to the broad distribution of the axial strain in NWs. In highly strained NWs, the mechanism of relaxation of the strain with misorientation was confirmed by the RSMs in Chap.4. With increasing Co concentration, the crystallographic disorder is enhanced. In this case, the mean value of ϵ_{zz} could be overestimated by XRD θ-2θ scan.

Table 6.6: Comparison of the characteristic fields for 18, 57 and 78% Co in Co_xNi_{1-x}: $H_{s,\parallel}^{eff}$, the effective IP saturation field with dipolar interaction corrected; H_{ms}, the field related to the shape effect; H_{me}^{eff}, the field stands for the effective magnetoelastic anisotropy contribution.

Co%	$\mu_0 H_{s,\parallel}^{eff}$ (T)	$\mu_0 H_{ms}$ (T)	$\mu_0 H_{me}^{eff}$ (T) (from cycles)	$\mu_0 H_{me}$ (T) (from strain)
18	0.54±0.10	0.42	0.12±0.10	0.06
57	1.45±0.10	0.63	0.82±0.10	1.26
78	1.66±0.10	0.75	0.91±0.10	2.07

6.2.3 Activation length

The FORC measurements provide the distributions of the coercive field for different Co concentrations. With the comparison between the coercive field H_c and the IP effective saturation field $H_{s,\parallel}^{eff}$ which is considered to be the anisotropy field H_a of the system, it is found that H_c is always smaller than $H_{s,\parallel}^{eff}$. This indicates a local magnetization reversal. Hence, it is important to estimate the effective anisotropy constant K_{eff} and the activation volume V^* or length δ involved in the magnetization reversal.

As the thermal evolution of H_c can be fitted by the Sharrock's thermal reduction: $H_c(T) = H_{c,0}(1-(T/T_b)^{2/3})$, where $H_{c,0} = 2K_{eff}/(\mu_0 M_s)$, the effective anisotropy constant K_{eff} is therefore deduced. With the expression $25k_BT_b = K_{eff}V^*$, the activation length δ are determined and listed in Tab.6.7, together with the domain wall width δ_0, given by $\delta_0 = \pi\sqrt{A/K_{eff}}$. It can be seen that the magnetic activation length δ is closed to the domain wall width δ_0. This indicates that the magnetization reversal process should be associated to the domain wall. As described by many reports [129, 130, 131, 132, 133], the magnetization reversal on a nanostructure is often dominated by a nucleation process and then by the propagation of the domain wall. Therefore, in our ultrathin Co_xNi_{1-x} NWs, it can be depicted that under an external field, the magnetization of about 1/4∼1/3

wire is firstly reversed, generating a domain wall, and then that of the whole wire is followed by domain wall propagation.

Table 6.7: Comparison of the activation length δ and the domain wall width δ_0 for 18, 57 and 78% Co in Co_xNi_{1-x} NWs.

Co%	$\mu_0 H_{c,0}$ (T)	T_b (K)	K_{eff} (10^5 J/m^3)	δ (nm)	δ_0 (nm)
18	0.24	197	0.8	39	39
57	0.56	492	2.8	31	28
78	0.69	632	4.1	28	24

6.2.4 Discussion

The study of the magnetic anisotropy in Co_xNi_{1-x} alloy NWs in CeO_2 matrix was carried out by Bonilla in 2013 [26]. The mismatch between Co_xNi_{1-x} and CeO_2 (a_{CeO_2} = 5.411 Å) is about 2.4%, which is lower than that between Co_xNi_{1-x} and $SrTiO_3$. Thus, for pure Ni, the magnetoelastic effect compensates the magnetostatic one, leading the system to be isotropic. By Co alloying, the magnetoelastic effect enhances the magnetostatic one leading to the easy magnetization axis along the wire axis with the blocking temperature reaching to 300 K at about 60% Co. For the present case, Co_xNi_{1-x} alloy with about 60% Co in $SrTiO_3$ matrix highly increases the total anisotropy due to the great magnetoelastic contribution introduced by a large strain (≈3%), giving a blocking temperature over 500 K. This is a good starting point to obtain stable ferromagnets at room temperature and to explore possibilities of the coupling with other materials to realize multifunctionality.

6.3 XMCD investigation at Ni and Co $L_{2,3}$ edges

In order to obtain element-specific information, XAS and XMCD measurements are performed on the series of Co_xNi_{1-x} samples to determine the orbital and spin magnetic moments. The measurements are done at DEIMOS beamline in Sychrotron SOLEIL.

6.3.1 XAS and XMCD spectra

Fig.6.7 shows XAS and XMCD spectra at Co and Ni $L_{2,3}$ edges for $Co_{0.78}Ni_{0.22}$. The XAS spectra contain both the Co L and Ba M edges for absorption at Co $L_{2,3}$ edges (Fig.6.7(a)) and both the Ni L and Ce M edges for that at Ni $L_{2,3}$ edges (Fig.6.7(b)). Ba and Ce are impurities in the $SrTiO_3$ target used for the growth. One should notice that the pollutions of Ba and Ce are eliminated in XMCD spectra. This may influence the determination of the absolute value of the orbital moments m_ℓ and the spin moment m_s. In order to correct the absorption spectra for the contribution of Ba, I have used the following procedure also employed in [134] as illustrated in Fig.6.8. The spectrum at Ba $M_{4,5}$ edges is used as a reference. This spectrum, scaled by an adjustable parameter, is subtracted from XAS spectrum of NWs. This allows to obtain spectra with contribution of Co only in the 765-820 eV range. At Ni L edges, as the absorption of Ce $M_{4,5}$ edges appears after that of Ni $L_{2,3}$ edges, I employ a simple procedure and keep only the signal at Ni L edges up to 876 eV.

6.3.2 Magnetic hysteresis cycles by XMCD measurements

The magnetic hysteresis cycles acquired by the XMCD measurements are depicted in Fig.6.9 for Co_xNi_{1-x} samples with different Co concentrations both at Co and Ni L_3 edge at 4.2 K, accompanied with the hysteresis cycles obtained by classical magnetometry, VSM. The cycles obtained by both XMCD at Co and Ni edges and by VSM are almost identical for Co_xNi_{1-x} alloy at different Co concentrations. This indicates that (i) Co and Ni are well alloyed; (ii) the ferromagnetic behavior of NWs in the vicinity of the surface can represent that of the whole sample. This allows the analysis of angle-dependent XMCD signals to be considered representative for the whole sample.

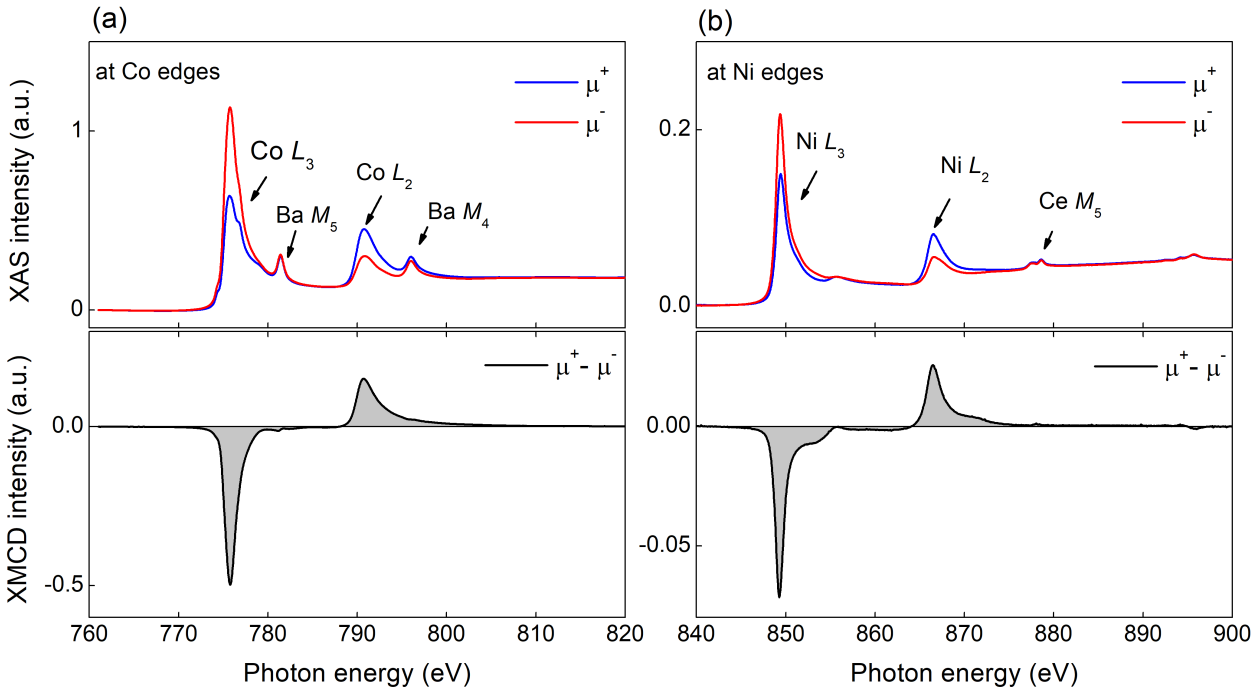

Figure 6.7: Absorption and dichroism spectra of sample S-9, $Co_{0.78}Ni_{0.22}$, for the external field H parallel to the sample normal ($\theta = 0°$) at 4.2 K: (a) at Co $L_{2,3}$ edges; (b) at Ni $L_{2,3}$ edges.

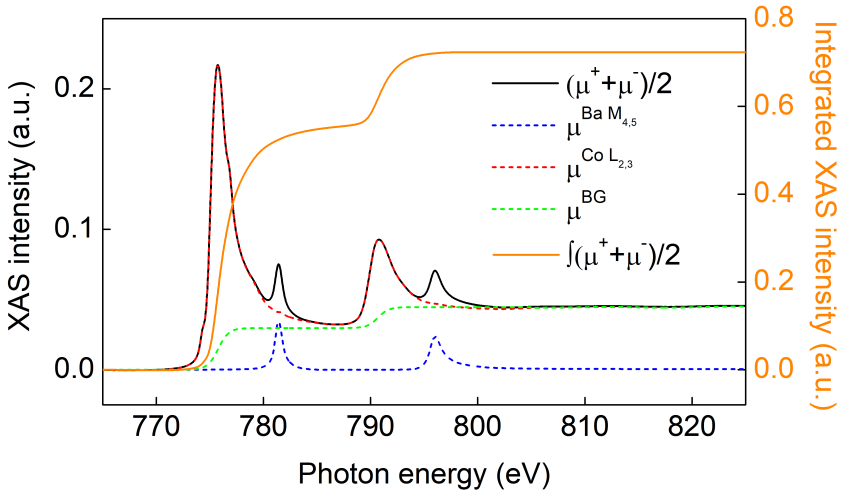

Figure 6.8: Elimination of the absorption at Ba $M_{4,5}$ edges influence on the XAS at Co $L_{2,3}$ edges. The single Co $L_{2,3}$ absorption spectrum (dashed red line) is obtained by removing the pure Ba $M_{4,5}$ absorption (dashed blue line) from the average spectrum of experimental measurements (black solid line). In eliminating the BG absorption (green dashed line), the integrated absorption intensity r is displayed in orange dashed line.

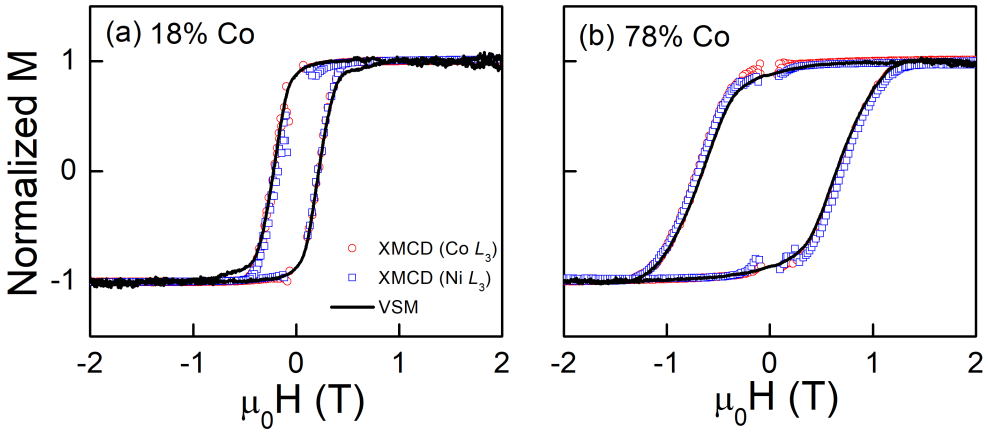

Figure 6.9: Hysteresis cycles deduced from XMCD measurements at Co and Ni L_3 edge at 4.2 K for $\theta = 0°$ of samples: (a) S-7, $Co_{0.18}Ni_{0.82}$; (b) S-9, $Co_{0.78}Ni_{0.22}$, with comparison to the cycle obtained from VSM.

Similar to the study of Ni NWs, the determination of magnetic moments allows to explore the angular dependence of the remanence in Co_xNi_{1-x} alloy NWs. In applying an external field to record absorption signal at saturation and in removing the field after the saturation to record that at remanence, the remanence is deduced as illustrated in Fig.6.10. With increasing angle between the wire axis and the magnetic field, the remance decreases from 0.8 to 0.4 for 18% and 78% Co at both Co and Ni $L_{2,3}$ edges. As 0° stands for $\perp$ case and 90° for $\parallel$ case, this angular evolution of the remanence evidences an easy magnetization axis along wire axis for these two samples. Moreover, the remanence at 90° can be estimated to be weak according to the evolution, indicating a nearly closed hysteresis cycle along hard magnetization direction. It is in agreement with the OP magnetic cycles obtained by VSM measurements: m_R decrease from 0.85 ($\perp$) to ≈0.1 ($\parallel$) (see Tab.6.1).

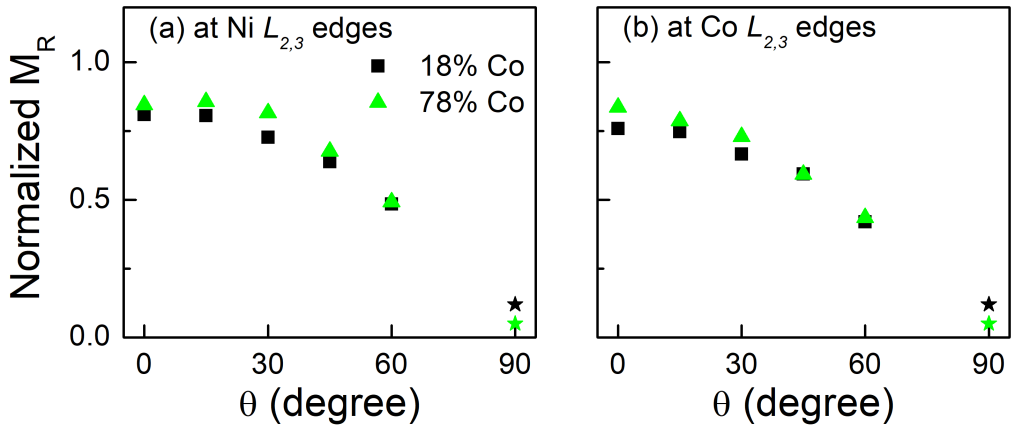

Figure 6.10: Evolution of the normalized remanence on θ deduced by XMCD measurements at (a) Ni and (b) Co $L_{2,3}$ edges at 4.2 K for 18 and 78% Co in Co_xNi_{1-x} alloy NWs. Square and triangle represent the remanence obtained by XMCD. Star stands for the IP remanence deduced from IP hysteresis cycles measured by VSM at 5 K (see Tab.6.1).

6.3.3 Determination of the orbital and spin moments

Recalling the determination of the spin moments in pure Ni NWs, m_s=m_s^{eff}, because the spin dipolar operator T_z is small enough to be neglected. This was supported by the small XLD signal

and by the fact that m_s^{eff} is independent of θ. In Co_xNi_{1-x} alloy NWs, the strain is increased with increasing Co concentration. This may lead to a larger XLD signal due to the anisotropic charge distribution in 3d band. However, the experimental values of m_s^{eff} of Co and Ni are almost constant in increasing θ in Co_xNi_{1-x} alloy. Therefore, we will consider that $m_s = m_s^{eff}$.

The orbital and spin moments of Ni and Co are determined using the XMCD sum rules for 18% and 78% Co in Co_xNi_{1-x} NWs. The hole number of Ni is taken as 1.3±0.2 and that of Co is 2.3±0.2 (n_h=1.45 and 2.5 in bulk Ni and Co, respectively). In addition, the error bars of the m_ℓ and m_s estimation are about 7% and 3% for Ni. For Co, the error bars of m_ℓ and m_s are 10% and 2%. Therefore, the absolute values of m_ℓ and m_s of Co and Ni in Co_xNi_{1-x} alloy NWs are displayed in Fig.6.11 with error bars due to the incertitude on the hole number and on measurements. The values of m_ℓ and m_s of bulk Ni and Co have been measured in many works [124, 135]: $m_\ell^{bulk\ Ni} = 0.058\ \mu_B$/atom and $m_s^{bulk\ Ni} = 0.58\ \mu_B$/atom; $m_\ell^{bulk\ Co} = 0.16\ \mu_B$/atom and $m_s^{bulk\ Co} = 1.6\ \mu_B$/atom. Compared to the bulk values, as can be seen, the absolute values of m_ℓ and m_s of Ni are much larger than the bulk ones for different Co concentrations. The ratio m_ℓ/m_s of Ni, independent of the hole number, is enhanced by 10% for 18% Co and by 40% for 78% Co at θ=0°. On the contrary, m_ℓ and m_s of Co for the Co-rich sample is much closer to the bulk value. They can fall at the bulk values for the Co-poor sample if the hole number is lowered to the minimum. The ratio m_ℓ/m_s is about 10% larger than the bulk one in the Co-poor sample and almost the same as the bulk one for Co-rich one.

For the angular evolution, m_s of Co and Ni for different Co concentrations are considered independent of θ. m_ℓ of Co and Ni is constant for 18% Co, indicating no related anisotropy contribution. For Co-rich alloy, m_ℓ of Co stays constant while that of Ni decreases with increasing θ, giving a non-null Δm_ℓ between the easy- and hard- magnetization axes. The anisotropy contribution related to Δm_ℓ of Ni will be determined to compare with the total magnetic anisotropy of alloy in the discussion section. As a consequence, only the ratio m_ℓ/m_s of Ni for 78% Co has a decay in function of θ.

6.3.4 Discussion

Orbital and spin magnetic moments

The hole number is a significant coefficient for the determination of the orbital and spin moments. However, its variations in Co_xNi_{1-x} alloy have not been studied. This has been studied in $Fe_{1-x}Ni_x$ alloys by Glaubitz *et al.* in 2011 [136], including the discussion of the hole number in the alloy. Fe has a larger hole number and m_ℓ and m_s than Ni. By Fe alloying, the orbital and spin moments of Ni increase with increasing Fe concentration due to the increase of the hole number. On the contrary, the orbital and spin moments of Fe slightly decreases with increasing Fe concentration.

Similar to FeNi alloy, in increasing Co concentration, the orbital and spin moments of Ni are enhanced a bit and those of Co are reduced when the Co concentration increases from 18% to 78%. This can be explained by the evolution of the hole number in the alloy. As the hole number is proportional to the integrated absorption, its evolution can be explored by comparing the absorption in samples with distinct compositions. For example, Fig.6.12 shows the absorption spectra at Co $L_{2,3}$ edges for 18 and 78% Co. The absorption signal is a bit larger for the Co-rich sample. The XAS integrated intensity decreases by about 6% when the Co concentration is reduced from 78 to 18%, indicating the decay of 6% of the hole number of Co. The orbital and spin moments of Co for 18% Co can be lowered in taking into account the hole number evolution. Similarly, comparing the absorption integrated intensity for pure Ni, 18% Co and 78% Co gives an indication that the hole number of Ni is almost the same as pure Ni for 18% Co and increases by 9% for 78% Co. This will enhance the increase of the orbital and spin moments of Ni in increasing Co concentration. Therefore, the total magnetic moment of Co_xNi_{1-x} alloy is mainly influenced by that of Ni.

Furthermore, if the total magnetic orbital moment of alloy is determined by the alloy composition, it is described as: $m_{tot}^{Co_xNi_{1-x}} = xm_{tot}^{Co} + (1-x)m_{tot}^{Ni}$, with $m_{tot} = m_\ell + m_s$. With m_ℓ and m_s, the total magnetic moment of Ni and Co for Co_xNi_{1-x} alloy with different Co concentrations are listed in Tab.6.8. Here the atomic magnetic moment of Co_xNi_{1-x} alloy is expressed in A/m unit

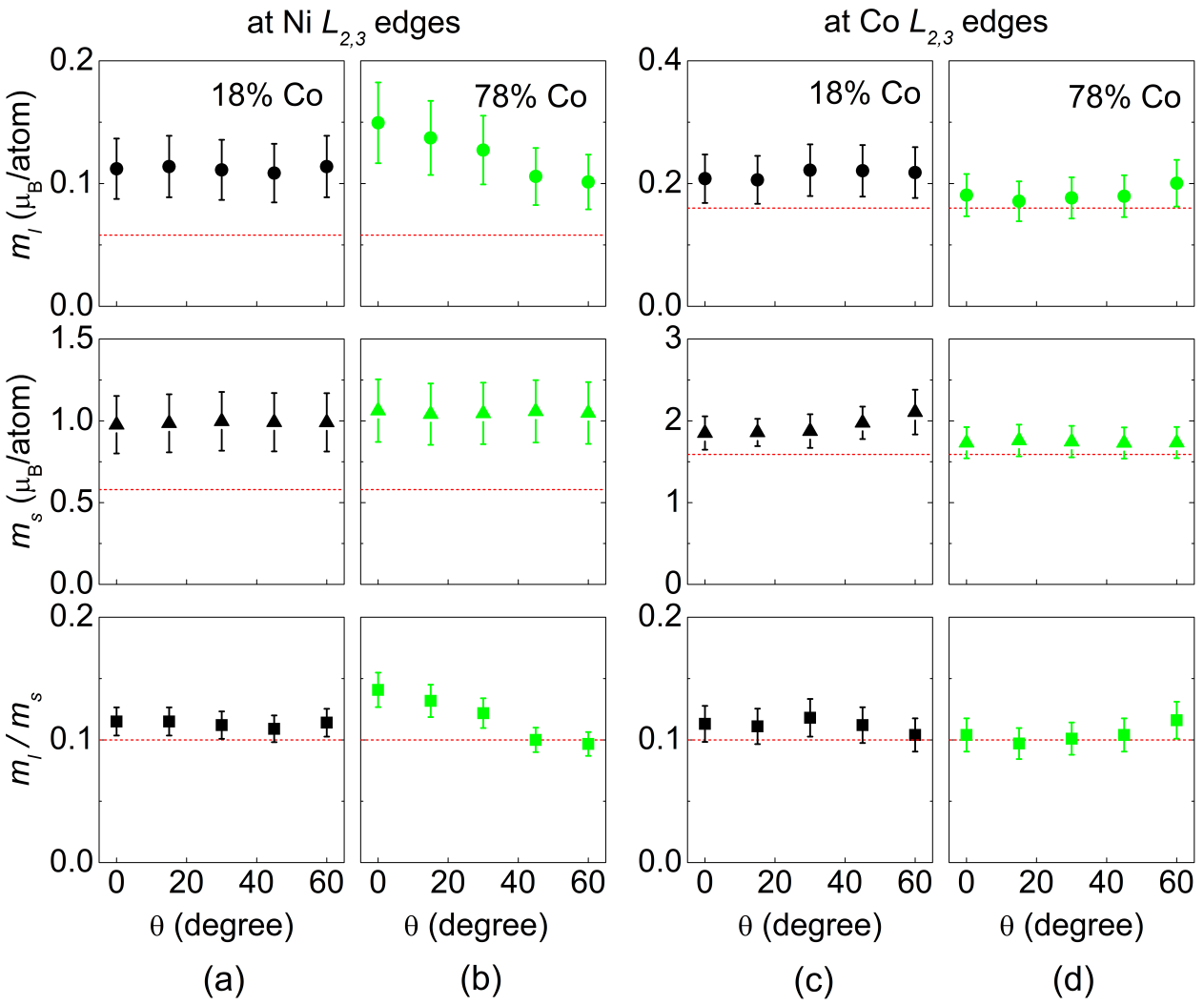

Figure 6.11: Angular dependence of magnetic moments of (a)(b) Ni and (c)(d) Co in Co_xNi_{1-x} alloy NWs with 18% and 78% Co, respectively. $n_h^{Ni} = 1.3 \pm 0.2$, $n_h^{Co} = 2.3 \pm 0.2$. The bulk values of m_ℓ, m_s and m_ℓ/m_s of Ni and Co are marked by red dashed line.

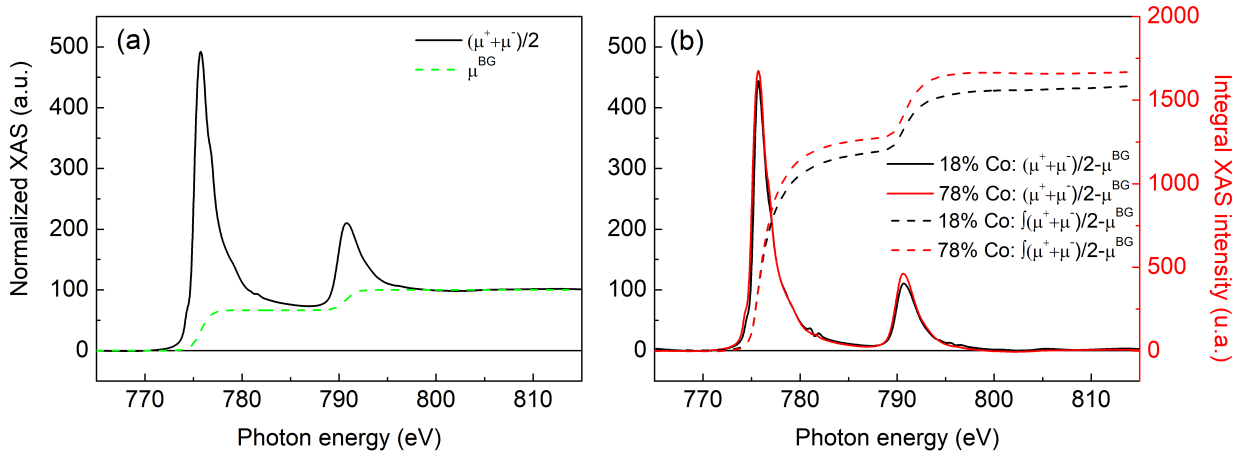

Figure 6.12: XAS spectra. (a) Average absorption spectrum (black line) with the background absorption one (green dashed line) of Co_xNi_{1-x} alloy NWs at 78% Co. The pre-edges are set to zero and the end to 100 for the normalization. (b) Comparison of the XAS spectra in removing the background absorption for 18 and 78% Co, together with their integration (dashed line).

($1\mu_B$=9.27×10^{-24} J/T). These values are compared to the reduced saturation moment deduced from the major hysteresis cycles. The agreement between the different methods is good, but it should be noted that the values extracted from XMCD measurements are larger than the ones extracted by VSM measurements.

Table 6.8: Determination of the total magnetic moment of Co_xNi_{1-x} alloy NWs with Co concentration of 0, 18 and 78%, together with the reduced saturation magnetization moment deduced from the major hysteresis cycle. Here the hysteresis responses are obtained along easy magnetization axis direction.

Co%	XMCD			Hysteresis cycle
	m_{tot}^{Ni} (μ_B/atom)	m_{tot}^{Co} (μ_B/atom)	$m_{tot}^{Co_xNi_{1-x}}$ (10^5 A/m)	$M_{sat} = m_{sat}/V^{NWs}$ (10^5 A/m)
0	0.83±0.13	/	6.9±1.1	4.5±0.7
18	1.00±0.14	1.88±0.17	9.4±1.2	6.2±0.9
78	1.13±0.18	1.94±0.27	13.7±2.0	12.9±1.9

Magnetic anisotropy energy (MAE)

With the angular dependence of m_ℓ, the MAE can be determined by the expression: MAE= $\alpha\frac{\xi}{4\mu_B}\Delta m_\ell$, where $\Delta m_\ell = m_\ell^0 - m_\ell^{\pi/2}$. Fig.6.13 shows the comparison of angular evolution of the orbital moment of Ni in Co_xNi_{1-x} alloy NWs with different Co concentrations: 0% (Ni), 18% and 78%. Comparison of these 3 systems leads to the following considerations:

- Firstly, m_ℓ is almost independent with θ for 18% Co. The fact that $\Delta m_\ell \approx 0$ indicates that the MAE is negligible. From the evolution of the magnetocrystalline anisotropy constant and the magnetostriction λ_{001} of Co_xNi_{1-x} alloy in Co concentration (Fig.6.6), it is found that these two terms fall at zero at about 20% Co, leading to weak contributions of the magnetocrystalline and magneto-elastic anisotropies to the total magnetic anisotropy. This is consistent with the absence of anisotropy of m_ℓ as determined by XMCD measurements.

- Secondly, opposite angular evolutions of m_ℓ are observed in pure Ni and 78% Co NWs, indicating that the m_ℓ contribution plays opposite roles. Ni NWs present a hard magnetization direction along wire axis with a negative Δm_ℓ. In contrary, 78% Co NWs show an easy axis along wire axis with a positive Δm_ℓ. This is in agreement with the result from VSM measurements.

- Thirdly, $\Delta m_\ell \neq 0$ indicates a magnetic anisotropy contribution related to m_ℓ of Ni in Co_xNi_{1-x} alloy with 78% Co. The MAE for alloys is more complex than for a single metal as the coefficients may vary with the alloy composition, such as the prefactor α and the spin-orbit coupling constant ξ. As the orbital and spin moments of Co are considered to be independent of θ, the angular evolution of the orbital moments of Ni contributes to the total magnetic anisotropy. In the following, I will make the simple assumption that Δm_ℓ, α and ξ can be extrapolated linearly as a function of x between the values of bulk Ni (x=0) and bulk Co (x=1). Δm_ℓ of Co_xNi_{1-x} is therefore expressed by:

$$\Delta m_\ell^{Co_xNi_{1-x}} = x\Delta m_\ell^{Co} + (1-x)\Delta m_\ell^{Ni} \tag{6.2}$$

  For 78% Co, only m_ℓ of Ni counts and occupies 22%. This results in Δm_ℓ of alloy to be 0.016 μ_B/atom. ξ is about 84 meV (ξ^{Ni}=105 meV and ξ^{Co}=79 meV [126]) and α about 0.17 (α =0.05 for Ni and 0.2 for Co [137]). The MAE associated to m_ℓ is thus estimated to 56±8 μeV/atom. The contribution of m_ℓ is related only to the magnetocrystalline and magnetoelastic anisotropy contributions. In our case, the cubic magnetocrystalline anisotropy contributes the same in the IP and OP directions. Therefore, I will give the estimation of the effective magnetoelastic anisotropy from the hysteresis cycles. The field corresponding to the effective magnetoelastic anisotropy contribution, H_{me}^{eff}, is 0.91±0.10 T for 78% Co (see Tab.6.6), leading to K_{me}^{eff} to be

5.5±0.6×10^5 J/m^3, *i.e.* 39±4 μeV/atom. Similar to Ni NWs, the contribution of m_ℓ is always larger than the magnetoelastic anisotropy effect deduced from the cycles. This may be related to the increase of m_ℓ of Ni in comparison with the bulk value. Thus, further study should be done on the origin of the large m_ℓ and m_s of Ni.

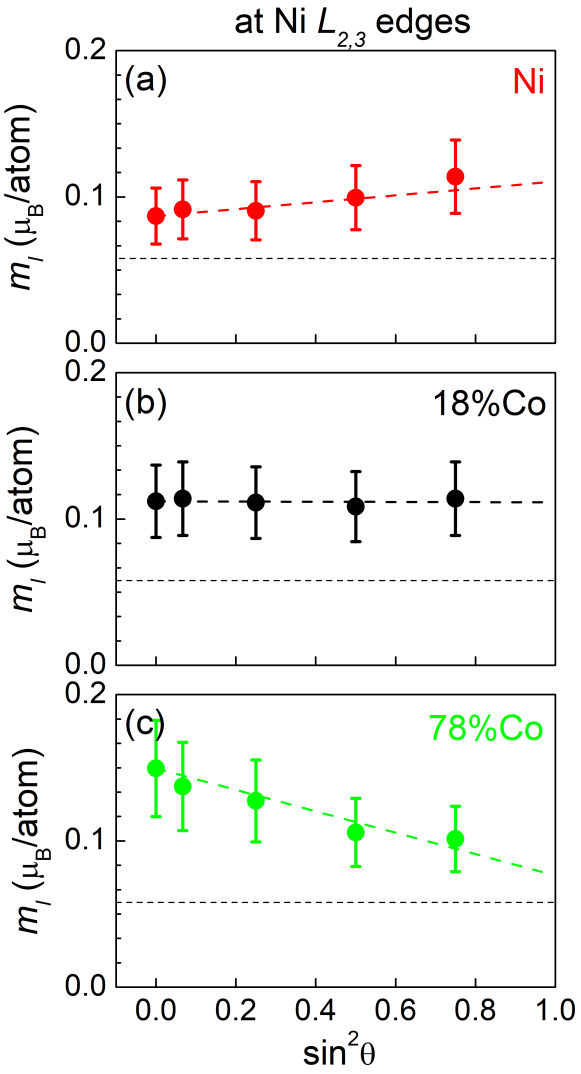

Figure 6.13: Angular dependence of the orbital magnetic moments at Ni $L_{2,3}$ edges for different Co concentrations: (a) Ni, (b) 18% Co and (c) 78% Co.

6.4 Conclusions

- The wire axis is a hard magnetization axis for highly strained Ni NWs due to the dominating negative magnetoelastic anisotropy contribution. By Co alloying, the magnetostriction coefficient λ_{001} becomes positive at Co concentrations over 17%, giving a positive magnetoelastic anisotropy contribution to the total anisotropy. Therefore, the wire axis is reversed from hard magnetization axis to an easy axis.

- With the increase of the axial strain and the magnetostriction in increasing Co concentration, the total magnetic anisotropy is enhanced due to the increase of the magnetoelastic anisotropy contribution, resulting in an increase of the blocking temperature.

- The blocking temperature of Co_xNi_{1-x} in Co-rich samples (>60% Co) is above room temperature. The thermal stability of Co_xNi_{1-x} alloy NWs in $SrTiO_3$ matrix is thus increased compared to in CeO_2 matrix. This provides a possibility of the coupling with other materials to achieve

multi-functionality stable at room temperature.

- The magnetic activation length for a local magnetization reversal is comparable to the domain wall width, indicating the fact that the magnetization reversal is related to the domain wall.
- The angular evolutions of the remanence and the magnetic orbital moment evidence the easy magnetization axis along wire axis.
- For the Co_xNi_{1-x} alloy NWs, only the magnetic orbital moment of Ni contributes. The contribution of orbital moment determined by XMCD is consistent with a uniaxial magnetoelastic anisotropy deduced from the hysteresis cycles.

Chapter 7

Conclusions and perspectives

7.1 Conclusions

The aim of this thesis was to grow epitaxial ferromagnetic NWs in an oxide matrix and to explore the interplay of the structural and magnetic properties. Self-assembled Co_xNi_{1-x} NWs were successfully grown in $SrTiO_3$ matrix by pulsed laser deposition (PLD). By the control of the growth condition, such as the sequential deposition, Ni NWs were elaborated with diameter below 6 nm. In addition, by using combinatorial schemes, Co_xNi_{1-x} alloy NWs were obtained. The alloy composition was confirmed by the energy-dispersive x-ray (EDX) spectrum in transmission electron microscopy (TEM).

The diameter of NWs is controlled in the 1.7-5.3 nm range, with a film thickness in the 50-250 nm range. The density of NWs is in the 10^{11}-10^{12} NWs/cm^2 range. The diameter can be controlled by the growth conditions: the section area is proportional to the ratio of the number of laser shots on the NW and matrix targets in a sequence. The metallic character of Co_xNi_{1-x} NWs was evidenced by x-ray absorption spectroscopy (XAS) measurements. Ni and Co_xNi_{1-x} alloy are both metallic in the matrix. X-ray diffraction (XRD) shows that Co_xNi_{1-x} alloy has a face-centered-cubic structure for Co content up to 80%.

The diameter-dependence of the vertical strain was studied by XRD: by decreasing the diameter from 5.3 to about 2 nm, the strain is enhanced from ∼2% to 4% for Ni NWs. Additionally, for Co_xNi_{1-x} alloy NWs, the strain is also influenced by the alloy composition: in maintaining the deposition quantity of NWs and matrix, the strain of Co_xNi_{1-x} NWs with similar diameter increases when the Co concentration increases. Compared to the strain of NWs in CeO_2 and $Sr(Ba)TiO_3$ matrix, it is highly increased in $SrTiO_3$ matrix.

For highly strained Ni NWs (ϵ_{zz} >2%), a misorientation of NWs with respect to the matrix occurs, accompanied by strain relaxation. This strain relaxation mechanism with misorientation in privileged directions of NWs allows the matching of (101) planes at the heterointerface, resulting in a lowered mismatch, as illustrated in Fig.7.1. In reducing the diameter or adding Co, the misorientation in privileged directions disappears and the disorder in NWs increases.

Due to the negative magnetostriction constant λ_{001} of Ni, the magnetoelastic anisotropy, $K_{me} = 3/2\lambda_{001}(c_{11} - c_{12})(\epsilon_{zz} - \epsilon_{rr})$, is uniaxial and in opposite with the shape anisotropy in Ni NWs. With large vertical strain ϵ_{zz} and negligible radial strain ϵ_{rr}, the magnetoelastic contribution becomes the dominating one, leading to a magnetic hard axis along the wire axis (Fig.7.2(a)). The peculiar magnetic behavior of Ni NWs could be explained satisfactorily by considering the impact of the inhomogeneous strain.

By Co alloying, the magnetostriction constant turns positive at 17% Co and above. Therefore, the wire axis is an easy magnetization axis for Co_xNi_{1-x} alloy NWs (Fig.7.2(b)(c)). In increasing the Co concentration, the coercive field and the blocking temperature increase. The blocking temperature reaches over 600 K at 78% Co, much larger than the room temperature. This temperature-stable anisotropic behavior may be exploited at room temperature in composite structures coupling NWs with other materials. Moreover, element-specific study of the magnetic moment have been performed on Ni and Co_xNi_{1-x} alloy NWs by x-ray magnetic circular dichroism (XMCD) measurements to determine the orbital and spin moments. The XAS spectra obtained at remanence and at saturation have evidenced the fact that the magnetization reversal is hard along wire axis for Ni and easy

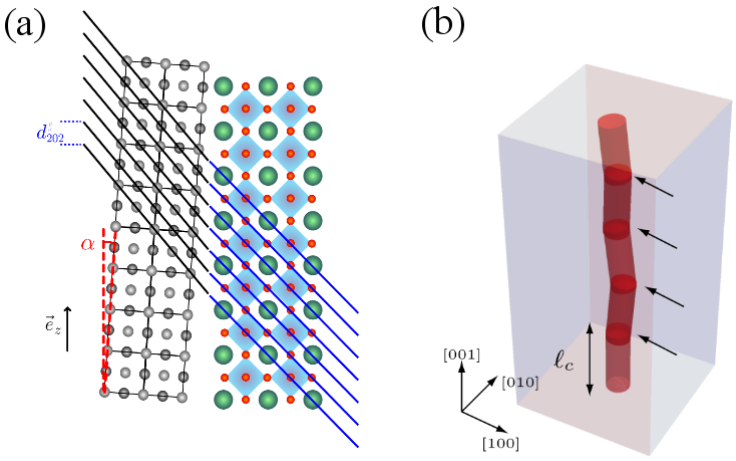

Figure 7.1: (a) Sketch of the lattice matching for Ni domains with misorientation by α of the [001] direction with respect to the [001] direction of the matrix. (b) Ni crystallite rotation induces creation of low angle GB (marked with arrows)

along wire axis for Co_xNi_{1-x} alloy at 18% Co and above. The superposition of the hysteresis cycles at Ni and Co $L_{2,3}$ edges indicates the successful alloying of Co and Ni. The total moment is in agreement with the saturation moment deduced from the hysteresis cycle for Co_xNi_{1-x} at different Co concentration. Besides, the angular evolution of the orbital magnetic moment m_ℓ allows to determine the magnetic anisotropy energy (MAE). The MAE is in the same order but a bit larger than that of the magnetoelastic anisotropy deduced from the hysteresis cycles or from calculation considering the mean strain.

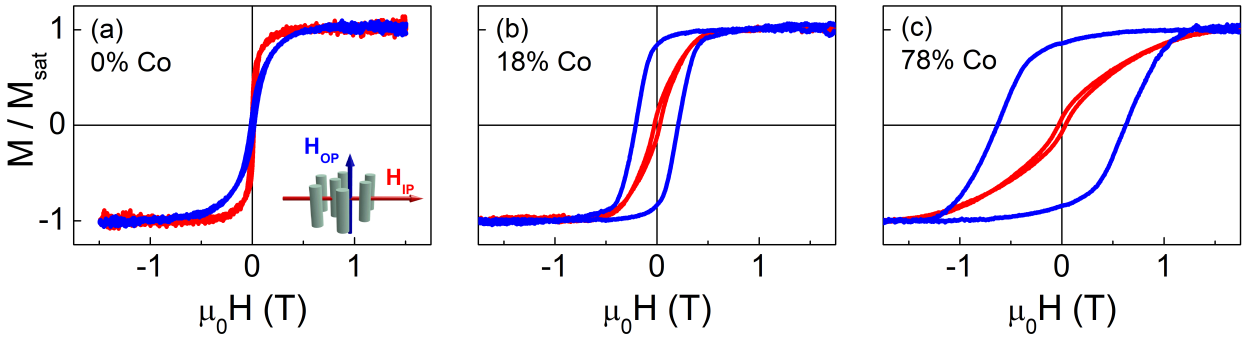

Figure 7.2: Comparison of VSM-hysteresis cycles at 10 K for Co_xNi_{1-x} NWs with (a) 0% Co, (b) 18% Co and (c) 78% Co. The external field is applied in IP (red) and OP (blue) directions.

In summary, epitaxial self-assembled Co_xNi_{1-x} NWs were successfully grown in $SrTiO_3$ matrix. The diameter is tunable by controlling the growth conditions. As the axial strain increases with decreasing diameter, the axial strain can be tuned by the control of the diameter. Finally, the magnetic anisotropy is controlled by the magnetoelastic anisotropy contribution related to the axial strain.

7.2 Perspectives

The fact that the magnetic anisotropy can be controlled in epitaxial self-assembled ferromagnetic Co_xNi_{1-x} NWs in $SrTiO_3$ matrix opens some perspectives.

- **Multifunctional nanocomposites**
  The stablity of the magnetic behavior in Co-rich sample provides a possibility to achieve multifunctionality in systems coupling well-defined magnetic anisotropy and another physical properties. For example, we have successfully grown bi-metallic AuCo NWs in $SrTiO_3$ matrix by adding a section of Au on top of a section of Co. This kind of system may be of interest in the field of magnetoplasmonics [138, 139, 140]. As shown in Fig.7.3, the cross-sectional and plan view indicate that the epitaxy of AuCo NWs in the matrix is achieved. By scanning transmission electron microscopy (STEM) equipped with a high angle annular dark-field (HAADF) detector and EDX chemical analysis, it is evidenced that Au and Co segregate, with Au on the top and Co in the bottom. Additionally, local plasmon resonance is evidenced in the optical response and the magnetic behavior is highly anisotropic, indicating the existence of the two targeted properties in AuCo NWs [141].

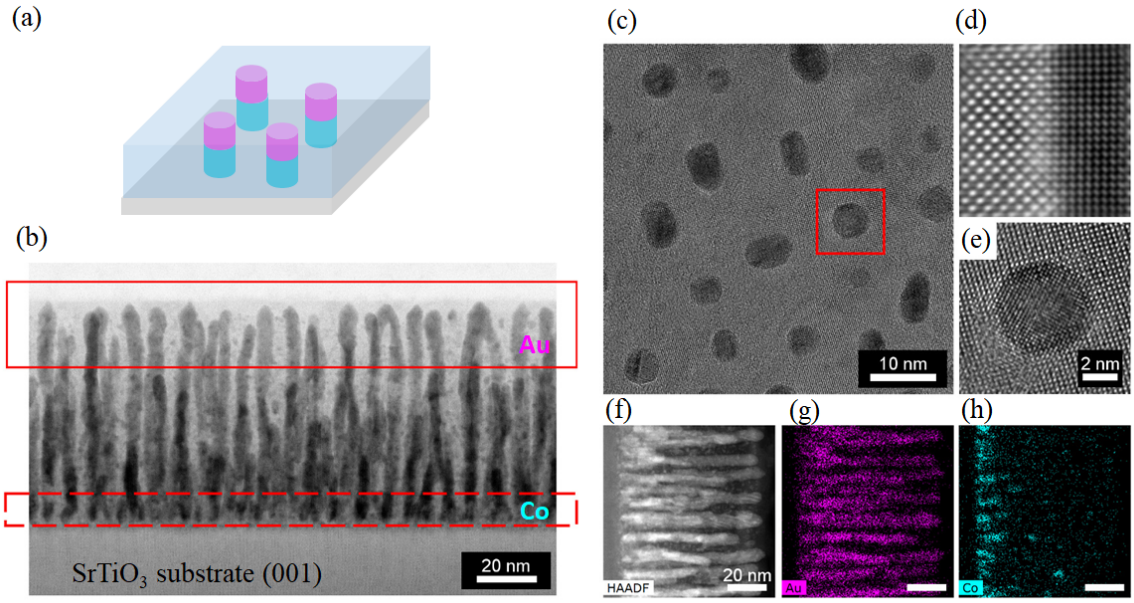

Figure 7.3: (a) Schematics of AuCo NWs in $SrTiO_3$ matrix. Electron microscopy images of AuCo:$SrTiO_3$ composite thin films: (b) cross-sectional and (c) plan views. (d) HRTEM imaging of the NW-$SrTiO_3$ interface in cross-sectional geometry and (e) single nanowire in plan view. (f–h) STEM-HAADF and EDX chemical mapping of Co and Au in cross-sectional view. Figure adapted from [141].

Although Co in the bi-metallic AuCo NWs has a fcc structure, the quality of the epitaxy has to be improved. Structural inhomogeneity of both Co and Au occurs along the wire axis. A short-term goal is to improve the epitaxial quality by all means, such as replacing Co by Co_xNi_{1-x} with ∼80% Co, which has better structural and magnetic properties.

- **Vertical epitaxial heterostructure architecture**
  The fact that the magnetic anisotropy is related to the NW diameter suggests to grow 3D nanomagnetic structures. For instance, a cylindrical NW with modulated diameter, with the magnetic anisotropy along wire axis depending on the diameter. The modulation of the diameter may be achieved by the control of the growth conditions, as illustrated in Fig.7.4(a). Otherwise, as the magnetic anisotropy is mainly influenced by the vertical strain, by changing the matrix, the strain of NWs varies, leading to the evolution of the magnetic anisotropy along wire even with similar diameter. For example, the Ni NWs is less strained in CeO_2 than in $SrTiO_3$

matrix. By sequential deposition of CeO_2 and $SrTiO_3$ matrix, the diameter or the strain may be manipulated along wire axis in order to obtained a NW with repetition of in-plane and out-of-plane anisotropies or large and small anisotropies (see Fig.7.4(b)).

Besides, the 3D nanomagnetism also inspires us to grow a complex structure by layering a in-plane anisotropy film on top of the vertical anisotropy NWs as shown in Fig.7.4(c). As the magnetization direction is expected to change at the junctions of wires and thin film, with the possible formation of a vortex, we would like to explore the magnetic configurations at the junctions.

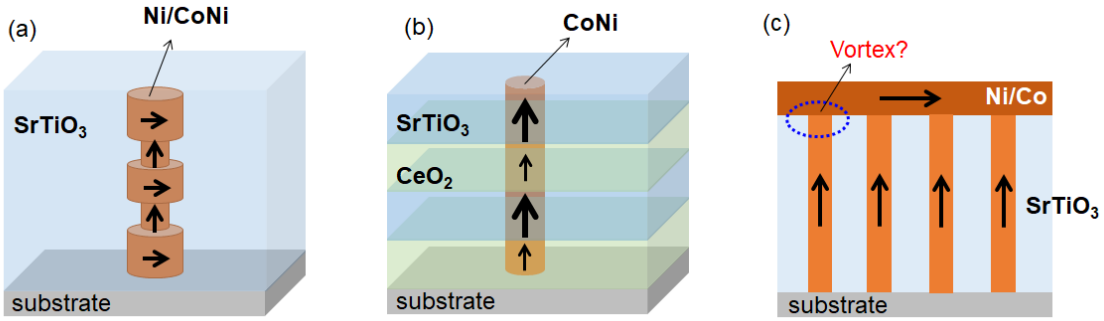

Figure 7.4: Illustrations of the hetero-epitaxial NWs in an oxide matrix. (a) Variation of the anisotropy directions by diameter modulation. (b) Manipulation of anisotropy along wire by changing the matrix. (c) Combination of vertically aligned NWs with vertical anisotropy and thin film with in-plane anisotropy. The magnetic configuration is indicated by black arrows.

Bibliography

[1] Nitin Samarth. Quantum materials discovery from a synthesis perspective. *Nature materials*, 16(11):1068–1076, 2017.

[2] M. Bowen, V. Cros, F. Petroff, A. Fert, C. Martınez Boubeta, J. L. Costa-Krämer, J. V. Anguita, A. Cebollada, F. Briones, J. M. de Teresa, L. Morellón, M. R. Ibarra, F. Güell, F. Peiró, and A. Cornet. Large magnetoresistance in Fe/MgO/FeCo(001) epitaxial tunnel junctions on GaAs(001). *Applied Physics Letters*, 79(11):1655–1657, 2001.

[3] J. Faure-Vincent, C. Tiusan, E. Jouguelet, F. Canet, M. Sajieddine, C. Bellouard, E. Popova, M. Hehn, F. Montaigne, and A. Schuhl. High tunnel magnetoresistance in epitaxial Fe/MgO/Fe tunnel junctions. *Applied Physics Letters*, 82(25):4507–4509, 2003.

[4] V. G. Menéndez Garcia, Stephane Fusil, Karim Bouzehouane, Shaima Enouz-Vedrenne, Neil D Mathur, Alain Barthélemy, and Manuel Bibes. Giant tunnel electroresistance for non-destructive readout of ferroelectric states. *Nature*, 460:81–84, 2009.

[5] Gabriel Bochi, C. A. Ballentine, H. E. Inglefield, C. V. Thompson, and R. C. O'Handley. Evidence for strong surface magnetoelastic anisotropy in epitaxial Cu/Ni/Cu(001) sandwiches. *Phys. Rev. B*, 53:R1729–R1732, 1996.

[6] Judith L MacManus-Driscoll, Patrick Zerrer, Haiyan Wang, Hao Yang, Jongsik Yoon, Arnaud Fouchet, Rong Yu, Mark G Blamire, and Quanxi Jia. Strain control and spontaneous phase ordering in vertical nanocomposite heteroepitaxial thin films. *Nature materials*, 7 4:314–20, 2008.

[7] F. Vidal, Y. Zheng, P. Schio, F. J. Bonilla, M. Barturen, J. Milano, D. Demaille, E. Fonda, A. J. A. de Oliveira, and V. H. Etgens. Mechanism of localization of the magnetization reversal in 3 nm wide Co nanowires. *Phys. Rev. Lett.*, 109:117205, 2012.

[8] Jie Yao, Zhaowei Liu, Yongmin Liu, Yuan Wang, Cheng Sun, Guy Bartal, Angelica M. Stacy, and Xiang Zhang. Optical negative refraction in bulk metamaterials of nanowires. *Science*, 321(5891), 2008.

[9] Andrei V. Kabashin, Peter Robert Evans, S Pastkovsky, W. R. Hendren, Gregory A. Wurtz, Ron Atkinson, Robert James Pollard, Viktor Podolskiy, and Anatoly V. Zayats. Plasmonic nanorod metamaterials for biosensing. *Nature materials*, 8 11:867–71, 2009.

[10] Leigang Li, Liuyang Sun, Juan Sebastian Gomez-Diaz, Nicki L. Hogan, Ping Lu, Fauzia Khatkhatay, Wenrui Zhang, Jie Jian, Jijie Huang, Qing Su, Meng Fan, Clement Jacob, Jin Li, Xinghang Zhang, Quanxi Jia, Matthew Sheldon, Andrea Alù, Xiaoqin Li, and Haiyan Wang. Self-assembled epitaxial au–oxide vertically aligned nanocomposites for nanoscale metamaterials. *Nano Letters*, 16(6):3936–3943, 2016. PMID: 27186652.

[11] Seiji Kawasaki, Ryota Takahashi, Takahisa Yamamoto, Masaki Kobayashi, Hiroshi Kumigashira, Jun Yoshinobu, Fumio Komori, Akihiko Kudo, and Mikk Lippmaa. Photoelectrochemical water splitting enhanced by self-assembled metal nanopillars embedded in an oxide semiconductor photoelectrode. *Nature communications*, 7:11818, 2016.

[12] Shinbuhm Lee and Judith L. MacManus-Driscoll. Research update: Fast and tunable nanoionics in vertically aligned nanostructured films. *APL Materials*, 5(4):042304, 2017.

[13] Judith MacManus-Driscoll, Ady Suwardi, Ahmed Kursumovic, Zhenxing Bi, Chen-Fong Tsai, Haiyan Wang, Quanxi Jia, and Oon Jew Lee. New strain states and radical property tuning of metal oxides using a nanocomposite thin film approach. *APL Materials*, 3(6):062507, 2015.

[14] Huaping Wu, Guozhong Chai, Ting Zhou, Zheng Zhang, Takayuki Kitamura, and Haomiao Zhou. Adjustable magnetoelectric effect of self-assembled vertical multiferroic nanocomposite

films by the in-plane misfit strain and ferromagnetic volume fraction. *Journal of Applied Physics*, 115(11):114105, 2014.

[15] H. Zheng, J. Wang, S. E. Lofland, Z. Ma, L. Mohaddes-Ardabili, T. Zhao, L. Salamanca-Riba, S. R. Shinde, S. B. Ogale, F. Bai, D. Viehland, Y. Jia, D. G. Schlom, M. Wuttig, A. Roytburd, and R. Ramesh. Multiferroic $BaTiO_3$-$CoFe_2O_4$ nanostructures. *Science*, 303(5658):661–663, 2004.

[16] N. M. Aimon, D. Hun-Kim, H. Kyoon Choi, and C. A. Ross. Deposition of epitaxial $BiFeO_3/CoFe_2O_4$ nanocomposites on (001) $SrTiO_3$ by combinatorial pulsed laser deposition. *Applied Physics Letters*, 100(9):092901, 2012.

[17] Nicolas M. Aimon, Hong Kyoon Choi, Xue Yin Sun, Dong Hun Kim, and Caroline A. Ross. Templated self-assembly of functional oxide nanocomposites. *Advanced Materials*, 26(19):3063–3067, 2014.

[18] Heng-Jui Liu, Long-Yi Chen, Qing He, Chen-Wei Liang, Yu-Ze Chen, Yung-Shun Chien, Ying-Hui Hsieh, Su-Jien Lin, Elke Arenholz, Chih-Wei Luo, Yu-Lun Chueh, Yi-Chun Chen, and Ying-Hao Chu. Epitaxial photostriction–magnetostriction coupled self-assembled nanostructures. *ACS Nano*, 6(8):6952–6959, 2012.

[19] Luc Piraux, Krystel Renard, Raphael Guillemet, Stefan Mátéfi-Tempfli, Mária Mátéfi-Tempfli, Vlad Andrei Antohe, Stéphane Fusil, Karim Bouzehouane, and Vincent Cros. Template-grown NiFe/Cu/NiFe nanowires for spin transfer devices. *Nano Letters*, 7(9):2563–2567, 2007. PMID: 17715984.

[20] Aiping Chen, Zhenxing Bi, Harshad Hazariwala, Xinghang Zhang, Qing Su, Li Chen, Quanxi Jia, Judith L MacManus-Driscoll, and Haiyan Wang. Microstructure, magnetic, and low-field magnetotransport properties of self-assembled $(La_{0.7}Sr_{0.3}MnO_3)_{0.5}$:$(CeO_2)_{0.5}$ vertically aligned nanocomposite thin films. *Nanotechnology*, 22(31):315712, 2011.

[21] Qing Su, Wenrui Zhang, Ping Lu, Shumin Fang, Fauzia Khatkhatay, Jie Jian, Leigang Li, Fanglin Chen, Xinghang Zhang, Judith L. MacManus-Driscoll, Aiping Chen, Quanxi Jia, and Haiyan Wang. Self-assembled magnetic metallic nanopillars in ceramic matrix with anisotropic magnetic and electrical transport properties. *ACS Applied Materials & Interfaces*, 8(31):20283–20291, 2016.

[22] Shaoguang Yang, Hao Zhu, Dongliang Yu, Zhiqiang Jin, Shaolong Tang, and Youwei Du. Preparation and magnetic property of Fe nanowire array. *Journal of Magnetism and Magnetic Materials*, 222(1):97 – 100, 2000.

[23] D.H Qin, M Lu, and H.L Li. Magnetic force microscopy of magnetic domain structure in highly ordered Co nanowire arrays. *Chemical Physics Letters*, 350(1):51 – 56, 2001.

[24] Xing Sun, Jijie Huang, Jie Jian, Meng Fan, Han Wang, Qiang Li, Judith L. Mac Manus-Driscoll, Ping Lu, Xinghang Zhang, and Haiyan Wang. Three-dimensional strain engineering in epitaxial vertically aligned nanocomposite thin films with tunable magnetotransport properties. *Mater. Horiz.*, 5:536–544, 2018.

[25] Amalio Fernández-Pacheco, Robert Streubel, Olivier Fruchart, Riccardo Hertel, Peter Fischer, and Russell P. Cowburn. Three-dimensional nanomagnetism. *Nature Communications*, 8:15756, 2017.

[26] Francisco Javier Bonilla, Anastasiia Novikova, Franck Vidal, Yunlin Zheng, Emiliano Fonda, Dominique Demaille, Vivien Schuler, Alessandro Coati, Alina Vlad, Yves Garreau, Michèle Sauvage Simkin, Yves Dumont, Sarah Hidki, and Victor Etgens. Combinatorial growth and anisotropy control of self-assembled epitaxial ultrathin alloy nanowires. *ACS Nano*, 7(5):4022–4029, 2013.

[27] V. Schuler, J. Milano, A. Coati, A. Vlad, M. Sauvage-Simkin, Y. Garreau, D. Demaille, S. Hidki, A. Novikova, E. Fonda, Y. Zheng, and F. Vidal. Growth and magnetic properties of vertically aligned epitaxial CoNi nanowires in (Sr, Ba)TiO_3 with diameters in the 1.8-6 nm range. *Nanotechnology*, 27(49), 2016.

[28] J. A. Osborn. Demagnetizing factors of the general ellipsoid. *Phys. Rev.*, 67:351–357, 1945.

[29] K. Honda and S. Kaya. On the magnetisation of single crystals of iron. *Sci. Rep. Tohoku Univ.*, 15:721–754, 1926.

[30] S. Kaya. On the magnetization of single crystals of nickel. *Sci. Rep. Tohoku Univ.*, 17:639–663, 1928.

[31] S. Kaya. On the magnetisation of single crystals of cobalt. *Sci. Rep. Tohoku Univ.*, 17:1157–1177, 1928.

[32] D. M. Paige, B. Szpunar, and B. K. Tanner. The magnetocrystalline anisotropy of cobalt. *Journal of Magnetism and Magnetic Materials*, 44(3):239–248, 1984.

[33] Eiji Tatsumoto, Tetsuhiko Okamoto, Nobuo Iwata, and Yowa Kadena. Temperature dependence of the magnetocrystalline anisotropy constants k_1 and k_2 of nickel. *Journal of the Physical Society of Japan*, 20(8):1541–1542, 1965.

[34] Charles Kittel. Physical theory of ferromagnetic domains. *Rev. Mod. Phys.*, 21:541–583, 1949.

[35] C. A.F. Vaz, J. A.C. Bland, and G. Lauhoff. Magnetism in ultrathin film structures. *Reports on Progress in Physics*, 71(5), 2008.

[36] M. Jamet, W. Wernsdorfer, C. Thirion, D. Mailly, V. Dupuis, P. Mélinon, and A. Pérez. Magnetic anisotropy of a single cobalt nanocluster. *Phys. Rev. Lett.*, 86:4676–4679, 2001.

[37] Matthieu Jamet, Wolfgang Wernsdorfer, Christophe Thirion, Véronique Dupuis, Patrice Mélinon, Alain Pérez, and Dominique Mailly. Magnetic anisotropy in single clusters. *Phys. Rev. B*, 69:024401, 2004.

[38] E. H. Frei, S. Shtrikman, and D. Treves. Critical size and nucleation field of ideal ferromagnetic particles. *Phys. Rev.*, 106:446–455, 1957.

[39] Riccardo Hertel and Jürgen Kirschner. Magnetization reversal dynamics in nickel nanowires. *Physica B: Condensed Matter*, 343(1-4):206–210, 2004.

[40] William Fuller Brown. Thermal fluctuations of a single-domain particle. *Phys. Rev.*, 130:1677–1686, Jun 1963.

[41] F. Tournus, A. Hillion, A. Tamion, and V. Dupuis. Effect of nonlinear superparamagnetic response on susceptibility curves for nanoparticle assemblies. *Phys. Rev. B*, 87:174404, 2013.

[42] F. Tournus and E. Bonet. Magnetic susceptibility curves of a nanoparticle assembly, I: Theoretical model and analytical expressions for a single magnetic anisotropy energy. *Journal of Magnetism and Magnetic Materials*, 323(9):1109 – 1117, 2011.

[43] F. Tournus and A. Tamion. Magnetic susceptibility curves of a nanoparticle assembly II. Simulation and analysis of ZFC/FC curves in the case of a magnetic anisotropy energy distribution. *Journal of Magnetism and Magnetic Materials*, 323(9):1118 – 1127, 2011.

[44] Olivier Fruchart and André Thiaville. Magnetism in reduced dimensions. *Comptes Rendus Physique*, 6(9):921–933, 2005.

[45] R. Skomski, D. Leslie-Pelecky, R.D. Kirby, A. Kashyap, and D.J. Sellmyer. Coercivity of disordered nanostructures. *Scripta Materialia*, 48(7):857–862, 2003.

[46] M. P. Sharrock. Time dependence of switching fields in magnetic recording media (invited). *Journal of Applied Physics*, 76(10):6413, 1994.

[47] R. Alben, J. J. Becker, and M. C. Chi. Random anisotropy in amorphous ferromagnets. *Journal of Applied Physics*, 49(3):1653–1658, mar 1978.

[48] E. M. Chudnovsky, W. M. Saslow, and R. A. Serota. Ordering in ferromagnets with random anisotropy. *Phys. Rev. B*, 33:251–261, 1986.

[49] Giselher Herzer. Anisotropies in soft magnetic nanocrystalline alloys. *Journal of Magnetism and Magnetic Materials*, 294(2):99 – 106, 2005. NANO2004.

[50] Eiji Kita, Naoki Tsukuhara, Hidenori Sato, Keishin Ota, Hideto Yangaihara, Hisanori Tanimoto, and Naoshi Ikeda. Structure and random anisotropy in single-phase Ni nanocrystals. *Applied Physics Letters*, 88(15):152501, 2006.

[51] T. Hauet, L. Piraux, S. K. Srivastava, V. A. Antohe, D. Lacour, M. Hehn, F. Montaigne, J. Schwenk, M. A. Marioni, H. J. Hug, O. Hovorka, A. Berger, S. Mangin, and F. Abreu Araujo. Reversal mechanism, switching field distribution, and dipolar frustrations in Co/Pt bit pattern media based on auto-assembled anodic alumina hexagonal nanobump arrays. *Phys. Rev. B*, 89:174421, 2014.

[52] U. Netzelmann. Ferromagnetic resonance of particulate magnetic recording tapes. *Journal of Applied Physics*, 68(4):1800–1807, 1990.

[53] A. Encinas-Oropesa, M. Demand, L. Piraux, I. Huynen, and U. Ebels. Dipolar interactions in arrays of nickel nanowires studied by ferromagnetic resonance. *Phys. Rev. B*, 63:104415, 2001.

[54] R. Eason. Pulsed laser deposition of thin films: applications-led growth of functional materials. *Published by John Wiley & Sons, Inc., Hoboken, New Jersey, Robert Eason (Editor)*, 2007.

[55] J. D. Ferguson, G. Arikan, D. S. Dale, A. R. Woll, and J. D. Brock. Measurements of Surface Diffusivity and Coarsening during Pulsed Laser Deposition. *Physical Review Letters*, 103(25):256103, 2009.

[56] E. J. Tarsa, E. A. Hachfeld, F. T. Quinlan, J. S. Speck, and M. Eddy. Growth-related stress and surface morphology in homoepitaxial $SrTiO_3$ films. *Applied Physics Letters*, 68(4):490–492, 1996.

[57] C. Barry Williams, David B. & Carter. Transmission electron microscopy - a textbook for materials science. *Springer*, 2009.

[58] R. F. Egerton. Electron energy-loss spectroscopy in the electron microscope. *3rd edition, Springer*, 2011.

[59] O. Robach, Y. Garreau, K. Aïd, and M. B. Véron-Jolliot. Corrections for surface X-ray diffraction measurements using the *Z*-axis geometry: finite size effects in direct and reciprocal space. *Journal of Applied Crystallography*, 33(4):1006–1018, 2000.

[60] Sander Roobol, Willem Onderwaater, Jakub Drnec, Roberto Felici, and Joost Frenken. *BINoculars*: data reduction and analysis software for two-dimensional detectors in surface X-ray diffraction. *Journal of Applied Crystallography*, 48(4):1324–1329, 2015.

[61] F. Preisach. Über die magnetische nachwirkung. *Zeitschrift für Physik*, 94(5):277–302, 1935.

[62] I. Mayergoyz. Mathematical models of hysteresis. *IEEE Transactions on Magnetics*, 22(5):603–608, 1986.

[63] Christopher R. Pike, Andrew P. Roberts, and Kenneth L. Verosub. Characterizing interactions in fine magnetic particle systems using first order reversal curves. *Journal of Applied Physics*, 85(9):6660–6667, 1999.

[64] C. R. Pike. First-order reversal-curve diagrams and reversible magnetization. *Phys. Rev. B*, 68:104424, 2003.

[65] C. R. Pike, C. A. Ross, R. T. Scalettar, and G. Zimanyi. First-order reversal curve diagram analysis of a perpendicular nickel nanopillar array. *Phys. Rev. B*, 71:134407, 2005.

[66] Costin-Ionuţ Dobrotă and Alexandru Stancu. What does a first-order reversal curve diagram really mean? A study case: Array of ferromagnetic nanowires. *Journal of Applied Physics*, 113(4):043928, 2013.

[67] Dustin A. Gilbert, T. Zimanyi Gergely, Randy K. Dumas, Michael Winklhofer, Alicia Gomez, Nasim Eibagi, J L Vicent, and Kai Liu. Quantitative Decoding of Interactions in Tunable Nanomagnet Arrays Using First Order Reversal Curves. *Scientific Reports*, pages 1–5, 2014.

[68] Sergiu Ruta, Ondrej Hovorka, Pin Wei Huang, Kangkang Wang, Ganping Ju, and Roy Chantrell. First order reversal curves and intrinsic parameter determination for magnetic materials; Limitations of hysteron-based approaches in correlated systems. *Scientific Reports*, 7(March):1–12, 2017.

[69] C. T. Chen, F. Sette, Y. Ma, and S. Modesti. Soft-x-ray magnetic circular dichroism at the $L_{2,3}$ edges of nickel. *Phys. Rev. B*, 42:7262–7265, 1990.

[70] Y. Wu, J. Stöhr, B. D. Hermsmeier, M. G. Samant, and D. Weller. Enhanced orbital magnetic moment on co atoms in Co/Pd multilayers: A magnetic circular x-ray dichroism study. *Phys. Rev. Lett.*, 69:2307–2310, 1992.

[71] Y.U. Idzerda, C.J. Gutierrez, L.H. Tjeng, H.-J. Lin, G. Meigs, and C.T. Chen. Magnetic circular dichroism of Fe_xCo_{1-x} single-crystal thin films. *Journal of Magnetism and Magnetic Materials*, 127(1):109 – 114, 1993.

[72] Jan Vogel and Maurizio Sacchi. Polarization and angular dependence of the $L_{2,3}$ absorption edges in Ni(110). *Phys. Rev. B*, 49:3230–3234, 1994.

[73] C. T. Chen, Y. U. Idzerda, H.-J. Lin, N. V. Smith, G. Meigs, E. Chaban, G. H. Ho, E. Pellegrin, and F. Sette. Experimental confirmation of the x-ray magnetic circular dichroism sum rules for iron and cobalt. *Phys. Rev. Lett.*, 75:152–155, 1995.

[74] J. Stöhr and Y. Wu. *X-Ray Magnetic Circular Dichroism: Basic Concepts and Theory for 3D Transition Metal Atoms*, pages 221–250. Springer Netherlands, Dordrecht, 1994.

[75] Maurizio Sacchi and Jan Vogel. *Dichroism in X-ray Absorption.* Springer Berlin Heidelberg, Berlin, Heidelberg, 2001.

[76] B. T. Thole, P. Carra, F. Sette, and G. van der Laan. X-ray circular dichroism as a probe of orbital magnetization. *Phys. Rev. Lett.*, 68:1943–1946, 1992.

[77] Paolo Carra, B. T. Thole, Massimo Altarelli, and Xindong Wang. X-ray circular dichroism and local magnetic fields. *Phys. Rev. Lett.*, 70:694–697, 1993.

[78] P. Ohresser, E. Otero, F. Choueikani, K. Chen, S. Stanescu, F. Deschamps, T. Moreno, F. Polack, B. Lagarde, J.-P. Daguerre, F. Marteau, F. Scheurer, L. Joly, J.-P. Kappler, B. Muller, O. Bunau, and Ph. Sainctavit. Deimos: A beamline dedicated to dichroism measurements in the 350–2500 ev energy range. *Review of Scientific Instruments*, 85(1):013106, 2014.

[79] L. Joly, E. Otero, F. Choueikani, F. Marteau, L. Chapuis, and P. Ohresser. Fast continuous energy scan with dynamic coupling of the monochromator and undulator at the DEIMOS beamline. *Journal of Synchrotron Radiation*, 21(3):502–506, 2014.

[80] J.-P. Kappler, E. Otero, W. Li, L. Joly, G. Schmerber, B. Muller, F. Scheurer, F. Leduc, B. Gobaut, L. Poggini, G. Serrano, F. Choueikani, E. Lhotel, A. Cornia, R. Sessoli, M. Mannini, M.-A. Arrio, Ph. Sainctavit, and P. Ohresser. Ultralow-temperature device dedicated to soft X-ray magnetic circular dichroism experiments. *Journal of Synchrotron Radiation*, 25(6):1727–1735, 2018.

[81] V Schuler. Self-assembled ferromagnetic nanowires embedded in an oxide matrix : growth, vertical epitaxy, magnetic properties. *PHD thesis of Université Pierre et Marie Curie*, 2015.

[82] M Hennes, V Schuler, X Weng, J Buchwald, D Demaille, Y Zheng, and F Vidal. Growth of vertically aligned nanowires in metal-oxide nanocomposites: Kinetic monte-carlo modeling: Versus experiments. *Nanoscale*, 10, 2018.

[83] K. J. Choi, M. Biegalski, Y. L. Li, A. Sharan, J. Schubert, R. Uecker, P. Reiche, Y. B. Chen, X. Q. Pan, V. Gopalan, L. Q. Che, D. C. Schlom, and C. B. Eom. Enhancement of ferroelectricity in strained $BaTiO_3$ thin films. *Science*, 306(5698):1005–1009, 2004.

[84] Hailong Wang, Chunhui Du, P. Chris Hammel, and Fengyuan Yang. Strain-tunable magnetocrystalline anisotropy in epitaxial $Y_3Fe_5O_2$ thin films. *Phys. Rev. B*, 89:134404, 2014.

[85] Chunhui Du, Rohan Adur, Hailong Wang, Adam J. Hauser, Fengyuan Yang, and P. Chris Hammel. Control of magnetocrystalline anisotropy by epitaxial strain in double perovskite sr_2femoo_6 films. *Phys. Rev. Lett.*, 110:147204, 2013.

[86] I. Bozovic, G. Logvenov, I. Belca, B. Narimbetov, and I. Sveklo. Epitaxial strain and superconductivity in $La_{2-x}Sr_xCuO_4$ thin films. *Phys. Rev. Lett.*, 89:107001, 2002.

[87] D. J. Sprouster, R. Giulian, L. L. Araujo, P. Kluth, B. Johannessen, N. Kirby, K. Nordlund, and M. C. Ridgway. Ion-irradiation-induced amorphization of cobalt nanoparticles. *Phys. Rev. B*, 81:155414, 2010.

[88] L. L. Araujo, R. Giulian, D. J. Sprouster, C. S. Schnohr, D. J. Llewellyn, P. Kluth, D. J. Cookson, G. J. Foran, and M. C. Ridgway. Size-dependent characterization of embedded Ge nanocrystals: Structural and thermal properties. *Phys. Rev. B*, 78:094112, 2008.

[89] Gary J. Long, Dimitri Hautot, Quentin A. Pankhurst, D. Vandormael, F. Grandjean, J. P. Gaspard, Valérie Briois, Taeghwan Hyeon, and Kenneth S. Suslick. Mössbauer-effect and x-ray-absorption spectral study of sonochemically prepared amorphous iron. *Phys. Rev. B*, 57:10716–10722, 1998.

[90] X. Weng, M. Hennes, A. Coati, A. Vlad, Y. Garreau, M. Sauvage-Simkin, E. Fonda, G. Patriarche, D. Demaille, F. Vidal, and Y. Zheng. Ultrathin ni nanowires embedded in $SrTiO_3$: Vertical epitaxy, strain relaxation mechanisms, and solid-state amorphization. *Phys. Rev. Materials*, 2:106003, 2018.

[91] M.A. Krivoglaz. Theory of the scattering of x-rays by crystals containing defects. *Fiz. Met. Metalloved.*, 12(4):465, 1961.

[92] V. Holý, J. Kuběna, E. Abramof, K. Lischka, A. Pesek, and E. Koppensteiner. X-ray double and triple crystal diffractometry of mosaic structure in heteroepitaxial layers. *Journal of Applied Physics*, 74(3):1736–1743, 1993.

[93] M.A. Krivoglaz. *X-Ray and Neutron Diffraction in Nonideal Crystals.* Springer, Berlin, 1996.

[94] V. M. Kaganer, R. Köhler, M. Schmidbauer, R. Opitz, and B. Jenichen. X-ray diffraction peaks due to misfit dislocations in heteroepitaxial structures. *Phys. Rev. B*, 55:1793–1810, 1997.

[95] V. M. Kaganer, O. Brandt, A. Trampert, and K. H. Ploog. X-ray diffraction peak profiles from threading dislocations in GaN epitaxial films. *Phys. Rev. B*, 72:045423, 2005.

[96] T. Nishizawa and K. Ishida. The CoNi (cobalt-nickel) system. *Bulletin of Alloy Phase Diagrams*, 4(4):390–395, 1983.

[97] C. Bran, J. A. Fernandez-Roldan, E. M. Palmero, E. Berganza, J. Guzman, R. P. del Real, A. Asenjo, A. Fraile Rodríguez, M. Foerster, L. Aballe, O. Chubykalo-Fesenko, and M. Vazquez. Direct observation of transverse and vortex metastable magnetic domains in cylindrical nanowires. *Phys. Rev. B*, 96:125415, 2017.

[98] L. G. Vivas, M. Vazquez, J. Escrig, S. Allende, D. Altbir, D. C. Leitao, and J. P. Araujo. Magnetic anisotropy in coni nanowire arrays: Analytical calculations and experiments. *Phys. Rev. B*, 85:035439, 2012.

[99] W. C. Nunes, W. S. D. Folly, J. P. Sinnecker, and M. A. Novak. Temperature dependence of the coercive field in single-domain particle systems. *Phys. Rev. B*, 70:014419, 2004.

[100] R. C. Hall. Single crystal anisotropy and magnetostriction constants of several ferromagnetic materials including alloys of NiFe, SiFe, AlFe, CoNi, and CoFe. *Journal of Applied Physics*, 30(6):816–819, 1959.

[101] R. Skomski, H. Zeng, M. Zheng, and D. J. Sellmyer. Magnetic localization in transition-metal nanowires. *Phys. Rev. B*, 62:3900–3904, 2000.

[102] M.I Chipara, R Skomski, and D.J Sellmyer. Magnetic modes in Ni nanowires. *Journal of Magnetism and Magnetic Materials*, 249(1):246 – 250, 2002.

[103] V. Franco and A. Conde. Thermal effects in a stoner–wohlfarth model and their influence on magnetic anisotropy determination. *Journal of Magnetism and Magnetic Materials*, 278(1):28 – 38, 2004.

[104] Q. Bian and M. Niewczas. Model for temperature-dependent magnetization of nanocrystalline materials. *Journal of Applied Physics*, 117(1):013909, 2015.

[105] N. Kazantseva, R. Wieser, and U. Nowak. Transition to linear domain walls in nanoconstrictions. *Phys. Rev. Lett.*, 94:037206, 2005.

[106] Jonathan Chico, Corina Etz, Lars Bergqvist, Olle Eriksson, Jonas Fransson, Anna Delin, and Anders Bergman. Thermally driven domain-wall motion in Fe on W(110). *Phys. Rev. B*, 90:014434, 2014.

[107] M. Foeth, P. Stadelmann, and M. Robert. Temperature dependence of the structure and energy of domain walls in a first-order ferroelectric. *Physica A: Statistical Mechanics and its Applications*, 373:439 – 444, 2007.

[108] J.I. Arnaudas, A. del Moral, P.A.J. de Groot, and C. de la Fuente. Non-linear susceptibility and ferromagnetic-like scaling in random magnetic anisotropy alloys. *Journal of Magnetism and Magnetic Materials*, 104-107:216 – 218, 1992.

[109] K.M.B. Alves, L.C. Sampaio, A.P. Guimar aes, and S.F. da Cunha. Coercive field and domain wall properties in $(Dy_xY_{1-x})Fe_2$ and $(Er_xY_{1-x})Fe_2$ intermetallic compounds. *Journal of Alloys and Compounds*, 210(1):325 – 330, 1994.

[110] X. Ning, Z. J. Wang, X. Zhao, C. Shih, W. Chang, and Z. Zhang. Exchange Bias Effect and Magnetic Properties in $La_{0.7}Sr_{0.3}MnO_3$-NiO Nanocomposite Films. *IEEE Transactions on Magnetics*, 50(1):1–4, 2014.

[111] A. Raghunathan, Y. Melikhov, J. E. Snyder, and D. C. Jiles. Theoretical model of temperature dependence of hysteresis based on mean field theory. *IEEE Transactions on Magnetics*, 46(6):1507–1510, 2010.

[112] Roger D. Kirby, Mingjun Yu, and D. J. Sellmyer. Activation volumes in thin film and particulate systems. *Journal of Applied Physics*, 87(9):5696–5698, 2000.

[113] S. Le Gall, F. Montaigne, D. Lacour, M. Hehn, N. Vernier, D. Ravelosona, S. Mangin, S. Andrieu, and T. Hauet. Statistical study of domain-wall depinning induced by magnetic field and current in an epitaxial Co/Ni-based spin-valve wire. *Phys. Rev. B*, 98:024401, 2018.

[114] J. Jorritsma and J. A. Mydosh. Temperature-dependent magnetic anisotropy in ni nanowires. *Journal of Applied Physics*, 84(2):901–906, 1998.

[115] E. C. Bain. The nature of martensite. *Transactions of the American Institute of Mining and Metallurgical Engineers*, 70:25, 1924.

[116] Till Burkert, Olle Eriksson, Peter James, Sergei I. Simak, Börje Johansson, and Lars Nordström. Calculation of uniaxial magnetic anisotropy energy of tetragonal and trigonal Fe, Co, and Ni. *Phys. Rev. B*, 69:104426, 2004.

[117] O. Hjortstam, K. Baberschke, J. M. Wills, B. Johansson, and O. Eriksson. Magnetic anisotropy and magnetostriction in tetragonal and cubic Ni. *Phys. Rev. B*, 55:15026–15032, 1997.

[118] S. Dubois, J. Colin, J. L. Duvail, and L. Piraux. Evidence for strong magnetoelastic effects in Ni nanowires embedded in polycarbonate membranes. *Phys. Rev. B*, 61:14315–14318, 2000.

[119] Kleber R. Pirota, Elvis L. Silva, Daniela Zanchet, David Navas, Manuel Vázquez, Manuel Hernández-Vélez, and Marcelo Knobel. Size effect and surface tension measurements in Ni and Co nanowires. *Phys. Rev. B*, 76:233410, 2007.

[120] Ruqian Wu and A. J. Freeman. Limitation of the magnetic-circular-dichroism spin sum rule for transition metals and importance of the magnetic dipole term. *Phys. Rev. Lett.*, 73:1994–1997, 1994.

[121] H. A. Dürr and G. van der Laan. Magnetic circular x-ray dichroism in transverse geometry: Importance of noncollinear ground state moments. *Phys. Rev. B*, 54:R760–R763, 1996.

[122] S. Andrieu, T. Hauet, M. Gottwald, A. Rajanikanth, L. Calmels, A. M. Bataille, F. Montaigne, S. Mangin, E. Otero, P. Ohresser, P. Le Fèvre, F. Bertran, A. Resta, A. Vlad, A. Coati, and Y. Garreau. Co/Ni multilayers for spintronics: High spin polarization and tunable magnetic anisotropy. *Phys. Rev. Materials*, 2:064410, 2018.

[123] P. Srivastava, N. Haack, H. Wende, R. Chauvistré, and K. Baberschke. Modifications of the electronic structure of Ni/Cu(001) as a function of the film thickness. *Phys. Rev. B*, 56:R4398–R4401, 1997.

[124] O. Hjortstam, J. Trygg, J. M. Wills, B. Johansson, and O. Eriksson. Calculated spin and orbital moments in the surfaces of the 3*d* metals Fe, Co, and Ni and their overlayers on Cu(001). *Phys. Rev. B*, 53:9204–9213, 1996.

[125] Patrick Bruno. Tight-binding approach to the orbital magnetic moment and magnetocrystalline anisotropy of transition-metal monolayers. *Phys. Rev. B*, 39:865–868, 1989.

[126] G. H. O. Daalderop, P. J. Kelly, and M. F. H. Schuurmans. First-principles calculation of the magnetocrystalline anisotropy energy of iron, cobalt, and nickel. *Phys. Rev. B*, 41:11919–11937, 1990.

[127] Richard J. Harrison and Joshua M. Feinberg. Forcinel: An improved algorithm for calculating first-order reversal curve distributions using locally weighted regression smoothing. *Geochemistry, Geophysics, Geosystems*, 9(5).

[128] Shizuo Kadowaki and Minoru Takahashi. Magnetocrystalline anisotropy of nickel-cobalt alloys. *Journal of the Physical Society of Japan*, 38(6):1612–1619, 1975.

[129] J. Pommier, P. Meyer, G. Pénissard, J. Ferré, P. Bruno, and D. Renard. Magnetization reversal in ultrathin ferromagnetic films with perpendicular anistropy: Domain observations. *Phys. Rev. Lett.*, 65:2054–2057, 1990.

[130] T. Ono, H. Miyajima, K. Shigeto, K. Mibu, N. Hosoito, and T. Shinjo. Propagation of a magnetic domain wall in a submicrometer magnetic wire. *Science*, 284(5413):468–470, apr 1999.

[131] Del Atkinson, Dan A. Allwood, Gang Xiong, Michael D. Cooke, Colm C. Faulkner, and Russell P. Cowburn. Magnetic domain-wall dynamics in a submicrometre ferromagnetic structure. *Nature Materials*, 2(2):85–87, 2003.

[132] Geoffrey S. D. Beach, Corneliu Nistor, Carl Knutson, Maxim Tsoi, and James L. Erskine. Dynamics of field-driven domain-wall propagation in ferromagnetic nanowires. *Nature Materials*, 4(10):741–744, 2005.

[133] Yoshinobu Nakatani, André Thiaville, and Jacques Miltat. Faster magnetic walls in rough wires. *Nature Materials*, 2(8):521–523, 2003.

[134] M Welke, J Gräfe, R K Govind, V H Babu, M Trautmann, K-M Schindler, and R Denecke. XMCD studies of thin Co films on $BaTiO_3$. *Journal of Physics: Condensed Matter*, 27(32):326001, 2015.

[135] Isabelle M. L. Billas, A. Châtelain, and Walt A. de Heer. Magnetism from the atom to the bulk in iron, cobalt, and nickel clusters. *Science*, 265(5179):1682–1684, 1994.

[136] Benjamin Glaubitz, Stefan Buschhorn, Frank Brüssing, Radu Abrudan, and Hartmut Zabel. Development of magnetic moments in $Fe_{1-x}Ni_x$. 23(25):254210, 2011.

[137] D. Weller, J. Stöhr, R. Nakajima, A. Carl, M. G. Samant, C. Chappert, R. Mégy, P. Beauvillain, P. Veillet, and G. A. Held. Microscopic origin of magnetic anisotropy in Au/Co/Au probed with x-ray magnetic circular dichroism. *Phys. Rev. Lett.*, 75:3752–3755, 1995.

[138] K. Yang, C. Clavero, J. R. Skuza, M. Varela, and R. A. Lukaszew. Surface plasmon resonance and magneto-optical enhancement on Au–Co nanocomposite thin films. *Journal of Applied Physics*, 107(10):103924, 2010.

[139] Gaspar Armelles, Alfonso Cebollada, Antonio García-Martín, and María Ujué González. Magnetoplasmonics: Combining magnetic and plasmonic functionalities. *Advanced Optical Materials*, 1:10–35, 2013.

[140] D. Martín-Becerra, J. M. García-Martín, Y. Huttel, and G. Armelles. Optical and magneto-optical properties of Au:Co nanoparticles and Co:Au nanoparticles doped magnetoplasmonic systems. *Journal of Applied Physics*, 117(5):053101, 2015.

[141] M. Hennes, X. Weng, E. Fonda, B. Gallas, G. Patriarche, D. Demaille, Y. Zheng, and F. Vidal. Phase separation and surface segregation in Co-Au-$SrTiO_3$ thin films: Self-assembly of bilayered epitaxial nanocolumnar composites. *Phys. Rev. Materials*, 3:035002, 2019.